

**STUDY OF SINGLE AND MULTIJUNCTION BISMUTH-
BASED PEROVSKITE PHOTOVOLTAIC CELLS:
SYNTHESIS, CHARACTERIZATION, SIMULATION,
AND PERFORMANCE**

単接合および多接合ビスマス系ペロブスカイト太陽電池の
研究：合成、特性評価、シミュレーション、性能



Md. Arif Ul Islam

Nagoya Institute of Technology

March 2025

DOCTORAL THESIS TITLE

Study of single and multijunction bismuth-based perovskite photovoltaic cells: Synthesis, characterization, simulation, and performance

Md. Arif Ul Islam

34516003

Supervised by

Prof. Dr. Tetsuo Soga

Department of Electrical and Mechanical Engineering

Nagoya Institute of Technology

Nagoya, Japan

March 2025

ACKNOWLEDGEMENTS

Throughout my PhD journey, I have been overwhelmed by the Almighty's endless blessings and boundless mercy, which have illuminated and eased every step. Without Allah's grace, none of this would have been possible. I am deeply grateful for his blessings throughout this research journey.

In his honor, I would also like to express my gratitude to my esteemed research supervisor, **Professor Dr. Tetsuo Soga**. My research has been greatly influenced by his intellectual guidance, unwavering support, and constant encouragement. There is no doubt that his insightful suggestions, approachability, and his depth knowledge have greatly contributed to my growth in this field, and I have always enjoyed the stimulating discussions we have in his office.

Also, I would like to thank **Associate Professor Dr. Shinay Kato** for her valuable advice and insightful feedback during the intermediate presentations. I am greatly grateful for his thoughtful and sensible comments on my dissertation and research, which have greatly enhanced their quality. A special thanks goes to **Associate Professor Dr. Naoki Kishi** for his valuable comments during the intermediate presentation. His constant encouragement and direction have been invaluable to me on this path. I am profoundly appreciative of **Professor Dr. Satoh Nobuo**, Chiba Institute of Technology, for his invaluable contributions to the enhancement of my dissertation. His constructive feedback and incisive comments have been crucial in the refinement of my research and the improvement of its overall quality. I am deeply thankful for the time and effort he invested in advising me, as his knowledge has motivated me to achieve new levels of excellence in my work.

For their financial support, which has been crucial to enabling this research to be carried out, I would like to express my gratitude to the Ministry of Education, Culture, Sports, Science, and Technology (**MEXT**), Japan. Additionally, I would like to express my sincere gratitude to my laboratory colleagues, whose assistance and support have been invaluable during my PhD research in Japan.

Finally, I wish to thank my family, university colleagues, and well-wishers for their support and encouragement. My pillars of strength throughout this research journey have been their love, care, encouragement, and support.

ABSTRACT

Lead-free copper silver bismuth iodide ($\text{Cu}_6\text{AgBiI}_{10}$), silver bismuth iodide (Ag_3BiI_6), and Methylammonium bismuth iodide $(\text{CH}_3\text{NH}_3)_3\text{BiI}_9$ films are explored in this work with the potential to be used as solar cell active materials. Special optical and photovoltaic characteristics are highlighted. In **Chapter 2** explores the importance of creating ecologically friendly materials for solar energy uses, underscoring the necessity of finding substitutes for conventional lead-based compounds. We report on the first thorough investigation of the best annealing temperature for $\text{Cu}_6\text{AgBiI}_{10}$ films, which are made by hot-casting droplets on substrates that have already been heated in a single step spin coating. The trigonal crystal structure was validated by structural characterization using X-ray diffraction (XRD), surface morphology was shown by scanning electron microscopy (SEM), and uniform elemental distribution was guaranteed by energy dispersive X-ray spectroscopy (EDX). The n-i-p structure's optical ($\text{ITO}/\text{SnO}_2/\text{Cu}_6\text{AgBiI}_{10}$) and photovoltaic ($\text{ITO}/\text{SnO}_2/\text{Cu}_6\text{AgBiI}_{10}/\text{P3HT}/\text{C}/\text{Ag}$) properties were studied, and the results showed a low reflectivity and high absorbance at 150 °C. According to analysis of photovoltaic attributes, we were able to achieve maximum current density of 0.45 mA/cm² and power conversion efficiency of 0.041%. As part of **Chapter 3**, we study several combinations of hole transport layers (HTLs) (such as Spiro-OMeTAD, P3HT, PEDOT:PSS, CuSCN, CuI and NiO_x) with (c+mp) TiO_2 as electron transport layers (ETLs) and $\text{Cu}_6\text{AgBiI}_{10}$ as absorbers. We found the best device structures ($\text{FTO}/(\text{c+mp})\text{TiO}_2/\text{Cu}_6\text{AgBiI}_{10}/\text{CuSCN}/\text{Au}$) that resulted in better PCEs via computations and experimentation; the best structure achieved 2.06% efficiency. In the next study, insights from **Chapters 4 and 5** are synthesized Ag_3BiI_6 film. These include optimization of non-toxic perovskites, especially Ag_3BiI_6 , single junctions, and their tandem integration with silicon. The remarkable efficiency of inspired perovskite solar cells has attracted a lot of attention, as seen

in **Chapter 4**. The study determines the most effective organic hole-transport layer (HTL) for the FTO/(c+mp)TiO₂/Ag₃BiI₆/HTLs/Au configuration, using experimental methods and SCAPS-1D simulations. It was found that by meticulously optimizing the total defect density and thickness of the absorbing layer, notable improvements in efficiency were achieved for Spiro-OMeTAD (8.50%), PTAA (7.20%), P3HT (7.60%), and PEDOT:PSS (7.00%). The Rudorffites/Silicon-based two terminal (2T) tandem solar cells are examined for the first time in **Chapter 5**, which shows that they have the potential to achieve hitherto unheard-of levels of efficiency. The efficiency of Ag₃BiI₆ increased from 5.77% to a remarkable 15.26%. Similarly, there was a significant improvement in the efficiency of Ag₂BiI₅, with an increase from 4.10% to 10.59%. Finally, AgBiI₄ shows significant improvement, with efficiency increasing from 4.06% to 10.44%. The 2T double junction solar cell configuration was investigated by combining rudorffites top cells with silicon bottom cells. According to the results, the efficiency of Ag₃BiI₆, Ag₂BiI₅, and AgBiI₄ tandem solar cells was 22.31%, 18.63%, and 18.89%, respectively, showing remarkable improvements over their single-cell counterparts. In **Chapter 6**, we performed experimental and simulations to enhance the efficiency of 2T perovskite/perovskite double junction and perovskite/perovskite/c-Si triple junction solar cells by using the MA₃Bi₂I₉ material. The power conversion efficiency was greatly increased by using 2T triple junction solar cells; the increase was around 116.59% from single junction (13.80% to 29.89%) and 31.91% from double junction (22.66% to 29.89%). As far as we know, this is the first investigation into the efficacy of MA₃Bi₂I₉ as a top layer in multijunction tandem configurations. This revolutionary approach allows both academics and industry experts to produce cost-effective and efficient tandem solar cells, thereby enhancing earth-based solar-energy development. The results of this research may help us

understand bismuth-based solar cells better, especially when it comes to their use in several types of junction designs (single, double, and triple).

CONTENTS

Contents

DOCTORAL THESIS TITLE	II
ACKNOWLEDGEMENTS	III
ABSTRACT	V
CONTENTS	VIII
LIST OF TABLES	XIII
LIST OF FIGURES	XIV
Chapter 1	22
Introduction	22
1.1 Background of study	22
1.2 Solar spectrum	23
1.3 Photovoltaic solar cells	24
1.4 Perovskite solar cells	26
1.5 Bismuth base perovskite solar cells	30
1.6 Perovskite base multi-junction solar cells	37
1.7 Research aims and objectives	41
1.8 Thesis outline	42
1.9 References	43
Chapter 2	64
Photovoltaic and surface morphological improvements of a novel material class $\text{Cu}_6\text{AgBiI}_{10}$...	64
2.1 Introduction	64
2.2 Experimental section	65

2.2.1 Chemicals	65
2.2.2 Cu ₆ AgBiI ₁₀ (CABI) thin film fabrication.....	65
2.2.3 CABI photovoltaic device fabrication.....	67
2.2.4 Characterization	68
2.3 Results and discussion	68
2.3.1 Structural analysis	68
2.3.2 Morphological and elemental analysis.....	71
2.3.3 Optical properties	79
2.3.4 Photovoltaic properties.....	81
2.4 Conclusions	84
2.5 References	85
Chapter 3	93
Study of Cu ₆ BiAgI ₁₀ perovskite with various organic and inorganic hole transport layers for improved photovoltaic performance	93
3.1 Introduction	93
3.2 Experimental and numerical simulation section.....	95
3.2.1 Chemicals	95
3.2.2 Cu ₆ AgBiI ₁₀ film fabrication on the electron transport layer (ETL)	95
3.2.3 Simulation methodology using SCAPS-1D	97
3.2.4 Cu ₆ AgBiI ₁₀ photovoltaic device structure.....	98
3.2.5 Characterization	101
3.3 Results and discussion	101
3.3.1 Experimental analysis	101

3.3.2 SCAPS-1D numerical simulation analysis.....	106
3.4 Conclusions	121
3.5 References	121
Chapter 4.....	128
Role of organic HTLs enhance the efficiency of Ag_3BiI_6 solar cells through the integration of experiment and simulation.....	128
4.1 Introduction	128
4.2 Experimental analysis and simulation modeling section.....	129
4.2.1 Chemical and reagents	129
4.2.2 Ag-Bi-I thin film fabrication process	130
4.2.3 Simulation modeling methodology	132
4.2.4 Ag_3BiI_6 solar cells device's structure.....	132
4.2.5 Measurements and characterizations.....	136
4.3 Results and discussion	136
4.3.1 Section of experimental investigation	136
4.3.2 Section of simulation analysis.....	146
4.4 Conclusions	166
4.5 References	167
Chapter 5.....	174
Tandem solar cell approach to unlocking the potential of Rudorffite/silicon combinations	174
5.1 Introduction	174
5.2 Simulation methodology.....	175
5.2.1 Device structure and simulation parameters	176

5.3 Result and discussion.....	183
5.3.1 Analysis of Rudorffite base top cell.....	183
5.3.2 Performance analysis of tandem cell.....	195
5.4 Conclusion.....	203
5.5 References	204
Chapter 6.....	209
Integrated study of perovskite/perovskite/c-Si triple junction solar cells with methylammonium bismuth iodide as a key component.....	209
6.1 Introduction	209
6.2 Experimental and simulation procedures	211
6.2.1 Chemicals and reagents.....	211
6.2.2 Fabrication of MBI top cell material.....	211
6.2.3 Measurements and characterizations.....	213
6.2.4 Device structure and simulation methodology.....	213
6.3 Experimental properties of top cell material	221
6.3.1 Morphology and structural properties analysis	221
6.3.2 Optical Properties Analysis.....	223
6.4 Simulation analysis of top cell.....	225
6.4.1 Energy alignment, generation and recombination rate analysis.....	225
6.4.2 Current density vs voltage (J-V) and quantum efficiency (QE) analysis.....	228
6.4.3 Impact of MBI thickness and total defect density	230
6.5 Simulation performance of 2T tandem cell	237
6.5.1 $\text{MA}_3\text{Bi}_2\text{I}_9/\text{FA}_x\text{Cs}_{1-x}\text{PbI}_3$ double junction cell	237

6.5.2 MA ₃ Bi ₂ I ₉ /FA _{0.45} Cs _{0.55} PbI ₃ /Si triple junction cell	243
6.6 Conclusion	247
6.7 References	248
Chapter 7	254
Conclusions	254
7.1 Conclusions	254
7.2 Future prospective	256
LIST OF PUBLICATIONS	258

LIST OF TABLES

Table 2.1 Comparative study of EDS elemental analysis of $\text{Cu}_6\text{AgBiI}_{10}$ film under various annealing temperature conditions.	77
Table 3.1 Input parameters of the FTO, ETL, Absorber layer and HTLs.....	100
Table 4.1 Numerical input parameters of the FTO, (c+mp) TiO_2 , SBI, and organic HTLs.....	135
Table 4.2 The elemental analysis of Ag_3BiI_6 film measured using EDS under optimum conditions.	139
Table 4.3 Ag_3BiI_6 -based solar cell experimental and theoretical performance comparison.....	165
Table 5.1 Presents the top cell input parameters that were collected from both the experiment and simulation studies.....	179
Table 5.2 Presents the bottom cell input parameters that were collected from both the experiment and simulation studies.....	180
Table 5.3 PV parameters of top, bottom and 2T tandem cell.....	201
Table 6.1 Employed input parameters for SCAPS-1D's top and middle sub cells.....	218
Table 6.2 Employed input parameters for SCAPS-1D's bottom sub cell.	219
Table 6.3 The input parameter for the interface layer with defects.	220
Table 6.4 Optimized numerical input parameters of the top cell and middle cell.	239
Table 6.5 Compared with and without current matching, output parameters of top, middle, and bottom, 2T double junction and 2T triple junction solar cells.....	246

LIST OF FIGURES

Figure 1.1 Energy spectrum above the atmosphere and at the surface of the earth.	24
Figure 1.2 Photovoltaic Solar cell.	25
Figure 1.3 Perovskite crystal structure ABX_3	27
Figure 1.4 Based on NREL's chart on perovskite solar cells efficiency.	28
Figure 1.5 Human health effects of toxic-lead exposure.	28
Figure 1.6 Bi-based perovskites solar cells: potential advantages.	31
Figure 1.7 Double perovskite crystal structure $A_2B'B''X_6$	32
Figure 1.8 Rudorffite crystal structure $NaVO_2$	34
Figure 1.9 (a) 2T and (c) 4T double-junction solar cells; (b) 2T and (d) 4T triple-junction solar cells.	38
Figure 1.10 Maximum efficiency chart of multi-junction solar cells.	39
Figure 2.1 Schematic flow diagram steps of Cu_6AgBiI_{10} thin film preparation.	66
Figure 2.2 n-i-p type device structure of the Cu_6AgBiI_{10} solar cell.	67
Figure 2.3 Experimental XRD signature of the $ITO/SnO_2/Cu_6AgBiI_{10}$ films at various annealing temperatures.	69
Figure 2.4 Three-dimensional crystal structure of Cu_6AgBiI_{10} film.	70
Figure 2.5 The changes of crystallite size as a result of annealing temperatures for Cu_6AgBiI_{10} film.	70
Figure 2.6 The top view of SEM images with various annealing temperatures of Cu_6AgBiI_{10} film on the ITO/SnO_2 structure.	73
Figure 2.7 Visual representation of the grain size distribution histogram of Cu_6AgBiI_{10} film under various annealing temperature conditions.	74

Figure 2.8 EDS elemental analysis of $\text{Cu}_6\text{AgBiI}_{10}$ film under various annealing temperature conditions (a) 130 °C, (b) 140 °C, (c) 150 °C, (d) 160 °C and (e) 170 °C.	76
Figure 2.9 EDS elemental profile of $\text{Cu}_6\text{AgBiI}_{10}$ film at 130 °C annealing temperature.	78
Figure 2.10 Reflectance spectra of $\text{Cu}_6\text{AgBiI}_{10}$ film at various annealing temperatures.	79
Figure 2.11 Absorbance spectra of $\text{Cu}_6\text{AgBiI}_{10}$ films at various annealing temperatures.	80
Figure 2.12 Current density-voltage curves of the CABI solar cells and J-V curve fitting by using Lambert W function at various annealing temperatures.	82
Figure 2.13 Variation of (a) film thickness, (b) Short circuit current density, (c) Open circuit voltage and (d) Efficiency with different annealing temperature of $\text{Cu}_6\text{AgBiI}_{10}$ solar cells.	83
Figure 3.1 Schematic flowchart of steps in the $\text{Cu}_6\text{AgBiI}_{10}$ film on $\text{FTO}/(\text{c}+\text{mp})\text{TiO}_2$ sample.	96
Figure 3.2 Conventional type device architecture and crystal structure of the $\text{Cu}_6\text{AgBiI}_{10}$ solar cell.	99
Figure 3.3 The $\text{FTO}/(\text{c}+\text{mp})\text{TiO}_2/\text{Cu}_6\text{AgBiI}_{10}$ film's experimental XRD profile at 150°C temperature.	102
Figure 3.4 SEM image at 150 °C annealing temperature of $\text{Cu}_6\text{AgBiI}_{10}$ film on the $\text{FTO}/(\text{c}+\text{mp})\text{TiO}_2$ structure.	104
Figure 3.5 Optical property of $\text{Cu}_6\text{AgBiI}_{10}$ film on coated $\text{FTO}/(\text{c}+\text{mp})\text{TiO}_2$ layer with annealing temperatures of 150°C: (a) Transmittance spectra, (b) Reflectance spectra, (c) Absorbance spectra, and (d) Tauc plot used for the calculation of energy band gap.	105
Figure 3.6 The n-i-p structure of CABI's solar cell devices energy band diagram with varying HTLs (a) Spiro-OMeTAD, (b) P3HT, (c) PEDOT:PSS, (d) CuSCN, (e) CuI, and (f) NiOx.	107
Figure 3.7 Various of the optimized parameter of the PV devices, i.e. V_{OC} J_{SC} , FF and PCE in the CABI absorber layer of structures, of $(\text{c}+\text{mp})\text{TiO}_2$ as an ETL using Au as the back contact as well	

as (a) Spiro-OMeTAD, (b) P3HT, (c) PEDOT:PSS (d) CuSCN, (e) CuI and (f) NiO _x , for the HTLs.	109
Figure 3.8 Effect of (a) J-V, and (b) QE for CABI solar cells with various HTL.	110
Figure 3.9 Analyzing (a) the rate of generation and (b) the rate of recombination in solar cells of CABI with different HTL.	112
Figure 3.10 Capacitance vs frequency curves with Nyquist plot of the CABI absorber layer.	114
Figure 3.11 Contour mapping of V _{OC} relative to the thickness of the CABI absorber and HTLs.	117
Figure 3.12 Contour mapping of J _{SC} relative to the thickness of the CABI absorber and HTLs.	117
Figure 3.13 Contour mapping of FF relative to the thickness of the CABI absorber and HTLs.	118
Figure 3.14 Contour mapping of efficiency relative to the thickness of the CABI absorber and HTLs.	118
Figure 3.15 Variation of (c+mp) TiO ₂ layer thickness with CABI absorber, and different HTLs such as (a) Spiro-OMeTAD, (b) P3HT, (c) PEDOT:PSS, (d) CuSCN, (e) CuI and (f) NiO _x .	120
Figure 4.1 Schematic flow chart showing the procedures involved in preparing Ag ₃ BiI ₆ films.	131
Figure 4.2 Device architecture of conventional n-i-p type of the Ag ₃ BiI ₆ solar cell.	133
Figure 4.3 The XRD profile of 50 wt% Ag ₃ BiI ₆ film, annealed at 100 °C with CB antisolvent.	137
Figure 4.4 The XRD profile of FTO/(c+mp)TiO ₂ thin film.	138
Figure 4.5 The EDS elemental distribution maps of Ag ₃ BiI ₆ films under optimal conditions.	139

Figure 4.6 SEM image of Ag_3BiI_6 film on the FTO/ETL layer after annealing at 100°C in the presence of CB antisolvent.	140
Figure 4.7 With 100°C annealing, Ag_3BiI_6 film shows a) transmittance spectrum, b) reflectance spectrum, c) absorbance spectrum, and d) Tauc plot for energy band gap calculation.	141
Figure 4.8 With 100°C annealing, Ag_3BiI_6 film shows a) extinction coefficient, b) refractive index, c) real part of dielectric constant, and d) imaginary part of dielectric constant with respect to wavelength.	143
Figure 4.9 With 100°C annealing, Ag_3BiI_6 film shows a) dielectric loss and b) optical conductivity, with respect to wavelength.....	145
Figure 4.10 The Energy band diagram for four of SBI's solar cell devices (a) Spiro-OMeTAD, (b) PTAA, (c) P3HT, and (d) PEDOT:PSS.	147
Figure 4.11 The PV devices optimized parameters e.g., the V_{OC} , J_{SC} , FF, and PCE, for FTO/(c+mp)TiO ₂ / Ag_3BiI_6 /HTLs/Au structures with four HTLs such as (a) Spiro-OMeTAD, (b) PTAA, (c) P3HT, and (d) PEDOT:PSS.	149
Figure 4.12 (a) J-V and (b) QE effects on Ag_3BiI_6 solar cells with different HTLs.....	150
Figure 4.13 SBI solar cells with different organic HTLs for (a) generation and (b) recombination rates.	152
Figure 4.14 Curves of C-f with Nyquist plots of SBI absorb layers.....	154
Figure 4.15 Contour mapping of J_{SC} relative to total defect density and thickness of the SBI, keeping the fixed ETL and HTLs.	156
Figure 4.16 Contour mapping of V_{OC} relative to total defect density and thickness of the SBI, keeping the fixed ETL and HTLs.	157

Figure 4.17 Contour mapping of FF relative to total defect density and thickness of the SBI, keeping the fixed ETL and HTLs.	158
Figure 4.18 Contour mapping of PCE relative to total defect density and thickness of the SBI, keeping the fixed ETL and HTLs.	159
Figure 4.19 Variation of HTLs thickness such as (a) Spiro-OMeTAD, (b) PTAA, (c)P3HT, and (d) PEDOT:PSS with respect to performance, keeping the fixed SBI and ETL thickness.	162
Figure 5.1 illustrates the device layout of a typical (a) single junction of Top and Bottom Cell and (b) 2T double junction Tandem cell.....	178
Figure 5.2 shows the device spectrums for (a) the top sub-cell's AM1.5 spectrum illumination, (b) the bottom sub-cell's filtered AM1.5 spectrum illumination (from Ag_3BiI_6 cell), (c) the bottom sub-cell's filtered AM1.5 spectrum illumination (from Ag_2BiI_5 cell), and (d) the bottom sub-cell's schematic illumination by AM1.5 spectrum illumination (from AgBiI_4 cell).....	181
Figure 5.3 Solar cell's parameters as a function of thickness of absorbing layer (a, b) Ag_3BiI_6 (c, d) Ag_2BiI_5 (e, f) AgBiI_4	185
Figure 5.4 illustrates the variation of (a) J_{sc} , (b) V_{oc} , (c) FF, and (d) PCE in relation to the thickness variation of PEDOT:PSS as HTL.	186
Figure 5.5 The impact of J-V on solar cell devices as the PCBM thickness varies for (a) Ag_3BiI_6 , (b) Ag_2BiI_5 , and (c) AgBiI_4 devices.....	187
Figure 5.6 Impact of J_{sc} , V_{oc} , FF, and PCE on the total defect density of (a) Ag_3BiI_6 , (b) Ag_2BiI_5 , and (c) AgBiI_4 solar devices.	189
Figure 5.7 The PV parameters vary in relation to the interface defect density for the following scenarios: (a) PEDOT:PSS/ Ag_3BiI_6 interface, (b) Ag_3BiI_6 /PCBM interface, (c)	

PEDOT:PSS/Ag ₂ BiI ₅ interface, (d) Ag ₂ BiI ₅ /PCBM interface, (e) PEDOT:PSS/AgBiI ₄ interface, and (f) AgBiI ₄ /PCBM interface.	191
Figure 5.8 The Nyquist plot of impedance for (a) Ag ₃ BiI ₆ , (b) Ag ₂ BiI ₅ , and (c) AgBiI ₄ solar cells varies with bias voltage.....	194
Figure 5.9 (a) The J-V characteristics of rudorffite cells under optimized condition, (b) the QE with respect to wavelength of the rudorffite cells under optimized condition, (c) J-V characteristics of the Si base cell (unfiltered Spectrum), (d) QE with respect to wavelength of the Si base cell.	196
Figure 5. 10 The 2T Tandem Cell's Energy Band Diagram.	198
Figure 5.11 The current matching between the top cells, namely (a) Ag ₃ BiI ₆ , (c) Ag ₂ BiI ₅ , and (e) AgBiI ₄ , and the bottom sub-cells are dependent on the thickness of c-Si in the bottom cell. The J-V characteristics for the 2T tandem cell and the top and bottom sub-cells under the present without matching and matching situation are shown in (b), (d), and (f).....	200
Figure 5. 12 (a) The current matching between the top cells and the bottom sub-cells with varying thickness of Ag ₃ BiI ₆ base top cell, and (b) The J-V characteristics for the 2T tandem cell and the top and bottom sub-cells under the present matching situation.	203
Figure 6.1 Diagram showing the deposition steps for ITO/(c+mp)TiO ₂ /MA ₃ Bi ₂ I ₉ film preparation.....	212
Figure 6.2 (a) The configuration of 2T Perovskite/Perovskite/c-Si Triple junction solar cell, and (b) the alignment of each energy band. FA _{0.45} CS _{0.55} PbI ₃ was assumed as FCPI.	215
Figure 6.3 (a) the standard AM1.5G spectrum illuminates on the top cell, (b) middle cell uses 1 st filtered spectrum from top sub-cell, and (c) bottom cell uses 2 nd filtered spectrum from both top and middle cells.	216

Figure 6.4 The Flake-shaped MBI surface morphology at 150°C.....	221
Figure 6.5 (a) XRD analysis of MBI film annealed at 150°C and (b) crystal structure.	222
Figure 6.6 At the post-annealing temperature, MBI film presents the following: (a) transmittance spectrum; (b) reflectance spectrum; (c) absorbance spectrum; and (d) optical band gap.....	224
Figure 6.7 The alignment of the energy bands of MBI base solar cells with different HTLs: (a) CuSCN, (b) Spiro-OMeTAD, (c) NiO _x , and (d) PEDOT:PSS.....	226
Figure 6.8 MBI base solar cells with various HTLs: (a) generation and (b) recombination rates.	227
Figure 6.9 Examination of the (a) J-V and (b) QE characteristics of MBI solar cells with varying HTLs.	229
Figure 6.10 Contour mapping: the variation of Voc with respect to the combined total defect density and thickness of the MBI, for (a) CuSCN, (b) Spiro-OMeTAD, (c) NiO _x and (d) PEDOT:PSS.....	231
Figure 6.11 Contour mapping: the variation of Jsc with respect to the combined total defect density and thickness of the MBI, for (a) CuSCN, (b) Spiro-OMeTAD, (c) NiO _x and (d) PEDOT:PSS.	232
Figure 6.12 Contour mapping: the variation of FF with respect to the combined total defect density and thickness of the MBI, for (a) CuSCN, (b) Spiro-OMeTAD, (c) NiO _x and (d) PEDOT:PSS.	233
Figure 6.13 Contour mapping: the variation of PCE with respect to the combined total defect density and thickness of the MBI, for (a) CuSCN, (b) Spiro-OMeTAD, (c) NiO _x and (d) PEDOT:PSS.....	234

Figure 6.14 J-V characteristics 2T double junction solar cells with current matching conditions for the various middle cells: (a) CsPbI_3 , (b) $\text{FA}_{0.15}\text{Cs}_{0.85}\text{PbI}_3$, (c) $\text{FA}_{0.45}\text{Cs}_{0.55}\text{PbI}_3$, (d) $\text{FA}_{0.75}\text{Cs}_{0.25}\text{PbI}_3$, and (e) FAPbI_3 240

Figure 6.15 (a) J_{sc} for the top and bottom junction solar cell depending on the two absorbing thicknesses, (b) J-V characteristics top, bottom and 2T double junction solar cells with current matching, and (c) their top and bottom junction QE. 241

Figure 6.16 J-V characteristics 2T triple junction solar cells with current matching conditions for the various middle cells: (a) CsPbI_3 , (b) $\text{FA}_{0.15}\text{Cs}_{0.85}\text{PbI}_3$, (c) $\text{FA}_{0.45}\text{Cs}_{0.55}\text{PbI}_3$, (d) $\text{FA}_{0.75}\text{Cs}_{0.25}\text{PbI}_3$, and (e) FAPbI_3 244

Figure 6.17 (a) J_{sc} for the top and bottom junction solar cell depending on the two absorbing thicknesses, (b) J-V characteristics top, middle, bottom and 2T triple junction solar cells with current matching, and (c) their top, middle and bottom junction QE. 245

Chapter 1

Introduction

1.1 Background of study

The world's economy has seen rapid development and has made it difficult for traditional fossil fuel energy to meet our energy needs. Due to global crises in energy and resources, ecology, climate change, as well as other environmental issues, the 21st century saw unprecedented challenges for humanity. All of these issues played a part of the rise of the green industry revolution. Solar energy is expected to become the primary source of energy because of its many benefits, including being renewable, clean, and abundant in energy.¹ In order to ensure that the world is not dependent on fossil fuels, the solar cells research has increased exponentially over the last several decades.²⁻⁸ Photovoltaic (PV) technology is safer and one of the most effective methods for energy production across the world that can help reduce emissions of greenhouse gases and can serve as a substitute for fossil or nuclear fuels. The technology is more environmentally sustainable and safe technology. Photovoltaic is a method of energy production that helps reduce dependence on fossil fuels and can be utilized to encourage the use and development of renewable energy sources.^{9,10} Also, solar cell research is now the focus of many researchers as the demand for renewable and eco-friendly energy sources is on the rising. Due to the increasing concerns over the effects of climate change, fossil fuel exhaustion, and other environmental concerns, it is crucial to develop technologies that generate energy more efficiently and are environmentally friendly. Additionally, the emphasis on solar cell technology could lead

to the creation of advanced materials, and new technologies that will improve the efficiency of the development of renewable energy.^{11,12}

1.2 Solar spectrum

Solar cell technology is based on the range of wavelengths that solar cells can convert into energy, which is determined by the sun's spectrum. Researchers can optimize solar cell materials and designs to maximize energy absorption, by studying the spectrum. In order to ensure effective energy harvesting, studying the sun spectrum also aids in forecasting solar panel performance under various environmental circumstances. By understanding the solar spectrum, solar cells can be made more efficient and applicable, contributing to the advancement of solar energy.¹³ The electromagnetic radiation that is produced by nuclear fusion in the Sun's core and released as the solar spectrum has a wide range of wavelengths. Massive amounts of energy in the form of photons are released as hydrogen nuclei collide and fuse to generate helium during this process. Electromagnetic waves are emitted when charged particles interact with the Sun's powerful gravitational and magnetic fields. As the radiation is generated, it propagates through space, heading towards the planet. Various interactions occur when solar radiation encounters Earth's atmosphere, including absorption, scattering, and reflection, which dramatically change its intensity and spectrum.¹⁴ The Sun's spectrum is classified by "Air Mass" (AM), which describes the wavelength of sunlight as it travels through the atmosphere. An example is AM0, a measurement of solar irradiance at the top of the atmosphere, which is free of atmospheric interference. Contrarily, the AM1.5 G spectra represents the whole solar spectrum taken at an angle of 48.2 degrees from zenith, which takes atmospheric factors into consideration and includes both direct and diffuse sunlight. Such classification is very valuable for assessing the efficiency of solar panels in practical scenarios. In contrast, AM1.5 D specifically targets direct sunlight at the

same angle, providing a more focused analysis of the solar energy that may be directly captured, without any interference from air scattering.

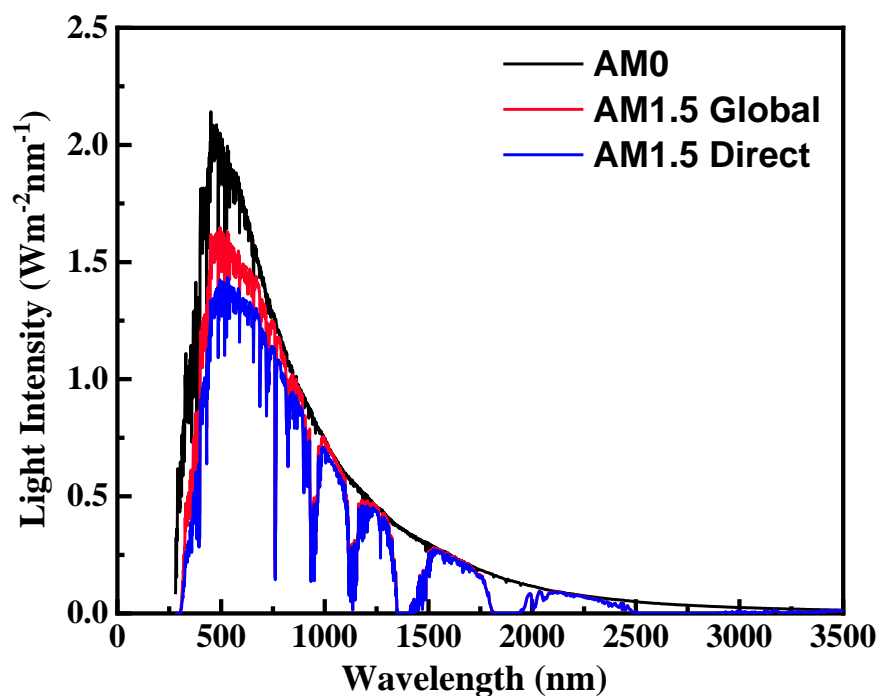


Figure 1.1 Energy spectrum above the atmosphere and at the surface of the earth.

These categories together provide useful insights for evaluating the potential of solar energy and maximizing the uses of solar technology.¹⁵ **Figure 1.1** shows the energy spectrum of AM0, AM1.5 Global, and AM1.5 Direct, which demonstrate their importance in solar energy research.

1.3 Photovoltaic solar cells

Solar cells are amazing devices that use semiconductor materials and the photovoltaic effect to turn sunshine into power. These materials absorb photons that have energy greater than the bandgap of the semiconductor when they are exposed to light as shown in **Figure 1.2**. The absorption of light causes the production of charge carriers: electrons migrate to the conduction

band, while holes are formed in the valence band, therefore facilitating the flow of electric current.¹⁶

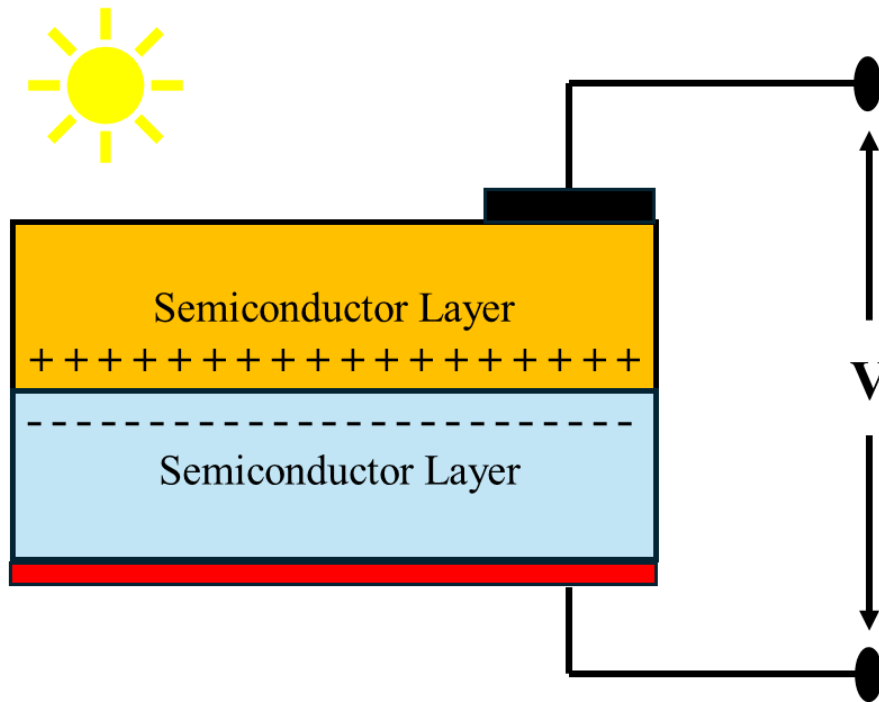


Figure 1.2 Photovoltaic Solar cell.

The origin of solar cell technology may be traced back to 1954 when Bell Labs produced the first solar cell made from single-crystal silicon.¹⁷ This photovoltaic device achieved an energy conversion efficiency of 6%. At first, these solar cells were mostly used in space applications, such as propulsion of satellites, where economic factors were of little importance. In 1955, the first commercially available solar cell made on silicon was shown; its efficiency was a meagre 2%.¹⁸ Residential solar cell adoption was slow due to high manufacturing costs; but, after the 1973 energy crisis, their popularity started to surge in daily applications. An important step forward was made in 1980 when the Institute of Energy Conversion developed thin-film solar cells. These cells had a cheap production cost and a 10% efficiency.¹⁹ Next year, the Kyocera Corporation began

large-scale manufacturing of polysilicon solar cells by using cutting-edge casting methods.¹⁹ The field of solar technology saw a significant shift in 1991 with the introduction of dye-sensitized solar cells (DSSCs) by researchers Michael Gratzel and Brian O'Regan.²⁰ The development of these cells achieved a 50% reduction in manufacturing costs when compared to conventional silicon cells by using solution processing. In the third generation of solar technologies, perovskite solar cells (PSCs) were developed as research advanced, drawing inspiration from the fundamental concepts of dye-sensitized solar cells.²¹ A prospective alternative to conventional silicon solar cells, PSCs have garnered substantial attention due to their competitive power conversion efficiencies (PCEs). These days, the development of cutting-edge materials and creative production processes is the main emphasis of solar technology. The objective is to further down expenses and improve efficiency, hence increasing the accessibility and sustainability of solar energy. Perovskite solar cells stand out as a crucial component in the ongoing evolution of photovoltaics, contributing to the search for more economical and efficient solar energy solutions.

1.4 Perovskite solar cells

Due to their low cost and ease of manufacture, perovskites are popular in research on solar cells. They also have the potential to achieve high efficiency. The term "perovskite" refers to the mineral calcium titanium oxide, which was found in the Ural Mountains in Russia in 1839 by German mineralogist Gustav Rose. Since then, any compound having a comparable crystal structure, whether organic or inorganic, can be referred to as a perovskite.²² The materials possess same crystal structure called perovskite, which is presented by the ABX_3 formula, as shown in **Figure 1.3**. This refers to how the cations and anions are arranged in the material, in which A is the metal

cation mostly from Group I, B represents the divalent metal cation that is the transitional metal, while anion X is the halide group.^{23–26}

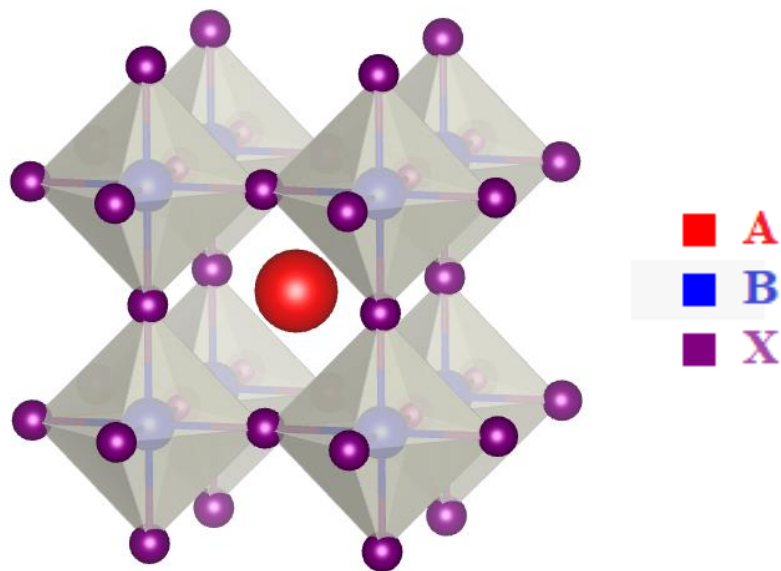


Figure 1.3 Perovskite crystal structure ABX₃.

Prominent optoelectronic properties of hybrid perovskite solar cell materials have led to being widely considered as one of the future's most promising candidates in photovoltaic technology. The perovskite photovoltaic technology has gained wide attention due to its low cost and greater than 25% certified efficiency in single junction architectures. This is almost comparable to silicon solar cells.^{27–30} The perovskite cell is now commercially attractive due to its low production cost and potential for higher efficiencies. Their short-term to longer-term stability is a research priority. In less than 10 years, research has revealed that the organic-inorganic-halide-based cells with Pb are experiencing a significant improvement in their efficiency as shown in **Figure 1.4**. Although they may have some advantages, lead is a very harmful material that can lead to grave health issues

for humans and animals as shown in **Figure 1.5**.³¹ Additionally, disposal of batteries and electronics made of lead poses a major environmental threat.

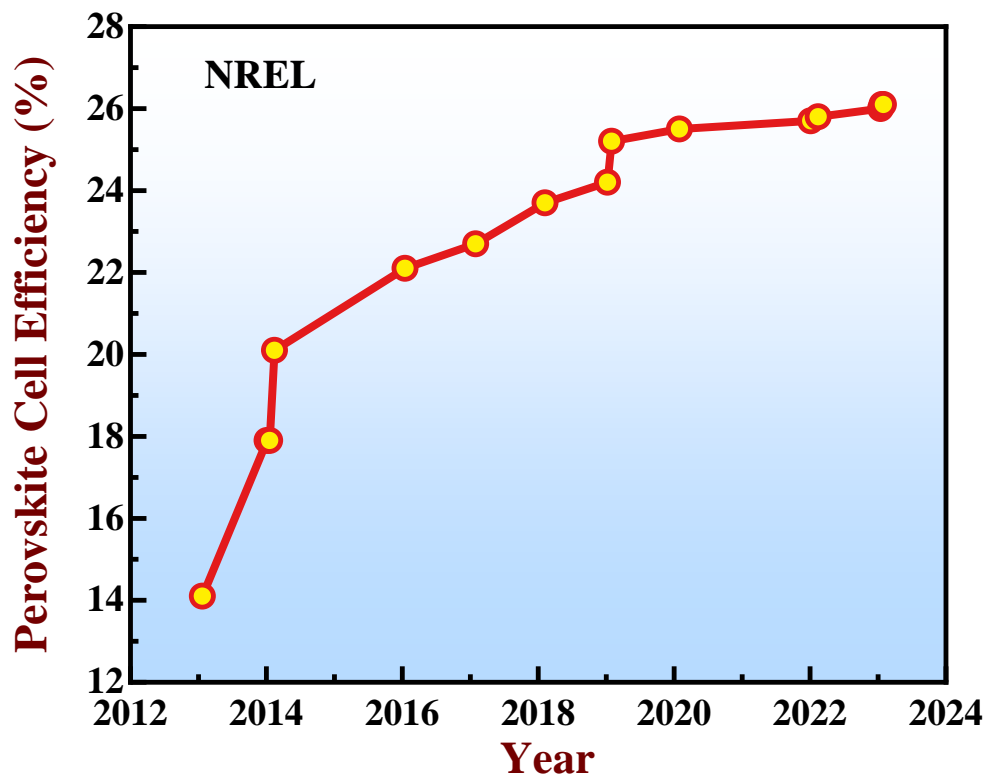


Figure 1.4 Based on NREL's chart on perovskite solar cells efficiency.³²

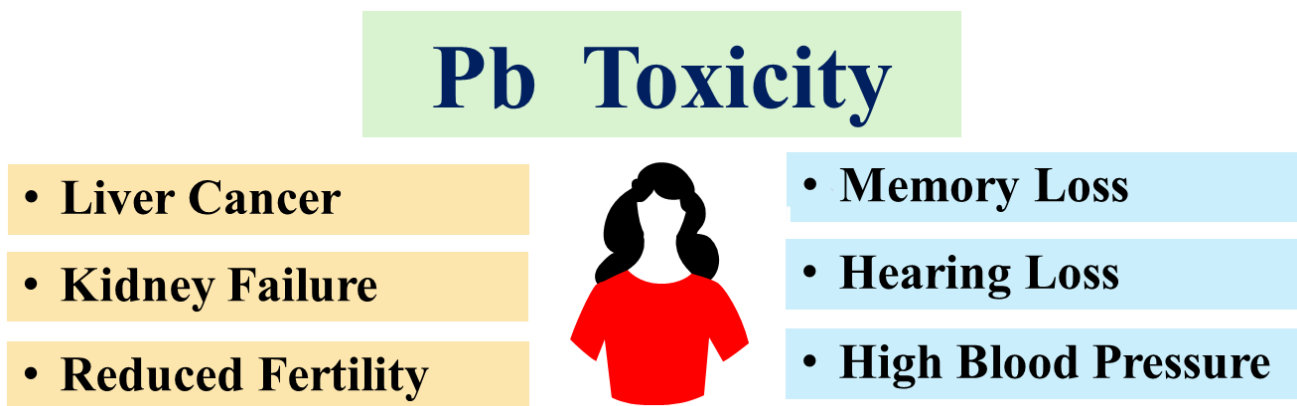


Figure 1.5 Human health effects of toxic-lead exposure.

Researchers are working on lead-free perovskite solar cells in response to health and environmental concerns.³³ Lead-free perovskite solar cells offer an alternative to conventional solar cells that contain lead. They are eco-friendly, are non-toxic and offer the potential of being highly efficient. Therefore, research into lead-free perovskite solar cells is crucial in advancing the transition to an environmentally sustainable and safer energy sector. There has been some progress in the creation of fully or partially Pb-free solar cells made of metals like Ge^{2+} and Sn^{2+} . Trivalent Bi^{3+} and Sb^{3+} can also be employed, as are the tetravalent Ge^{4+} as well as Sn^{4+} . In all these possibilities, there are only Sn -based PSCs that have reached acceptable efficiency. This is due to their comparable outer electron orbits ($ns^2 np^2$) and Ion radii Sn^{2+} (135 pm) as compared with Pb^{2+} (149 pm). They also have tunable bandgaps and the ability to move carriers with high mobility.^{34–}

³⁶ Unfortunately, because of the spontaneous oxidation process that transforms Sn^{2+} to Sn^{4+} , in the presence of oxygen and moisture, Sn-based films undergo irreparable degradation, which results in Sn vacancies. This oxidation triggers an accelerated phase transition, the degradation of the material when exposed to thermal or light stress. Ge-based perovskites face a more severe oxidation problem than Sn-based perovskites due to its $4s^2$ (Ge^{2+}) electronic structure, which quickly eliminates the single electron pair. This may lead to the development of low dimensional perovskites with drastically reduced electrical conductivities. Perovskites that are based on Ge exhibit higher defects. The instability of the material and the high density of defects limit the power conversion efficiency (PCE) of Ge-based solar cells.^{37–42} Similarly, bismuth belongs to group 15 in the periodic table and has similar electrical configuration. Its ionic radius is also comparable with that of lead. Bi is almost nontoxic compared to Pb. Perovskites that are based on the lead halide have stability and some health concerns. Bismuth-based perovskites are the newest area of study since they can solve both issues simultaneously.

1.5 Bismuth base perovskite solar cells

Solar cells based on Bi and Sb halide perovskites and their derivatives have emerged as promising research avenues because of their excellent stability and non-toxicity. The two elements Bi and Sb are also readily available from natural sources in large quantities. The group VA metal halide-based perovskite and its derivatives have recently undergone significant advances in photovoltaic research. In the context of photovoltaics, searching for Bi-based (stable) solar cells is crucial for a number of purposes.^{43,44} First of all, compared to traditional lead halide perovskites, their composition is lead-free, resolving toxicological issues and opening the door for sustainable solar solutions.⁴⁵ Moreover, Bi-based materials show better stability with increased resistance against moisture, exposure to light, and heat degradation.⁴⁶ This results in extended device longevity and lower maintenance costs. Bi-based perovskites exhibit excellent absorption coefficients as well as long carrier lifetimes. Bi-based perovskites are also thermally stable, which makes them more durable at high temperatures.^{47–50} Furthermore, element doping, and compositional engineering may easily modify their electrical band structure, providing exact control over their optical absorption as well as emission spectra.^{37,51} Due to their adaptability, materials may be designed for a variety of solar spectrum applications, leading to a wide range of photovoltaic as well as optoelectronic functions.^{52,53} Bi-based materials are becoming more and more appealing even if their present efficiencies are not as high as those of their lead halide counterparts. Furthermore, the special qualities of Bi-based materials go beyond photovoltaics and show potential for use in X-ray detectors, scintillators, as well as light-emitting diodes, underscoring their scientific value and adaptability.^{54–56} To sum up, research on Bi-based (stable) solar cells provides an essential route to the development of effective and sustainable photovoltaic technology as shown in **Figure 1.6**. Their innate lack of lead, exceptional stability, adjustable optoelectronic characteristics,

potential for increased efficiency, and broader range of applications make them an attractive subject for study and open the door to a brighter future regarding solar energy.^{57–59}

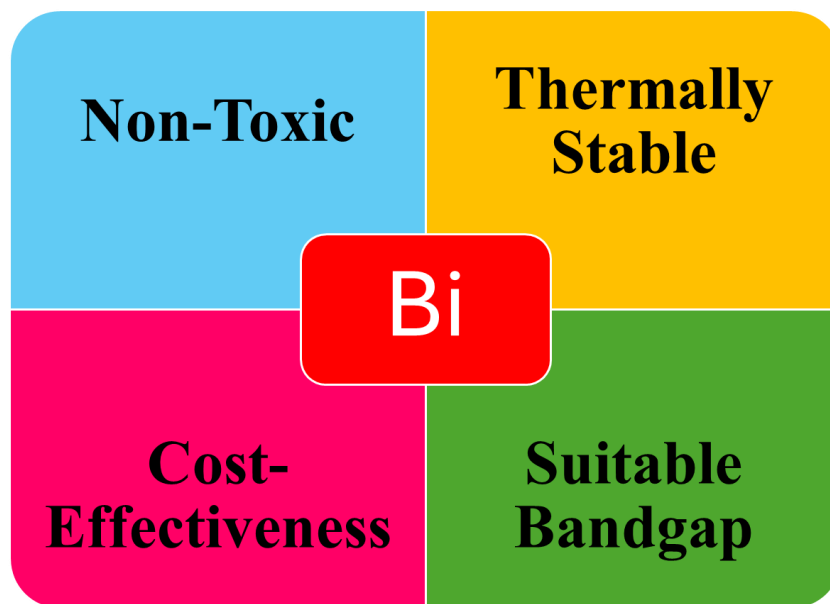


Figure 1.6 Bi-based perovskites solar cells: potential advantages.

Bismuth-based compounds have three distinct structures: vacancy ordered, double perovskite, and rudorffite. The unique characteristics of each structure contribute to the performance of solar cells. The bandgap can be modulated, and charge carrier separation can be enhanced by vacancy ordered structures.

In order to convert solar energy efficiently, double perovskites, with their two different metallic cations, offer reduced bandgaps and better stability. In particular, halide double perovskites such as $A_2B'B''X_6$ (where A is the monovalent cation, B' is the monovalent metal ion, while B'' is trivalent metal ion and X represents halide anion) have gained attention for their three-dimensional structures as shown in **Figure 1.7**. They are also ideal for advanced materials engineering because their crystal structure allows them to be modified at both A and B sites to tune the physical and electronic properties. Low structural dimensionality like 0D/ 2D however has many disadvantages.

Several disadvantages include poor carrier transportation, large effective masses for carriers and high excitation binding energy. They are therefore not suitable for photovoltaics. Lead-free double perovskite, which has a larger structure dimension is more suitable for solar cells with high efficiency.^{60–69}

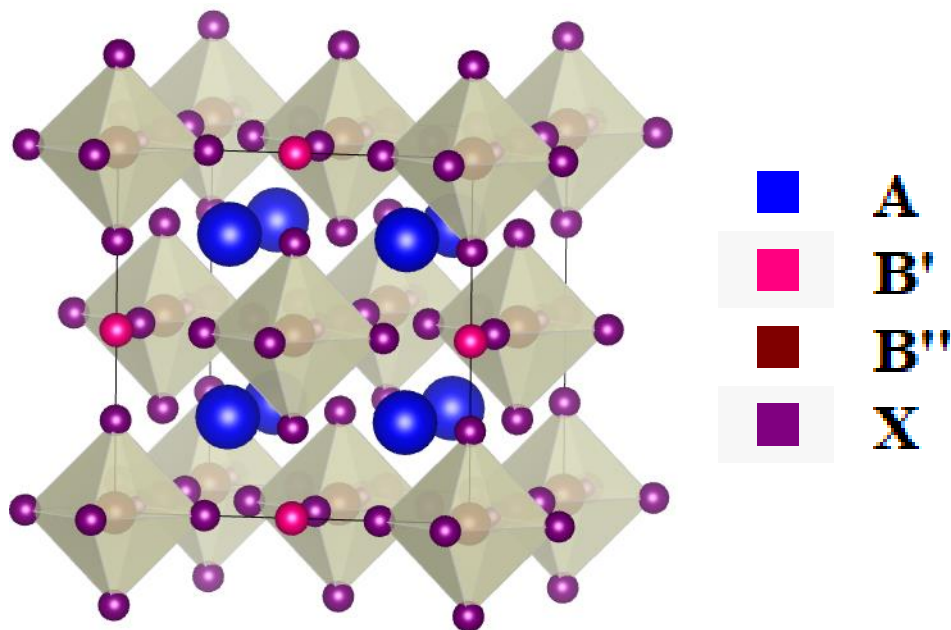


Figure 1.7 Double perovskite crystal structure $A_2B'B''X_6$.

Recent reports have shown that double perovskites based on Bi^{3+} with Ag^+ monovalent cation are up-and-coming candidates for photovoltaics. In the case of the bromide-based material, they had photoluminescence lifetimes (PL) of several hundred nanoseconds and a band gap of around 2 eV. The estimated effective masses of charge carriers are also close to the computed values for methylammonium-lead-iodide. Preparing high-quality double perovskite films for optoelectronic uses is challenging, particularly for bromide or iodide systems.^{70–74} The PCE of $\text{Cs}_2\text{AgBiX}_6$ thin-film solar cells has been improved by various strategies, including substrate preparation, vacuum deposition, additives, low-pressure, cationic doping, and the introduction of photosensitive dyes.

Greul et al. have developed a $\text{Cs}_2\text{AgBiBr}_6$ double perovskite cell with a mesoporous structure and achieved a PCE of 2.5 %.⁷⁰ Yang et al. have improved their quality $\text{Cs}_2\text{AgBiBr}_6$ thin film by achieving a PCE of PSCs increasing to 3.07 %.⁷⁵ Although many attempts have been made to optimize the optoelectronic characteristics of $\text{Cs}_2\text{AgBiBr}_6$ PV cells, the PCE has increased slowly. The previous maximum PCE for $\text{Cs}_2\text{AgBiBr}_6$ PV cells was only 4.23%.^{76,77} Furthermore, using a hydrogenation technique, the tuning band gap of $\text{Cs}_2\text{AgBiBr}_6$'s double perovskite solar cells PCE has increased to 6.37 %, a record-breaking high efficiency so far.⁷⁸ This is significantly lower than the organic-inorganic lead-based hybrid PSCs. Thus, a better improvement in PCE in the $\text{Cs}_2\text{AgBiBr}_6$ has been essential.⁷⁸⁻⁸⁷ However, two issues must be addressed for progress to continue that are the lower electronic dimensionality as well as the performance-limiting band-structure issue of $\text{Cs}_2\text{AgBiBr}_6$ double perovskites. These issues are expected to be solved following switching to an iodide counterpart, such as $\text{Cs}_2\text{AgBiI}_6$.^{66,84,88,89} The double perovskites based on iodide were expected to be free of these issues and to show a direct band transition and greater dimensionality. However, $\text{Cs}_2\text{AgBiI}_6$ has been found to be thermodynamically unstable.^{90,91} One approach that could be employed to prevent the decomposition of the phase of the compound $\text{Cs}_2\text{AgBiI}_6$ is to replace the larger cation such as Cs^+ with a smaller cation, such as Cu^+ the result of the stable $\text{Cu}_2\text{AgBiI}_6$ compound, which was found.⁹²⁻⁹⁴

On the other hand, the rudorffite structure as shown in **Figure 1.8**, however, is a relatively new member of the family. Bismuth and other elements such as silver and antimony are typically found in rudorffite, a layered structure with corner-sharing octahedra. The structure facilitates efficient charge transport and has a high light absorption capacity, making it an ideal structure for solar cells. The stability of rudorffite structures is another quality that is well-known and important for

solar cells' long-term efficiency. The material is resistant to degradation caused by moisture and heat, which are common problems for other perovskites.⁹⁵

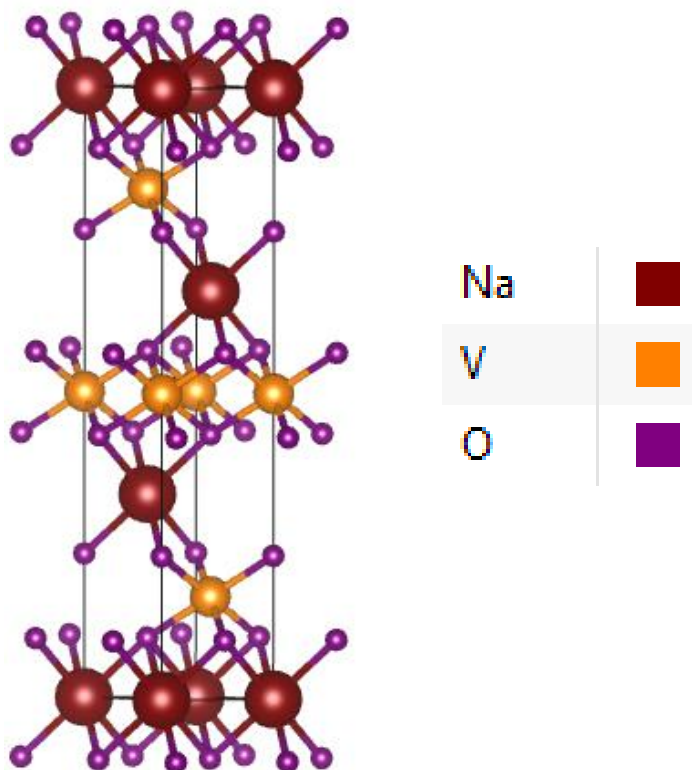


Figure 1.8 Rudorffite crystal structure NaVO_2 .

The development of an air-stable silver bismuth iodide photovoltaic material ($\text{Ag}_a\text{Bi}_b\text{I}_{a+3b}$, SBI) is thus the main focus of current research.^{96,97} Rudorffite is the name given to this SBI solar energy source photovoltaic material that exhibits direct band gaps between 1.79 and 1.83 eV as well as edge-shared $[\text{AgI}_6]$ as well as $[\text{BiI}_6]$ octahedra.⁹⁸ It has been discovered that altering the AgI/BiI_3 ratio may adjust the optical band gaps. AgBi_2I_7 ($E_g = 1.87$ eV) was shown to be viable in 2016 by the Sargent group, who also accomplished a Power Conversion Efficiency (PCE) of 1.22% with excellent stability.⁹⁹ $\text{AgBi}_3\text{I}_{10}$ ($E_g = 1.8$ eV) was made by spin-coating plus thermally treating at

150°C, as described by Wang et al. The resulting devices had a PCE of 2.73%.¹⁰⁰ Ag_2BiI_5 (PCE = 2.6%) along with Ag_3BiI_6 (PCE = 4.3%) were successfully used in rudorffite solar cells by adjusting the stoichiometric proportion of AgI to BiI_3 , exhibiting adequate air stability. However, the total solar energy generation is limited by the continuous restriction of the short-circuit current (J_{SC}) to values less than 10 mA cm^{-2} . The addition of monovalent metal cations as well as organic cations seems to be a successful method for raising the J_{SC} and total PCE of rudorffite solar cells, much like lead-based PSCs.^{101,102} In recent years, several approaches have been investigated to improve the rudorffite solar cells' stability and efficiency. Sulfur was added by Simonov et al. to several SBI composites, which caused the valence band edge to noticeably move upward. $\text{AgBi}_2\text{I}_7 - 2x\text{S}_x$ ($x = 4$ at%) treated with sulfide showed a 35% increase in J_{SC} and good long-term stability in ambient settings.¹⁰³ Cu-doped Ag_2BiI_5 was created by Lee et al. via a solid-state technique, which resulted in a substantial increase in light absorption and a commensurate improvement in PCE to 2.53%, which was mostly attributable to enhanced J_{SC} .¹⁰⁴ Some groups effectively added Cs to AgBiI_4 rudorffite substance by injecting alkali metal ions onto perovskite materials, producing a dense yet pinhole-free layer.¹⁰⁵ Due to inhibited recombination, lower defect density, plus improved carrier transport, Cs-incorporated film showed reduced nonradiative recombination, which resulted in a 40% reduction in instrument PCE after adjustment. The J_{SC} of the gadget rose from 2.46 to 3.34 mA cm^{-2} as a result of the enhanced carriers' segregation and movement.¹⁰⁶ These efforts point to a great deal of promise for improving the photovoltaic efficiency of rudorffite solar cells, establishing integration as a useful method for raising current density and stabilizing the rudorffite framework. A study on Ag_3BiI_6 rudorffite solar cells with the highest PCE of 2.77% was reported.¹⁰⁷ In lieu of the traditional lead-based perovskite active layer, the study group used Ag_3BiI_6 rudorffite, which was produced via the thermally facilitated doctor blade coating process.

The two transport carrier levels in this work were doped to match the electrical energy states within the carrier transportation layer with the light absorbing layer. The doctor blade device's PCE should be raised about 2.06% to 2.77%. Additionally, a sizable 1.00 cm² device with a PCE of 2.03% was shown in the research.¹⁰⁷ Doping Sulfur in SBI shifted the valence spectrum upwards resulting a PCE of 5.56% and showed excellent carrier-transfer capability.¹⁰³ Because of the vacant d-orbital in SBI materials, the edge of the conduction band may move lower if copper is added as a dopant to partly replace silver. Both SBI's carrier adaptability and absorption capacity were enhanced by the altered conduction band. As a consequence, the PCE went from 2.04% to 2.53%.¹⁰⁴ While a lot of work has gone into doping as well as deposition architecture of SBI to increase their PCE, there is still a dearth of knowledge on compositional engineering, particularly with regard to Bi cation. Bismuth iodide (BiI₃) is likely to sublime or break down from an as-casted thin film during the thermally aided crystallization of SBI. This leads to achieve PCE of 2.60%.¹⁰⁸ One of the teams used ambient humidity controlled condition to achieve PCE of 2.32%.¹⁰⁹ Turkevych et al. discovered that when BiI₃ is present, AgI is soluble in heated Dimethyl sulfoxide (110 °C).¹¹⁰ The first solution processed Ag₃BiI₆ solar cell was created after AgI was dissolved, showing an encouraging PCE of 4.3%. Following this, Pai et al. modified Ag₃BiI₆'s optical bandgap by partly replacing I⁻ with S²⁻ (Ag₃BiI_{5.92}S_{0.4}), the modified compound, had a PCE of 5.44%, which was ascribed to Ag₃BiI₆'s valence spectrum being elevated. Fabrication of printable triple mesoscopic solar cell of Ag₃BiI₆ was tried out but the PCE was very low - around 0.33%.¹⁰³

1.6 Perovskite base multi-junction solar cells

The multi-junction solar cell is essential in the renewable energy industry because it greatly enhances the efficiency of solar energy conversion. The layers of diverse semiconductor materials used in these cells enable these cells to absorb a broader range of sunlight, thus optimizing energy absorption. Consequently, they are ideal for applications with limited space because they are able to produce more power from a given surface area. In addition to being highly efficient, multi-junction solar cells have a low cost of production, making solar power more cost-effective and feasible. Thus, the transition to clean energy may be accelerated by their implementation. Renewable energy systems can be made more efficient and expandable using their capabilities, thereby promoting sustainability and reducing carbon emissions.^{111–114} In light of this, multi-junction solar cells have become a compelling option; nonetheless, the creation of functional and reasonably priced sub-cells is still necessary. The solar cells configuration with double junctions, (a) 2T and (c) 4T, and triple junctions, (b) 2T and (d) 4T, are shown in **Figure 1.9**. The perovskites are low-cost materials that are suitable for multi-junction applications. In tandem solar cells, perovskite/silicon produces 33.9%¹¹⁵ efficiency, which is the highest efficiency reported for double-junction structures. However, tandem solar cells consisting of all perovskites also showed impressive power conversion efficiencies exceeding 25.1%.¹¹⁵ The efficiency of a system can be further enhanced by adding additional junctions as shown in **Figure 1.10**. Multijunction solar cells based on perovskites offer significant potential for revolutionizing renewable energy.^{116,117}

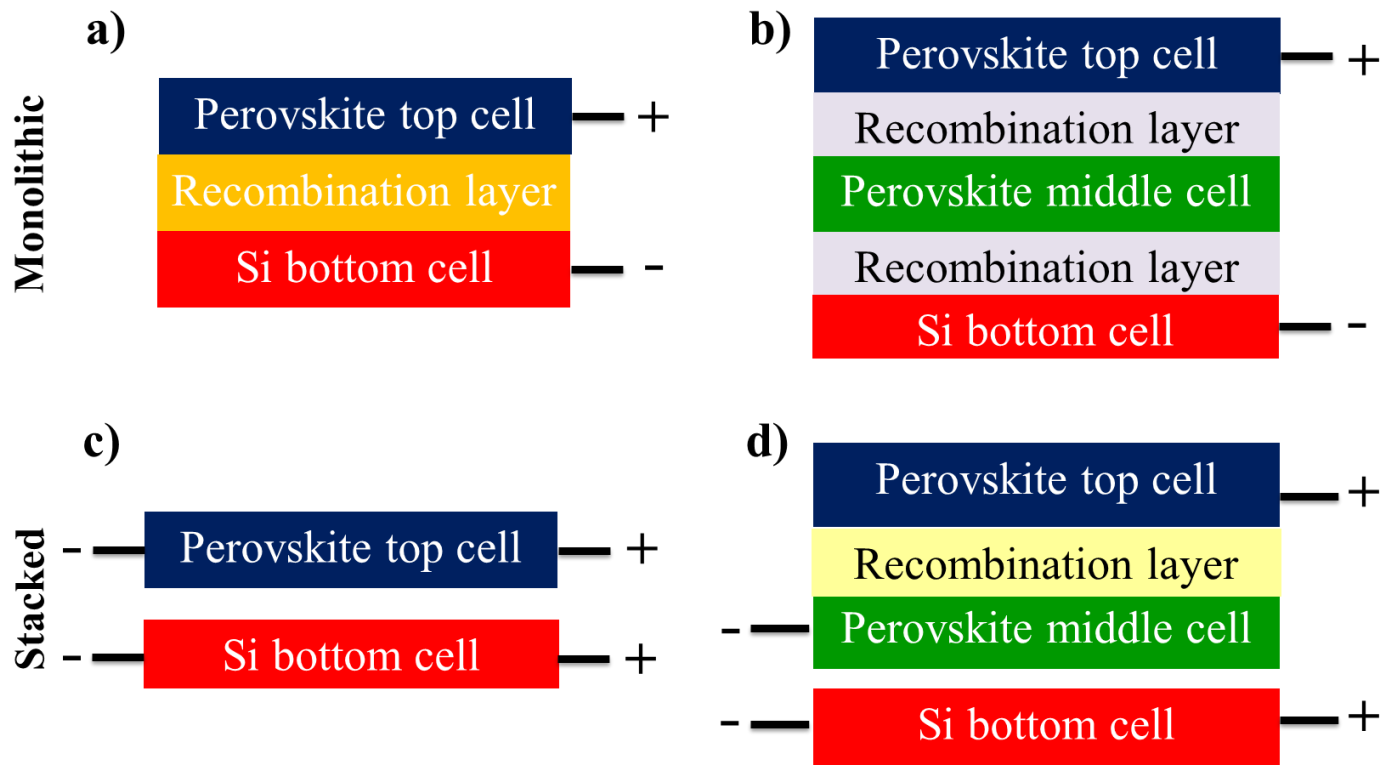


Figure 1.9 (a) 2T and (c) 4T double-junction solar cells; (b) 2T and (d) 4T triple-junction solar cells.

The triple-junction construction, which is a double junction stack with an extra sub-cell included, increases energy yield even more. Adding an extra sub-cell can further increase energy conversion efficiency by reducing thermalization loss. Triple junction photovoltaic (PV) panels have a maximum detailed balance limit of 51%¹¹⁸, while double junction PVs have a maximum balance limit of 45.5%.^{119,120} Hence, this limit also establishes the absolute limit for the highest efficiency of future perovskite-based multi-junction photovoltaics.

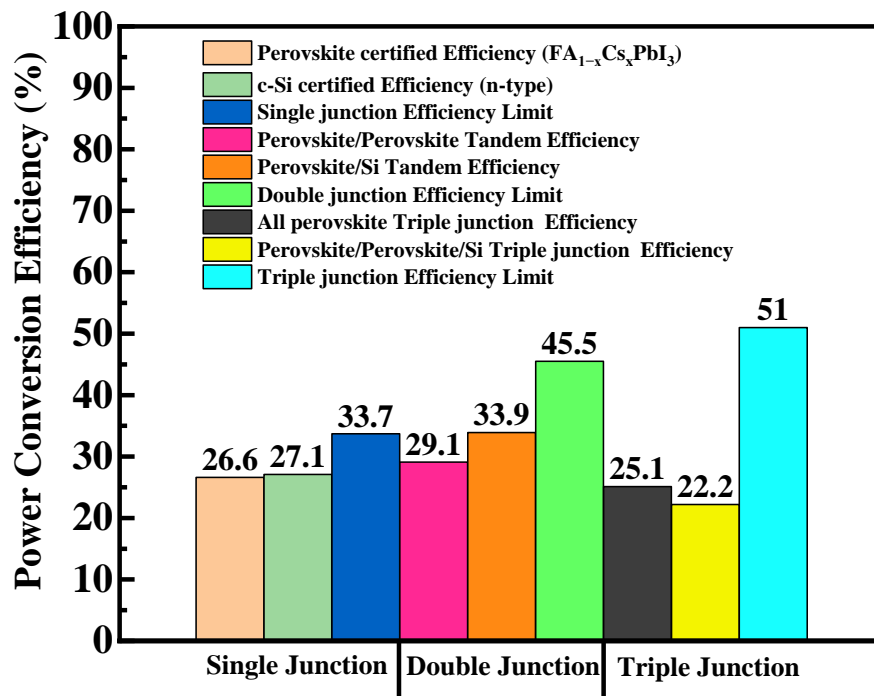


Figure 1.10 Maximum efficiency chart of perovskite-based single and multi-junction solar cells.

Investigations into triple-junction perovskite-based tandem solar cells are still nascent, signifying a substantial possibility in this underexplored domain. The current efficiencies of these devices are comparatively low, with PCEs of 25.1% for all-perovskite cells, 19.4% for perovskite/perovskite/organic photovoltaic (OPV) cells, and 22.2% for perovskite/perovskite/crystalline silicon (c-Si) monolithic two-terminal tandem cells.^{121–123} More thorough research is required because these performance levels are below the theoretical PCE limits for perovskite triple-junction devices. There is a special challenge and opportunity for creativity in closing this gap. Researchers can greatly increase the efficiency and competitiveness of these solar systems by concentrating on developments in materials, design, and production techniques. This project is essential to achieving the full potential of perovskite-based tandem solar cells and developing sustainable energy solutions. Based on III-V compound semiconductors such

as GaAs and GaInP have thus far achieved the highest performance in multijunction solar cells, with 32.9%¹¹⁵ efficiency in double junctions and 39.46%¹¹⁵ efficiency in triple and quad junction solar cells under standard simulated air mass (AM) 1.5 solar radiation, achieving a remarkable efficiency of 47.6% respectively.^{115,124} III-V semiconductor materials show that further improvements may be achieved by using three junctions instead of two. However, the high production costs of III-V semiconductor materials prevent their use in terrestrial solar cells despite their high efficiency. The high cost is primarily due to the use of rare or exotic materials and complex manufacturing techniques. This impedes the widespread implementation of III-V solar cells due to their lack of economic viability.^{118,120,125,126} In the solar energy sector, perovskite solar cells (PSCs) have emerged as a revolutionary material, particularly for tandem solar cells. Their rapid increase in power conversion efficiency, from just 3.8% in 2009¹²⁷ to 26.6% by 2024,^{115,128–130} is testament to the great potential of solar power. Having tunable bandgaps from 1.2 to 2.3 eV makes these materials ideal for triple-junction devices because they allow for optimal light absorption.¹²⁶ A perovskite's bandgap can be tailored by modifying chemically, such as substituting anions and cations within its structure. The perovskite/silicon tandem cells are currently at the forefront, achieving the highest efficiencies even among double junction cells based on perovskites.^{131,132} In the perovskite community, triple-junction solar cells combining perovskite, perovskite, and silicon have been the most sought-after technology. Their ability to improve the efficiency and performance of solar energy conversion makes them particularly attractive. In this specific arrangement, perovskites, with their high absorption coefficients and tunable band gaps, work in conjunction with silicon solar cells, which are well established and technically advanced. In this triple-junction arrangement, multiple layers of perovskites are combined with silicon to maximize solar spectrum utilization and efficiency.

1.7 Research aims and objectives

The objective of this thesis is to study Bi-based materials that are both non-toxic and cost-effective, with a particular emphasis on Pb-free alternatives that can minimize environmental impact while retaining their high performance. This study aims to meet the increasing need for sustainable energy solutions by using advanced materials and technology in the solar energy industry. These studies share the common goal of examining methods to improve the performance of a variety of solar cell configurations, with a particular emphasis on single, double, and triple junction systems. These configurations are recognized for their ability to achieve a higher level of efficiency in comparison to traditional designs. This study has two main goals at the beginning. The first is to find the best annealing temperature for the novel $\text{Cu}_6\text{BiAgI}_{10}$ solar cell so that it can improve its photovoltaic properties. The second is to find and analyze HTLs that can make both the $\text{Cu}_6\text{BiAgI}_{10}$ and Ag_3BiI_6 perovskite solar cells more efficient. Additionally, this study investigated the use of advanced materials like Rudorffite in tandem solar cell designs to enhance overall efficiency, investigating the potential for junction layers to work together. Further, the study will evaluate methylammonium bismuth iodide's possibilities for producing high-performance triple junction solar cells, which have the ability to greatly enhance the efficiency of energy conversion. The results of this study should contribute to the advancement of knowledge in science as well as the global shift to cleaner energy production. In order to improve overall efficiency, this study will also look into the use of novel materials like Rudorffite in tandem solar cell designs. It will also look into the possibility of multifunction cooperating.

1.8 Thesis outline

In this thesis, seven chapters examine different aspects of the research conducted on non-toxic and cost-effective Bi perovskite solar cells. In **Chapter 1**, we have the introduction, which gives a synopsis of the relevant literature and explains why Pb free perovskite is important. It finishes with an overview of the research goals and objectives after a discussion of the opportunities and threats facing solar cell technology. In **Chapter 2**, photovoltaic and surface morphological improvements of a novel material class $\text{Cu}_6\text{AgBiI}_{10}$, the synthesis and characterization of $\text{Cu}_6\text{BiAgI}_{10}$ are examined. The annealing temperature's effects on the performance and efficiency of the solar cells are reviewed. The potential of the material is demonstrated in this chapter by experimental results and findings. In **Chapter 3**, study of $\text{Cu}_6\text{BiAgI}_{10}$ perovskite with various organic and inorganic hole transport layers for improved photovoltaic performance. This is done through an experimental and simulation study of $\text{Cu}_6\text{BiAgI}_{10}$ photovoltaics with various organic and inorganic HTLs for improved photovoltaic performance of solar cells. The chapter delves into the implications for future solar cell designs by comparing experimental findings with simulation data in order to determine ideal combinations. In **Chapter 4**, the role of organic HTLs enhances the efficiency of Ag_3BiI_6 solar cells through the integration of experiment and simulation. To provide a whole picture, it combines simulation and experiment to find the best HTL combinations for efficiency gains. The examination of the tandem solar cell configuration including Rudorffite and silicon is presented in **Chapter 5**, titled: Tandem solar cell approach to unlocking the potential of Rudorffite/silicon combinations. This chapter evaluates the performance gains made possible by this combination and provides simulation results and possible uses. Then **Chapter 6**, integrated study of perovskite/perovskite/c-Si triple junction solar cells with methylammonium bismuth iodide as a key component. Delves into the efficacy of methylammonium bismuth iodide-based

triple junction solar cells, which are a kind of integrated study focusing on 2-terminal (2T) perovskite/perovskite/c-Si solar cells. Looking forward to the potential of triple junction solar cell technology, it delves into the methodology used and the performance measures that came from them. Lastly, **Chapter 7** concludes the study by summarizing its main points and discussing their significance, with an eye towards the future of solar energy. Sustainable solar cell technology may potentially benefit from the recommendations made for future studies.

1.9 References

- (1) Wang, M.; Wang, W.; Ma, B.; Shen, W.; Liu, L.; Cao, K.; Chen, S.; Huang, W. Lead-Free Perovskite Materials for Solar Cells. *Nano-micro Lett.* **2021**, *13* (1), 1–36.
- (2) Ranabhat, K.; Patrikeev, L.; Revina, A. A. evna; Andrianov, K.; Lapshinsky, V.; Sofronova, E. An Introduction to Solar Cell Technology. *J. Appl. Eng. Sci.* **2016**, *14* (4), 481–491.
- (3) Seo, Y.; Ha, S. R.; Yoon, S.; Jeong, S. M.; Choi, H.; Kang, D. W. Dynamic Casting in Combination with Ramped Annealing Process for Implementation of Inverted Planar Ag₃BiI₆ Rudorffite Solar Cells. *J. Power Sources* **2020**, *453*, 227903.
- (4) Kulkarni, A.; Ünlü, F.; Pant, N.; Kaur, J.; Bohr, C.; Jena, A. K.; Öz, S.; Yanagida, M.; Shirai, Y.; Ikegami, M.; Miyano, K.; Tachibana, Y.; Chakraborty, S.; Mathur, S.; Miyasaka, T. Concerted Ion Migration and Diffusion-Induced Degradation in Lead-Free Ag₃BiI₆ Rudorffite Solar Cells under Ambient Conditions. *Solar RRL* **2021**, *5* (8), 2100077.
- (5) Yi, Z.; Zhang, T.; Ban, H.; Shao, H.; Gong, X.; Wu, M.; Liang, G.; Zhang, X. L.; Shen, Y.; Wang, M. AgBi₃I₁₀ Rudorffite for Photovoltaic Application. *Solar Energy* **2020**, *206*, 436–442.

- (6) Wu, M. C.; Wang, Q. H.; Hsiao, K. C.; Chen, S. H.; Ho, C. M.; Jao, M. H.; Chang, Y. H.; Su, W. F. Composition Engineering to Enhance the Photovoltaic Performance and to Prolong the Lifetime for Silver Bismuth Iodide Solar Cell. *Chem. Eng. J. Adv.* **2022**, *10*, 100275.
- (7) He, Z.; Gong, Y.; Tan, Z. Recent Advances in Bismuth-Based Solar Cells: Fundamentals, Fabrication, and Optimization Strategies. *Adv. Sustain. Syst.* **2022**, *6* (6), 2200051.
- (8) Jung, K. W.; Sohn, M. R.; Lee, H. M.; Yang, I. S.; Sung, S. Do; Kim, J.; Wei-Guang Diao, E.; Lee, W. I. Silver Bismuth Iodides in Various Compositions as Potential Pb-Free Light Absorbers for Hybrid Solar Cells. *Sustain. Energy Fuels* **2017**, *2* (1), 294–302.
- (9) Radhakrishna, K.; Manjunath, S. B.; Devadiga, D.; Chetri, R.; Nagaraja, A. T. Review on Carbazole-Based Hole Transporting Materials for Perovskite Solar Cell. *ACS Appl. Energy Mater.* **2023**, *6*(7), 3635–3664.
- (10) Zelai, T. Study of Lead Free Double Perovskites $\text{Na}_2\text{XAgCl}_6$ ($\text{X} = \text{Ga}, \text{In}, \text{Tl}$) for Solar Cells and Transport Applications. *Phys. Scr.* **2023**, *98* (4), 045802.
- (11) Cotal, H.; Fetzer, C.; Boisvert, J.; Kinsey, G.; King, R.; Hebert, P.; Yoon, H.; Karam, N. III–V Multijunction Solar Cells for Concentrating Photovoltaics. *Energy Environ. Sci.* **2009**, *2* (2), 174–192.
- (12) Tao, S.; Polavarapu, L.; Vivo, P. Perovskite Photovoltaics: Stability and Scalability. *Sci. Rep.* **2023**, *13* (1), 1–3.
- (13) Polly, S. J.; Bittner, Z. S.; Bennett, M. F.; Raffaele, R. P.; Hubbard, S. M. Development of

- a Multi-Source Solar Simulator for Spatial Uniformity and Close Spectral Matching to AM0 and AM1.5. *2011 37th IEEE Photovoltaic Specialists Conference* **2011**, 001739–001743.
- (14) Zharkova, V. V.; Vasilieva, I.; Shepherd, S. J.; Popova, E.; Zharkova, V. V.; Vasilieva, I.; Shepherd, S. J.; Popova, E. Periodicities in Solar Activity, Solar Radiation and Their Links with Terrestrial Environment. *Nat. Sci.* **2023**, *15* (3), 111–147.
 - (15) Solar Spectra | Grid Modernization | NREL <https://www.nrel.gov/grid/solar-resource/spectra.html> (accessed Sep 17, 2024).
 - (16) Light Generated Current | PVEducation <https://www.pveducation.org/pvcdrom/solar-cell-operation/light-generated-current> (accessed Sep 17, 2024).
 - (17) Chapin, D. M.; Fuller, C. S.; Pearson, G. L. A New Silicon P-n Junction Photocell for Converting Solar Radiation into Electrical Power. *J. Appl. Phys.* **1954**, *25* (5), 676–677.
 - (18) Green, M. A. Silicon Photovoltaic Modules: A Brief History of the First 50 Years. *Prog. Photovolt.: Res. Appl.* **2005**, *13* (5), 447–455.
 - (19) Bragagnolo, J. A.; Barnett, A. M.; Phillips, J. E.; Hall, R. B.; Meakin, J. D.; Rothwarf, A. The Design and Fabrication of Thin-Film CdS/Cu₂S Cells of 9.15-Percent Conversion Efficiency. *IEEE Trans. Electron Dev.* **1980**, *27* (4), 645–651.
 - (20) O'Regan, B.; Grätzel, M. A Low-Cost, High-Efficiency Solar Cell Based on Dye-Sensitized Colloidal TiO₂ Films. *Nature* **1991**, *353* (6346), 737–740.
 - (21) Kojima, A.; Teshima, K.; Shirai, Y.; Miyasaka, T. Organometal Halide Perovskites as Visible-Light Sensitizers for Photovoltaic Cells. *J. Am. Chem. Soc.* **2009**, *131* (17), 6050–

6051.

- (22) Kour, R.; Arya, S.; Verma, S.; Gupta, J.; Bandhoria, P.; Bharti, V.; Datt, R.; Gupta, V. Potential Substitutes for Replacement of Lead in Perovskite Solar Cells: A Review. *Global chall.* **2019**, *3* (11), 1900050.
- (23) Islam, M. A.; Islam, J.; Islam, M. N.; Sen, S. K.; Hossain, A. K. M. A. Enhanced Ductility and Optoelectronic Properties of Environment-Friendly CsGeCl₃ under Pressure. *AIP Adv.* **2021**, *11* (4), 45014.
- (24) Islam, M. R.; Mojumder, M. R. H.; Moshwan, R.; Islam, A. S. M. J.; Islam, M. A.; Rahman, M. S.; Kabir, M. H. Strain-Driven Optical, Electronic, and Mechanical Properties of Inorganic Halide Perovskite CsGeBr₃. *ECS J. Solid State Sci. Technol.* **2022**, *11* (3), 033001.
- (25) Islam, M. A.; Rahaman, M. Z.; Sen, S. K. A Comparative Study of Hydrostatic Pressure Treated Environmentally Friendly Perovskites CsXBr₃ (X = Ge/Sn) for Optoelectronic Applications. *AIP Adv.* **2021**, *11* (7).
- (26) Sirbu, D.; Balogun, F. H.; Milot, R. L.; Docampo, P. Layered Perovskites in Solar Cells: Structure, Optoelectronic Properties, and Device Design. *Adv. Energy Mater.* **2021**, *11* (24), 2003877.
- (27) Ye, Y.; Yin, Y.; Chen, Y.; Li, S.; Li, L.; Yamauchi, Y. Metal-Organic Framework Materials in Perovskite Solar Cells: Recent Advancements and Perspectives. *Small* **2023**, 2208119.
- (28) Truong, M. A.; Funasaki, T.; Ueberricke, L.; Nojo, W.; Murdey, R.; Yamada, T.; Hu, S.;

- Akatsuka, A.; Sekiguchi, N.; Hira, S.; Xie, L.; Nakamura, T.; Shioya, N.; Kan, D.; Tsuji, Y.; Iikubo, S.; Yoshida, H.; Shimakawa, Y.; Hasegawa, T.; Kanemitsu, Y.; Suzuki, T.; Wakamiya, A. Tripodal Triazatruxene Derivative as a Face-On Oriented Hole-Collecting Monolayer for Efficient and Stable Inverted Perovskite Solar Cells. *J. Am. Chem. Soc.* **2023**, 145(13), 7528–7539.
- (29) Su, S.; Lv, P.; Hu, M.; Zhang, Y.; Yin, H.; Zhu, Y.; Pan, J.; Wang, Y.; Li, W.; Rong, Y.; Ku, Z.; Huang, F.; Cheng, Y.-B.; Lu, J. Low-Cost and LiTFSI-Free Diphenylamine-Substituted Hole Transporting Materials for Highly Efficient Perovskite Solar Cells and Modules. *Mater. Chem. Front.* **2023**, 7, 2241-2250.
- (30) Liang, K.; Huang, L.; Wang, T.; Wang, C.; Guo, Y.; Yue, Y.; Liu, X.; Zhang, J.; Hu, Z.; Zhu, Y. Rational Design of Formamidine Tin-Based Perovskite Solar Cell with 30% Potential Efficiency via 1-D Device Simulation. *Phys. Chem. Chem. Phys.* **2023**, 25 (13), 9413–9427.
- (31) Miyasaka, T.; Kulkarni, A.; Kim, G. M.; Öz, S.; Jena, A. K. Perovskite Solar Cells: Can We Go Organic-Free, Lead-Free, and Dopant-Free? *Adv. Energy Mater.* **2020**, 10 (13), 1902500.
- (32) Best Research-Cell Efficiency Chart | Photovoltaic Research | NREL <https://www.nrel.gov/pv/cell-efficiency.html> (accessed Sep 19, 2024).
- (33) Manisalidis, I.; Stavropoulou, E.; Stavropoulos, A.; Bezirtzoglou, E. Environmental and Health Impacts of Air Pollution: A Review. *Front. Public Health* **2020**, 8, 505570.
- (34) Li, J.; Duan, J.; Yang, X.; Duan, Y.; Yang, P.; Tang, Q. Review on Recent Progress of Lead-

- Free Halide Perovskites in Optoelectronic Applications. *Nano Energy* **2021**, *80*, 105526.
- (35) Gu, S.; Lin, R.; Han, Q.; Gao, Y.; Tan, H.; Zhu, J. Tin and Mixed Lead–Tin Halide Perovskite Solar Cells: Progress and Their Application in Tandem Solar Cells. *Adv. Mater.* **2020**, *32* (27), 1907392.
- (36) Hao, F.; Stoumpos, C. C.; Cao, D. H.; Chang, R. P. H.; Kanatzidis, M. G. Lead-Free Solid-State Organic–Inorganic Halide Perovskite Solar Cells. *Nat. Photon.* **2014**, *8* (6), 489–494.
- (37) Cui, Y.; Yang, L.; Wu, X.; Deng, J.; Zhang, X.; Zhang, J. Recent Progress of Lead-Free Bismuth-Based Perovskite Materials for Solar Cell Applications. *J. Mater. Chem. C.* **2022**, *10* (44), 16629–16656.
- (38) Krishnamoorthy, T.; Ding, H.; Yan, C.; Leong, W. L.; Baikie, T.; Zhang, Z.; Sherburne, M.; Li, S.; Asta, M.; Mathews, N.; Mhaisalkar, S. G. Lead-Free Germanium Iodide Perovskite Materials for Photovoltaic Applications. *J. Mater. Chem. A* **2015**, *3* (47), 23829–23832.
- (39) Hoefler, S. F.; Trimmel, G.; Rath, T. Progress on Lead-Free Metal Halide Perovskites for Photovoltaic Applications: A Review. *Monatsh. fur Chem.* **2017**, *148* (5), 795–826.
- (40) Yue, S.; McGuire, S. C.; Yan, H.; Chu, Y. S.; Cotlet, M.; Tong, X.; Wong, S. S. Synthesis, Characterization, and Stability Studies of Ge-Based Perovskites of Controllable Mixed Cation Composition, Produced with an Ambient Surfactant-Free Approach. *ACS Omega* **2019**, *4* (19), 18219–18233.
- (41) Wu, T.; Liu, X.; Luo, X.; Lin, X.; Cui, D.; Wang, Y.; Segawa, H.; Zhang, Y.; Han, L. Lead-Free Tin Perovskite Solar Cells. *Joule* **2021**, *5* (4), 863–886.

- (42) Noel, N. K.; Stranks, S. D.; Abate, A.; Wehrenfennig, C.; Guarnera, S.; Haghighirad, A. A.; Sadhanala, A.; Eperon, G. E.; Pathak, S. K.; Johnston, M. B.; Petrozza, A.; Herz, L. M.; Snaith, H. J. Lead-Free Organic–Inorganic Tin Halide Perovskites for Photovoltaic Applications. *Energy Environ. Sci.* **2014**, 7 (9), 3061–3068.
- (43) Fan, E.; Liu, M.; Yang, K.; Jiang, S.; Li, B.; Zhao, D.; Guo, Y.; Zhang, Y.; Zhang, P.; Zuo, C.; Ding, L.; Zheng, Z. One-Step Gas–Solid-Phase Diffusion-Induced Elemental Reaction for Bandgap-Tunable $\text{Cu}_x\text{Ag}_{m1}\text{Bi}_{m2}\text{In}/\text{CuI}$ Thin Film Solar Cells. *Nano-micro Lett.* **2023**, 15 (1), 1–11.
- (44) Zhu, H.; Turkevych, I.; Lohan, H.; Liu, P.; Martin, R. W.; Massabuau, F. C. P.; Hoye, R. L. Z. Progress and Applications of (Cu–)Ag–Bi–I Semiconductors, and Their Derivatives, as next-Generation Lead-Free Materials for Photovoltaics, Detectors and Memristors. *Int. Mater. Rev.* **2024**, 1–16.
- (45) Podapangi, S. K.; Jafarzadeh, F.; Mattiello, S.; Korukonda, T. B.; Singh, A.; Beverina, L.; Brown, T. M. Green Solvents, Materials, and Lead-Free Semiconductors for Sustainable Fabrication of Perovskite Solar Cells. *RSC Adv.* **2023**, 13 (27), 18165–18206.
- (46) Xu, M.; Yang, J.; Sun, C.; Liu, L.; Cui, Y.; Liang, B. Performance Enhancement Strategies of Bi-Based Photocatalysts: A Review on Recent Progress. *Chem. Eng. J.* **2020**, 389, 124402.
- (47) Mohan, R. Green Bismuth. *Nat. Chem.* **2010**, 2 (4), 336–336.
- (48) Ran, Z.; Wang, X.; Li, Y.; Yang, D.; Zhao, X. G.; Biswas, K.; Singh, D. J.; Zhang, L. Bismuth and Antimony-Based Oxyhalides and Chalcogenides as Potential Optoelectronic

- Materials. *npj Comput. Mater.* **2018**, *4* (1), 1–7.
- (49) Zhang, C.; Gao, L.; Teo, S.; Guo, Z.; Xu, Z.; Zhao, S.; Ma, T. Design of a Novel and Highly Stable Lead-Free Cs₂NaBiI₆ Double Perovskite for Photovoltaic Application. *Sustain. Energy Fuels* **2018**, *2* (11), 2419–2428.
- (50) Creutz, S. E.; Liu, H.; Kaiser, M. E.; Li, X.; Gamelin, D. R. Structural Diversity in Cesium Bismuth Halide Nanocrystals. *Chem. Mater.* **2019**, *31* (13), 4685–4697.
- (51) Sun, T.; Ma, Z.; Yao, M.; Wei, J.; Liu, Y.; Ming, X. Direct Band-Gap Iodide Double Perovskite Solar Cell Materials by Doping Strategy: First-Principles Predictions. *Mater. Today Commun.* **2023**, *37*, 107055.
- (52) Wu, C.; Zhang, Q.; Liu, G.; Zhang, Z.; Wang, D.; Qu, B.; Chen, Z.; Xiao, L. From Pb to Bi: A Promising Family of Pb-free Optoelectronic Materials and Devices. *Adv. Energy Mater.* **2020**, *10* (13), 1902496.
- (53) Nishikubo, R.; Kanda, H.; Garcia-Benito, I.; Molina-Ontoria, A.; Pozzi, G.; Asiri, A. M.; Nazeeruddin, M. K.; Saeki, A. Optoelectronic and Energy Level Exploration of Bismuth and Antimony-Based Materials for Lead-Free Solar Cells. *Chem. Mat.* **2020**, *32* (15), 6416–6424.
- (54) Zhou, C.; Han, M.; Xiao, Y.; Tan, W.; Jin, X.; Wu, X.; Yang, Y.; Zhu, S.; Lin, H.; Lin, S. Lead-Free Perovskites and Derivatives Enable Direct and Scintillation-Type X-Ray Detection. *Mater. Sci. Eng. R: Rep.* **2023**, *156*, 100756.
- (55) Gao, Y.; Pan, Y.; Zhou, F.; Niu, G.; Yan, C. Lead-Free Halide Perovskites: A Review of

- the Structure–Property Relationship and Applications in Light Emitting Devices and Radiation Detectors. *J. Mater. Chem. A*. **2021**, 9 (20), 11931–11943.
- (56) Zhang, X.; Yu, S.; Meng, X.; Xiao, S. A Review on Lead-Free Perovskites for X-Ray Detection and Imaging. *Cryst. Res. Technol.* **2023**, 58 (5), 2200232.
- (57) Gao, P.; Grätzel, M.; Nazeeruddin, M. K. Organohalide Lead Perovskites for Photovoltaic Applications. *Energy Environ. Sci.* **2014**, 7 (8), 2448–2463.
- (58) Lee, M. M.; Teuscher, J.; Miyasaka, T.; Murakami, T. N.; Snaith, H. J. Efficient Hybrid Solar Cells Based on Meso-Super-structured Organometal Halide Perovskites. *Science* **2012**, 338 (6107), 643–647.
- (59) Conings, B.; Drijkoningen, J.; Gauquelin, N.; Babayigit, A.; D’Haen, J.; D’Olieslaeger, L.; Ethirajan, A.; Verbeeck, J.; Manca, J.; Mosconi, E. Intrinsic Thermal Instability of Methylammonium Lead Trihalide Perovskite. *Adv. Energy Mater.* **2015**, 5 (15), 1500477.
- (60) Arabpour Roghabadi, F.; Alidaei, M.; Mousavi, S. M.; Ashjari, T.; Tehrani, A. S.; Ahmadi, V.; Sadrameli, S. M. Stability Progress of Perovskite Solar Cells Dependent on the Crystalline Structure: From 3D ABX₃ to 2D Ruddlesden–Popper Perovskite Absorbers. *J. Mater. Chem. A*. **2019**, 7 (11), 5898–5933.
- (61) Zhang, J.; Hua, Y.; Xu, B.; Yang, L.; Liu, P.; Johansson, M. B.; Vlachopoulos, N.; Kloo, L.; Boschloo, G.; J Johansson, E. M.; Sun, L.; Hagfeldt, A.; Zhang, J.; Johansson, M. B.; Boschloo, G.; J Johansson, E. M.; Hua, Y.; Xu, B.; Sun, L.; Yang Nanotechnology, L.; Materials, F.; Liu, P.; Kloo, L.; Vlachopoulos, N.; Hagfeldt, A. The Role of 3D Molecular Structural Control in New Hole Transport Materials Outperforming Spiro-OMeTAD in

- Perovskite Solar Cells. *Adv. Energy Mater.* **2016**, 6 (19), 1601062.
- (62) Zhao, X. G.; Yang, J. H.; Fu, Y.; Yang, D.; Xu, Q.; Yu, L.; Wei, S. H.; Zhang, L. Design of Lead-Free Inorganic Halide Perovskites for Solar Cells via Cation-Transmutation. *J. Am. Chem. Soc.* **2017**, 139 (7), 2630–2638.
- (63) Luo, J.; Wang, X.; Li, S.; Liu, J.; Guo, Y.; Niu, G.; Yao, L.; Fu, Y.; Gao, L.; Dong, Q.; Zhao, C.; Leng, M.; Ma, F.; Liang, W.; Wang, L.; Jin, S.; Han, J.; Zhang, L.; Etheridge, J.; Wang, J.; Yan, Y.; Sargent, E. H.; Tang, J. Efficient and Stable Emission of Warm-White Light from Lead-Free Halide Double Perovskites. *Nature* **2018**, 563 (7732), 541–545.
- (64) Ning, W.; Gao, F.; Ning, W.; Gao, F. Structural and Functional Diversity in Lead-Free Halide Perovskite Materials. *Adv. Mater.* **2019**, 31 (22), 1900326.
- (65) McClure, E. T.; Ball, M. R.; Windl, W.; Woodward, P. M. Cs₂AgBiX₆ (X = Br, Cl): New Visible Light Absorbing, Lead-Free Halide Perovskite Semiconductors. *Chem. Mat.* **2016**, 28 (5), 1348–1354.
- (66) Slavney, A. H.; Hu, T.; Lindenberg, A. M.; Karunadasa, H. I. A Bismuth-Halide Double Perovskite with Long Carrier Recombination Lifetime for Photovoltaic Applications. *J. Am. Chem. Soc.* **2016**, 138 (7), 2138–2141.
- (67) Wu, B.; Ning, W.; Xu, Q.; Manjappa, M.; Feng, M.; Ye, S.; Fu, J.; Lie, S.; Yin, T.; Wang, F.; Goh, T. W.; Harikesh, P. C.; Tay, Y. K. E.; Shen, Z. X.; Huang, F.; Singh, R.; Zhou, G.; Gao, F.; Sum, T. C. Strong Self-Trapping by Deformation Potential Limits Photovoltaic Performance in Bismuth Double Perovskite. *Sci. Adv.* **2021**, 7 (8), 3160–3177.

- (68) Park, B.-W.; Philippe, B.; Zhang, X.; Rensmo, H.; Boschloo, G.; Johansson, E. M. J.; Park, B.-W.; Zhang, X.; Boschloo, G.; Johansson, E. M. J.; Philippe, B.; Rensmo, H. Bismuth Based Hybrid Perovskites $A_3Bi_2I_9$ (A: Methylammonium or Cesium) for Solar Cell Application. *Adv. Mater.* **2015**, 27 (43), 6806–6813.
- (69) Ji, F.; Boschloo, G.; Wang, F.; Gao, F. Challenges and Progress in Lead-Free Halide Double Perovskite Solar Cells. *Solar RRL* **2023**, 7 (6), 2201112.
- (70) Greul, E.; Petrus, M. L.; Binek, A.; Docampo, P.; Bein, T. Highly Stable, Phase Pure $Cs_2AgBiBr_6$ Double Perovskite Thin Films for Optoelectronic Applications. *J. Mater. Chem. A* **2017**, 5 (37), 19972–19981.
- (71) Liu, Y.; Huang, Y.; Yang, Z.; Li, Y.; Xu, J.; Li, H.; Chen, W.; Chen, K. Hexagonal Lead-Free Cs_2AgBiI_6 Perovskite Nanocrystals: A Promising Material for Solar Cell Application. *ACS Appl. Energy Mater.* **2023**, 6, 5196.
- (72) Filip, M. R.; Hillman, S.; Haghighirad, A. A.; Snaith, H. J.; Giustino, F. Band Gaps of the Lead-Free Halide Double Perovskites $Cs_2BiAgCl_6$ and $Cs_2BiAgBr_6$ from Theory and Experiment. *J. Phys. Chem. Lett.* **2016**, 7 (13), 2579–2585.
- (73) Wei, F.; Deng, Z.; Sun, S.; Zhang, F.; Evans, D. M.; Kieslich, G.; Tominaka, S.; Carpenter, M. A.; Zhang, J.; Bristowe, P. D.; Cheetham, A. K. Synthesis and Properties of a Lead-Free Hybrid Double Perovskite: $(CH_3NH_3)_2AgBiBr_6$. *Chem. Mater.* **2017**, 29 (3), 1089–1094.
- (74) Volonakis, G.; Filip, M. R.; Haghighirad, A. A.; Sakai, N.; Wenger, B.; Snaith, H. J.; Giustino, F. Lead-Free Halide Double Perovskites via Heterovalent Substitution of Noble Metals. *J. Phys. Chem. Lett.* **2016**, 7 (7), 1254–1259.

- (75) Yang, X.; Xiang, H.; Huang, J.; Zhou, C.; Ran, R.; Wang, W.; Zhou, W.; Shao, Z. Thiourea with Sulfur-Donor as an Effective Additive for Enhanced Performance of Lead-Free Double Perovskite Photovoltaic Cells. *J. Colloid. Interface Sci.* **2022**, *628*, 476–485.
- (76) Wang, B.; Li, N.; Yang, L.; Dall’agnese, C.; Jena, A. K.; Sasaki, S. I.; Miyasaka, T.; Tamiaki, H.; Wang, X. F. Chlorophyll Derivative-Sensitized TiO₂ Electron Transport Layer for Record Efficiency of Cs₂AgBiBr₆ Double Perovskite Solar Cells. *J. Am. Chem. Soc.* **2021**, *143* (5), 2207–2211.
- (77) Wang, B.; Li, N.; Yang, L.; Dall’Agnese, C.; Jena, A. K.; Miyasaka, T.; Wang, X. F. Organic Dye/Cs₂AgBiBr₆ Double Perovskite Heterojunction Solar Cells. *J. Am. Chem. Soc.* **2021**, *143* (36), 14877–14883.
- (78) Zhang, Z.; Sun, Q.; Lu, Y.; Lu, F.; Mu, X.; Wei, S. H.; Sui, M. Hydrogenated Cs₂AgBiBr₆ for Significantly Improved Efficiency of Lead-Free Inorganic Double Perovskite Solar Cell. *Nat. Commun.* **2022**, *13* (1), 1–12.
- (79) Zhang, Z.; Wu, C.; Wang, D.; Liu, G.; Zhang, Q.; Luo, W.; Qi, X.; Guo, X.; Zhang, Y.; Lao, Y.; Qu, B.; Xiao, L.; Chen, Z. Improvement of Cs₂AgBiBr₆ Double Perovskite Solar Cell by Rubidium Doping. *Org. Electron.* **2019**, *74*, 204–210.
- (80) Li, J.; Duan, J.; Du, J.; Yang, X.; Wang, Y.; Yang, P.; Duan, Y.; Tang, Q. Alkali Metal Ion-Regulated Lead-Free, All-Inorganic Double Perovskites for HTM-Free, Carbon-Based Solar Cells. *ACS Appl. Mater. Interfaces.* **2020**, *12* (42), 47408–47415.
- (81) Wu, C.; Zhang, Q.; Liu, Y.; Luo, W.; Guo, X.; Huang, Z.; Ting, H.; Sun, W.; Zhong, X.; Wei, S.; Wang, S.; Chen, Z.; Xiao, L.; Wu, C.; Zhang, Q.; Liu, Y.; Luo, W.; Guo, X.; Huang,

- Z.; Ting, H.; Sun, W.; Zhong, X.; Wei, S.; Wang, S.; Chen, Z.; Xiao, L. The Dawn of Lead-Free Perovskite Solar Cell: Highly Stable Double Perovskite $\text{Cs}_2\text{AgBiBr}_6$ Film. *Adv. Sci.* **2018**, *5* (3), 1700759.
- (82) Rodkey, N.; Kaal, S.; Sebastia-Luna, P.; Birkhölzer, Y. A.; Ledinsky, M.; Palazon, F.; Bolink, H. J.; Morales-Masis, M. Pulsed Laser Deposition of $\text{Cs}_2\text{AgBiBr}_6$: From Mechanochemically Synthesized Powders to Dry, Single-Step Deposition. *Chem. Mater.* **2021**, *33* (18), 7417–7422.
- (83) Yang, X.; Chen, Y.; Liu, P.; Xiang, H.; Wang, W.; Ran, R.; Zhou, W.; Shao, Z.; Yang, X.; Chen, Y.; Xiang, H.; Wang, W.; Ran, R.; Zhou, W.; Shao, Z.; Liu, P. Simultaneous Power Conversion Efficiency and Stability Enhancement of $\text{Cs}_2\text{AgBiBr}_6$ Lead-Free Inorganic Perovskite Solar Cell through Adopting a Multifunctional Dye Interlayer. *Adv. Funct. Mater.* **2020**, *30* (23), 2001557.
- (84) McClure, E. T.; Ball, M. R.; Windl, W.; Woodward, P. M. $\text{Cs}_2\text{AgBiX}_6$ (X = Br, Cl): New Visible Light Absorbing, Lead-Free Halide Perovskite Semiconductors. *Chem. Mat.* **2016**, *28* (5), 1348–1354.
- (85) Wang, M.; Zeng, P.; Bai, S.; Gu, J.; Li, F.; Yang, Z.; Liu, M. High-Quality Sequential-Vapor-Deposited $\text{Cs}_2\text{AgBiBr}_6$ Thin Films for Lead-Free Perovskite Solar Cells. *Solar RRL* **2018**, *2* (12), 1800217.
- (86) Gao, W.; Ran, C.; Xi, J.; Jiao, B.; Zhang, W.; Wu, M.; Hou, X.; Wu, Z. High-Quality $\text{Cs}_2\text{AgBiBr}_6$ Double Perovskite Film for Lead-Free Inverted Planar Heterojunction Solar Cells with 2.2 % Efficiency. *Chem. Phys. Chem.* **2018**, *19* (14), 1696–1700.

- (87) Sirtl, M. T.; Hooijer, R.; Armer, M.; Ebadi, F. G.; Mohammadi, M.; Maheu, C.; Weis, A.; van Gorkom, B. T.; Häringer, S.; Janssen, R. A. J.; Mayer, T.; Dyakonov, V.; Tress, W.; Bein, T. 2D/3D Hybrid $\text{Cs}_2\text{AgBiBr}_6$ Double Perovskite Solar Cells: Improved Energy Level Alignment for Higher Contact-Selectivity and Large Open Circuit Voltage. *Adv. Energy Mater.* **2022**, *12* (7), 2103215.
- (88) Bartesaghi, D.; Slavney, A. H.; Gélvez-Rueda, M. C.; Connor, B. A.; Grozema, F. C.; Karunadasa, H. I.; Savenije, T. J. Charge Carrier Dynamics in $\text{Cs}_2\text{AgBiBr}_6$ Double Perovskite. *J. Phys. Chem. C* **2018**, *122* (9), 4809–4816.
- (89) Delor, M.; Slavney, A. H.; Wolf, N. R.; Filip, M. R.; Neaton, J. B.; Karunadasa, H. I.; Ginsberg, N. S. Carrier Diffusion Lengths Exceeding 1 Mm despite Trap-Limited Transport in Halide Double Perovskites. *ACS Energy Lett.* **2020**, *5* (5), 1337–1345.
- (90) Zhao, X. G.; Yang, J. H.; Fu, Y.; Yang, D.; Xu, Q.; Yu, L.; Wei, S. H.; Zhang, L. Design of Lead-Free Inorganic Halide Perovskites for Solar Cells via Cation-Transmutation. *J. Am. Chem. Soc.* **2017**, *139* (7), 2630–2638.
- (91) Xiao, Z.; Meng, W.; Wang, J.; Yan, Y. Thermodynamic Stability and Defect Chemistry of Bismuth-Based Lead-Free Double Perovskites. *Chem. Sus. Chem.* **2016**, *9* (18), 2628–2633.
- (92) Li, M.; Li, F.; Gong, J.; Zhang, T.; Gao, F.; Zhang, W.-H.; Liu, M. Advances in Tin(II)-Based Perovskite Solar Cells: From Material Physics to Device Performance. *Small Struct.* **2022**, *3* (1), 2100102.
- (93) Sansom, H. C.; Longo, G.; Wright, A. D.; Buizza, L. R. V.; Mahesh, S.; Wenger, B.; Zanella, M.; Abdi-Jalebi, M.; Pitcher, M. J.; Dyer, M. S.; Manning, T. D.; Friend, R. H.;

- Herz, L. M.; Snaith, H. J.; Claridge, J. B.; Rosseinsky, M. J. Highly Absorbing Lead-Free Semiconductor $\text{Cu}_2\text{AgBiI}_6$ for Photovoltaic Applications from the Quaternary CuI-AgI-BiI_3 Phase Space. *J. Am. Chem. Soc.* **2021**, *143* (10), 3983–3992.
- (94) Pai, N.; Chatti, M.; F  rer, S. O.; Scully, A. D.; Raga, S. R.; Rai, N.; Tan, B.; Chesman, A. S. R.; Xu, Z.; Rietwyk, K. J.; Reddy, S. S.; Hora, Y.; Sepalage, G. A.; Gl  ck, N.; Lira-Cant  , M.; Bach, U.; Simonov, A. N. Solution Processable Direct Bandgap Copper-Silver-Bismuth Iodide Photovoltaics: Compositional Control of Dimensionality and Optoelectronic Properties. *Adv. Energy Mater.* **2022**, *12* (32), 2201482.
- (95) Park, J.-G.; Park, S. W.; Hong, K.-H. High-Throughput Screening of Perovskite Inspired Bismuth Halide Materials: Toward Lead-Free Photovoltaic Cells and Light-Emitting Diodes. *Nanotechnology* **2022**, *33* (48), 485706.
- (96) Jin, Z.; Zhang, Z.; Xiu, J.; Song, H.; Gatti, T.; He, Z. A Critical Review on Bismuth and Antimony Halide Based Perovskites and Their Derivatives for Photovoltaic Applications: Recent Advances and Challenges. *J. Mater. Chem. A* **2020**, *8* (32), 16166–16188.
- (97) Ghosh, B.; Wu, B.; Guo, X.; Cholakkal Harikesh, P.; Abraham John, R.; Baikie, T.; S Wee, A. T.; Guet, C.; Chien Sum, T.; Mhaisalkar, S.; Mathews, N.; Ghosh, B.; Harikesh, P. C.; Baikie, T.; Guet, C.; Mhaisalkar, S.; Mathews, N.; Guo, X.; Wu, B.; Sum, T. C.; S Wee, A. T.; John, R. A. Superior Performance of Silver Bismuth Iodide Photovoltaics Fabricated via Dynamic Hot-Casting Method under Ambient Conditions. *Adv. Energy Mater.* **2018**, *8* (33), 1802051.
- (98) Jung, K. W.; Sohn, M. R.; Lee, H. M.; Yang, I. S.; Sung, S. Do; Kim, J.; Wei-Guang Diao,

- E.; Lee, W. I. Silver Bismuth Iodides in Various Compositions as Potential Pb-Free Light Absorbers for Hybrid Solar Cells. *Sustain. Energy Fuels* **2018**, 2 (1), 294–302.
- (99) Kim, Y.; Yang, Z.; Jain, A.; Voznyy, O.; Kim, G.; Liu, M.; Quan, L. N.; García de Arquer, F. P.; Comin, R.; Fan, J. Z. Pure Cubic-Phase Hybrid Iodobismuthates AgBi_2I_7 for Thin-Film Photovoltaics. *Angew. Chem. Int. Ed.* **2016**, 55 (33), 9586–9590.
- (100) Yi, Z.; Zhang, T.; Ban, H.; Shao, H.; Gong, X.; Wu, M.; Liang, G.; Zhang, X. L.; Shen, Y.; Wang, M. $\text{AgBi}_3\text{I}_{10}$ Rudorffite for Photovoltaic Application. *Solar Energy* **2020**, 206, 436–442.
- (101) Kausar, A.; Sattar, A.; Xu, C.; Zhang, S.; Kang, Z.; Zhang, Y. Advent of Alkali Metal Doping: A Roadmap for the Evolution of Perovskite Solar Cells. *Chem. Soc. Rev.* **2021**, 50 (4), 2696–2736.
- (102) Tang, S.; Huang, S.; Wilson, G. J.; Ho-Baillie, A. Progress and Opportunities for Cs Incorporated Perovskite Photovoltaics. *Trends Chem.* **2020**, 2 (7), 638–653.
- (103) Pai, N.; Lu, J.; Gengenbach, T. R.; Seeber, A.; Chesman, A. S. R.; Jiang, L.; Senevirathna, D. C.; Andrews, P. C.; Bach, U.; Cheng, Y. B.; Simonov, A. N. Silver Bismuth Sulfoiodide Solar Cells: Tuning Optoelectronic Properties by Sulfide Modification for Enhanced Photovoltaic Performance. *Adv. Energy Mater.* **2019**, 9 (5), 1803396.
- (104) Park, J. W.; Lim, Y.; Doh, K.-Y.; Jung, M. T.; Jeon, Y. I.; Yang, I. S.; Choi, H.; Kim, J.; Lee, D.; Lee, W. I. Enhancement of the Photovoltaic Properties of Ag_2BiI_5 by Cu Doping. *Sustain. Energy Fuels* **2021**, 5 (5), 1439–1447.

- (105) Hooijer, R.; Weis, A.; Kaiser, W.; Biewald, A.; Dörflinger, P.; Maheu, C.; Arsatiants, O.; Helminger, D.; Dyakonov, V.; Hartschuh, A. Cu/Ag–Sb–I Rudorffite Thin Films for Photovoltaic Applications. *Chem. Mat.* **2023**.
- (106) Yu, F.; Wang, L.; Ren, K.; Yang, S.; Xu, Z.; Han, Q.; Ma, T. Cs-Incorporated AgBiI₄ Rudorffite for Efficient and Stable Solar Cells. *ACS Sustain. Chem. Eng.* **2020**, 8 (27), 9980–9987.
- (107) Hsiao, K.-C.; Yu, Y.-F.; Ho, C.-M.; Jao, M.-H.; Chang, Y.-H.; Chen, S.-H.; Chang, Y.-H.; Su, W.-F.; Lee, K.-M.; Wu, M.-C. Doping Engineering of Carrier Transporting Layers for Ambient-Air-Stable Lead-Free Rudorffite Solar Cells Prepared by Thermal-Assisted Doctor Blade Coating. *Chem. Eng. J.* **2023**, 451, 138807.
- (108) Wu, M.-C.; Wang, Q.-H.; Hsiao, K.-C.; Chen, S.-H.; Ho, C.-M.; Jao, M.-H.; Chang, Y.-H.; Su, W.-F. Composition Engineering to Enhance the Photovoltaic Performance and to Prolong the Lifetime for Silver Bismuth Iodide Solar Cell. *Chem. Eng. J. Adv.* **2022**, 10, 100275.
- (109) Kulkarni, A.; Ünlü, F.; Pant, N.; Kaur, J.; Bohr, C.; Jena, A. K.; Öz, S.; Yanagida, M.; Shirai, Y.; Ikegami, M.; Miyano, K.; Tachibana, Y.; Chakraborty, S.; Mathur, S.; Miyasaka, T. Concerted Ion Migration and Diffusion-Induced Degradation in Lead-Free Ag₃BiI₆ Rudorffite Solar Cells under Ambient Conditions. *Solar RRL* **2021**, 5 (8), 2100077.
- (110) Turkevych, I.; Kazaoui, S.; Ito, E.; Urano, T.; Yamada, K.; Tomiyasu, H.; Yamagishi, H.; Kondo, M.; Aramaki, S. Photovoltaic Rudorffites: Lead-Free Silver Bismuth Halides Alternative to Hybrid Lead Halide Perovskites. *Chem. Sus. Chem.* **2017**, 10 (19), 3754–

3759.

- (111) Ravidas, B. K.; Das, A.; Agnihotri, S. K.; Pandey, R.; Madan, J.; Hossain, M. K.; Roy, M. K.; Samajdar, D. P. Design Principles of Crystalline Silicon/CsGeI₃ Perovskite Tandem Solar Cells Using a Combination of Density Functional Theory and SCAPS-1D Frameworks. *Sol. Energy Mater. Sol. Cells* **2024**, 267, 112688.
- (112) Eisler, C. N.; Abrams, Z. R.; Sheldon, M. T.; Zhang, X.; Atwater, H. A. Multijunction Solar Cell Efficiencies: Effect of Spectral Window, Optical Environment and Radiative Coupling. *Energy Environ. Sci.* **2014**, 7 (11), 3600–3605.
- (113) Nguyen, T. T.; Kim, J.; Kim, Y. S.; Nguyen, B. P.; Jo, W. Wide-Bandgap Perovskites for Multijunction Solar Cells: Improvement of Crystalline Quality of Cs_{0.1}FA_{0.9}PbI_{1.4}Br_{1.6} by Using Lead Thiocyanate. *J. Mater. Chem. A* **2023**, 11 (19), 10254–10266.
- (114) Cotal, H.; Fetzer, C.; Boisvert, J.; Kinsey, G.; King, R.; Hebert, P.; Yoon, H.; Karam, N. III–V Multijunction Solar Cells for Concentrating Photovoltaics. *Energy Environ. Sci.* **2009**, 2 (2), 174–192.
- (115) Interactive Best Research-Cell Efficiency Chart | Photovoltaic Research | NREL <https://www.nrel.gov/pv/interactive-cell-efficiency.html> (accessed May 24, 2024).
- (116) Heydarian, M.; Heydarian, M.; Bett, A. J.; Bivour, M.; Schindler, F.; Hermle, M.; Schubert, M. C.; Schulze, P. S. C.; Borchert, J.; Glunz, S. W. Monolithic Two-Terminal Perovskite/Perovskite/Silicon Triple-Junction Solar Cells with Open Circuit Voltage >2.8 V. *ACS Energy Lett.* **2023**, 8 (10), 4186–4192.

- (117) Isikgor, F. H.; Maksudov, T.; Chang, X.; Adilbekova, B.; Ling, Z.; Hadmojo, W. T.; Lin, Y.; Anthopoulos, T. D. Monolithic Perovskite-Perovskite-Organic Triple-Junction Solar Cells with a Voltage Output Exceeding 3 V. *ACS Energy Lett.* **2022**, *7* (12), 4469–4471.
- (118) McMeekin, D. P.; Mahesh, S.; Noel, N. K.; Klug, M. T.; Lim, J. C.; Warby, J. H.; Ball, J. M.; Herz, L. M.; Johnston, M. B.; Snaith, H. J. Solution-Processed All-Perovskite Multi-Junction Solar Cells. *Joule* **2019**, *3* (2), 387–401.
- (119) Hu, H.; An, S. X.; Li, Y.; Orooji, S.; Singh, R.; Schackmar, F.; Laufer, F.; Jin, Q.; Feeney, T.; Diercks, A.; Gota, F.; Moghadamzadeh, S.; Pan, T.; Rienäcker, M.; Peibst, R.; Nejand, B. A.; Paetzold, U. W. Triple-Junction Perovskite–Perovskite–Silicon Solar Cells with Power Conversion Efficiency of 24.4%. *Energy Environ. Sci.* **2024**, *17* (8), 2800–2814.
- (120) Zheng, J.; Wang, G.; Duan, W.; Mahmud, M. A.; Yi, H.; Xu, C.; Lambertz, A.; Bremner, S.; Ding, K.; Huang, S.; Ho-Baillie, A. W. Y. Monolithic Perovskite-Perovskite-Silicon Triple-Junction Tandem Solar Cell with an Efficiency of over 20%. *ACS Energy Lett.* **2022**, *7* (9), 3003–3005.
- (121) Green, M. A.; Dunlop, E. D.; Yoshita, M.; Kopidakis, N.; Bothe, K.; Siefert, G.; Hao, X.; Jiang, J. Y. Solar Cell Efficiency Tables (Version 65). *Prog. Phot. Res. Appl.* **2024**, 1–13.
- (122) Li, S.; Jiang, Y.; Xu, J.; Wang, D.; Ding, Z.; Zhu, T.; Chen, B.; Yang, Y.; Wei, M.; Guo, R.; Hou, Y.; Chen, Y.; Sun, C.; Wei, K.; Qaid, S. M. H.; Lu, H.; Tan, H.; Di, D.; Chen, J.; Grätzel, M.; Sargent, E. H.; Yuan, M. High-Efficiency and Thermally Stable FACsPbI₃ Perovskite Photovoltaics. *Nature* **2024**, *635* (8037), 82–88.
- (123) Li, F.; Wu, D.; Shang, L.; Xia, R.; Zhang, H.; Huang, Z.; Gong, J.; Mao, L.; Zhang, H.; Sun,

- Y.; Yang, T.; Sun, X.; Feng, Z.; Liu, M. Highly Efficient Monolithic Perovskite/Perovskite/Silicon Triple-Junction Solar Cells. *Adv. Mater.* **2024**, *36* (16), 2311595.
- (124) Hörantner, M. T.; Leijtens, T.; Ziffer, M. E.; Eperon, G. E.; Christoforo, M. G.; McGehee, M. D.; Snaith, H. J. The Potential of Multijunction Perovskite Solar Cells. *ACS Energy Lett.* **2017**, *2* (10), 2506–2513.
- (125) Hao, F.; Stoumpos, C. C.; Chang, R. P. H.; Kanatzidis, M. G. Anomalous Band Gap Behavior in Mixed Sn and Pb Perovskites Enables Broadening of Absorption Spectrum in Solar Cells. *J. Am. Chem. Soc.* **2014**, *136* (22), 8094–8099.
- (126) Noh, J. H.; Im, S. H.; Heo, J. H.; Mandal, T. N.; Seok, S. Il. Chemical Management for Colorful, Efficient, and Stable Inorganic-Organic Hybrid Nanostructured Solar Cells. *Nano Lett.* **2013**, *13* (4), 1764–1769.
- (127) Kojima, A.; Teshima, K.; Shirai, Y.; Miyasaka, T. Organometal Halide Perovskites as Visible-Light Sensitizers for Photovoltaic Cells. *J. Am. Chem. Soc.* **2009**, *131* (17), 6050–6051.
- (128) Liu, C.; Yang, Y.; Chen, H.; Xu, J.; Liu, A.; Bati, A. S. R.; Zhu, H.; Grater, L.; Hadke, S. S.; Huang, C.; Sangwan, V. K.; Cai, T.; Shin, D.; Chen, L. X.; Hersam, M. C.; Mirkin, C. A.; Chen, B.; Kanatzidis, M. G.; Sargent, E. H. Bimolecularly Passivated Interface Enables Efficient and Stable Inverted Perovskite Solar Cells. *Science* **2023**, *382* (6672), 810–815.
- (129) Park, S. M.; Wei, M.; Xu, J.; Atapattu, H. R.; Eickemeyer, F. T.; Darabi, K.; Grater, L.; Yang, Y.; Liu, C.; Teale, S.; Chen, B.; Chen, H.; Wang, T.; Zeng, L.; Maxwell, A.; Wang,

- Z.; Rao, K. R.; Cai, Z.; Zakeeruddin, S. M.; Pham, J. T.; Risko, C. M.; Amassian, A.; Kanatzidis, M. G.; Graham, K. R.; Grätzel, M.; Sargent, E. H. Engineering Ligand Reactivity Enables High-Temperature Operation of Stable Perovskite Solar Cells. *Science* **2023**, *381* (6654), 209–215.
- (130) Peng, W.; Mao, K.; Cai, F.; Meng, H.; Zhu, Z.; Li, T.; Yuan, S.; Xu, Z.; Feng, X.; Xu, J.; McGehee, M. D.; Xu, J. Reducing Nonradiative Recombination in Perovskite Solar Cells with a Porous Insulator Contact. *Science* **2023**, *379* (6633), 683–690.
- (131) Snaith, H. J. Perovskites: The Emergence of a New Era for Low-Cost, High-Efficiency Solar Cells. *J. Phys. Chem. Lett.* **2013**, *4* (21), 3623–3630.
- (132) Yang, T. C. J.; Fiala, P.; Jeangros, Q.; Ballif, C. High-Bandgap Perovskite Materials for Multijunction Solar Cells. *Joule* **2018**, *2* (8), 1421–1436.

Chapter 2

Photovoltaic and surface morphological improvements of a novel material class $\text{Cu}_6\text{AgBiI}_{10}$

2.1 Introduction

The inorganic ternary or quaternary compounds of the CuI-AgI-BiI_3 phase have great potential for optoelectronic and photovoltaic. Their excellent stability, suitable band gaps, high absorption coefficients, as well as charges carrier transport properties make them attractive.¹⁻⁵ On the other hand, the halide double-perovskite $\text{Cs}_2\text{AgBiBr}_6$ has a low excitonic absorption peak, which is 2.8 eV and its band gap at 3.03 eV. Theoretically, this compound might have a narrow band gap, but it is not stable. As a result, a significant gap in the ability of lead free metal-halide materials is filled by the materials from the CuI-AgI-BiI_3 phase.⁶⁻⁹ Recent studies showed that the Silver Bismuth Sulfoiodide based solar cells obtained power conversion efficiency greater than 5%.¹⁰ $\text{Cu}_6\text{AgBiI}_{10}$ is-, a fairly novel material that has been found to have a higher light absorption and a narrow band-gap than $\text{Cu}_2\text{AgBiI}_6$ and CuAgBiI_5 which makes it more efficient at converting sunlight into electricity. Additionally, $\text{Cu}_2\text{AgBiI}_6$ has been found to be more stable when subjected to humidity and air and moisture, making it more suitable for practical applications. CuAgBiI_5 and $\text{Cu}_2\text{AgBiI}_6$ solar cells with power conversion efficiency of 1.01 % and 2.39%, respectively, have been reported. This result suggests the improvement of efficiency with increasing copper content. In 2021, Leonardo et al. first investigation revealed crystal structural, charge carrier localization and dynamics properties for $\text{Cu}_6\text{AgBiI}_{10}$ material.¹ But, there have not yet been any reports of photovoltaic devices that are based on $\text{Cu}_6\text{AgBiI}_{10}$. In order to address this problem, we present a

study of the influence of annealing temperatures on photovoltaic performance in the $\text{Cu}_6\text{AgBiI}_{10}$ materials. In this research solar cells were prepared using a mixed solvent-based hot-casting technique. The improved surface morphology of the material and better coverage surface allowed us to achieve the highest possible photovoltaic performances. It is expected that the optimization of suitable device architectures and transport layers will lead to advanced photovoltaic devices using these materials.

2.2 Experimental section

2.2.1 Chemicals

Bismuth (III) iodide (BiI_3), Silver iodide (AgI) and Poly (3-hexylthiophene-2-5-diyl) (P3HT) were purchased from Sigma-Aldrich. Copper (I) iodide, O-Dichlorobenzene, 2-propanol, Acetone and Ethanol were purchased from Kanto chemical, Co. Tin (IV) Oxide, 15% in H_2O colloidal dispersion was purchased from Alfa Aesar. Pelco colloidal graphite powder (Iso-propanal base) was purchased from Ted Pella, Inc. N, N-dimethylformamide (DMF) was purchased from Fujifilm wako pure chemical Co. and Dimethylsulfoxide (DMSO) was purchased from Nacalai tesque. This experiment used highly purified N_2 gas and water purified using Direct-Q Water Purification Systems.

2.2.2 $\text{Cu}_6\text{AgBiI}_{10}$ (CABI) thin film fabrication

In order to make the CABI solutions in 50 wt.%, the 6:1:1 molar ratios (MR) of CuI , AgI and BiI_3 were dissolved into a 3:1 mix consisting of DMSO and DMF according to the proper ratio of stoichiometry as shown in **Figure 2.1** (Step-1). The mixture solution shown in **Figure 2.1** (Step-2) was then stirred at 150 °C and 700 rpm for 30 minutes in a glove box that contained pure N_2 gas. Then, the solution was kept at a temperature of 80 °C within the glove box for around 16

hours. The solution in warm and red color was filtered using a PTFE membrane filter of 0.2 μm pore size.

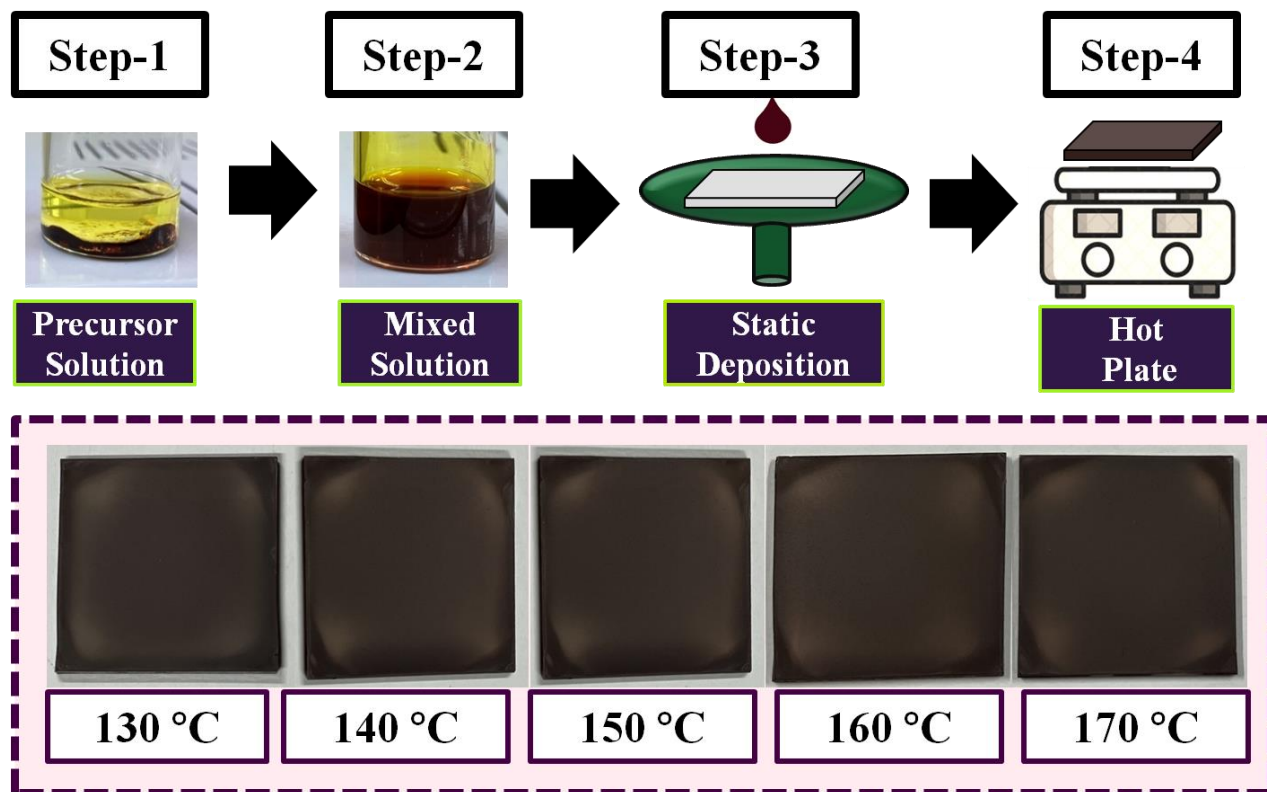


Figure 2.1 Schematic flow diagram steps of $\text{Cu}_6\text{AgBiI}_{10}$ thin film preparation.

The hot casting, as shown in **Figure 2.1** (step-3), was accomplished by heating the filtered solution at 100 °C for one hour and then preheating the substrate at the same temperature for five minutes before starting the spin-coating process. The solution was spin-coated at 3000 rpm for 30 seconds. In the glove box, natural drying took about 30 minutes. The films were then annealed in a glovebox at 75 °C for 3 minutes and then heated at different temperatures (130 to 170 °C) for six minutes on the hot-plate. Then the films were allowed to naturally cool to the ambient temperature. Anti-solvent was not used during spin-coating.

2.2.3 CABI photovoltaic device fabrication

The ITO substrates resistance was $10 \Omega/\text{cm}^2$. These were then cut into pieces $2 \text{ cm} \times 2 \text{ cm}$. After cleaning them in de-ionized water, acetone and ethanol, they were then exposed for 15 minutes with an Ozone-killer. The spin-coating process was used to prepare the inorganic Electron transport layer (ETL) of SnO_2 on the top of ITO substrates as shown in **Figure 2.2**. This was done at a speed of 5000 rpm for 20 second. After being prepared, the films were annealed at 150°C for 30 minutes in air. Following this, the CABI film was coated on ETL layer according to the thin film fabrication section.

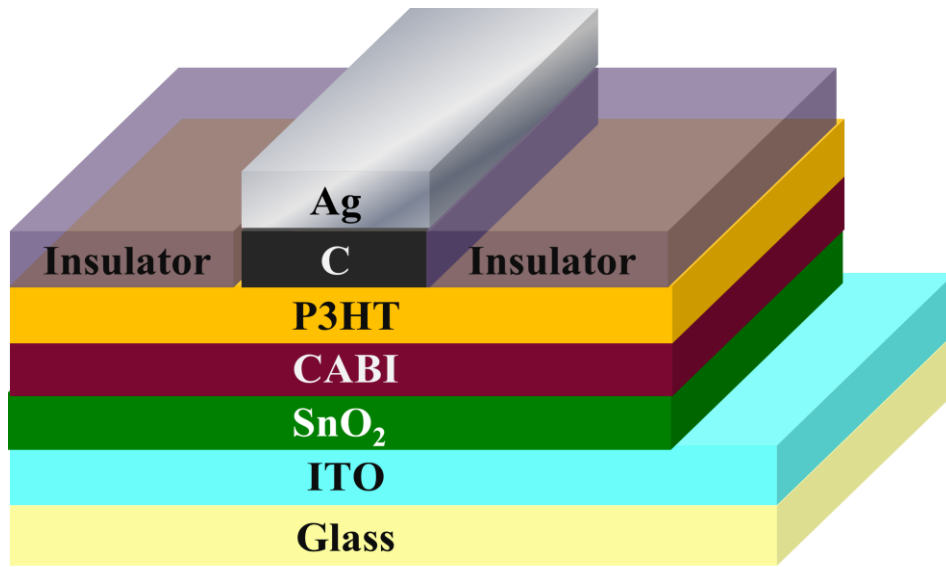


Figure 2.2 n-i-p type device structure of the $\text{Cu}_6\text{AgBiI}_{10}$ solar cell.

Here, O-chlorobenzene (1 mL) is used to dissolve 15 mg of P3HT, which acts as a hole transportation layer (HTL). The solution was deposited using spin coating at 3000 rpm for 20 seconds on the CABI layers. After that, it was annealed at 120°C for 20 minutes in the glovebox. As the last step in the preparation of a solar cell is to attach an insulation tape with small hole (0.07

cm²), which also known as active area. It was then attached to the HTL layer. The graphite solution is prepared of colloidal graphite with 2-propanol. On the active area, this solution was then coated with a static spin coating. Ag paste was used to strengthen the connection between the probe and the graphite. The entire CABI cell's structure is illustrated in **Figure 2.2**.

2.2.4 Characterization

The patterns of X-ray diffraction (XRD) of the CABI films were captured using Rigaku SmartLab at NITech using the scan step 0.02 which has *Cu-K_α* as the target source. The morphology of the surface of the CABI films were revealed using the Scanning Electron Microscope (SEM), model number JSM 6510 (From JEOL). The energy dispersive X-ray spectrometer (EDS) was carried out with the help of a field emission scanning electron microscope, model no. JSM-7001FF manufactured by JEOL. It was used to analysis of elements in CABI films. The optical properties of CABI films are analyzed using the "JASCO V-570" UV/VIS/NIR spectrophotometer. The thicknesses of the CABI films were measured using the Veeco Dektak 150 model machine. The photovoltaic performance was recorded using the solar simulator under the conditions AM 1.5 and 100 mW.cm⁻².

2.3 Results and discussion

2.3.1 Structural analysis

The investigation of structural properties is vital in solar cell materials as it helps in understanding the structure of crystals, the purity of their phases, the morphology and other important properties that affect the performance of solar cells.

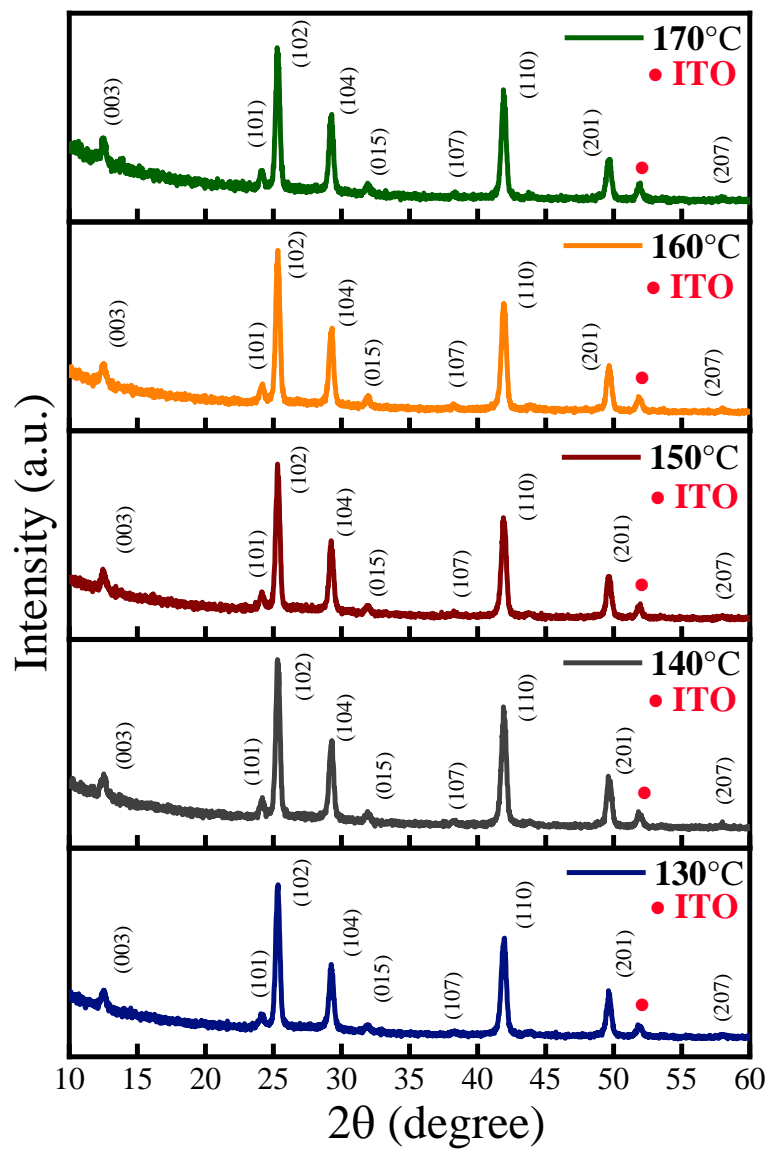


Figure 2.3 Experimental XRD signature of the ITO/SnO₂/Cu₆AgBiI₁₀ films at various annealing temperatures.

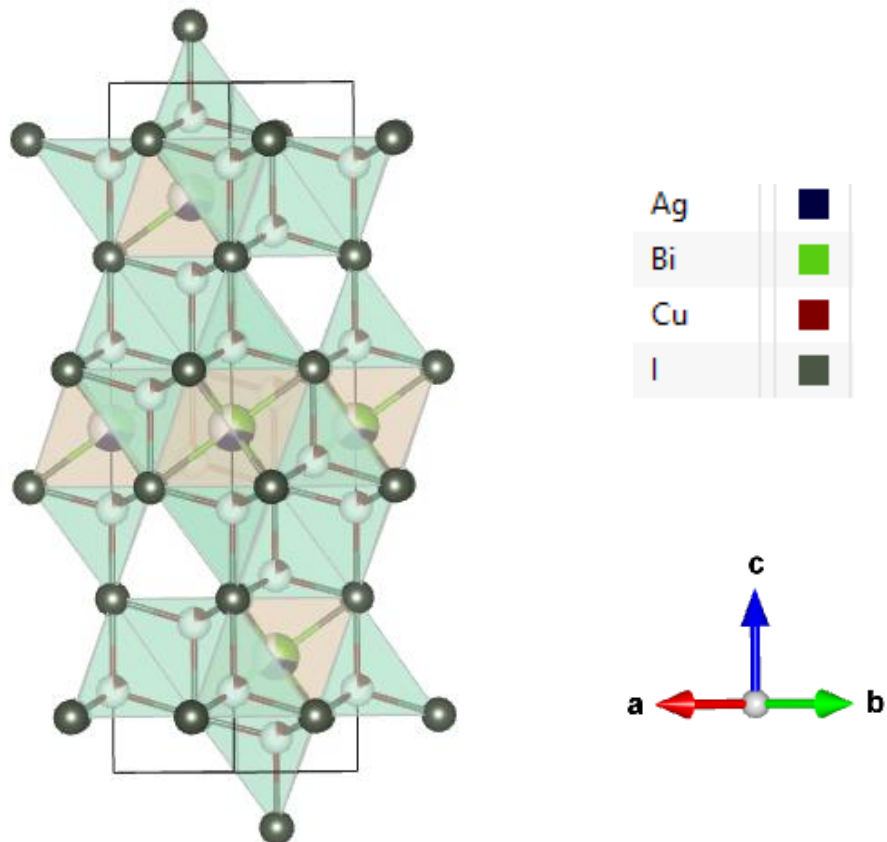


Figure 2.4 Three-dimensional crystal structure of $\text{Cu}_6\text{AgBiI}_{10}$ film.

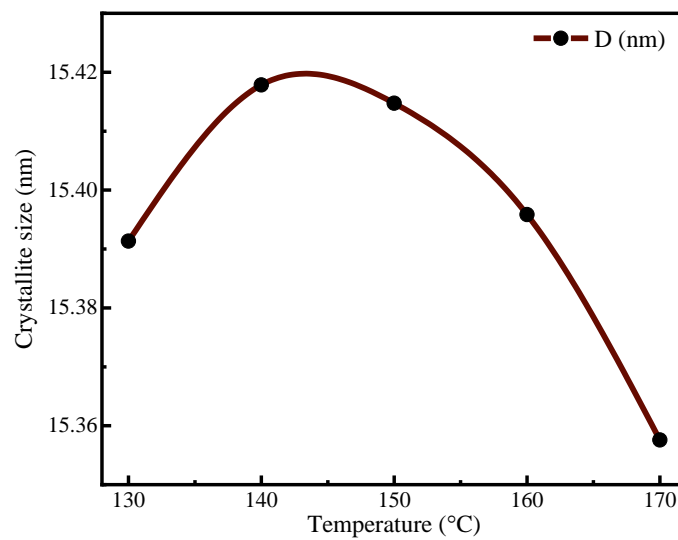


Figure 2.5 The changes of crystallite size as a result of annealing temperatures for $\text{Cu}_6\text{AgBiI}_{10}$ film.

Figure 2.3 illustrates the XRD spectrums of CABI layers deposited above the ITO/SnO₂ layer. The X-ray diffractometer was used to study CABI films at various annealing temperatures in order to confirm their crystal structure and crystallinity. The XRD profile clearly identifies defined peaks as (003), (101), (102), (104), (015) (107), (110), (201) and (207), which indicates that the various temperature annealed CABI films have the trigonal structure as shown in **Figure 2.4**. Moreover, it also matches well with previous defining reflections.^{1,11} The ITO layers only show a peak at 52.00°, while SnO₂ layers do not have any peak. This is because of the disordered structure caused by colloidal dispersion in SnO₂ water. Another reason is the thinness of the SnO₂ layers.¹² The XRD pattern of trigonal CABI films revealed three sharp peaks, which are asymmetrically arranged. So, the CABI films have a rhombohedral unit cell.¹ Under various annealing temperatures, the peak positions and the peak intensity remained nearly constant. The crystallite size of the sample at different annealing temperatures is determined by using the Debye Scheer formula. $D = \frac{0.9\lambda}{\beta \cos \theta}$,^{13,14} Here, λ represents the X-ray wavelength, the angle of the incident beam is θ , and the full width at half maximum (FWHM) is β . The range of crystallite sizes calculated is 15.36 to 15.42 nm as shown in **Figure 2.5**. In order to form a more stable trigonal crystal structure, annealing at 140 and 150°C promotes optimal atomic diffusion. At these temperatures, crystallites grow larger and more well-defined, reducing defects and enhancing charge transport. When temperatures are high, grain growth may be excessive, whereas when they are low, crystallization may not be optimal.

2.3.2 Morphological and elemental analysis

It is essential to understand surface morphology in order to improve our fundamental understanding of materials and their properties. The performance and quality of solar cells will be

affected by their surface morphology. The SEM analysis has shown that grain size is affected by annealing temperature.¹⁵⁻¹⁸ The grain size is increased and becomes flat from 130 °C to 150 °C, then decrease and becomes more island-type from 150 °C to 170 °C, as illustrated in the **Figure 2.6**. From 130°C to 150°C temperature range, it is likely that a process called grain growth dominates. Grain growth occurs when small grains within a material coalesce and grow in size. At 130°C, the diffusion of atoms is relatively slow, leading to a gradual increase in grain size. As the grains grew larger, they tended to merge with neighboring grains, resulting in a flatter morphology at 150°C. The film's smooth, flat surface is suitable for making uniform contact with the hole transport layer.¹⁹ The thermal energy causes grain to expand when CABI film is annealed. The films that were annealed to 150 °C have the best quality surface morphology, because that has the biggest average grain sizes. This can be seen in the fact that the temperature of annealing can show distinct morphologies. It is evident that the average size of grain increased up to a maximum of 10.30 µm when the temperatures of annealing were raised. However, at 170°C, the copper-silver and bismuth based components in solar cell materials tend to form island-type grains.²⁰⁻²³ This is due to the fact that the high temperature causes the materials to diffuse and segregate, resulting in the formation of small clusters or islands. These islands can have a significant impact on the performance of the solar cell, as they can affect the flow of electrons and the efficiency of the energy conversion process.^{24,25} At 170°C, annealing temperature is island-type, but uniform and stable grain boundary form is shown in **Figure 2.6**. The surface morphology shows that films annealed at 150°C have the most homogeneous and smooth surface morphology. Light absorption and charge carrier mobility depend on surface homogeneity, which reduces flaws. Uneven surfaces or smaller grain sizes may reduce performance at temperatures above or below this ideal limit.

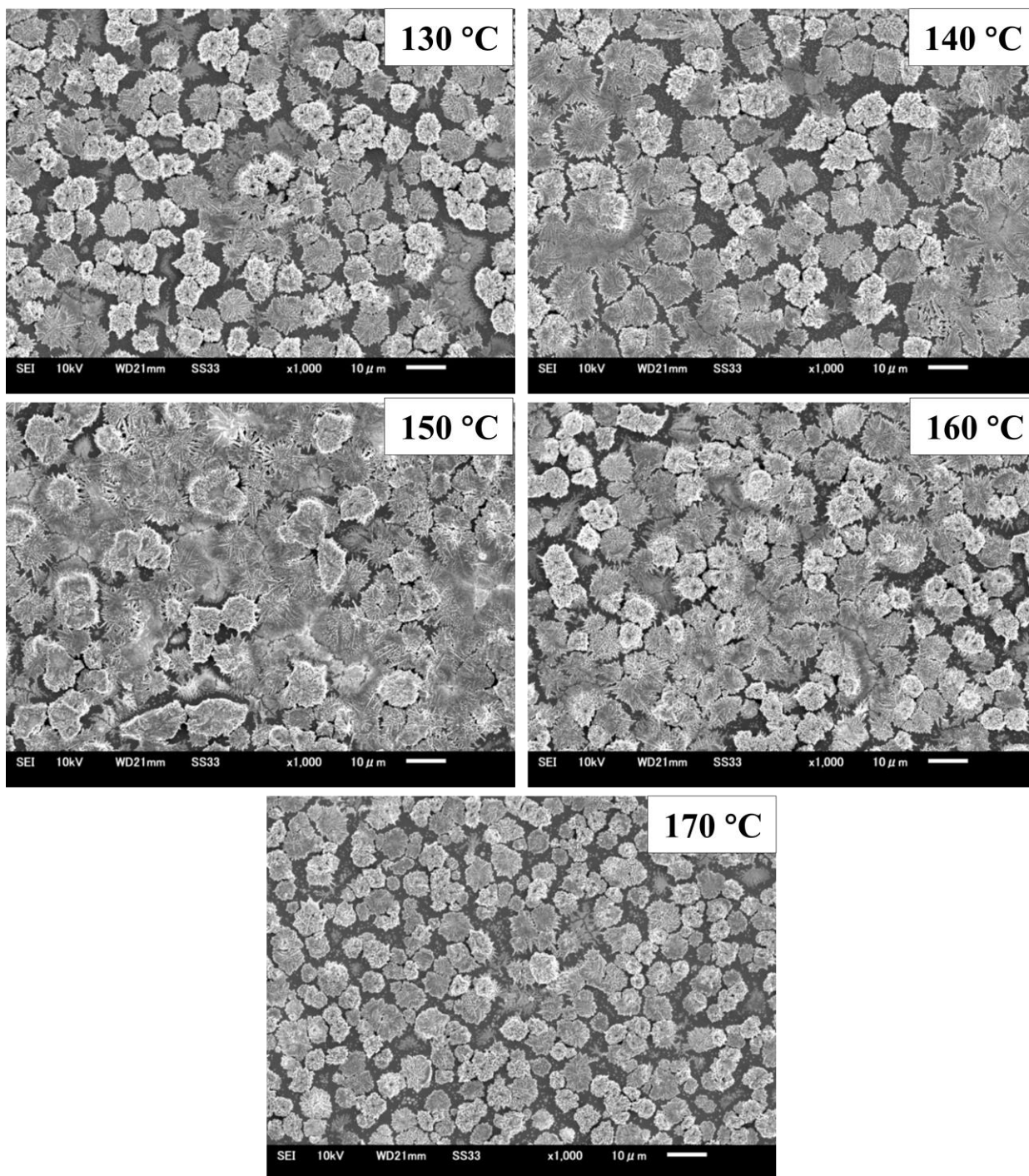


Figure 2.6 The top view of SEM images with various annealing temperatures of $\text{Cu}_6\text{AgBiI}_{10}$ film on the ITO/ SnO_2 structure.

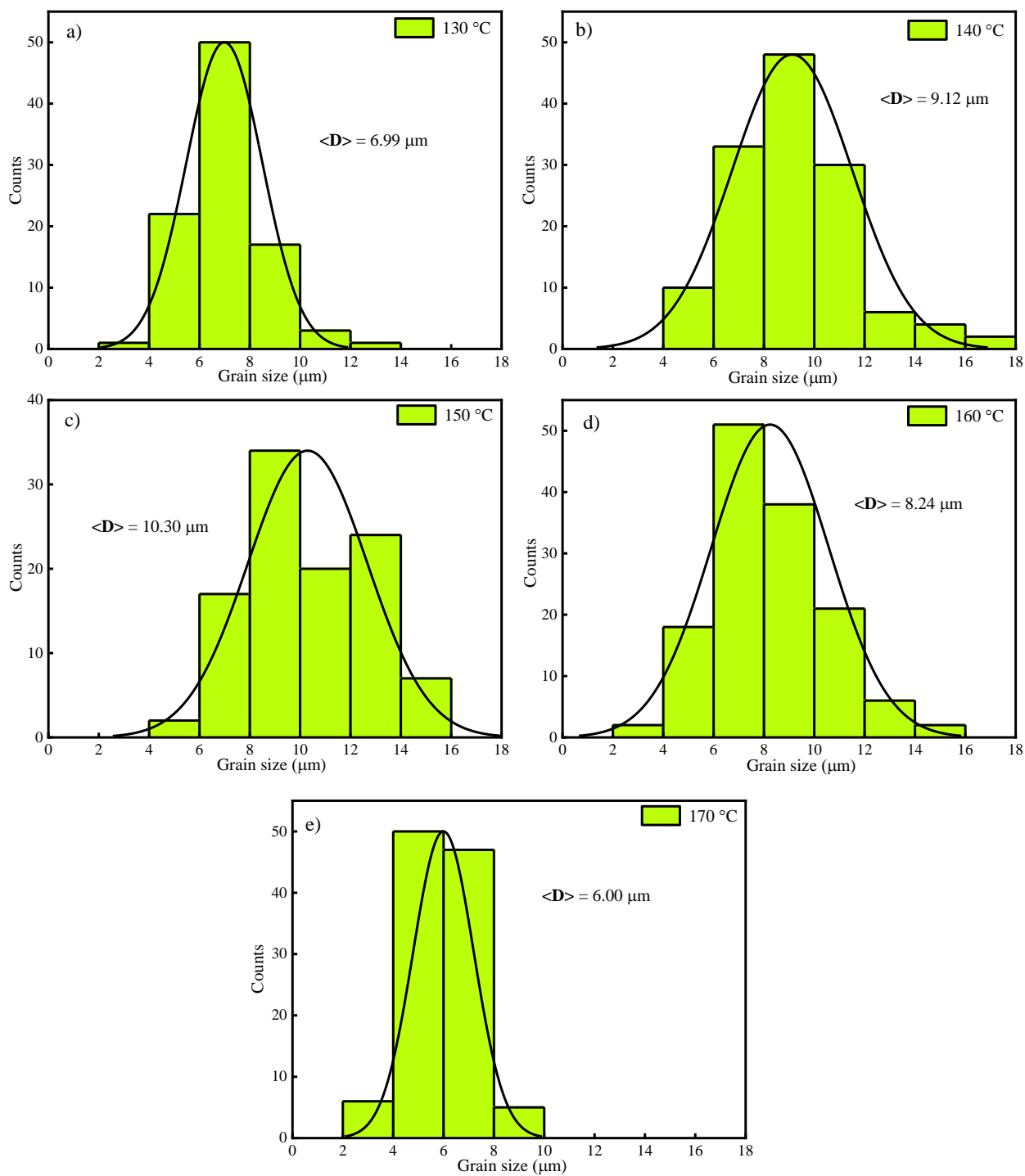


Figure 2.7 Visual representation of the grain size distribution histogram of $\text{Cu}_6\text{AgBiI}_{10}$ film under various annealing temperature conditions.

Histogram graphs provide valuable information about the grain distribution of film, such as its uniformity as well as the average grain size. By analyzing the shape and width of the histogram, we can get a better understanding of the grain distribution. **Figure 2.7** showed the same trend that we discussed in the SEM micrograph. The average grain size rises from 6.99 to 10.30 μm at temperatures up to 150 $^{\circ}\text{C}$ during annealing. It then gradually decreases.

The EDS analysis is an effective tool to examine and characterize materials. In terms of chemical composition, element distribution, and surface characteristics, it provides crucial information.²⁶⁻²⁸

In the ambient temperature EDX investigation was performed to evaluate the elemental compositions of CABI films at different annealing temperatures. From **Figure 2.8** and **Table 2.1** we could see that the $\text{Cu}_6\text{AgBiI}_{10}$ composition is part of the corresponding peaks, which are Cu, Ag, Bi and I. **Figure 2.8** illustrates the appropriate percentages of $\text{Cu}_6\text{AgBiI}_{10}$ that were determined through experiments of weight and atomics of the different elements and this composition is totally impurity-free. **Figure 2.9** shows the typical SEM image and corresponding EDS mapping images of Cu, Ag, Bi and I for 130 $^{\circ}\text{C}$ annealed sample. The EDS profile confirms that the constituent elements are distributed in the homogeneous way. The EDS spectrum shows that the proportion of elements in component matches the nominal composition of CABI films.

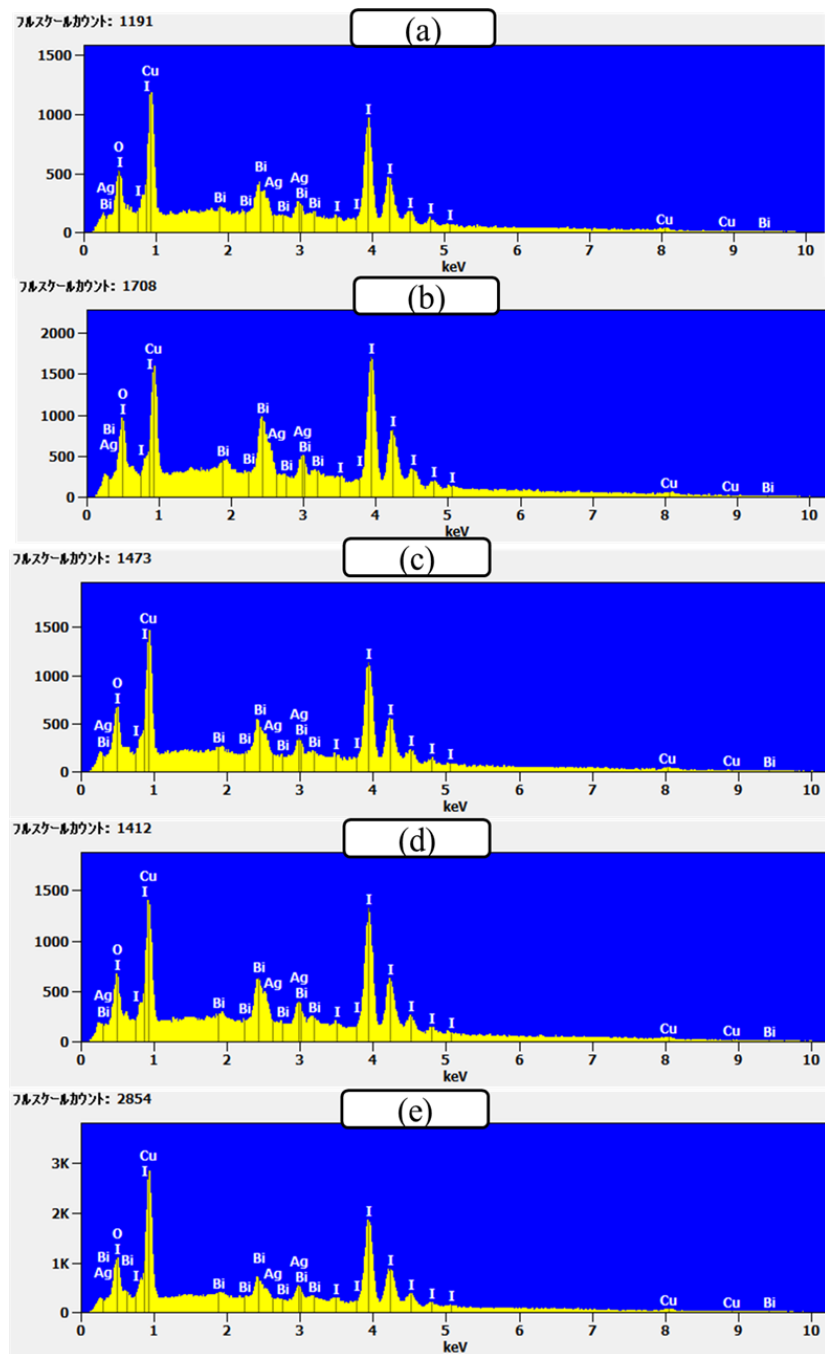


Figure 2.8 EDS elemental analysis of $\text{Cu}_6\text{AgBiI}_{10}$ film under various annealing temperature conditions (a) 130 °C, (b) 140 °C, (c) 150 °C, (d) 160 °C and (e) 170 °C.

Table 2.1 Comparative study of EDS elemental analysis of Cu₆AgBiI₁₀ film under various annealing temperature conditions.

Annealing Temperature	130°C		140°C		150°C		160°C		170°C	
Element	Weight (%)	Atomic (%)	Weight (%)	Atomic (%)	Weight (%)	Atomic (%)	Weight (%)	Atomic (%)	Weight (%)	Atomic (%)
<i>Cu L</i>	23.25	38.41	17.06	30.12	22.30	37.17	19.32	33.12	25.77	41.35
<i>Ag L</i>	5.21	5.07	5.61	5.84	5.73	5.63	6.33	6.39	5.59	5.28
<i>I L</i>	63.36	52.42	64.89	57.37	63.14	52.72	64.44	55.32	62.94	50.58
<i>Bi M</i>	8.18	4.11	12.43	6.67	8.83	4.48	9.91	5.16	5.70	2.78
Total	100.00	100.00	100.00	100.00	100.00	100.00	100.00	100.00	100.00	100.00

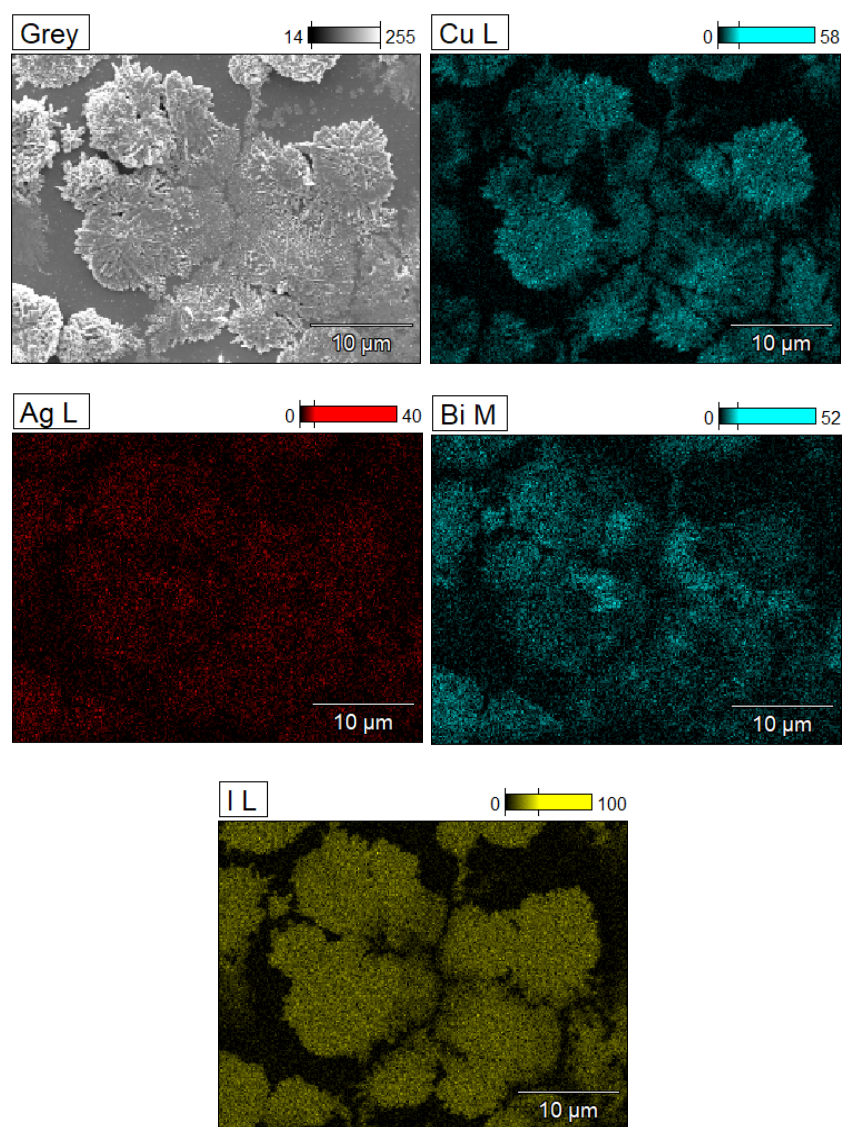


Figure 2.9 EDS elemental profile of $\text{Cu}_6\text{AgBiI}_{10}$ film at 130 °C annealing temperature.

2.3.3 Optical properties

Solar cells need optical properties analysis to understand how they absorb and convert light rays into electricity. The reflectivity, transmittance and absorption of light rays in the solar cell material can affect its efficiency. The solar cell is able to absorb more light, meaning that more electricity will be generated. It is essential to decrease the reflectance of solar cells so that it can maximize the absorption of light.²⁹⁻³⁵ As shown in **Figure 2.10** shows clearly that reflectance decreases as the annealing temperature increases up to 150°C, and then increase again. The film's grain size directly influences its reflectance. Films with larger grain sizes reflect less light than films with smaller grains. Larger grains allow light to penetrate deeper into the material and reflect back less. This is why CABI films with larger grain sizes have lower reflectance.

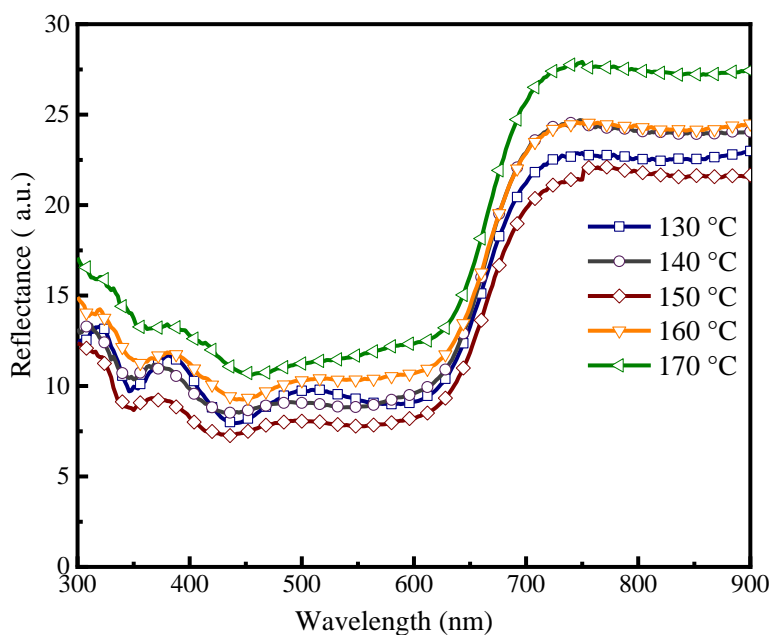


Figure 2.10 Reflectance spectra of $\text{Cu}_6\text{AgBiI}_{10}$ film at various annealing temperatures.

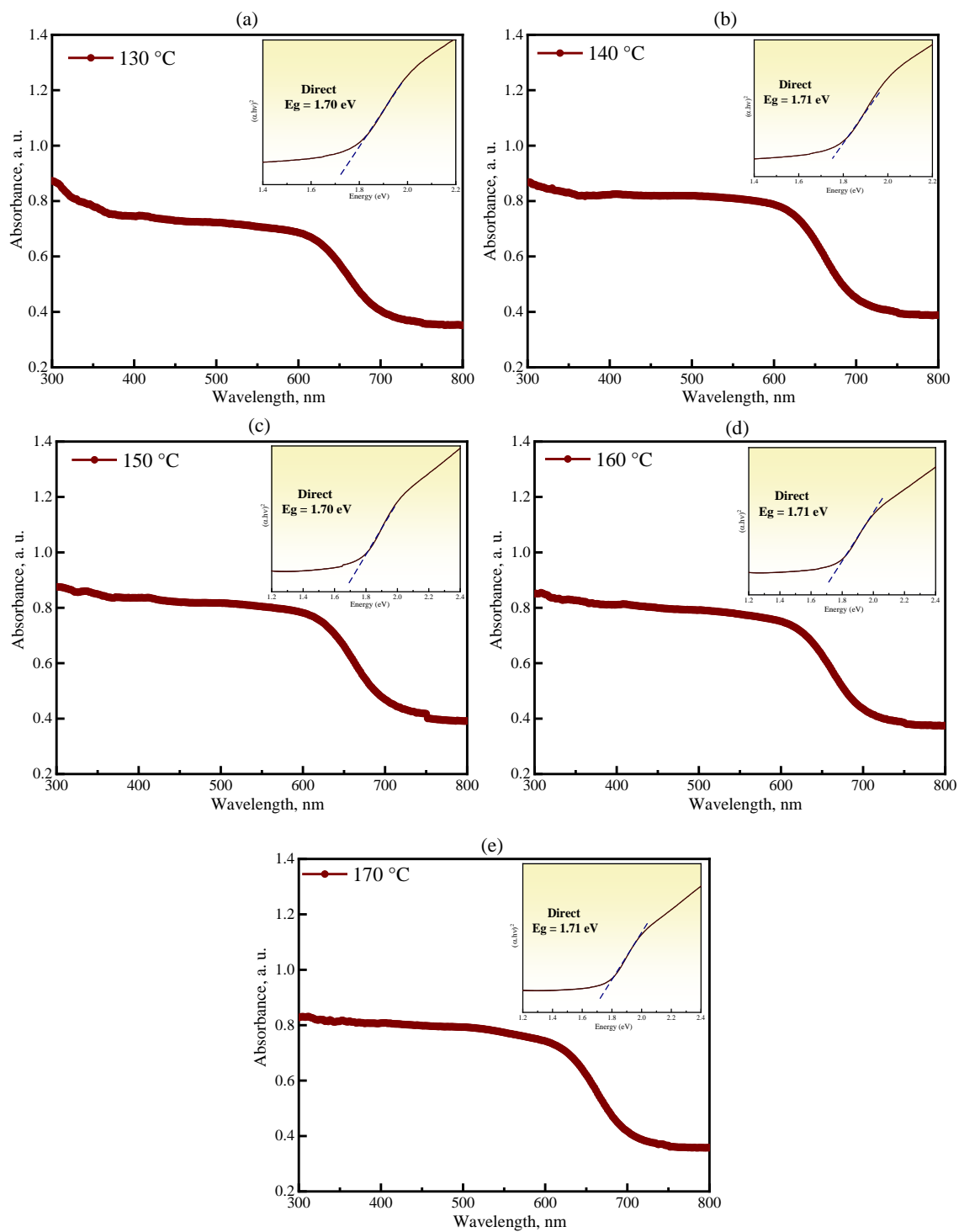


Figure 2.11 Absorbance spectra of $\text{Cu}_6\text{AgBiI}_{10}$ films at various annealing temperatures.

The absorption spectra were determined using the formula $A = 1 - (T + R)$ in which A is the absorbance, while T and R are the materials transmittance and reflectance.²⁹ As illustrated in **Figure 2.11**, the absorption spectrums of the CABI films of different annealing temperatures are similar to each other but the samples that have been annealed at 150 °C exhibit the highest intensity. The larger grain increases the absorption capacity of the 150 °C annealed film. This is due to the extended path length. The optical performance is improved at this temperature because it promotes the production of a well-structured film that can capture more light. If this temperature is exceeded, there may be less light absorption because of the inferior surface shape or crystalline. The absorption coefficients in the visible range for all the samples were greater than 10^4 cm^{-1} . The band gap calculations of the CABI films were shown by plotting $(\alpha h\nu)^{1/n}$ in relation to the energy of the photon: $(\alpha h\nu)^{1/n} = A(h\nu - E_g)$; Where, α is the absorption coefficient, $h\nu$ is the energy of the photon, A is constant, and E_g is the band gap energy. In this case, the exponent n is dependent upon the kind of transition $n=1/2$ and 2 for indirect and direct transitions, respectively. The energy spectrum of photons shows a straight line, indicating that the optical changes take place directly across the band gap of the material. **Figure 2.11** shows details about the direct band gap for these absorbing layers. The band gap values vary between 1.70 to 1.71. The band gap values are almost the same at all temperatures. This is due to the fact that the annealing temperature has no significant influence on the electronics properties of CABI films.

2.3.4 Photovoltaic properties

The study of the photovoltaic properties of solar cells can be a valuable tool for understanding and optimizing efficiency as well as their structure. Researchers can analyze the efficiency of solar cells under various conditions and develop strategies to boost their efficiency.³⁶⁻³⁸

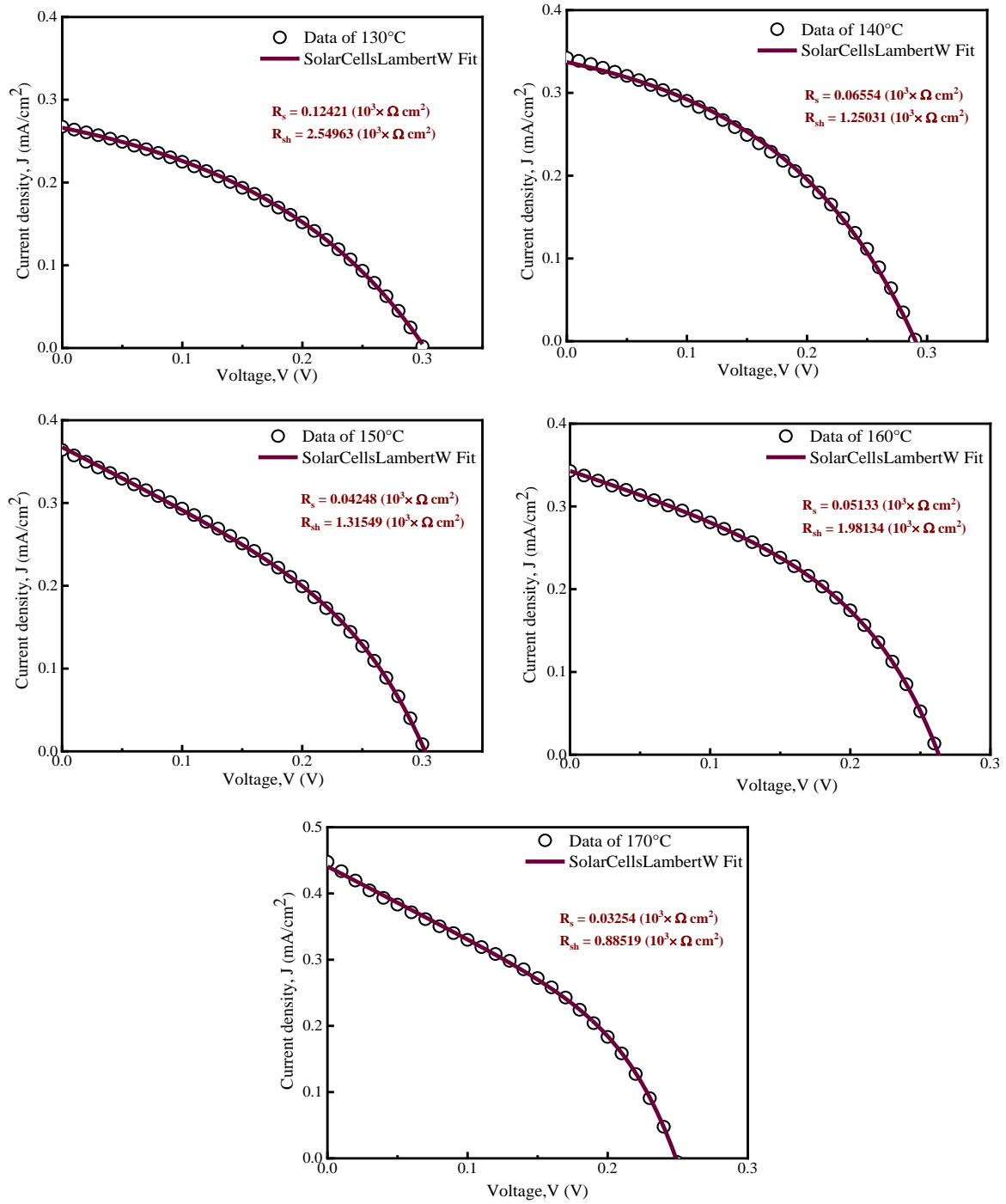


Figure 2.12 Current density-voltage curves of the CABI solar cells and J - V curve fitting by using Lambert W function at various annealing temperatures.

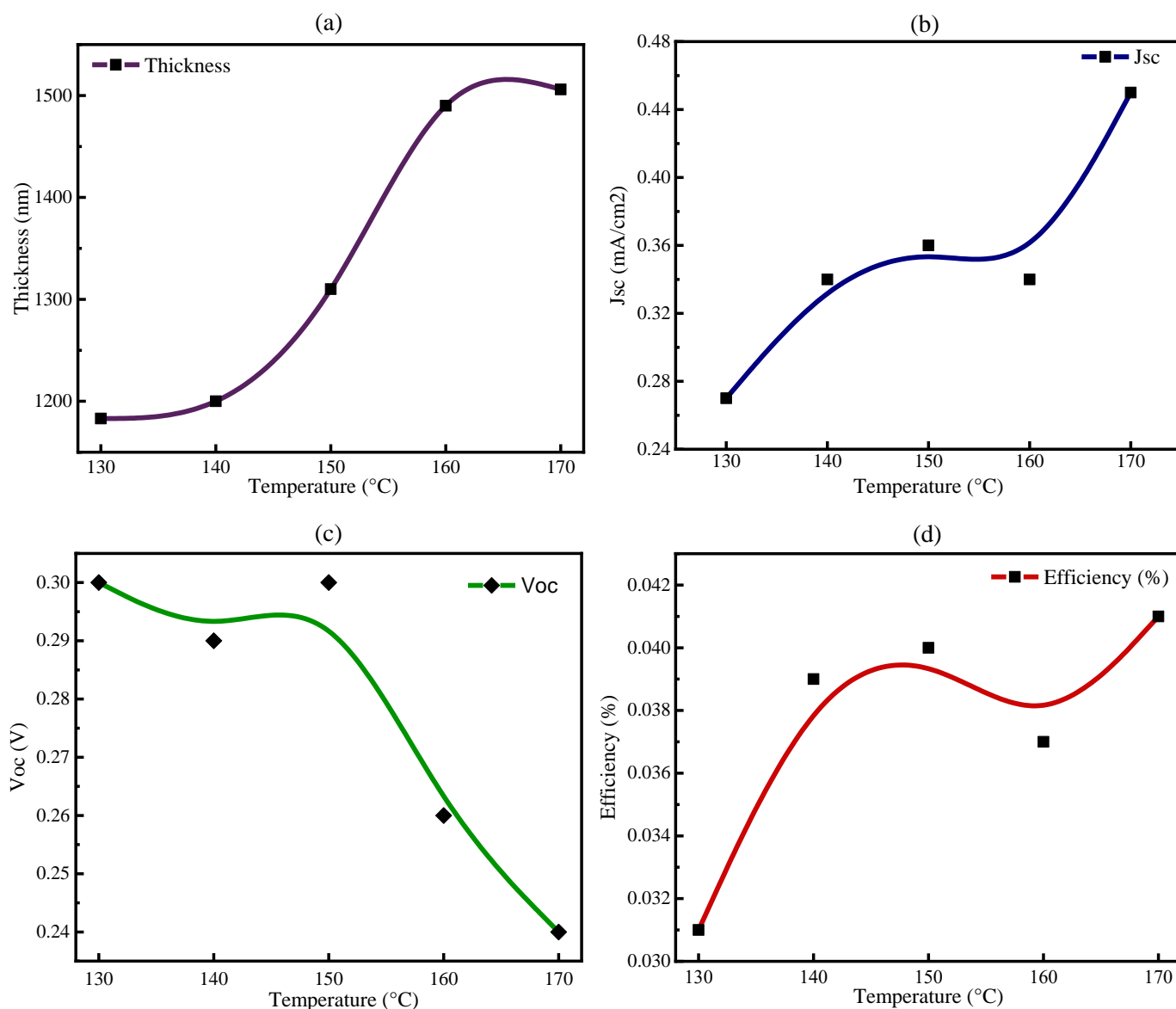


Figure 2.13 Variation of (a) film thickness, (b) Short circuit current density, (c) Open circuit voltage and (d) Efficiency with different annealing temperature of Cu₆AgBiI₁₀ solar cells.

Figure 2.12 illustrates the current voltage characteristics (J-V) of these CABI solar cells with different annealing temperatures under illumination. The J-V curves fitted by using Lambert W function are also indicated, showing the J-V curves are well fitted. The series resistance R_s and parallel resistance R_{sh} are also shown in **Figure 2.12**. The thickness, the short circuit current

density J_{sc} , the open circuit voltage V_{oc} and the power conversion efficiency (PCE) fit different annealing temperatures are plotted in **Figure 2.13 (a), (b), (c) and (d)**, respectively. In the higher annealing temperature, the CABI films with increased thickness were deposited on an ITO/SnO₂ layer. The cell absorbs more light as the thickness of the active layer increases. This leads to an increase in J_{sc} as shown in **Figure 2.13 (b)**. The decrease of series resistance observed in **Figure 2.13** also contributes to the increase of J_{sc} at high annealing temperature. At 160 °C, it appears that there is an inconsistent relationship between the J_{sc} and the thickness results, as well as the absorption findings, which was attributed to the increase in the series resistance of the film. The decrease of V_{oc} at high annealing temperature is due to the decrease of parallel resistance as shown in **Figure 2.13**. The open circuit voltage is expressed as $V_{oc} = \frac{nkT}{q} \ln \left(\frac{J_{sc}}{J_0} + 1 \right)$, where n is an ideality factor which represents the rate at which recombination of charge carriers occurs, the k value is a Boltzmann constant, and T is the temperature. J_{sc} represents the density of photocurrent and J_0 is the saturation current.³⁹ Therefore, if the parallel resistance decreases due to the island-type surface morphology at 170 °C as shown in **Figure 2.6**, V_{oc} decreases as shown in **Figure 2.13 (c)**. As the surface morphology changes to an island type, roughness increases. This can lead to an increase in effective cell surface. It can cause an increase in recombination rates of photo carriers on the surface. As a result of the increased J_0 , V_{oc} decreases as the voltage across the cell drops due to the recombination loss.^{40,41} But the decrease of V_{oc} with increasing annealing temperature is small; the power conversion efficiency gradually increases with annealing temperature.

2.4 Conclusions

One step spin coating with hot casting assistance is followed by the preparation of CABI film and optimization of the annealing temperature. The temperature of annealing has an influence on the

film's crystal structural as well as morphological and photovoltaic characteristics. We observed that from XRD analysis that Cu rich films belong the trigonal phase with no impurity peak. We now have a clear view of homogeneity and crystallite from the EDS and morphological studies. The analysis of optical characteristics showed that CABI films with direct band gaps exhibited high absorbance and low reflection. The thickness of CABI films varied between 1183 and 1506 nm. The highest power conversion efficiency in prepared photovoltaic solar cell is 0.041% at ambient conditions. This study will benefit the researchers to further improve the efficiency for CABI solar cells.

2.5 References

- (1) Buizza, L. R. V; Sansom, H. C.; Wright, A. D.; Ulatowski, A. M.; Johnston, M. B.; Snaith, H. J.; Herz, L. M.; Buizza, L. R. V; Sansom, H. C.; Wright, A. D.; Ulatowski, A. M.; Johnston, M. B.; Snaith, H. J.; Herz, L. M. Interplay of Structure, Charge-Carrier Localization and Dynamics in Copper-Silver-Bismuth-Halide Semiconductors. *Adv. Funct. Mater.* **2022**, 32 (6), 2108392.
- (2) Turkevych, I.; Kazaoui, S.; Ito, E.; Urano, T.; Yamada, K.; Tomiyasu, H.; Yamagishi, H.; Kondo, M.; Aramaki, S. Photovoltaic Rudorffites: Lead-Free Silver Bismuth Halides Alternative to Hybrid Lead Halide Perovskites. *Chem. Sus. Chem.* **2017**, 10 (19), 3754–3759.
- (3) Kim, Y.; Yang, Z.; Jain, A.; Voznyy, O.; Kim, G. H.; Liu, M.; Quan, L. N.; García de Arquer, F. P.; Comin, R.; Fan, J. Z.; Sargent, E. H. Pure Cubic-Phase Hybrid Iodobismuthates AgBi_2I_7 for Thin-Film Photovoltaics. *Angew. Chem. Int. Ed.* **2016**, 55 (33), 9586–9590.

- (4) Sansom, H. C.; Longo, G.; Wright, A. D.; Buizza, L. R. V.; Mahesh, S.; Wenger, B.; Zanella, M.; Abdi-Jalebi, M.; Pitcher, M. J.; Dyer, M. S.; Manning, T. D.; Friend, R. H.; Herz, L. M.; Snaith, H. J.; Claridge, J. B.; Rosseinsky, M. J. Highly Absorbing Lead-Free Semiconductor $\text{Cu}_2\text{AgBiI}_6$ for Photovoltaic Applications from the Quaternary CuI-AgI-BiI_3 Phase Space. *J. Am. Chem. Soc.* **2021**, *143* (10), 3983–3992.
- (5) Sansom, H. C.; Whitehead, G. F. S.; Dyer, M. S.; Zanella, M.; Manning, T. D.; Pitcher, M. J.; Whittles, T. J.; Dhanak, V. R.; Alaria, J.; Claridge, J. B.; Rosseinsky, M. J. AgBiI_4 as a Lead-Free Solar Absorber with Potential Application in Photovoltaics. *Chem. Mat.* **2017**, *29* (4), 1538–1549.
- (6) Sansom, H. C.; Buizza, L. R. V.; Zanella, M.; Gibbon, J. T.; Pitcher, M. J.; Dyer, M. S.; Manning, T. D.; Dhanak, V. R.; Herz, L. M.; Snaith, H. J.; Claridge, J. B.; Rosseinsky, M. J. Chemical Control of the Dimensionality of the Octahedral Network of Solar Absorbers from the CuI-AgI-BiI_3 Phase Space by Synthesis of 3D CuAgBiI_5 . *Inorg. Chem.* **2021**, *60* (23), 18154–18167.
- (7) Savory, C. N.; Walsh, A.; Scanlon, D. O. Can Pb-Free Halide Double Perovskites Support High-Efficiency Solar Cells? *ACS Energy Lett.* **2016**, *1* (5), 949–955.
- (8) Wright, A. D.; Buizza, L. R. V.; Savill, K. J.; Longo, G.; Snaith, H. J.; Johnston, M. B.; Herz, L. M. Ultrafast Excited-State Localization in $\text{Cs}_2\text{AgBiBr}_6$ Double Perovskite. *J. Phys. Chem. Lett.* **2021**, *12* (13), 3352–3360.
- (9) Schade, L.; Wright, A. D.; Johnson, R. D.; Dollmann, M.; Wenger, B.; Nayak, P. K.; Prabhakaran, D.; Herz, L. M.; Nicholas, R.; Snaith, H. J.; Radaelli, P. G. Structural and

- Optical Properties of Cs₂AgBiBr₆ Double Perovskite. *ACS Energy Lett.* **2019**, 4 (1), 299–305.
- (10) Pai, N.; Lu, J.; Gengenbach, T. R.; Seeber, A.; Chesman, A. S. R.; Jiang, L.; Senevirathna, D. C.; Andrews, P. C.; Bach, U.; Cheng, Y. B.; Simonov, A. N. Silver Bismuth Sulfoiodide Solar Cells: Tuning Optoelectronic Properties by Sulfide Modification for Enhanced Photovoltaic Performance. *Adv. Energy Mater.* **2019**, 9 (5), 1803396.
 - (11) Pai, N.; Chatti, M.; Fürer, S. O.; Scully, A. D.; Raga, S. R.; Rai, N.; Tan, B.; Chesman, A. S. R.; Xu, Z.; Rietwyk, K. J.; Reddy, S. S.; Hora, Y.; Sepalage, G. A.; Glück, N.; Lira-Cantú, M.; Bach, U.; Simonov, A. N. Solution Processable Direct Bandgap Copper-Silver-Bismuth Iodide Photovoltaics: Compositional Control of Dimensionality and Optoelectronic Properties. *Adv. Energy Mater.* **2022**, 12 (32), 2201482.
 - (12) Song, K.; Zou, X.; Zhang, H.; Zhang, C.; Cheng, J.; Liu, B.; Yao, Y.; Wang, X.; Li, X.; Wang, Y.; Ren, B. Effect of SnO₂ Colloidal Dispersion Solution Concentration on the Quality of Perovskite Layer of Solar Cells. *Coatings* **2021**, 11 (5), 1–10.
 - (13) Cullity, B. D.; Stock, S. R. Elements of X-Ray Diffraction, Third Edition. Prentice-Hall 2001.
 - (14) Islam, M. A.; Hasan, M.; Hossain, A. K. M. A. Enhancement of Initial Permeability and Reduction of Loss Factor in Zn Substituted Nanocrystalline Li_{0.35-0.5x}Ni_{0.3}Zn_xFe_{2.35-0.5x}O₄. *J. Magn. Magn. Mater.* **2017**, 424, 108–114.
 - (15) Matiur, R. M.; Abuelwafa, A. A.; Putri, A. A.; Kato, S.; Kishi, N.; Soga, T. Annealing Effects on Structural and Photovoltaic Properties of the Dip-SILAR-Prepared Bismuth

- Oxyhalides (BiOI, Bi₇O₉I₃, Bi₅O₇I) Films. *SN Appl. Sci.* **2021**, 3 (2), 1–11.
- (16) Achoi, M. F.; Aiba, S.; Kato, S.; Kishi, N.; Soga, T. Influence of Post-Annealing on the Properties of Methylammonium Bismuth Iodide Perovskite Solar Cells Through the Hot Immersion Method. *J. Electron. Mater.* **2023**, 52 (1), 351–367.
 - (17) Pawar, P. S.; Nandi, R.; Neerugatti, K. R. E.; Cho, J. Y.; Heo, J. Hydrothermal Growth of Sb₂S₃ Thin Films on Molybdenum for Solar Cell Applications: Effect of Post-Deposition Annealing. *J. Alloys Compd.* **2022**, 898, 162891.
 - (18) Hernández-Saz, J.; Herrera, M.; Pizarro, J.; Gonzalez, M.; Abell, J.; Walters, R.; Galindo, P. L.; Duguay, S.; Molina, S. I. Effect of the Thermal Annealing and the Nominal Composition in the Elemental Distribution of In_xAl_{1-x}As_ySb_{1-y} for Triple Junction Solar Cells. *J. Alloys Compd.* **2019**, 792, 1021–1027.
 - (19) Lokhande, A. C.; Chalapathy, R. B. V.; Jang, J. S.; Babar, P. T.; Gang, M. G.; Lokhande, C. D.; Kim, J. H. Fabrication of Pulsed Laser Deposited Ge Doped CZTSSe Thin Film Based Solar Cells: Influence of Selenization Treatment. *Sol. Energy Mater. Sol. Cells* **2017**, 161, 355–367.
 - (20) Masawa, S. M.; Li, J.; Zhao, C.; Liu, X.; Yao, J. 0D/2D Mixed Dimensional Lead-Free Caesium Bismuth Iodide Perovskite for Solar Cell Application. *Materials* **2022**, 15 (6), 2180.
 - (21) Williamson, B. W.; Eickemeyer, F. T.; Hillhouse, H. W. Solution-Processed BiI₃ Films with 1.1 eV Quasi-Fermi Level Splitting: The Role of Water, Temperature, and Solvent during Processing. *ACS Omega* **2018**, 3 (10), 12713–12721.

- (22) Wu, S.; Chen, R.; Zhang, S.; Babu, B. H.; Yue, Y.; Zhu, H.; Yang, Z.; Chen, C.; Chen, W.; Huang, Y.; Fang, S.; Liu, T.; Han, L.; Chen, W. A Chemically Inert Bismuth Interlayer Enhances Long-Term Stability of Inverted Perovskite Solar Cells. *Nat. Commun.* **2019**, *10* (1), 1–11.
- (23) Chakraborty, A.; Pai, N.; Zhao, J.; Tuttle, B. R.; Simonov, A. N.; Pecunia, V.; Chakraborty, A.; Zhao, J.; Pai, N.; Tuttle, B. R.; Simonov, A. N.; Pecunia, V. Rudorffites and Beyond: Perovskite-Inspired Silver/Copper Pnictohalides for Next-Generation Environmentally Friendly Photovoltaics and Optoelectronics. *Adv. Funct. Mater.* **2022**, 2203300.
- (24) Shadabroo, M. S.; Abdizadeh, H.; Golobostanfard, M. R. Dimethyl Sulfoxide Vapor-Assisted $\text{Cs}_2\text{AgBiBr}_6$ Homogenous Film Deposition for Solar Cell Application. *ACS Appl. Energy Mater.* **2021**, *4* (7), 6797–6805.
- (25) Halin, D. S. C.; Talib, I. A.; Daud, A. R.; Hamid, M. A. A. Effect of Annealing Atmosphere on the Morphology of Copper Oxide Thin Films Deposited on TiO_2 Substrates Prepared by Sol-Gel Process. *Key Eng. Mater.* **2014**, 594–595, 113–117.
- (26) Yang, K. J.; Sim, J. H.; Son, D. H.; Kim, D. H.; Kim, G. Y.; Jo, W.; Song, S.; Kim, J. H.; Nam, D.; Cheong, H.; Kang, J. K. Effects of the Compositional Ratio Distribution with Sulfurization Temperatures in the Absorber Layer on the Defect and Surface Electrical Characteristics of $\text{Cu}_2\text{ZnSnS}_4$ Solar Cells. *Prog. Phot. Res. Appl.* **2015**, *23* (12), 1771–1784.
- (27) Lu, X.; Xu, B.; Ma, C.; Chen, Y.; Yang, P.; Chu, J.; Sun, L. Improving the Efficiency of $\text{Cu}_2\text{ZnSnS}_4$ Solar Cells by Promoting the Homogeneous Distribution of Sn Element. *Appl. Surf. Sci.* **2020**, 529, 147160.

- (28) Abuelwafa, A. A.; Matiur, R. M.; Putri, A. A.; Soga, T. Synthesis, Structure, and Optical Properties of the Nanocrystalline Bismuth Oxyiodide (BiOI) for Optoelectronic Application. *Opt. Mater.* **2020**, *109*, 110413.
- (29) Matiur, R. M.; Noman, M. A. A.; Kato, S.; Soga, T. A Novel Modest Synthesis of Device Applicable Flakes Based Stable BiOI Film by the Oxidation of BiI₃ Film. *J. Alloys Compd.* **2021**, *873*, 159715.
- (30) Matiur, R. M.; Kato, S.; Soga, T. All-Solution-Processed Environment-Friendly Solid-State BiOI Photovoltaic Cell with High-Short-Circuit Current by Successive Ionic Layer Adsorption and Reaction (SILAR). *J. Mater. Sci.: Mater. Electron.* **2021**, *32* (13), 18342–18350.
- (31) Chamola, P.; Mittal, P. PPV–PCBM Bulk Heterojunction Organic Solar Cell to Power Modern Pacemakers. *J. Mater. Res.* **2023**, 1–13.
- (32) Aftab, S.; Iqbal, M. Z.; Haider, Z.; Iqbal, M. W.; Nazir, G.; Shehzad, M. A. Bulk Photovoltaic Effect in 2D Materials for Solar-Power Harvesting. *Adv. Opt. Mater.* **2022**, *10* (23), 2201288.
- (33) Scheul, T. E.; Khorani, E.; Rahman, T.; Charlton, M. D. B.; Boden, S. A. Light Scattering from Black Silicon Surfaces and Its Benefits for Encapsulated Solar Cells. *Sol. Energy Mater. Sol. Cells* **2022**, *235*, 111448.
- (34) Islam, M. A.; Islam, J.; Islam, M. N.; Sen, S. K.; Hossain, A. K. M. A. Enhanced Ductility and Optoelectronic Properties of Environment-Friendly CsGeCl₃ under Pressure. *AIP Adv.* **2021**, *11* (4), 45014.

- (35) Islam, M. A.; Rahaman, M. Z.; Sen, S. K. A Comparative Study of Hydrostatic Pressure Treated Environmentally Friendly Perovskites CsXBr_3 ($\text{X} = \text{Ge/Sn}$) for Optoelectronic Applications. *AIP Adv.* **2021**, *11* (7).
- (36) Hosseini, S.; Adelifard, M. The Impact of Cesium and Antimony Alloying on the Photovoltaic Properties of Silver Bismuth Iodide Compounds. *Phys. Status Solidi A* **2021**, *218* (7), 2000774.
- (37) Hosseini, S. S.; Adelifard, M. The Effect of Multi-Walled Carbon Nanotubes and Reduced Graphene Oxide Doping on the Optical and Photovoltaic Performance of Ag_2BiI_5 -Based Solar Cells. *J. Electron. Mater.* **2020**, *49* (10), 5790–5800.
- (38) Ghosh, B.; Wu, B.; Guo, X.; Cholakkal Harikesh, P.; Abraham John, R.; Baikie, T.; S Wee, A. T.; Guet, C.; Chien Sum, T.; Mhaisalkar, S.; Mathews, N.; Superior Performance of Silver Bismuth Iodide Photovoltaics Fabricated via Dynamic Hot-Casting Method under Ambient Conditions. *Adv. Energy Mater.* **2018**, *8* (33), 1802051.
- (39) Zhang, M.; Chen, Q.; Xue, R.; Zhan, Y.; Wang, C.; Lai, J.; Yang, J.; Lin, H.; Yao, J.; Li, Y.; Chen, L.; Li, Y. Reconfiguration of Interfacial Energy Band Structure for High-Performance Inverted Structure Perovskite Solar Cells. *Nat. Commun.* **2019**, *10* (1), 1–9.
- (40) Tress, W.; Yavari, M.; Domanski, K.; Yadav, P.; Niesen, B.; Correa Baena, J. P.; Hagfeldt, A.; Graetzel, M. Interpretation and Evolution of Open-Circuit Voltage, Recombination, Ideality Factor and Sub gap Defect States during Reversible Light-Soaking and Irreversible Degradation of Perovskite Solar Cells. *Energy Environ. Sci.* **2018**, *11* (1), 151–165.
- (41) Han, D.; Kumari, T.; Jung, S.; An, Y.; Yang, C. A Comparative Investigation of

Cyclohexyl-End-Capped Versus Hexyl-End-Capped Small-Molecule Donors on Small Donor/Polymer Acceptor Junction Solar Cells. *Solar RRL* **2018**, 2 (5), 1800009.

Chapter 3

Study of $\text{Cu}_6\text{BiAgI}_{10}$ perovskite with various organic and inorganic hole transport layers for improved photovoltaic performance

3.1 Introduction

Cu-Ag-Bi-I solar cells have made significant advances in recent years, leading to improved performance and increased interest. To enhance the efficiency and stability of solar cells, researchers have developed new compounds and optimized device architectures. An important advancement has been the development of $\text{Cu}_2\text{AgBiI}_6$ and CuAgBiI_5 solar cells. According to Pia et al., $\text{Cu}_2\text{AgBiI}_6$ has a higher PCE of 2.39% compared to CuAgBiI_5 which has an effectiveness of 1.01%.¹ The properties of optoelectronics are also shown to improve dramatically with a growing copper content, which enhances photoluminescence intensity and charge-carrier transport. In addition, the higher Cu^+ content has reduced exciton binding energies, and higher mobilities.² In 2021, Buizza et al. first studied the optical, structural and charge carrier characteristics of $\text{Cu}_6\text{AgBiI}_{10}$ material.² In 2023, Islam et al. first reported the photovoltaic characteristics that are present in $\text{Cu}_6\text{AgBiI}_{10}$ solar cells that have the power conversion rate of 0.045 %.³ An earlier study focused on optimizing $\text{Cu}_6\text{AgBiI}_{10}$ solar cells' annealing temperature. It was found that the best results were obtained when the annealing temperature was 150 °C, with a current density of 0.45 mA/cm^2 maximum.³ However, the effectiveness in $\text{Cu}_6\text{AgBiI}_{10}$ solar cells is extremely low. To address this issue, we have conducted our present research focused on the impact on the organic or inorganic hole transportation layers (HTLs) to improve the performance of PV for $\text{Cu}_6\text{AgBiI}_{10}$

solar cells in this paper. A suitable HTL is vital for solar cells because it plays a significant role in enhancing the effectiveness and stability of the solar cells and good HTLs must have excellent hole mobility, high optical transparency, and a suitable energy level aligned with the absorber layer.^{4,5} The well-matched energy levels for Cu₆AgBiI₁₀ light absorbers are essential to ensure efficient charge transfer. In this research, we studied the surface morphology, structure, and optical properties of the Cu₆AgBiI₁₀ material on FTO/(c+mp)TiO₂ for the first time experimentally. We then studied by SCAPS-1D simulation, the interaction of organic and inorganic materials and how it affects the performance of solar cells. This is the first-time experiments and simulations have been combined to investigate Cu₆AgBiI₁₀ solar cells with different HTLs. In our investigation, Spiro-MeOTAD, P3HT, PEDOT:PSS, CuSCN, CuI, and NiOx material were used as HTLs alongside with (c+mp) TiO₂ of ETLs. A thorough study was conducted using a SCAPS-1D simulation software of solar cell to investigate the n-i-p structural FTO/ETL/CABI/HTLs/Au combinations. In our experiments, we found power conversion efficiencies (PCE) of 1.50% for Spiro-MeOTAD, 1.13% for P3HT, 1.10% for PEDOT:PSS, 1.98% for CuSCN, 1.54% for CuI, and 1.44% for NiOx for each combination before thickness optimization. We identified three key factors affecting device performance, namely the thickness of the absorbing layer, the thickness of the ETL, and the material of the HTLs. We have also achieved record efficiencies of 2.06% for inorganic HTL and 1.67% for organic HTL in optimizing solar cell performance, which provides evidence that CABI has a potential as a lead-free solar cell material. For environmental and human health reasons, our research is significant for providing insight into the design and optimization of lead-free solar cells based on CABI. It is important to note, however, that the SCAPS-1D simulator may not accurately reproduce certain phenomena observed in experiments due to inherent limitations. In our case, there may be discrepancies between simulation and experimental data due

to the complexities of material properties, interface effects, and environmental factors. The PCEs of CABI solar cells may still be relatively low compared to other solar cell materials. In addition to its higher surface defect levels, CABI may also have a higher band gap to contribute to its lower efficiency. To improve the performance of CABI solar cells, further research and optimization are needed.

3.2 Experimental and numerical simulation section

3.2.1 Chemicals

Fluorine-doped tin oxide (FTO) coated glass slides (surface resistivity $\sim 10\Omega/\text{sq}$) were purchased from Merck. Titanium (IV) oxide (99.7%) (P-25 powder), TTIP (99.99%) (titanium (IV) Isopropoxide), Triton X-100 (laboratory grade), Bismuth (III) iodide (99%) (BiI_3) and Silver iodide (99%) (AgI) were purchased from Sigma-Aldrich. Copper (I) iodide (99%) (CuI), HCl , Acetone (99.8%), 1-butanol (99%) and Ethanol (99.5%) were purchased from Kanto Chemical, and Dimethylsulfoxide (98%) (DMSO) was purchased from Nacalai tesque. This experiment was conducted using extremely purified gas N_2 . Gas, and purified distilled water.

3.2.2 $\text{Cu}_6\text{AgBiI}_{10}$ film fabrication on the electron transport layer (ETL)

To conduct this study, we utilized FTO substrates ($2\text{ cm} \times 2\text{ cm}$) that were washed with the solution of water (distilled), acetone and ethanol in an ultrasonic bath for about 20 minutes and dried with N_2 following which cleaned FTO were treated with an Ozone-killing UV light. On top of the clean FTO substrate, the compact TiO_2 layer was created by spin coating a precursor solution made by mixing 0.06 mL of titanium diisopropoxide bis (acetylacetonate) with 1.1 mL 1-Butanol, and then annealing at 450°C for 1h. The mesoporous TiO_2 layer was created through spin coating. The precursor solution was prepared by mixing 0.10 gm of P-25 powder diluted into 2.5 mL of 2-

propanol and one drop of HCl with a drop of Triton X-100. After this, the layer was annealed at 450 °C for 1h. To fabricate $\text{Cu}_6\text{AgBiI}_{10}$ film, at the first step, we prepared the solution with 50 wt.%, the 6:1:1 molar ratio of AgI, BiI_3 , and CuI was dissolving into DMSO in accordance with the correct ratio of stoichiometry, as illustrated in **Figure 3.1**. The mixture that is shown in **Figure 3.1** was stirred at 150 °C for 30 min and was kept at an 80 °C temperature for 24 hours under conditions of stirring inside the glovebox. The hot solution was then filtered with the PTFE membrane filter that has the pore size of 0.2 μm . This same solution was then stirred with temperatures of 100 °C for one hour. In the following step, the prepared CABI solution was spin coated at 3000 rpm for 30 seconds on FTO/(c+mp) TiO_2 substrate. The absorber layer was then annealed by two steps inside the glovebox. The initial step was 75 °C for three minutes, then at the second stage, 150 °C for 6 minutes on the hot plate to anneal. Then, the final film of the active layer was achieved.

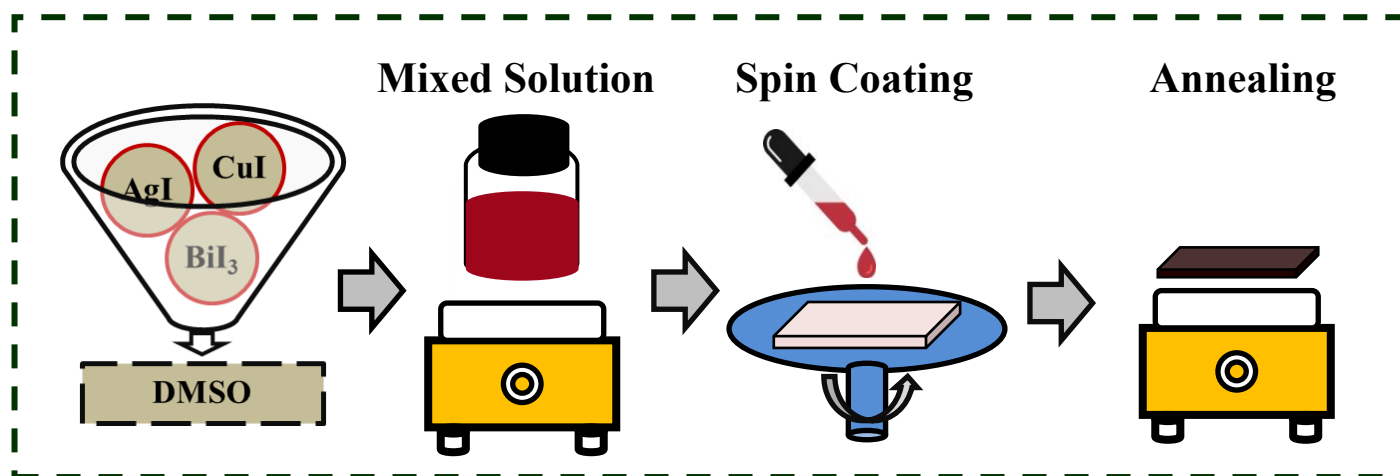


Figure 3.1 Schematic flowchart of steps in the $\text{Cu}_6\text{AgBiI}_{10}$ film on FTO/(c+mp) TiO_2 sample.

3.2.3 Simulation methodology using SCAPS-1D

A Solar Cell Capacitance Simulator in One Dimension (SCAPS-1D) simulation technique is important for understanding high-efficiency solar cells' fundamental characteristics and device properties. It is utilized to study and optimize the efficiency of solar cells in different circumstances and was developed through the research work of Professor. M. Burgelman.⁶⁻⁸ Equations of continuity as well as Poisson's equation are utilized within SCAPS 1D because they are fundamental in the field of semiconductor device Physics. Poisson's equation connects an electric voltage to density of charge in a semiconductor device. In contrast, the continuity equations explain the movement of charged carriers (electrons as well as holes) through the device.⁹⁻¹² Poisson's equation and continuity equations could be written in the following manner:

$$\nabla^2\psi = \frac{q}{\epsilon} (n - p + N_A - N_D) \quad (1)$$

where N_A and N_D represent concentrations of the acceptor and doner, and the electrostatic potential is ψ .

And

$$\nabla \cdot J_n - q \frac{\delta n}{\delta t} = + qR \quad (2)$$

$$\nabla \cdot J_p + q \frac{\delta p}{\delta t} = - qR \quad (3)$$

where J_n and J_p represent the electron and hole current density, and R is the rate of recombination in carriers.

The diffusion and drift current relationships utilized to determine total current densities as a result of the influence of an electric concentration gradient and field are shown below:

$$J_n = qn\mu_n E + qD_n \nabla_n \quad (4)$$

$$J_p = qp\mu_p E - qD_p \nabla_p \quad (5)$$

In this case, D_n and D_p represent the electron and hole diffusion coefficients.

3.2.4 $\text{Cu}_6\text{AgBiI}_{10}$ photovoltaic device structure

For the first time ever, a simulation study for this solar cell was carried out in this study, which has an n-i-p planar structure, which includes the FTO, ETL as (c+mp) TiO_2 , $\text{Cu}_6\text{AgBiI}_{10}$ as an absorber, both organic and inorganic HTLs, in addition to Gold (Au) as a back contact, as illustrated in **Figure 3.2**. Using mesoporous and compact TiO_2 layers in solar cells can increase the efficiency of conversion within the solar cell because of the suitable band gap, better energy level, and environmental stability. TiO_2 is among the most extensively used ETL for perovskite.¹³

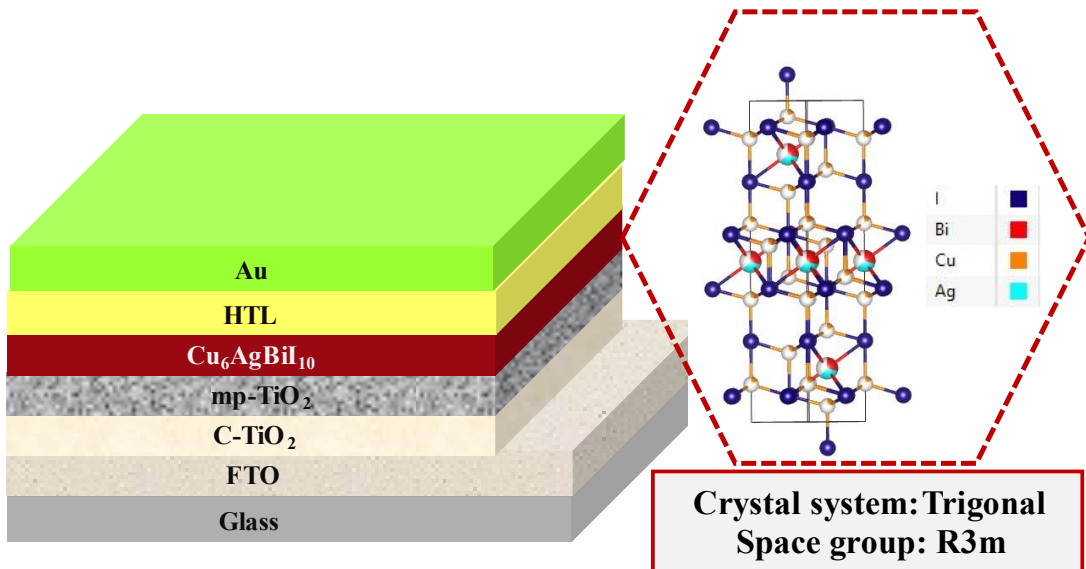


Figure 3.2 Conventional type device architecture and crystal structure of the $\text{Cu}_6\text{AgBiI}_{10}$ solar cell.

Table 3.1 lists the simulation parameters for those layers: FTO, ETL, absorber, as well as several HTL layers. Additionally, all interface defect layer input parameters are neutral for FTO/ETL, ETL/CABI, and CABI/HTL; the capture cross-sections are $1.0 \times 10^{17} \text{ cm}^2$ (electron) and $1.0 \times 10^{18} \text{ cm}^2$ (hole); the energetic distribution has a single value; the defect energy level has an energy level above the VB maximum; and the total density is $1.0 \times 10^{10} \text{ cm}^{-2}$. The simulation is conducted under the conditions of an AM1.5G simulated solar light exposure, with a power density of 100 mW/cm^2 when operating at ambient temperature. In the initial simulation, and subsequent optimization, an absorption model using the square root $(h\nu - E_g)$ law was employed.

Table 3.1 Input parameters of the FTO, ETL, Absorber layer and HTLs.

Parameters	FTO	(c+mp) TiO ₂	CABI	Spiro- OMeTAD	P3HT	PEDOT:PS S	CuSCN	CuI	NiOx
Thickness (nm)	525 ^E	350 ^E	650 ^E	200	50	33	50	100	50
Band Gap (eV)	3.48 ^E	3.25 ^E	1.72 ^E	3	1.70	2.2	3.4	3.1	3.6
Electron affinity (eV)	4	4	3.90	2.2	3.5	2.9	1.9	2.1	2.1
Permittivity	9	9	6.5	3	3	3	10	6.5	11.75
Mobility of electron (cm ² .V ⁻¹ .s ⁻¹)	20	20	1	2.1×10 ⁻³	1.8×10 ⁻³	10	100	100	1×10 ⁻³
Mobility of hole (cm ² .V ⁻¹ .s ⁻¹)	10	10	1	2.16×10 ⁻³	1.86×10 ⁻²	10	25	43.9	1×10 ⁻³
Shallow uniform donor density, N _D (cm ⁻³)	1×10 ¹⁵	9×10 ¹⁶	0	0	0	0	0	0	0
Shallow uniform acceptor density, N _A (cm ⁻³)	0	0	1×10 ¹⁵	1×10 ¹⁸	1×10 ¹⁸	3.17×10 ¹⁴	1×10 ¹⁸	1×10 ¹⁸	1×10 ¹⁹
Density of defect (cm ⁻³)	1×10 ¹⁸	1×10 ¹⁵	1.4×10 ^{17E}	1×10 ¹⁵	1×10 ¹⁵	1×10 ¹⁴	1×10 ¹⁵	1×10 ¹⁵	1×10 ⁸
DOS at CB (cm ⁻³)	2.2×10 ¹⁸	2×10 ¹⁸	1×10 ¹⁹	2.2×10 ¹⁸	2×10 ²¹	2.2×10 ¹⁵	2.2×10 ¹⁹	2.8×10 ¹⁹	2.5×10 ²⁰
DOS at VB (cm ⁻³)	2.2×10 ¹⁸	1.8×10 ¹⁹	1×10 ¹⁹	1.8×10 ¹⁹	2×10 ²¹	1.8×10 ¹⁸	1.8×10 ¹⁸	1×10 ¹⁹	2.5×10 ²⁰
Electron thermal velocity (cm.s ⁻¹)	1×10 ^{7C}	1×10 ^{7C}	1×10 ^{7C}	1×10 ^{7C}	1×10 ^{7C}	1×10 ^{7C}	1×10 ^{7C}	1×10 ^{7C}	1×10 ^{7C}
Hole thermal velocity (cm.s ⁻¹)	1×10 ^{7C}	1×10 ^{7C}	1×10 ^{7C}	1×10 ^{7C}	1×10 ^{7C}	1×10 ^{7C}	1×10 ^{7C}	1×10 ^{7C}	1×10 ^{7C}
References	14	15	2,316	15	15	17	18	15	19

^E Experimental measured, ^C Constant Value, Series resistance 100 Ω. cm^{2 3} and Shunt resistance 1000 Ω. cm^{2 3}.

3.2.5 Characterization

The crystallographic characteristics observed in $\text{Cu}_6\text{AgBiI}_{10}$ film were measured using the X-ray Diffraction (XRD) in NITech Rigaku SmartLab on the following settings: scanning step 0.02 using the target source $\text{Cu-K}\alpha$. The top surface morphology of the $\text{Cu}_6\text{AgBiI}_{10}$ film was determined by JSM 6510 Model Scanning Electron Microscope (SEM) operating at a voltage of 10 kV. The profiles of UV-Vis were determined on freshly made $\text{CABI}/(\text{c+mp})\text{TiO}_2/\text{FTO}$ films in both reflectance and transmission modes by using the JASCO V-570 model of the spectrophotometer. The film thicknesses were recorded in a highly precarious manner using the Veeco Dektak machine. The performance of photovoltaics was measured by using the SCAPS-1D solar simulation software with the conditions of AM 1.5 as well as 100 mW.cm^{-2} .

3.3 Results and discussion

3.3.1 Experimental analysis

3.3.1.1 Structural analysis

The XRD analysis is crucial for the development of new solar cell materials in order to determine their structural properties such as the size of the crystal and shape, as well as orientation and imperfections, which could impact the efficiency of solar cells.²⁰⁻²²

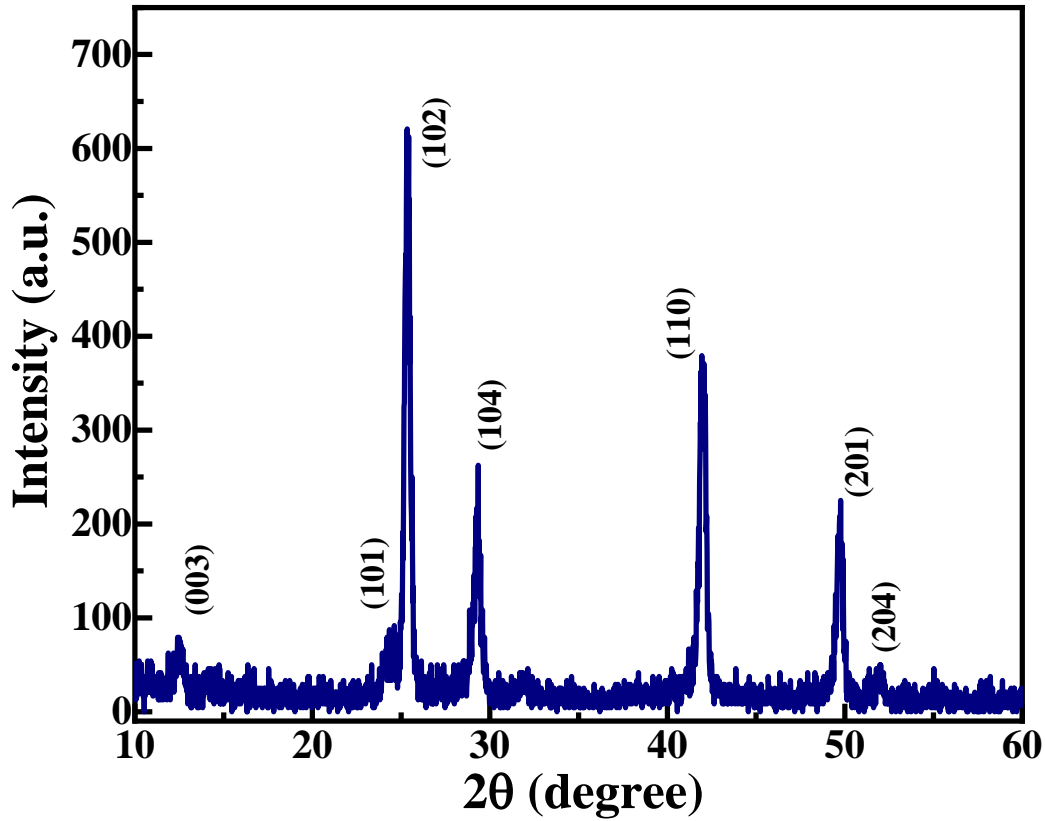


Figure 3.3 The FTO/(c+mp)TiO₂/Cu₆AgBiI₁₀ film's experimental XRD profile at 150°C temperature.

The crystal structure of PV film that was obtained from a 50 wt.% concentration solution of Cu₆AgBiI₁₀ deposited on top of the FTO/(c+mp)TiO₂ layer was studied using XRD; the results can be seen in **Figure 3.3**. The XRD profile in the 10° to 60° ranges of the Cu₆AgBiI₁₀ film is in nominally good agreement with earlier experiment with respect to both position and intensity, reflecting on (003) ($2\Theta = 12.44^\circ$), (101) ($2\Theta = 24.31^\circ$), (102) ($2\Theta = 25.29^\circ$), (104) ($2\Theta = 29.31^\circ$), (110) ($2\Theta = 42.07^\circ$), (201) ($2\Theta = 49.72^\circ$), (204) ($2\Theta = 51.78^\circ$) planes of respective trigonal phases where the impurity peak did not appear. The XRD patterns of the Cu-rich Cu₆AgBiI₁₀ film showed reflections from highly crystalline phase that has R-3m symmetry. Also, the XRD confirmed the

arrangement of atoms in the trigonal asymmetrical crystals.³ The size of the crystallite in the film at 150 °C temperature is calculated using the Debye Scheer formula²³⁻²⁵:

$$D = \frac{0.9\lambda}{\beta \cos \theta} \quad (6)$$

In this case, the λ stands for the X-ray wavelength and θ is the angle of the incident beam. At the same time, β is the full width at half maximum (FWHM). The estimated crystallite size is 19.33 nm.

3.3.1.2 Surface morphology analysis

Analysis of surface morphology is vital for solar cells since it affects the performance in the efficiency of solar cells, as well as the capacity to transform sunlight into electric energy. Improving the morphology and surface appearance of solar cells can improve their performance, including the absorption of light and trapping. It is obvious that quality of coverage on the surface, grain size, and pinholes are the main aspects that influence the performance of solar cells. The temperature of annealing and the precursor solubility are the two most significant elements in determining the nucleation as well as growth processes.²⁶⁻²⁸

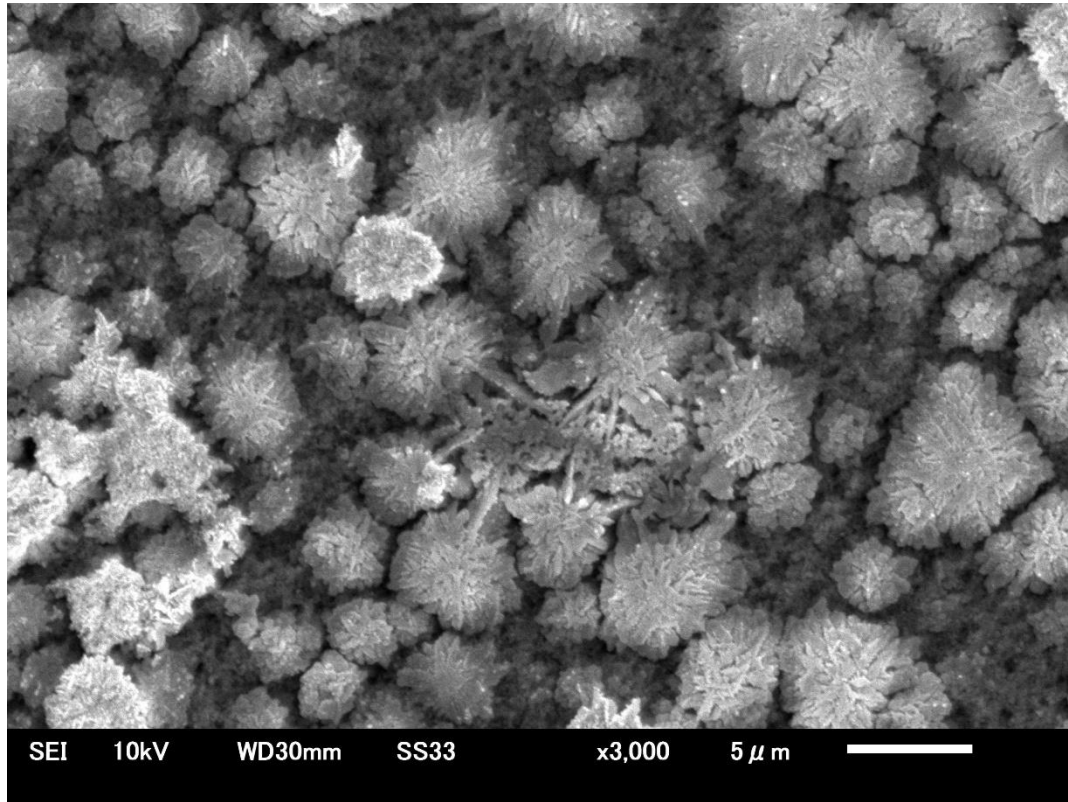


Figure 3.4 SEM image at 150 °C annealing temperature of $\text{Cu}_6\text{AgBiI}_{10}$ film on the FTO/(c+mp)TiO₂ structure.

The morphology of the surface of $\text{Cu}_6\text{AgBiI}_{10}$ film as shown in **Figure 3.4** suggests that to be used for photovoltaic applications, the annealing temperature has been set at 150 °C. Scanning electron microscopy (SEM) analysis showed that the coating with an optimized condition gave island-type grain. The average size of the grain is 3.93 μm.

3.3.1.3 Optical properties analysis

The study of optical properties of solar cells is vital because it can provide crucial information on the ways solar cells absorb, reflect, and transmit light. The results are utilized to maximize the

performance and design of solar cells, eventually improving cost-effectiveness and efficiency. The absorption coefficient, for instance, is an essential optical measurement that indicates the capability of a material to absorb sunlight. Different materials show different levels of effectiveness when it comes to absorbing and turning sunlight into electricity, which is mainly determined by the optical properties of their materials.^{29,30}

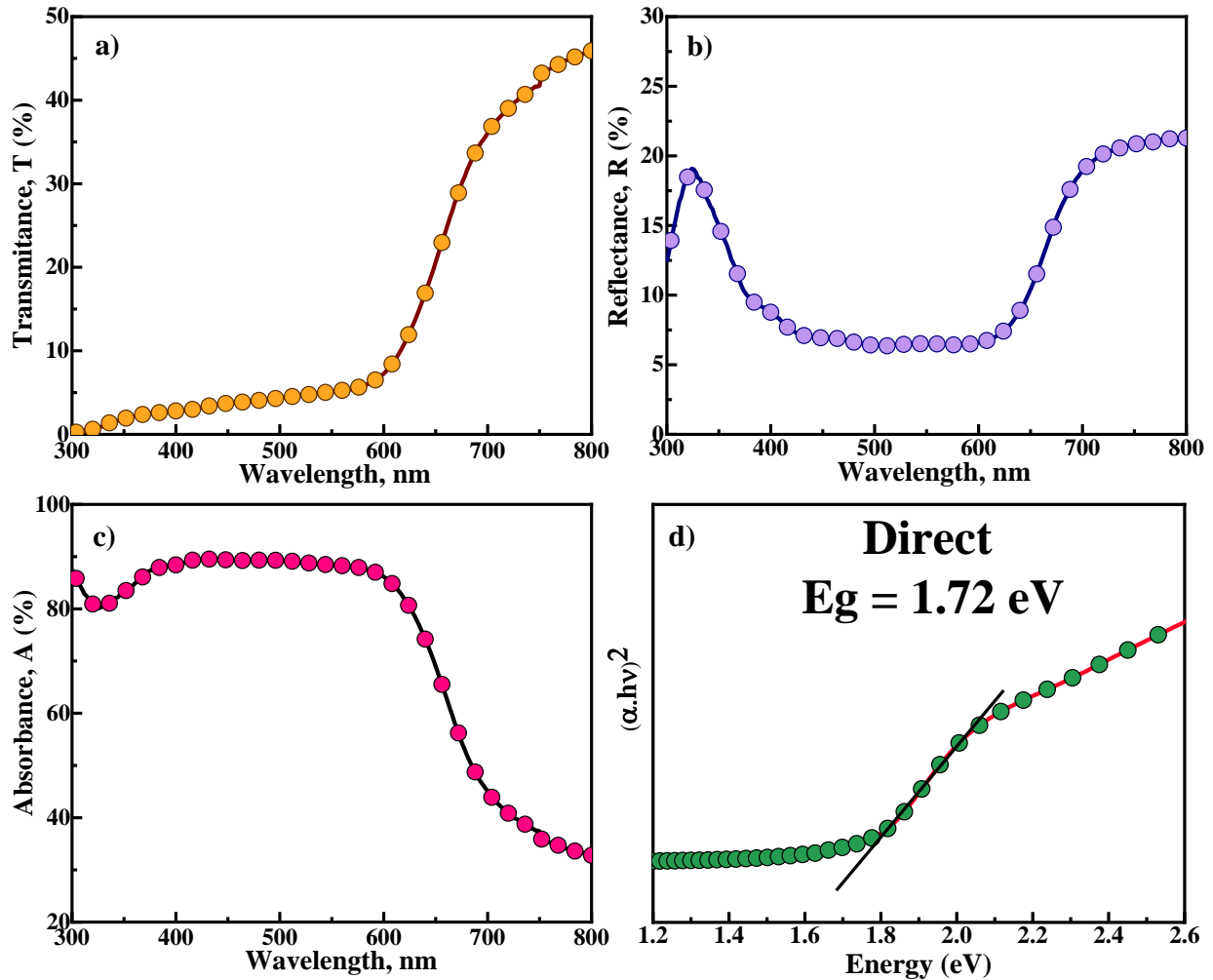


Figure 3.5 Optical property of $\text{Cu}_6\text{AgBiI}_{10}$ film on coated FTO/(c+mp) TiO_2 layer with annealing temperatures of 150°C : (a) Transmittance spectra, (b) Reflectance spectra, (c) Absorbance spectra, and (d) Tauc plot used for the calculation of energy band gap.

Transmittance spectra play a crucial part in perovskite solar cells as they decide how much light is able to pass through the cells and reflectance is a measure of the amount of light that is reflected off a surface. $\text{Cu}_6\text{AgBiI}_{10}$ film has low reflectance and transmittance in the visible area, which helps to absorb more light and as consequently has a higher absorption within that visible area as illustrated in **Figure 3.5**. The following Tauc equation is utilized to calculate the band gap $\text{Cu}_6\text{AgBiI}_{10}$ films:

$$\alpha h\nu = A (h\nu - E_g)^n$$

Where it is the case that A remains constant that is known as the Tauc parameter. Then n is the number used to describe the transition process. Additionally, the film has a 1.72 eV band gap as shown in **Figure 3.5 (d)**, like this film, it has been applied to the design of multijunction solar cells, which can be used to achieve more efficient performance by combining several semiconductor layers with different band gaps in a single device.

3.3.2 SCAPS-1D numerical simulation analysis

3.3.2.1 CABI compound band energy alignment

A solar cell's band diagram can be used to visualize electrons and holes flowing within the cell and the alignment of these energy levels. There are usually multiple layers of materials in solar cells, each with its own band structure and energy level. In the cell, how much current and voltage can be generated within a cell depends on the level of alignment between these layers. In order to maximize the performance of solar cells, it is essential to understand and control the energy level alignment. It is possible to accomplish this through a number of methods such as optimizing interfaces, tuning the absorption layer's bandgap and using the right ETL and HTL materials.^{31,32}

A series of band alignment diagrams (**Figure 3.6 (a-f)**) for CABI absorber with quasi-Fermi electron and hole levels are shown, plotted as F_n and F_p and conduction band minima and valence band maxima, respectively, for the conduction band (E_C) and valence band (E_V). Within these six structures, CABI acts as an absorber, (c+mp)TiO₂ for an ETL layer as well as FTO for a substrate, These three layers remain in all the structures. However, HTLs can vary between organic and inorganic, to determine the most suitable structure.

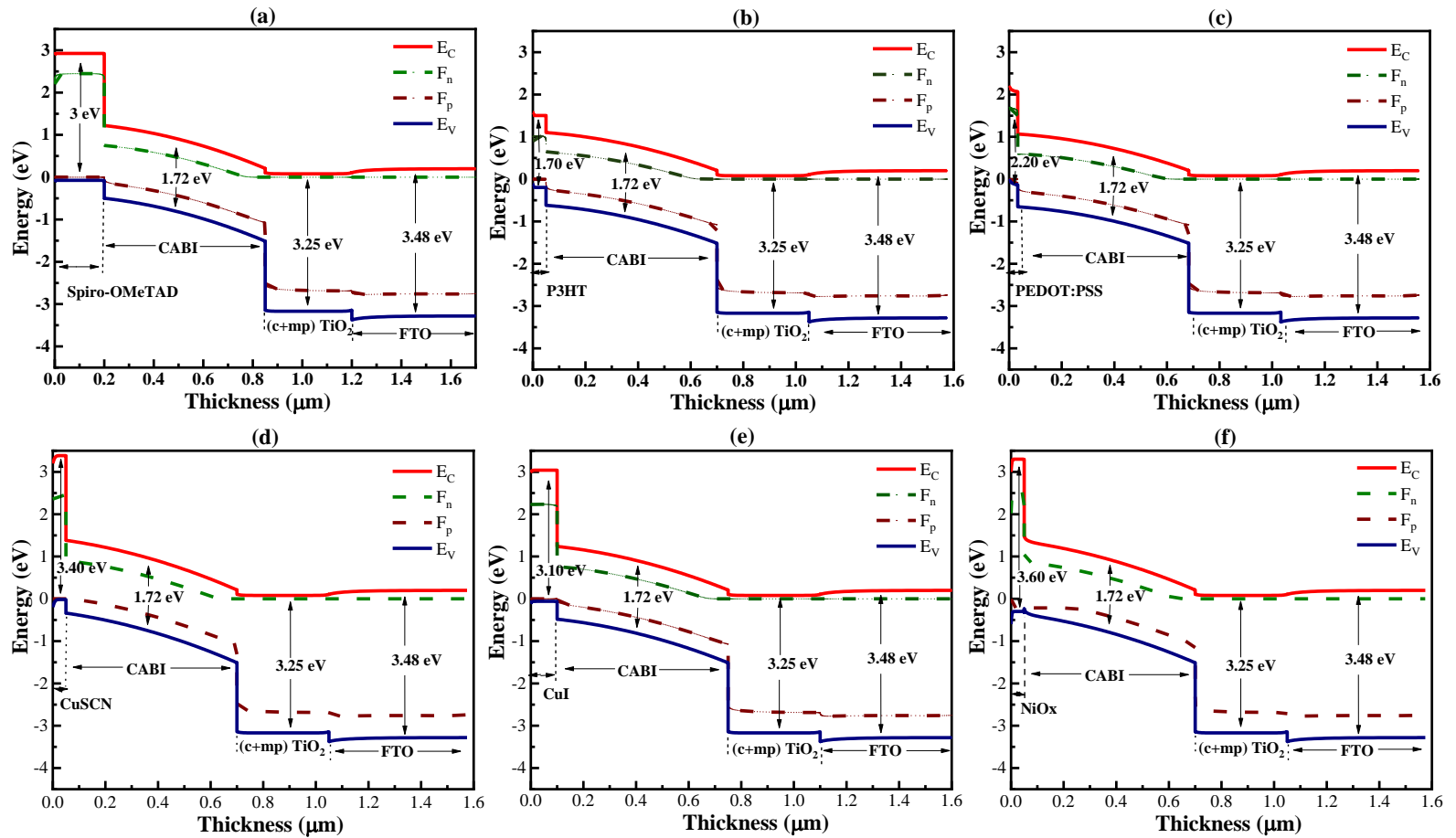


Figure 3.6 The n-i-p structure of CABI's solar cell devices energy band diagram with varying HTLs (a) Spiro-OMeTAD, (b) P3HT, (c) PEDOT:PSS, (d) CuSCN, (e) CuI, and (f) NiOx.

Figure 3.6 demonstrates that inorganic HTLs have a higher band gap in the band diagram, compared to organic HTLs, which have an impact on I-V properties. The larger band gap in the HTLs has created an excellent slop, with a CABI absorber layer within the band alignment, which makes carrier transport easy in the device due to J_{SC} increasing in that configuration. In the case of both organic and inorganic HTLs, the most suitable energy alignment was identified for spiro-OMeTAD as well as CuSCN HTLs, which resulted in the most efficient. Based on the built-in voltages shown in **Figure 3.6**, the band gap and band alignment of the HTLs have a significant influence on the mobility and I-V properties of the device.

3.3.2.2 J-V and QE properties of HTL variation

J-V analysis is crucial for solar cells since it gives information on the electrical properties of the cell like the short-circuit current density (J_{SC}) and open-circuit voltage (V_{OC}) as well as the fill factor (FF). These are vital in determining the performance of the solar cell.³³ With the use of various organic and inorganic HTLs with (c+mp)TiO₂ and Au as the ETL and back contact, CABI-based PSC was optimized in terms of performance. While other parameters were kept constant, the following parameters were retrieved experimentally for the optimization of the device: the series resistance, the shunt resistance, the thickness and band gap of the substrate, the thickness and band gap of the ETL, and the thickness and band gap of the absorber as mentioned in **Table 3.1**. The CABI solar cell device performance parameters that attain the highest PCE using (c+mp)TiO₂ along with organic-inorganic HTLs are illustrated in **Figure 3.7**. The configuration of FTO/(c+mp)TiO₂/CABI/Spiro-OMeTAD/Au achieved 1.50% PCE among all organic HTLs, while the configuration of FTO/(c+mp)TiO₂/CABI/CuSCN/Au achieved 1.98% PCE among all inorganic HTLs. In both cases, the short circuit current density (J_{SC}), the fill factor (FF) and the

open circuit voltage (V_{oc}) are maximum. However, organic HTLs shown an extremely low performance when compared with inorganic HTLs.

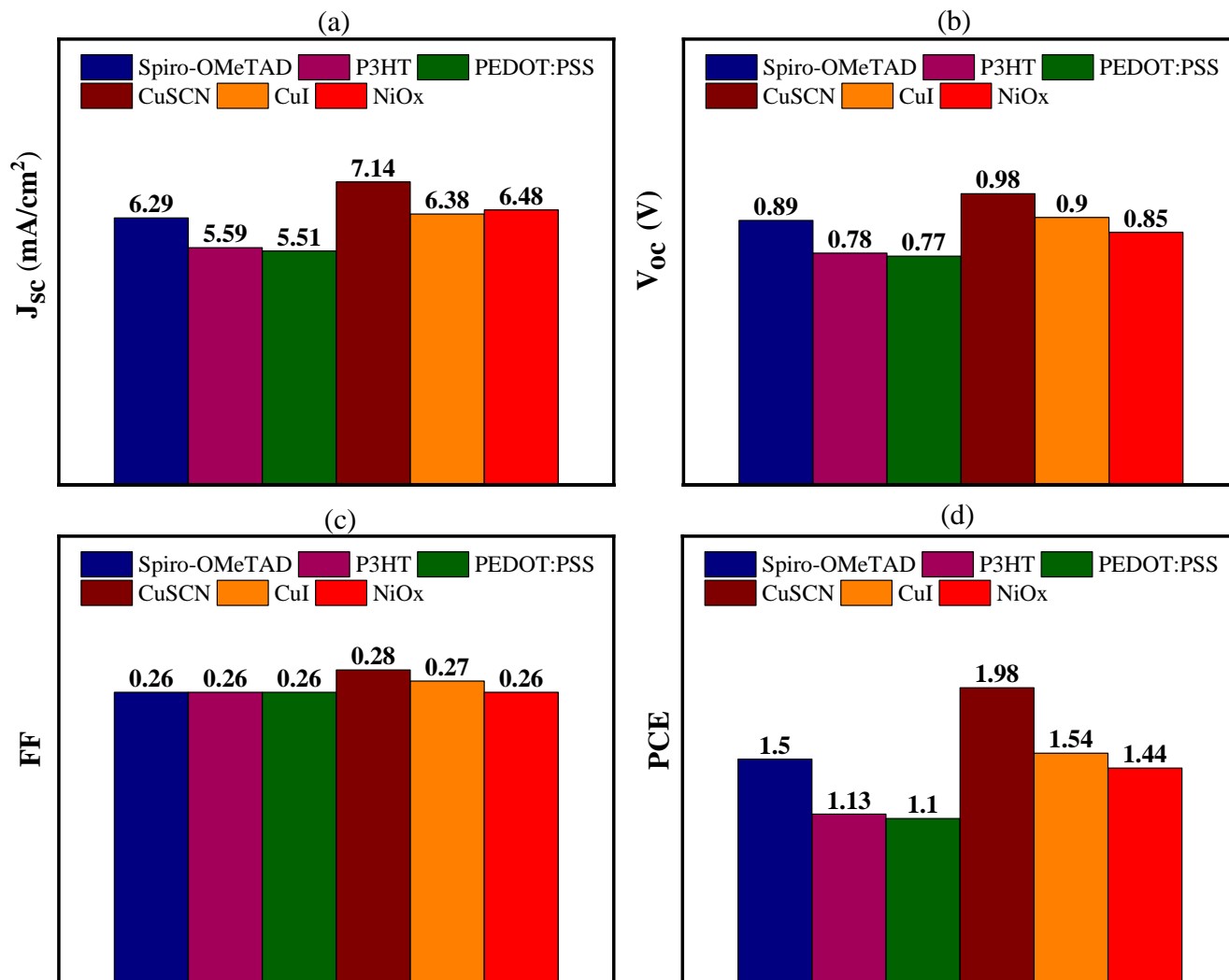


Figure 3.7 Various of the optimized parameter of the PV devices, i.e. V_{oc} , J_{sc} , FF and PCE in the CABI absorber layer of structures, of (c+mp)TiO₂ as an ETL using Au as the back contact as well as (a) Spiro-OMeTAD, (b) P3HT, (c) PEDOT:PSS (d) CuSCN, (e) CuI and (f) NiOx, for the HTLs.

It was clear when plotting the performance J-V curve of different combinations as shown in **Figure 3.8(a)**. Because of higher carrier mobility and positive pooling within energy level alignment, inorganic HTLs have been found to be better performers than organic HTLs. A study of quantum efficiency (QE) is essential for the assessment and improvement of photovoltaic cells as it gives valuable insights into the efficiency with which incident photons are converted into electricity. It allows the identification of areas for improvement and a better understanding of the mechanisms behind the loss of energy in cells.^{34,35} As shown in **Figure 3.8(b)**, the corresponding QE was investigated as a function of wavelength (300–800 nm). The value of QE started increasing at 300 nm, then, it increased by almost 80% in an nm range of 350. The value then dropped to the zero value at 730 nm at the boundary of the spectrum of each active material.

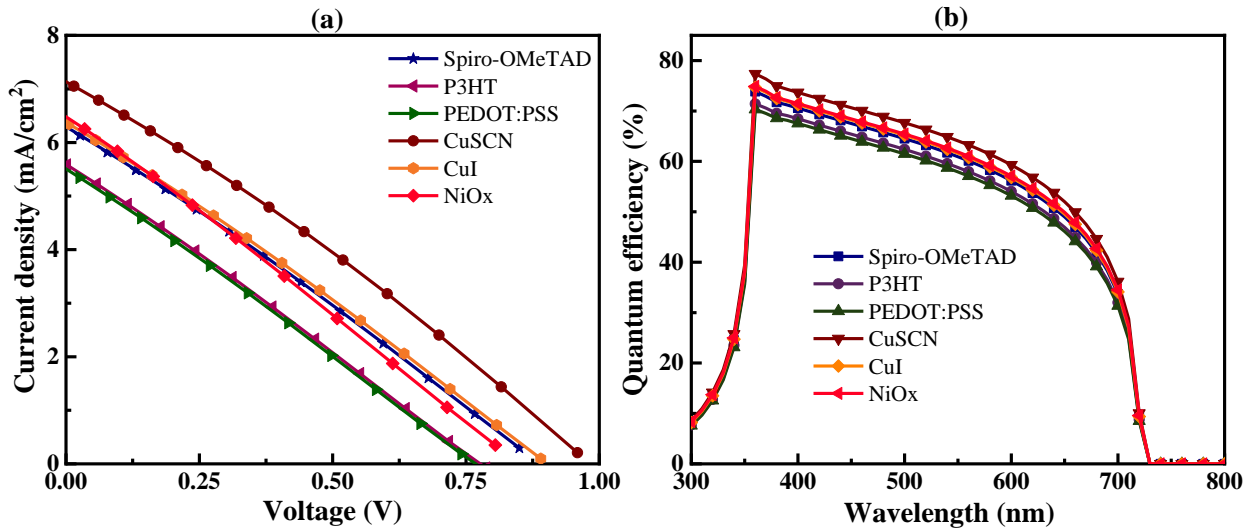


Figure 3.8 Effect of (a) J-V, and (b) QE for CABI solar cells with various HTL.

As shown in **Figure 3.8 (b)**, the QE is decreasing gradually as wavelength increases. This is due to the fact that longer wavelength photons possess energy, and therefore will be more likely to cause the electron-hole pairs to recombine prior to being collected. As a result, the QE will be lower when the wavelength is longer.

3.3.2.3 Generation and recombination rate analysis

Analysis of recombination and generation rates is crucial to understanding, characterizing and developing solar cell devices. The cell's generation and recombination rates of CABI can be seen in **Figure 3.9**. Generation rate is a crucial parameter for solar cell devices as it directly impacts the amount of electric current that can be produced. An increase in the generation rate signifies that there is a greater rate of electron hole pair creation, which may result in a greater current output from a solar cell. As sunlight's photons enter the CABI material of solar cells and are absorbed, they may be captured creating electrons inside the substance and forming electron-hole pairs. The amount of energy generated is a measure of the number of pairs of electrons generated in a given time, and per unit volume within the cell as shown in **Figure 3.9**. The highest rates of generation of the devices were observed at the point that photons pass through ETL into Absorbing material (within 0.7 to 0.9 μm) and the rates were nearly the same for all HTLs since at this point the rate of generation is the highest number of electrons produced at the particular location in the device because of the greater absorption of light when compared to other locations.

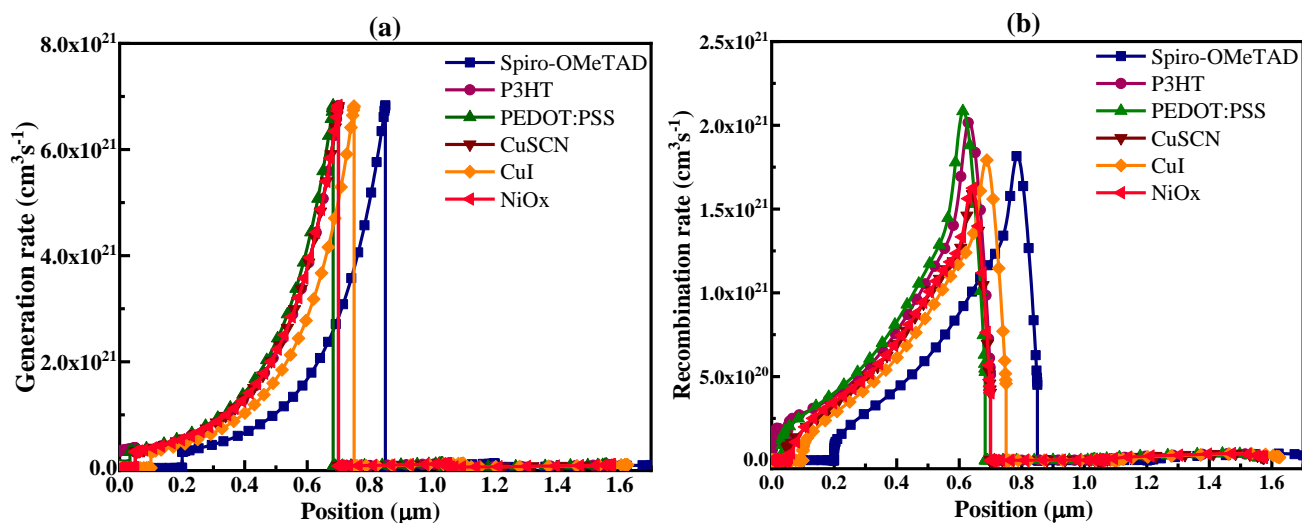


Figure 3.9 Analyzing (a) the rate of generation and (b) the rate of recombination in solar cells of CABI with different HTL.

The process by which charged carriers, such as electrons and holes, recombine results in a loss of electrical energy and a decline in device performance. This process is referred to as recombination. The physical characteristics of the solar cell, its doping amount, and the presence of any defects are only a few examples of the factors that affect recombination rates. The highest rates of recombination were seen at the ETL and absorber interfaces for various HTLs. Organic HTLs exhibit higher recombination than HTLs that are inorganic. Recombination rates are affected by charge carrier mobility and life span, and the resulting energy levels influence the rate of recombination in the electron hole within the solar device. Additionally, imperfections and grain boundaries permit the distribution of recombination rates in the structure of solar cells not to be uniform. A lower V_{OC} is associated with a higher recombination rate for these solar cells.

3.3.2.4 Capacitance-frequency (C-f) and Nyquist plot analysis

C-f analysis is a valuable method to analyze the electrical properties that solar cells exhibit. It gives details on the capacitance and frequency behavior of solar cells, which can be utilized to analyze various charge transport processes, such as carrier recombination, trapping, and diffusion. In the process of varying frequency and measuring the equivalent capacitance, the C-f curve is shown in **Figure 3.10**. **Figure 3.10** shows a higher value of capacitance at low frequency. After the frequency reaches a higher value, it abruptly reduces before it becomes stable. Negative capacitances can be measured at a higher frequency of 10^6 Hz. This is when the capacitance transition occurs from a positive to negative quadrant. When the frequency of signal exceeds 10^5 Hz minority carriers rise quickly. This process leads to an increase in the frequency of recombination in the junction with the most capacitance-inducing value.

The impedance of a solar cell device is shown in **Figure 3.10** graphically by the Nyquist plots. The real and imaginary parts of the impedance are plotted on the horizontal and vertical axes, respectively, to form a semicircular arc in the complex plane. The Nyquist plots are useful for studying the processes of charge transfer and recombination within cells. The shape that is depicted on the Nyquist plot can provide information about the various capacitive and resistive behavior of the solar cell along with the prevailing frequency. This data can be used for improving the design and performance of solar cells.

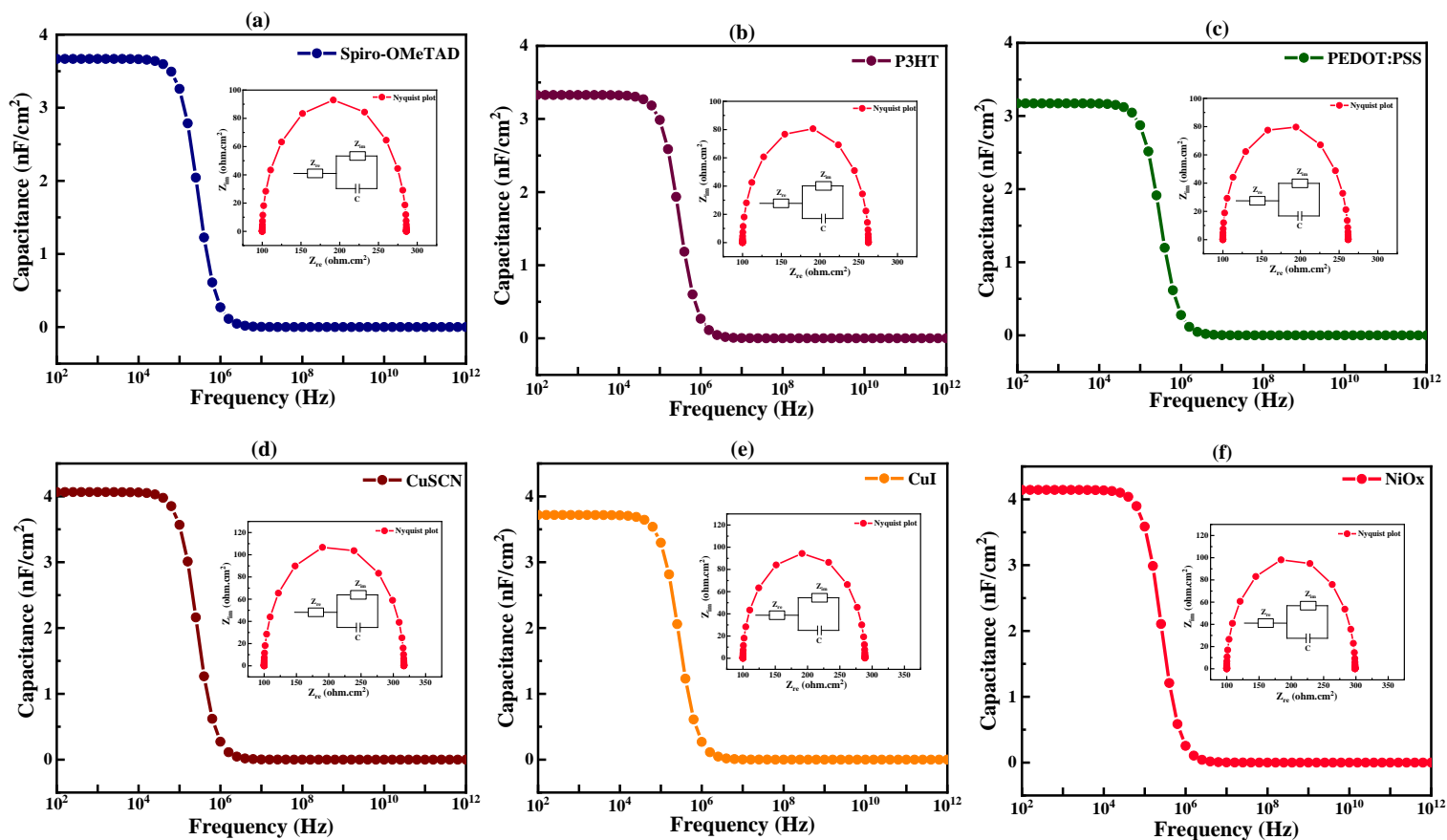


Figure 3.10 Capacitance vs frequency curves with Nyquist plot of the CABI absorber layer.

In **Figure 3.10**, the semicircle Nyquist plot, it is evident that the diameter of the semicircle is big, which indicates that the resistance of solar cells is very high. The semicircle's angle is also low, which indicates that the capacity of the solar cell is very low. It is possible that a high resistance combined with a low capacitance is caused by rapid recombination, or perhaps low concentration of doping. All of these factors could contribute to the decrease in the effectiveness of solar cells. In contrast, Inorganic HTLs have larger capacitance than organic HTLs due to the fact that they possess a greater dielectric constant. The higher dielectric constant indicates that the material can hold more charge, resulting in a higher capacitance.

3.3.2.5 Analysis of device performance on the CABI and HTLs thickness

The efficiency and performance of solar cells are directly affected by the proper optimization of the absorber and HTLs thickness. In the absorber, the layer absorbs photons to create charge carriers, which are then transported to the collector electrode by HTLs, which are positive charged carriers. The calculated V_{OC} , J_{SC} , FF and efficiency contour maps of CABI-based solar cells dependent on different HTL thicknesses between 50-250 nm and the thickness of the absorber in range 400-2000 nm can be shown in **Figures 3.11-3.14**. In **Figure 3.11**, when the thickness of the CABI absorber layer was around 800 nm and HTLs thickness was low impact, within limits as well (c+mp)TiO₂ thickness was constant at 350 nm and the solar cells that had inorganic HTLs, such as CuSCN, CuI, and NiOx showed the highest V_{OC} at 0.99 V, and the minimum V_{OC} that was 0.85 V. In contrast, solar cells that have organic HTLs like Spiro-OMeTAD and P3HT, as well as PEDOT:PSS had the highest V_{OC} of 0.93 V, and the minimum V_{OC} was 0.75 V. Inorganic HTLs are more higher in V_{OC} than organic HTLs due to the fact that they possess a greater bandgap. **Figure 3.12** shows how changing the HTLs, and absorber layer thickness affects the J_{SC} characteristics for CABI solar cells. In the case of optimization of thickness, it exhibits the same trend as V_{OC} . When the absorber's thickness is more than 1200 nm and the highest J_{SC} is achieved. For organic HTLs, the highest and lowest J_{SC} were found to be 6.78 mA/cm² and 4.46 mA/cm², respectively, while for inorganic HTLs, the highest and lowest J_{SC} was noted to be 7.42 and 6.33 mA/cm², respectively. When the thickness of the absorber layer grows, the amount of light which is absorbed increases and leads to an amplification in the number of charge carriers that are produced. This is the reason why the J_{SC} of the solar cell increases as the thickness of the absorber. The J_{SC} is relatively low in comparison to V_{OC} . This could be due to the larger band gap, higher the rate of recombination, or defects.

According to **Figure 3.13**, the maximum value of fill factor (FF) is within the range of 0.28-0.26 for the investigated structures with varying absorber and HTL layer thickness. The highest value for FF was more than 800 nm for absorber thickness. In both the organic and inorganic HTLs, FF are very low because of the high resistance and greater recombination losses. As can be seen from **Figure 3.13**, in these solar cells, FF patterns are nearly identical to all organic and inorganic HTLs. As shown in **Figure 3.14**, the highest efficiency was 2.07%, which was revealed with CuSCN of inorganic HTL between 50-250 nm thickness and 1000-1400 nm absorber thickness. Based on the V_{OC} , J_{SC} and FF outcomes, efficiency was highest for inorganic HTLs, but not for organic HTLs. Organic HTL Spiro-OMeTAD was observed to be high at 1.67% with an absorber thickness of greater than 800 nm. Additionally, inorganic HTLs tend to be preferred due to their stability and mobility, especially for long-term and outdoor applications. But organic HTLs offer their own benefits, like flexibility and lower prices, making them the ideal choice for specific applications.

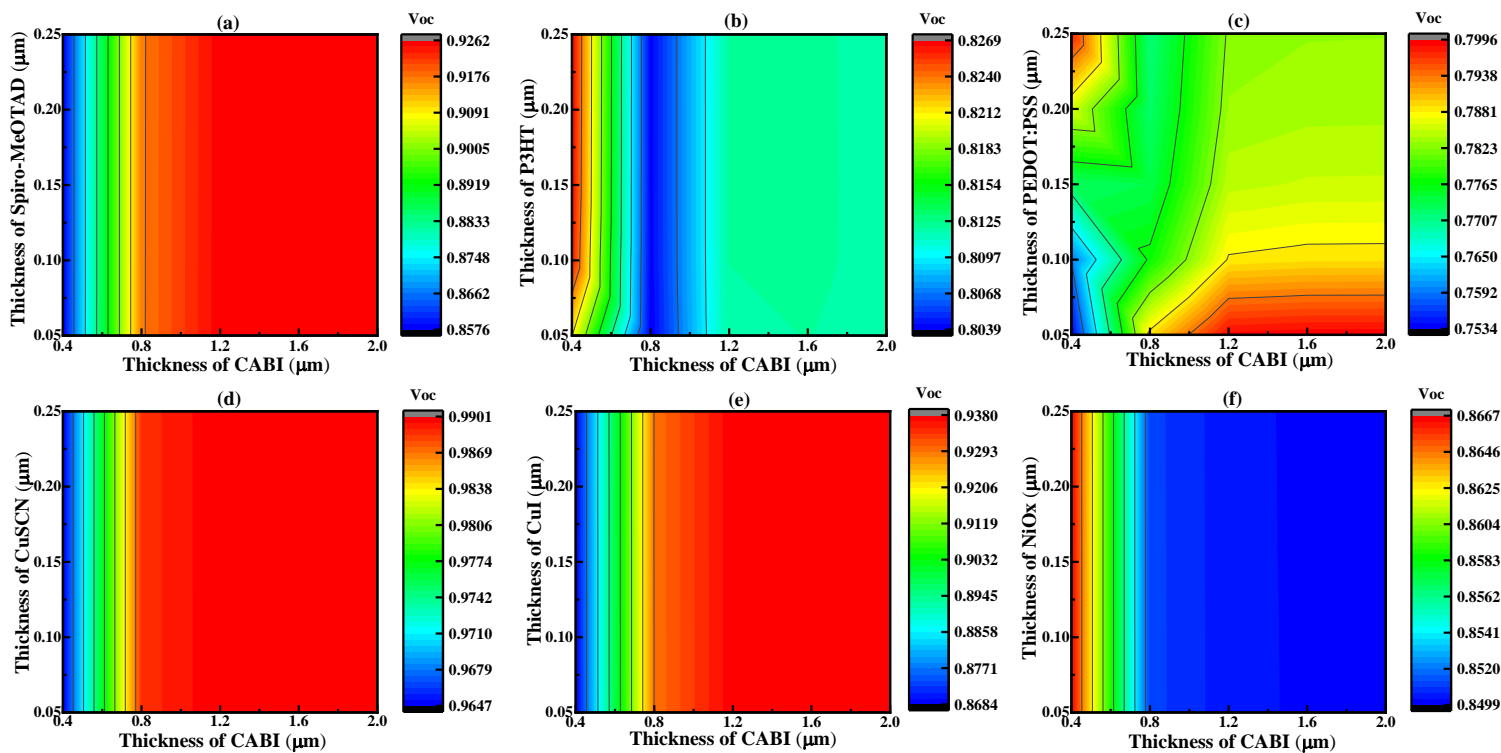


Figure 3.11 Contour mapping of V_{OC} relative to the thickness of the CABI absorber and HTLs.

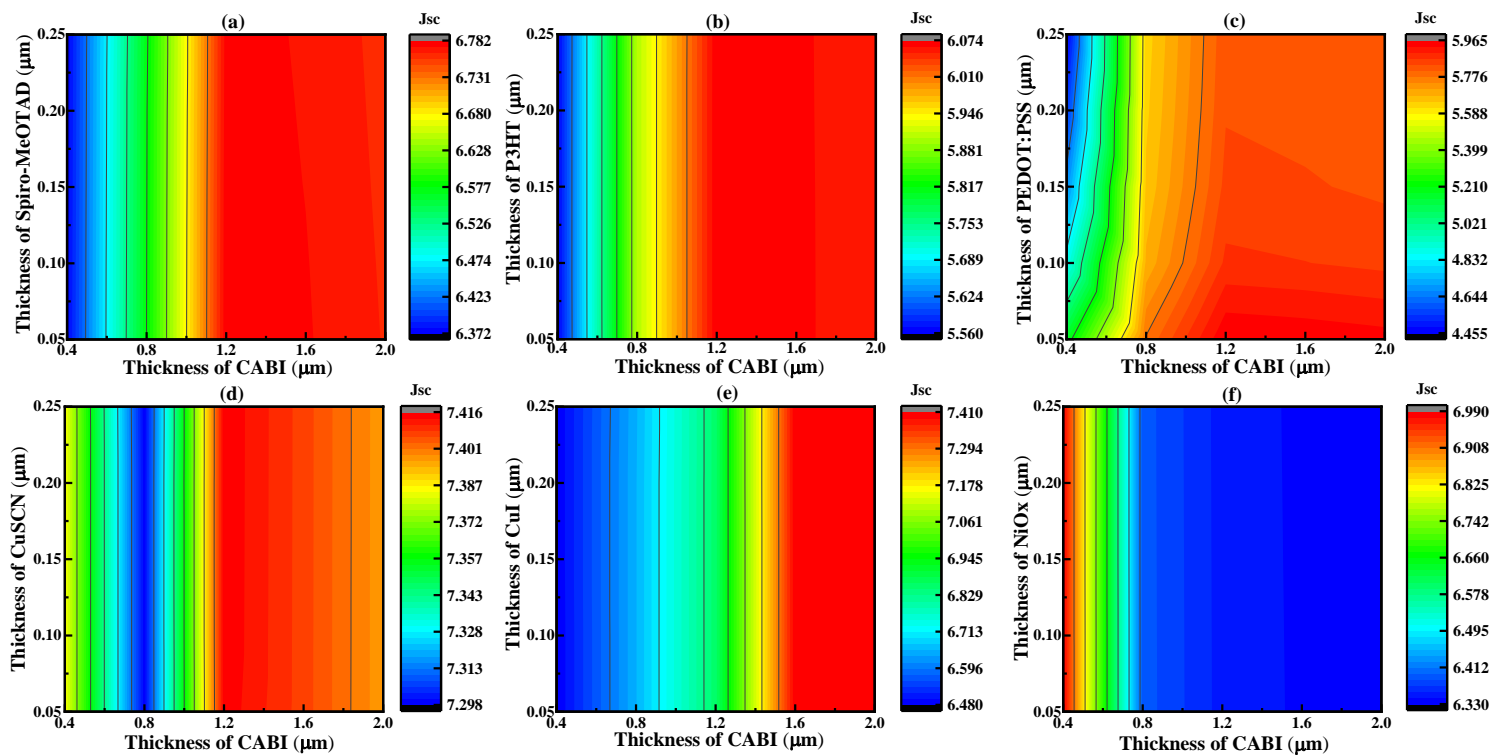


Figure 3.12 Contour mapping of J_{SC} relative to the thickness of the CABI absorber and HTLs.

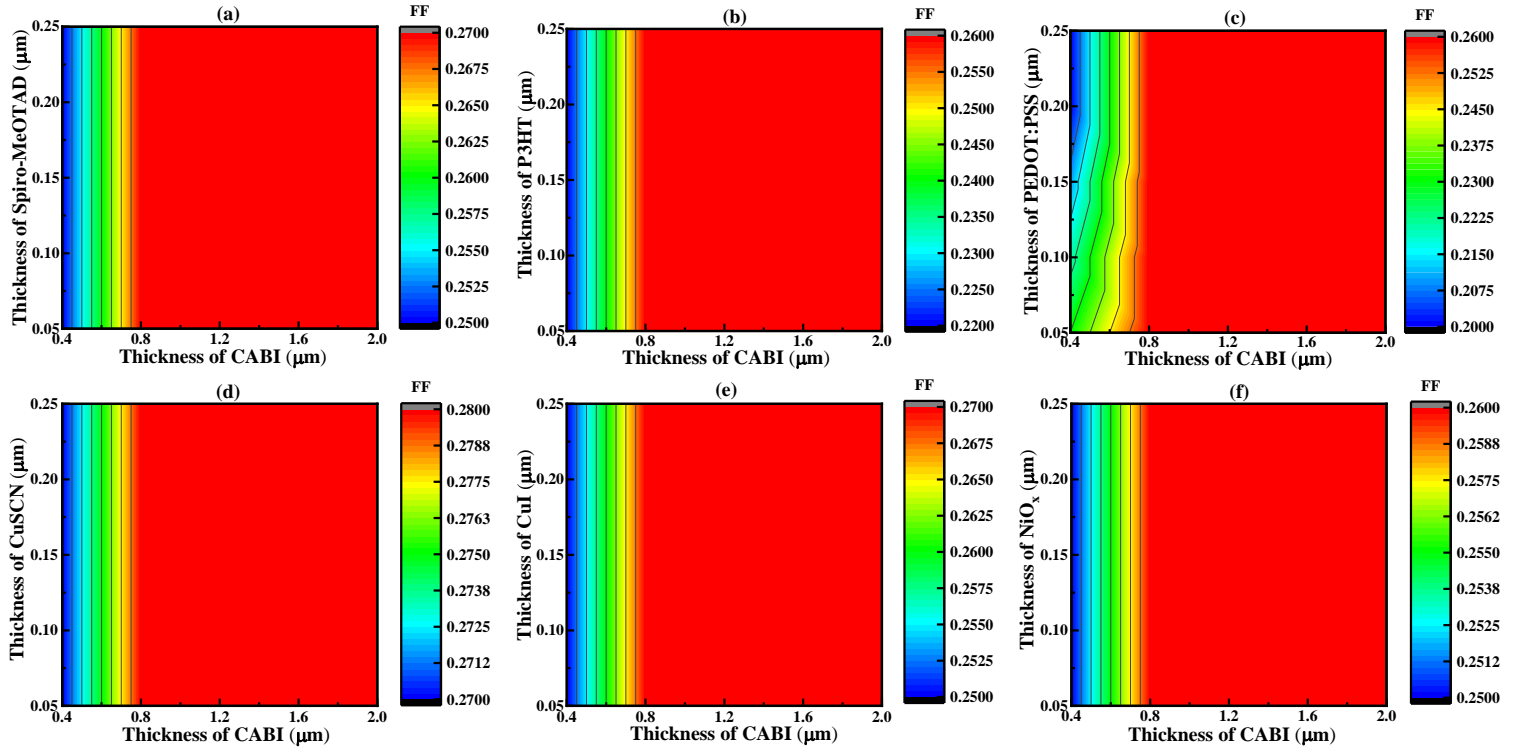


Figure 3.13 Contour mapping of FF relative to the thickness of the CABI absorber and HTLs.

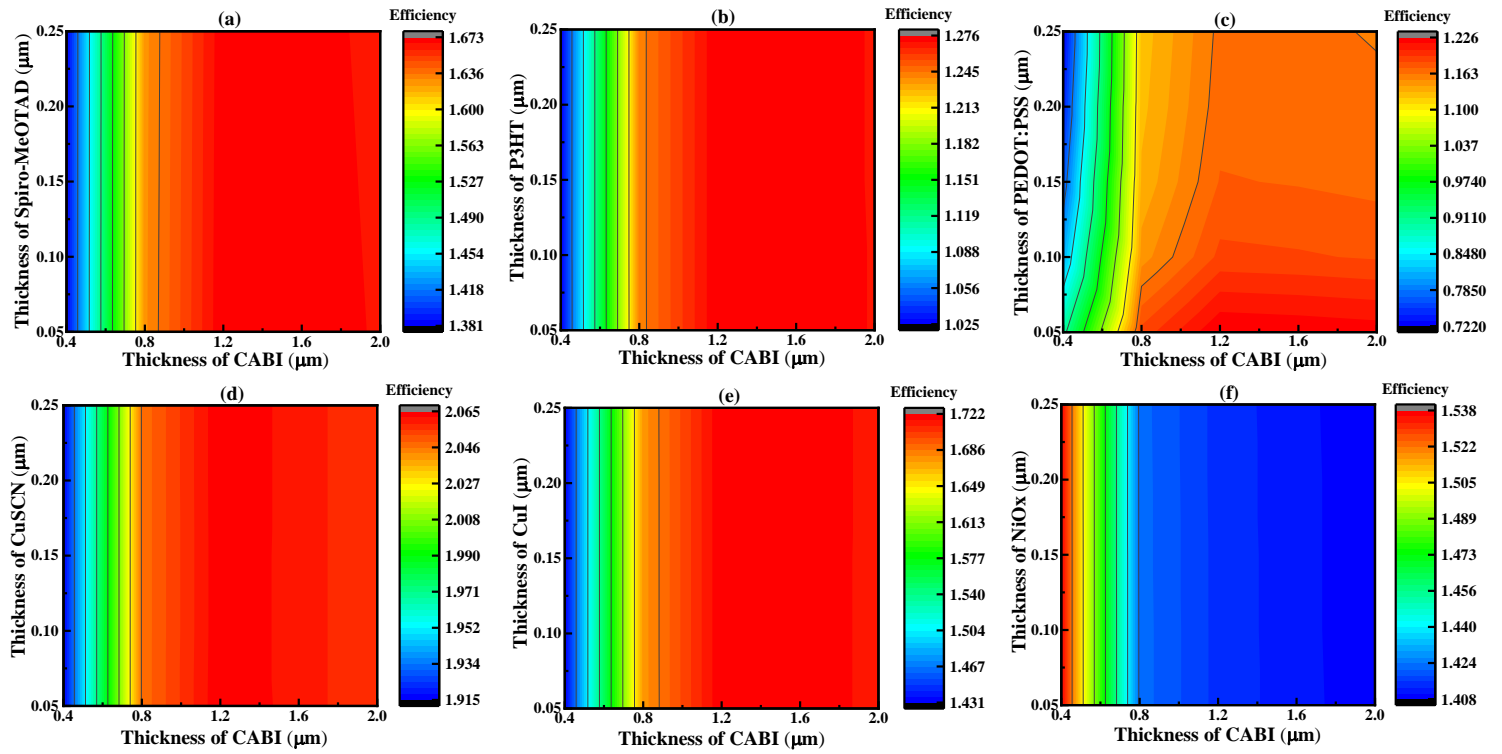


Figure 3.14 Contour mapping of efficiency relative to the thickness of the CABI absorber and

HTLs.

3.3.2.6 Effect of ETL thickness on device performance

The ETL is an essential element in solar cells. It functions as an intermediary between the absorption layer and the electrode. It helps the extraction and transfer of electrons produced by the absorption of sunlight. The optimization of the thickness of the ETL is a crucial aspect of the development of solar cells with high performance. To optimize device performance, the ETL thickness was varied from 100 to 500 nm, and the absorber thickness was fixed at 650 nm with Spiro-OMeTAD (200 nm), P3HT (50 nm), PEDOT:PSS (33 nm), CuSCN (50 nm), CuI (100 nm), and NiOx (50 nm) used as HTLs as shown in **Figure 3.15**. The highest values for J_{sc} , V_{oc} , and overall efficiency were observed when the thickness of (c+mp) TiO_2 was 100 nm. The fill factors for the six types of structures are the same for all. However, all of these performance metrics decline noticeably as (c+mp) TiO_2 thickness increases beyond 100 nm. This is because the thin ETL decreases the resistance as well as the distance electrons must travel to travel between in the layer of active to reach the electrode which results in better performance. Consequently, using an inorganic CuSCN HTL, we attain a maximum efficiency of 1.98%, while using an organic PEDOT:PSS HTL, we achieve a minimum efficiency of 1.11%.

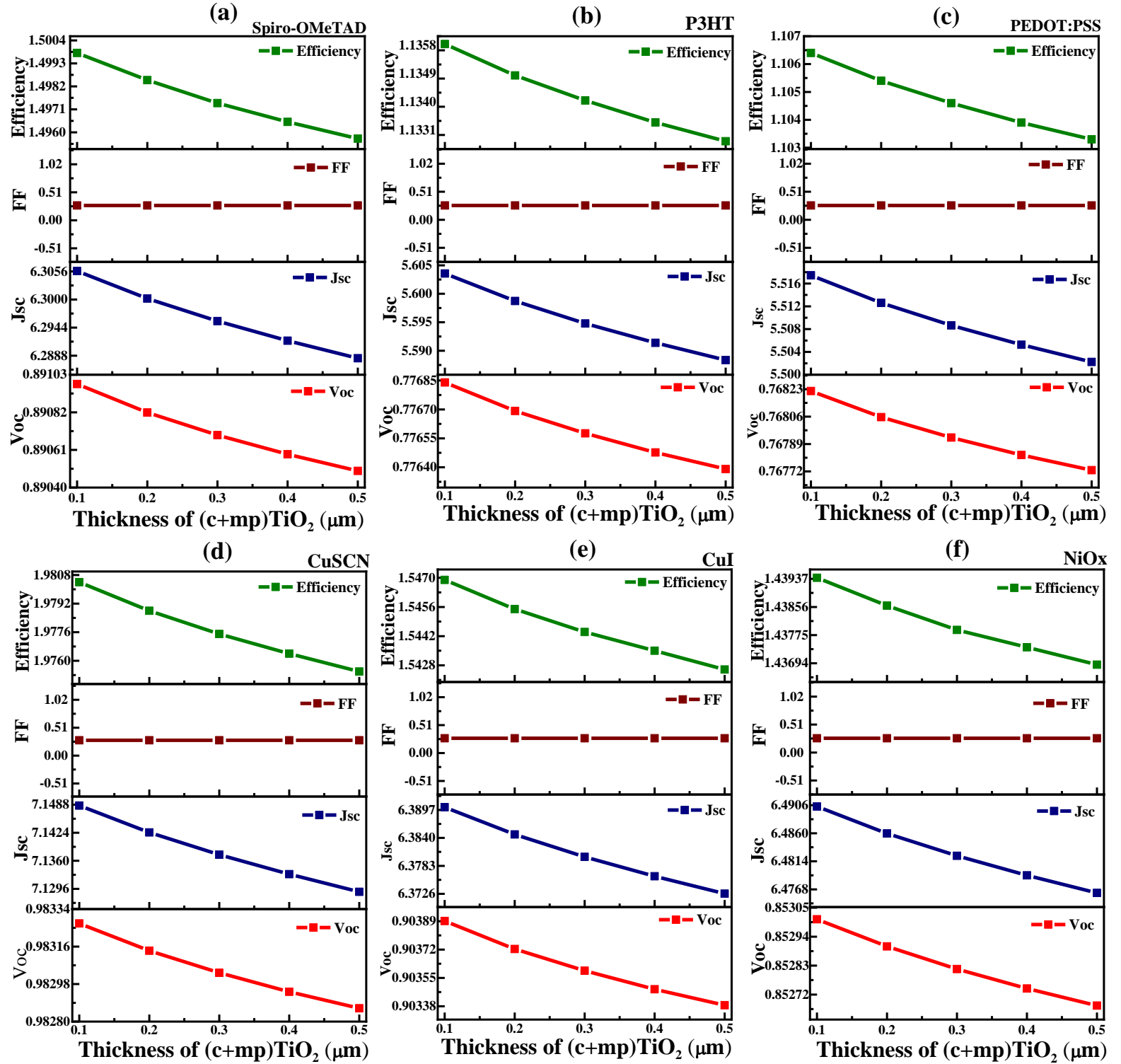


Figure 3.15 Variation of (c+mp) TiO₂ layer thickness with CABI absorber, and different HTLs such as (a) Spiro-OMeTAD, (b) P3HT, (c) PEDOT:PSS, (d) CuSCN, (e) CuI and (f) NiO_x.

3.4 Conclusions

Inorganic $\text{Cu}_6\text{AgBiI}_{10}$ film, a highly stable and low-cost material, has shown great potential in photovoltaics and for a variety of other applications. Among the many advantages of these films are their better ability to transfer charged carriers and their high absorption coefficients. In this combination of experimental and simulative studies, CABI films' properties were comprehensively understood. The CABI films were fabricated using a spin coating method, whose characterizations confirmed trigonal structure by XRD, island-type grains by SEM, and high absorbance by UV. It is clear that the absorbing layer and ETL thickness have the greatest impact on PV characteristics. However, the HTL thickness had a negligible impact. According to the optimization process, the ideal thickness of the absorber and ETL was 800 nm and 100 nm, respectively. A direct bandgap, electron affinity, charge carrier mobility, and compatibility with absorbing layer are other factors that made inorganic CuSCN the best performing HTL. Compared with previous studies, the optimized $\text{FTO}/(\text{c}+\text{mp})\text{TiO}_2/\text{CABI}/\text{CuSCN}/\text{Au}$ device structure delivers the best efficiency of 2.06%. Our study also found maximum PCE and Voc values of 1.67% and 0.93 V for Spiro-MeOTAD, 1.28% and 0.83 V for P3HT, and 1.22% and 0.80 V for PEDOT:PSS. We also found 1.72% and 0.94 V for CuI, and 1.54% and 0.87 V for NiOx. Based on the results of this study, it is concluded that inorganic HTLs (CuSCN, CuI and NiOx) have better photovoltaic performance in solar cell devices than organic HTLs (Spiro-OMeTAD, P3HT and PEDOT:PSS).

3.5 References

- (1) Pai, N.; Chatti, M.; Fürer, S. O.; Scully, A. D.; Raga, S. R.; Rai, N.; Tan, B.; Chesman, A. S. R.; Xu, Z.; Rietwyk, K. J.; Reddy, S. S.; Hora, Y.; Sepalage, G. A.; Glück, N.; Lira-Cantú, M.; Bach, U.; Simonov, A. N. Solution Processable Direct Bandgap Copper-Silver-

- Bismuth Iodide Photovoltaics: Compositional Control of Dimensionality and Optoelectronic Properties. *Adv. Energy Mater.* **2022**, 12 (32), 2201482.
- (2) Buizza, L. R. V; Sansom, H. C.; Wright, A. D.; Ulatowski, A. M.; Johnston, M. B.; Snaith, H. J.; Herz, L. M.; Buizza, L. R. V; Sansom, H. C.; Wright, A. D.; Ulatowski, A. M.; Johnston, M. B.; Snaith, H. J.; Herz, L. M. Interplay of Structure, Charge-Carrier Localization and Dynamics in Copper-Silver-Bismuth-Halide Semiconductors. *Adv. Funct. Mater.* **2022**, 32 (6), 2108392.
 - (3) Islam, M. A.; Kato, S.; Kishi, N.; Soga, T. Enhanced Surface Morphology and Photovoltaic Properties of a New Class of Material Copper Silver Bismuth Iodide Solar Cell. *J. Mater. Res. Technol.* **2023**, 25, 4171–4186.
 - (4) Li, X.; Yang, J.; Jiang, Q.; Lai, H.; Li, S.; Tan, Y.; Chen, Y.; Li, S. Perovskite Solar Cells Employing an Eco-Friendly and Low-Cost Inorganic Hole Transport Layer for Enhanced Photovoltaic Performance and Operational Stability. *Mater. Chem. A.* **2019**, 7 (12), 7065–7073.
 - (5) Yao, Y.; Cheng, C.; Zhang, C.; Hu, H.; Wang, K.; De Wolf, S.; Yao, Y.; Cheng, C.; Zhang, C.; Wang, K.; Hu, H.; De Wolf, S. Organic Hole-Transport Layers for Efficient, Stable, and Scalable Inverted Perovskite Solar Cells. *Adv. Mater.* **2022**, 34 (44), 2203794.
 - (6) Burgelman, M.; Nollet, P.; Degraeve, S. Modelling Polycrystalline Semiconductor Solar Cells. *Thin Solid Films* **2000**, 361–362, 527–532.
 - (7) Srivastava, A.; Dua, P.; Lenka, T. R.; Tripathy, S. K. Numerical Simulations on CZTS/CZTSe Based Solar Cell with ZnSe as an Alternative Buffer Layer Using SCAPS-

1D. *Mater. Today Proc.* **2021**, 43, 3735–3739.

- (8) Chen, Q.; Ni, Y.; Dou, X.; Yoshinori, Y. The Effect of Energy Level of Transport Layer on the Performance of Ambient Air Prepared Perovskite Solar Cell: A SCAPS-1D Simulation Study. *Crystals* **2022**, 12 (1), 68.
- (9) Rahman, M. F.; Habib, M. J. A.; Ali, M. H.; Rubel, M. H. K.; Islam, M. R.; Abu, A. B.; Hossain, M. K. Design and Numerical Investigation of Cadmium Telluride (CdTe) and Iron Silicide (FeSi₂) Based Double Absorber Solar Cells to Enhance Power Conversion Efficiency. *AIP Adv.* **2022**, 12 (10).
- (10) Ali, M. H.; Al Mamun, M. A.; Haque, M. D.; Rahman, M. F.; Hossain, M. K.; Abu, A. Z. Performance Enhancement of an MoS₂-Based Heterojunction Solar Cell with an In₂Te₃ Back Surface Field: A Numerical Simulation Approach. *ACS Omega* **2023**, 8 (7), 7017–7029.
- (11) Bichave, S.; Mundupuzhakal, J.; Gajjar, P. N.; Gupta, S. K. Analysis of Varying ETL/HTL Material for an Effective Perovskite Solar Cell by Numerical Simulation. *Mater. Today Proc.* **2023**.
- (12) Hossain, M. K.; Ishraque Toki, G. F.; Samajdar, D. P.; Rubel, M. H. K.; Mushtaq, M.; Islam, M. R.; Rahman, M. F.; Bhattarai, S.; Bencherif, H.; Mohammed, M. K. A.; Pandey, R.; Madan, J. Photovoltaic Performance Investigation of Cs₃Bi₂I₉-Based Perovskite Solar Cells with Various Charge Transport Channels Using DFT and SCAPS-1D Frameworks. *Energy and Fuels* **2023**.
- (13) Giordano, F.; Abate, A.; Correa Baena, J. P.; Saliba, M.; Matsui, T.; Im, S. H.; Zakeeruddin,

- S. M.; Nazeeruddin, M. K.; Hagfeldt, A.; Graetzel, M. Enhanced Electronic Properties in Mesoporous TiO₂ via Lithium Doping for High-Efficiency Perovskite Solar Cells. *Nat. Commun.* **2016**, *7* (1), 1–6.
- (14) Karthick, S.; Bouclé, J.; Velumani, S. Effect of Bismuth Iodide (BiI₃) Interfacial Layer with Different HTL's in FAPI Based Perovskite Solar Cell – SCAPS – 1D Study. *Solar Energy* **2021**, *218*, 157–168.
- (15) Hossain, M. K.; Rubel, M. H. K.; Toki, G. F. I.; Alam, I.; Rahman, M. F.; Bencherif, H. Effect of Various Electron and Hole Transport Layers on the Performance of CsPbI₃-Based Perovskite Solar Cells: A Numerical Investigation in DFT, SCAPS-1D, and WxAMPS Frameworks. *ACS Omega* **2022**, *7* (47), 43210–43230.
- (16) Hossain, M. K.; Arnab, A. A.; Das, R. C.; Hossain, K. M.; Rubel, M. H. K.; Rahman, M. F.; Bencherif, H.; Emetere, M. E.; Mohammed, M. K. A.; Pandey, R. Combined DFT, SCAPS-1D, and WxAMPS Frameworks for Design Optimization of Efficient Cs₂BiAgI₆-Based Perovskite Solar Cells with Different Charge Transport Layers. *RSC Adv.* **2022**, *12* (54), 35002–35025.
- (17) Chowdhury, M. S.; Shahahmadi, S. A.; Chelvanathan, P.; Tiong, S. K.; Amin, N.; Techato, K.; Nuthammachot, N.; Chowdhury, T.; Suklueng, M. Effect of Deep-Level Defect Density of the Absorber Layer and n/i Interface in Perovskite Solar Cells by SCAPS-1D. *Results Phys.* **2020**, *16*, 102839.
- (18) Luo, W.; Xu, J.; Liu, S. Optimization of All-Inorganic CsPbI₃-Based Inverted Perovskite Solar Cells by Numerical Simulation. *J. Electron. Mater.* **2023**, *52* (3), 2216–2226.

- (19) Deepthi Jayan, K.; Sebastian, V. Comprehensive Device Modelling and Performance Analysis of MASnI_3 Based Perovskite Solar Cells with Diverse ETM, HTM and Back Metal Contacts. *Solar Energy* **2021**, *217*, 40–48.
- (20) Matiur, R. M.; Nor, F.; Arima, Y.; Kato, S.; Soga, T. Compact Continuous BiOI Film for Solid-State Solar Cell via Faster Lifting Speed of the Dip-SILAR Technique at Room Temperature. *Mater. Sci. Semicond. Process.* **2021**, *130*, 105808.
- (21) Matiur, R. M.; Noman, M. A. A.; Kato, S.; Soga, T. A Novel Modest Synthesis of Device Applicable Flakes Based Stable BiOI Film by the Oxidation of BiI_3 Film. *J. Alloys Compd.* **2021**, *873*, 159715.
- (22) Sen, S. K.; Jalil, M. A.; Hossain, M.; Manir, M. S.; Hoque, K.; Islam, M. A.; Hossain, M. N. Silver Incorporated $\alpha\text{-MoO}_3$ Nanoplates to Nanorods: Exploring the Effects of Doping on Structural, Morphological and Optical Properties. *Mater. Today Commun.* **2021**, *27*, 102404.
- (23) Sen, S. K.; Munshi, M. R.; Kumar, A.; Mortuza, A. A.; Manir, M. S.; Islam, M. A.; Hossain, M. N.; Hossain, M. K. Structural, Optical, Magnetic, and Enhanced Antibacterial Properties of Hydrothermally Synthesized Sm-Incorporating $\alpha\text{-MoO}_3$ 2D-Layered Nanoplates. *RSC Adv.* **2022**, *12* (53), 34584–34600.
- (24) Islam, M. A.; Rahaman, M. Z.; Hasan, M. M.; Hossain, A. K. M. A. Analysis of Grain Growth, Structural and Magnetic Properties of Li-Ni-Zn Ferrite under the Influence of Sintering Temperature. *Heliyon* **2019**, *5* (2), e01199.
- (25) Achoi, M. F.; Noman, M. A. A.; Kato, S.; Kishi, N.; Soga, T. Pinhole-Free

- Methylammonium Bismuth Iodide Perovskite Solar Cells Via All-Solution-Processed Multi-Step Spin Coating. *J. Electron. Mater.* **2022**, *51* (2), 577–585.
- (26) Yi, Z.; Zhang, T.; Ban, H.; Shao, H.; Gong, X.; Wu, M.; Liang, G.; Zhang, X. L.; Shen, Y.; Wang, M. AgBi₃I₁₀ Rudorffite for Photovoltaic Application. *Solar Energy* **2020**, *206*, 436–442.
- (27) Ameri, T.; Khoram, P.; Heumüller, T.; Baran, D.; MacHui, F.; Troeger, A.; Sgobba, V.; Guldi, D. M.; Halik, M.; Rathgeber, S.; Scherf, U.; Brabec, C. J. Morphology Analysis of near IR Sensitized Polymer/Fullerene Organic Solar Cells by Implementing Low Bandgap Heteroanalogue C-/Si-PCPDTBT. *J. Mater. Chem. A* **2014**, *2* (45), 19461–19472.
- (28) Zeng, W.; Liu, X.; Guo, X.; Niu, Q.; Yi, J.; Xia, R.; Min, Y.; Kim, Y.; Kim, H. Morphology Analysis and Optimization: Crucial Factor Determining the Performance of Perovskite Solar Cells. *Molecules* **2017**, *22* (4), 520.
- (29) Al Ghaithi, A. O.; Aravindh, S. A.; Hedhili, M. N.; Ng, T. K.; Ooi, B. S.; Najjar, A. Optical Properties and First-Principles Study of CH₃NH₃PbBr₃ Perovskite Structures. *ACS Omega* **2020**, *5* (21), 12313–12319.
- (30) Erb, T.; Zhokhavets, U.; Gobsch, G.; Raleva, S.; Stühn, B.; Schilinsky, P.; Waldauf, C.; Brabec, C. J. Correlation Between Structural and Optical Properties of Composite Polymer/Fullerene Films for Organic Solar Cells. *Adv. Funct. Mater.* **2005**, *15* (7), 1193–1196.
- (31) Hawash, Z.; Raga, S. R.; Son, D. Y.; Ono, L. K.; Park, N. G.; Qi, Y. Interfacial Modification of Perovskite Solar Cells Using an Ultrathin MAI Layer Leads to Enhanced Energy Level

- Alignment, Efficiencies, and Reproducibility. *J. Phys. Chem. Lett.* **2017**, 8 (17), 3947–3953.
- (32) Wang, Y.; Ji, S.; Shin, B. Interface Engineering of Antimony Selenide Solar Cells: A Review on the Optimization of Energy Band Alignments. *JPhys. Energy* **2022**, 4 (4), 044002.
- (33) Glowienka, D.; Galagan, Y. Light Intensity Analysis of Photovoltaic Parameters for Perovskite Solar Cells. *Adv. Mater.* **2022**, 34 (2), 2105920.
- (34) Anderson, A. Y.; Bouhadana, Y.; Barad, H. N.; Kupfer, B.; Rosh-Hodesh, E.; Aviv, H.; Tischler, Y. R.; Rühle, S.; Zaban, A. Quantum Efficiency and Bandgap Analysis for Combinatorial Photovoltaics: Sorting Activity of Cu-O Compounds in All-Oxide Device Libraries. *ACS Comb. Sci.* **2014**, 16 (2), 53–65.
- (35) Holovsky, J. H.; Ridzoň, K.; Amalathas, A. P.; Conrad, B.; Sharma, R. K.; Chin, Y.; Bastola, E.; Bhandari, K.; Ellingson, R. J.; De Wolf, S. Below the Urbach Edge: Solar Cell Loss Analysis Based on Full External Quantum Efficiency Spectra. *ACS Energy Lett.* **2023**, 8 (7), 3221–3227.

Chapter 4

Role of organic HTLs enhance the efficiency of Ag_3BiI_6 solar cells through the integration of experiment and simulation

4.1 Introduction

Nevertheless, Ag_3BiI_6 solar cells have very poor efficacy. There is a lack of research and understanding regarding organic hole transport layers (HTLs) for Ag_3BiI_6 -based perovskites. In this work, we report the results of our current investigation into the influence on the organic hole transport layers (HTLs) to enhance photovoltaic efficiency for Ag_3BiI_6 base solar cells in order to solve this problem. Because it significantly improves the air stability and efficiency of the solar cells, an appropriate HTL is essential. Effective HTLs need to have great hole mobility, excellent optical transparency, along with an appropriate energy level aligned with the absorber layer.^{1,2} The novelty of this study lies in examining the effects of different organic HTLs on Ag_3BiI_6 perovskites. For the Ag_3BiI_6 light absorbers to enable effective charge transfer, their energy levels must match. An experimental investigation of the optical, morphological and structural properties of Ag_3BiI_6 on $\text{FTO}/(\text{c}+\text{mp})\text{TiO}_2$ has been conducted. Then, using the SCAPS-1D modeling, we looked at how the PCE of solar cells is impacted by the interplay of organic components. This is the first time that models and experiments have been coupled to study Ag_3BiI_6 solar cells at various HTLs. Spiro-OMeTAD, PTAA, P3HT, and PEDOT:PSS materials were employed as HTLs in our study in addition to $(\text{c}+\text{mp})\text{TiO}_2$ as Electron Transport Layers (ETLs).³ The structural $\text{FTO}/\text{ETL}/\text{SBI}/\text{HTLs}/\text{Au}$ combinations were thoroughly studied using a solar cell modeling program called SCAPS-1D. Before device parameters optimization, we observed in our initial

structure that the PCEs for each combination were 4.59% for spiro-OMeTAD, 4.26% for PTAA, 3.95% for P3HT, and 3.48% for PEDOT:PSS. Then, the defect density and thickness of the absorbing layer and HTLs were optimized to increase efficiency by almost twofold for Spiro-OMeTAD (8.49%), PTAA (7.27%), P3HT (7.62%), and PEDOT:PSS (6.97%) compared to their initial structures. In addition, we have optimized the efficiency of solar cells to record-breaking efficiencies of 8.49% for Spiro-OMeTAD, indicating that Ag_3BiI_6 may have use as a lead-free solar cell component in the future. Our study is relevant because it sheds light on the development and optimization of lead-free solar cells utilizing SBI, which is important for both the environment along with human health. As far as we know, no numerical simulations with experimental studies have been conducted on Ag_3BiI_6 solar cells. It is crucial to remember, nevertheless, that owing to its inherent drawbacks, the SCAPS-1D simulator might not be able to exactly replicate certain experimental effects seen in studies. In this instance, the complexity of material characteristics, interface effects, and ambient environmental variables may lead to differences between simulated and some results from experiments. According to our study, the initial optimized power conversion efficiency (PCE) closely matched the experimental reported PCE for Ag_3BiI_6 .

4.2 Experimental analysis and simulation modeling section

4.2.1 Chemical and reagents

Our experiments were conducted on fluorine-doped tin oxide (FTO) substrates. The resistivity of the FTO-coated slides was $10\ \Omega/\text{sq}$. From Sigma-Aldrich, Triton X-100, silver iodide (AgI) (99%), P-25 titanium (IV) oxide (99.7%), bismuth (III) iodide (BiI_3) (99%) and titanium (IV) isopropoxide (TTIP) (99.99%) were purchased. Kanto Chemical supplied Acetone (99.8%), HCl , Ethanol (99.5%), and 1-butanol (99%), while Nacalai Tesque supplied Dimethylsulfoxide (98%) (DMSO).

The chlorobenzene (CB) (98.0%) was purchased from the Japanese chemical company Tokyo Chemical Industry. Purified distilled water and highly purified gas N_2 were used in this experiment.

4.2.2 Ag-Bi-I thin film fabrication process

As part of the sample preparation, 2 cm x 2 cm FTO substrates were washed in distilled water, acetone, and ethanol in an ultrasonic bath for about 15 minutes, then dried by N_2 flow, followed by UV light treatment to kill ozone on the cleaned FTO. In addition to the Compact TiO_2 layer being deposited on top of the FTO substrate, the 0.5 M precursor solution was prepared by mixing 1.428 gm Titanium (IV) isopropoxide (TTIP) with 8.52 mL of ethanol, two drops of HCl, a drop of Triton X-100 and one drop of distilled water. Using spin coating, we synthesized the c- TiO_2 layer. As part of the spin coating procedure, we first spun the sample at 1000 rpm for 5 seconds, then at 3000 rpm for 30 seconds, and finally at 1000 rpm for 5 seconds. The layer was then annealed for 1 hour at 450 °C. Through spin coating, a "mesoporous TiO_2 layer" (mp- TiO_2) was deposited on top of the c- TiO_2 /FTO substrate by mixing P-25 TiO_2 powder (0.04687 g) with 1-Butanol (10 mL). Using a spin coating approach, the 0.25 M concentration of mp- TiO_2 film is deposited. The process entails spinning at 1000 rpm for 5 seconds, increasing the speed to 4000 rpm for 30 seconds, then spinning at 1000 rpm for an additional 5 seconds. To ensure good film formation and crystallinity, the films go through an annealing phase after the spin coating process, when they are heated to 500°C for an hour.

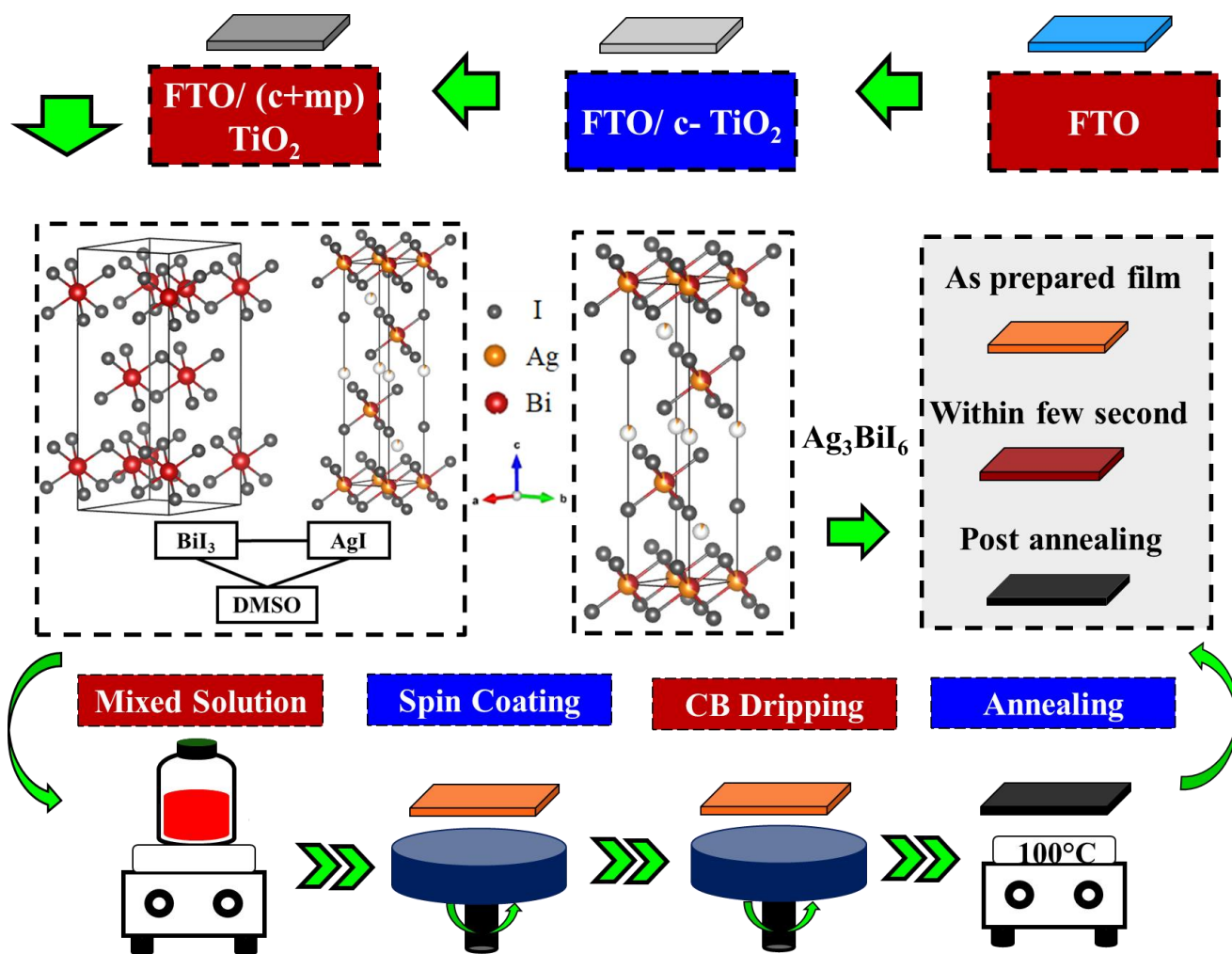


Figure 4.1 Schematic flow chart showing the procedures involved in preparing Ag_3BiI_6 films.

The process for fabricating the Ag_3BiI_6 absorbing layer over the ETL layer was obtained by dissolving 50 wt.% of AgI and BiI_3 into DMSO in accordance with the 3:1 ratio shown in **Figure 4.1**, in order to achieve the correct stoichiometry. It was necessary to mix the solution properly, which is shown in **Figure 4.1**, for 5 hours at a temperature of 75°C while the glovebox was being stirred inside the glovebox to achieve the desired result. Afterwards, the same solution was stirred again at temperatures of 90°C for one hour, before being deposited. After the Ag_3BiI_6 solution was prepared, it was spin-coated for 40 seconds at 5000 rpm on $\text{FTO}/(\text{c}+\text{mp})\text{TiO}_2$ substrates for 10 seconds before the coating was completed, and anti-solvent dripping chlorobenzene was added.

As a final step, the absorbing layer was annealed by two steps inside the glovebox, with the initial step being 75 °C for five minutes, followed by the second step, which was 100 °C for twenty minutes on a hot plate, and the final layer of the active layer was then achieved.⁴

4.2.3 Simulation modeling methodology

In the Solar Cell Capacitance Simulator in One Dimension (SCAPS-1D), electrical and optical properties of solar cells are simulated in one dimension.^{5,6} In order to calculate the performance characteristics of a solar cell, a variety of parameters are taken into account, including material properties, device structure, and operating conditions. It is used to investigate and maximize solar cell efficiency under various conditions, and it was created by Burgelman et al.'s research.⁷⁻⁹ Poisson's equation and equation of continuation are used in SCAPS 1D since they are essential to the study regarding semiconductor device physics. Poisson's equation establishes a relationship between the semiconductor device's electric voltage and charge density. Conversely, the flow of charged carriers-holes and electrons-through the apparatus is explained by the continuity equations.¹⁰⁻¹² The behavior of charge carriers in a semiconductor is described by the equations given in **Chapter 3**, namely Poisson's equation and the continuity equation.

4.2.4 Ag₃BiI₆ solar cells device's structure

The following solar cell, which has a planar structural framework and contains the FTO, ETL as (c+mp) TiO₂, Ag₃BiI₆ as an absorber, the organic HTLs, as well as gold (Au) used as a back contact, was studied using simulation techniques for the initial moments ever. **Figure 4.2** has been reformulated in order to offer a more descriptive and graphical explanation of the depicted architecture for solar cells. Firstly, the device is constructed using fluorine-doped tin oxide (FTO), which is a transparent conductive oxide (TCO). In the following, a mixed-phase titanium dioxide

film called (c+mp)TiO₂ acts as the electron transport layer (ETL). As a result of this layer, electrons can be moved more efficiently within the device, facilitating the transfer of charge. While mesoporous along with compacted TiO₂ layers have an appropriate band gap, a superior energy level, as well as stability in the environment, they may improve the efficiency of conversion inside solar cells. One of the most popular ETLs for perovskite is TiO₂ and it is the most efficient.¹³ As a crucial part of harnessing solar energy, the absorbing layer, known as Ag₃BiI₆, is crucial. The conversion of solar energy into electrical energy is initiated as a result of photons being absorbed by the absorber. Electron holes are generated by the absorber, converting photons into electrons. To enhance device performance, various organic layers are employed as hole transport layers (HTLs). Positive charges, or holes, are transported towards the electrode by these HTLs. The last component of the device is the electrode material, which is gold (Au). This substance makes it easier to collect the electrical current that is produced.

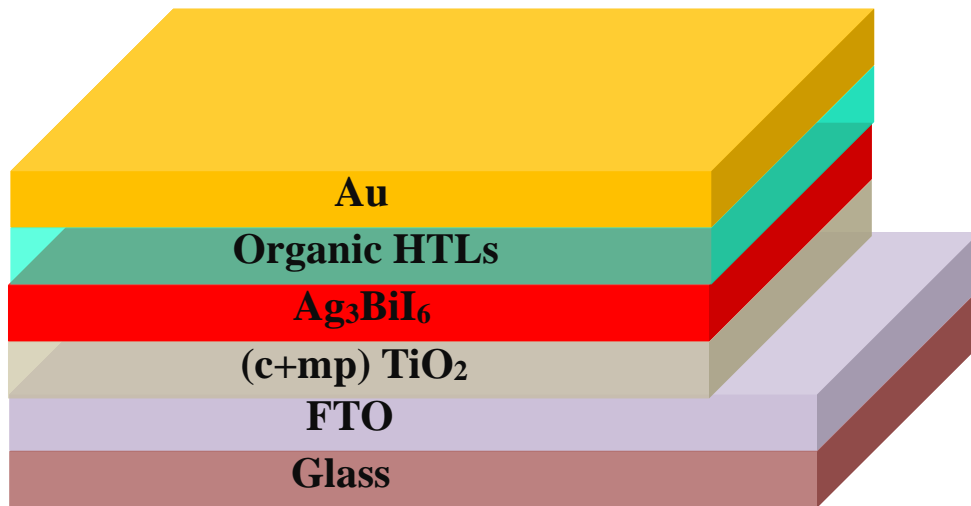


Figure 4.2 Device architecture of conventional n-i-p type of the Ag₃BiI₆ solar cell.

The modeling settings for the absorber, FTO, ETL, and several HTL layers are listed in **Table 4.1**. The capture section sizes are $1.0 \times 10^{17} \text{ cm}^2$ (electron) as well as $1.0 \times 10^{18} \text{ cm}^2$ (hole), the energetic transportation has one value, the defect level of energy has a value that is above the VB maximum, when the overall density is $1.0 \times 10^{10} \text{ cm}^{-2}$. Furthermore, all interface imperfections layer parameter values are unbiased for FTO/ETL, ETL/SBI, and SBI/HTL. Operating at room temperature, the model is run with a power density equal to 100 mW/cm^2 and an AM1.5G-simulated solar light irradiation. An absorption model based on the square root of $(h\nu - E_g)$ rule was used in the first simulation plus the optimization that followed.

Table 4.1 Numerical input parameters of the FTO, (c+mp)TiO₂, SBI, and organic HTLs.

Parameters	FTO	(c+m) TiO ₂	SBI	P3HT	PEDOT: PSS	Spiro- OMeTA D	PTAA
Thickness (nm)	525 [†]	350 [†]	1100 [†]	50	50	50	50
Band Gap (eV)	3.48 [†]	3.25 [†]	1.71 [†]	1.70	1.6	3	2.96
Electron affinity (eV)	4	4	3.90	3.5	3.4	2.2	2.3
Permittivity	9	9	6.5	3	3	3	9
DOS at CB (cm ⁻³)	2.2×10 ¹⁸	2×10 ¹⁸	1×10 ¹⁹	2×10 ²¹	2.2×10 ¹⁸	2.2×10 ¹⁸	2×10 ²¹
DOS at VB (cm ⁻³)	2.2×10 ¹⁸	1.8×10 ¹⁹	1×10 ¹⁹	2×10 ²¹	1.8×10 ¹⁹	1.8×10 ¹⁹	2×10 ²¹
Electron thermal velocity (cm.s ⁻¹)	1×10 ^{7‡}	1×10 ^{7‡}	1×10 ^{7‡}	1×10 ^{7‡}	1×10 ^{7‡}	1×10 ^{7‡}	1×10 ^{7‡}
Hole thermal velocity (cm.s ⁻¹)	1×10 ^{7‡}	1×10 ^{7‡}	1×10 ^{7‡}	1×10 ^{7‡}	1×10 ^{7‡}	1×10 ^{7‡}	1×10 ^{7‡}
Mobility of electron (cm ² .V ⁻¹ .s ⁻¹)	20	20	1	1.8×10 ⁻³	4.5×10 ⁻²	2.1×10 ⁻³	1
Mobility of hole (cm ² .V ⁻¹ .s ⁻¹)	10	10	1	1.86×10 ⁻²	4.5×10 ⁻²	2.16×10 ⁻³	40
Shallow uniform donor density, N _D (cm ⁻³)	1×10 ¹⁵	9×10 ¹⁶	0	0	0	0	0
Shallow uniform acceptor density, N _A (cm ⁻³)	0	0	1×10 ¹⁵	1×10 ^{17‡}	1×10 ^{17‡}	1×10 ^{17‡}	1×10 ^{17‡}
Density of defect (cm ⁻³)	1×10 ¹⁸	1×10 ¹⁵	1.5×10 ¹⁶	1×10 ¹⁵	1×10 ¹⁵	1×10 ¹⁵	1×10 ¹⁵
References	14	14	14,15	14	16	14	17

In the Superscript ‡: constant value; Superscript †: experimentally calculated; Shunt resistant, 100 Ω . cm²; Series resistant, 20 Ω . cm².

4.2.5 Measurements and characterizations

An X-ray Diffraction (XRD) analysis of Ag_3BiI_6 film was performed in Rigaku Smart Lab using the following scanning parameters: scanning step 0.02, target source Cu-K α . Scanning Electron Microscope (SEM) JSM 6510 Model operated at 12 kV was used to determine the surface morphology of the Ag_3BiI_6 film. A spectrophotometer model V-570 from JASCO, was used to determine the optical profiles of fresh FTO/(c+mp)TiO₂/ Ag_3BiI_6 films in reflectance and transmission modes. A highly precarious method was employed to measure the thickness of the film with the Veeco Dektak machine. A solar simulation using SCAPS-1D software was used to measure the performance of photovoltaics under conditions of AM 1.5G 1 sun.

4.3 Results and discussion

4.3.1 Section of experimental investigation

4.3.1.1 Structural and elemental properties analysis

In **Figure 4.3**, the crystal structure of the Ag_3BiI_6 film has been determined using XRD measurements in the 5°-60° ranges, which were conducted on a solution with a 50 wt.% concentration deposited over an FTO/ETL layer. The crystal structure is indicated by **Figure 4.3** five peaks, which correspond to the planes' reported reflections for the Ag_3BiI_6 trigonal phase of (003), (010), (104), (110) and (108) planes. The XRD peaks suggest that certain planes are preferentially oriented, contributing to the dominant crystallinity of the material. However, peak angles appear consistent with JCPDS card no. 00-039-0936, variations in peak intensities may show deviations in atomic orientation. In the XRD pattern, silver iodide (AgI) residual peaks appear at 22.47°, 39.14° and 46.24°. It is also possible that the presence of unreacted AgI peaks may also cause unreacted BiI_3 . As a result of the overlap between some XRD peaks of BiI_3 and

Ag_3BiI_6 , residual BiI_3 peaks were not detected in the XRD pattern.^{4,18} XRD analysis reveals two peaks at 37.75° and 54.62° associated with (c+mp) TiO_2 , at peaks 26.51° , 33.71° and 51.67° associated with FTO. As shown in **Figure 4.4**, there are six peaks observed in the XRD pattern of FTO/(c+mp) TiO_2 . There are two peaks attributed to (c+mp) TiO_2 and four peaks attributed to FTO among these peaks.

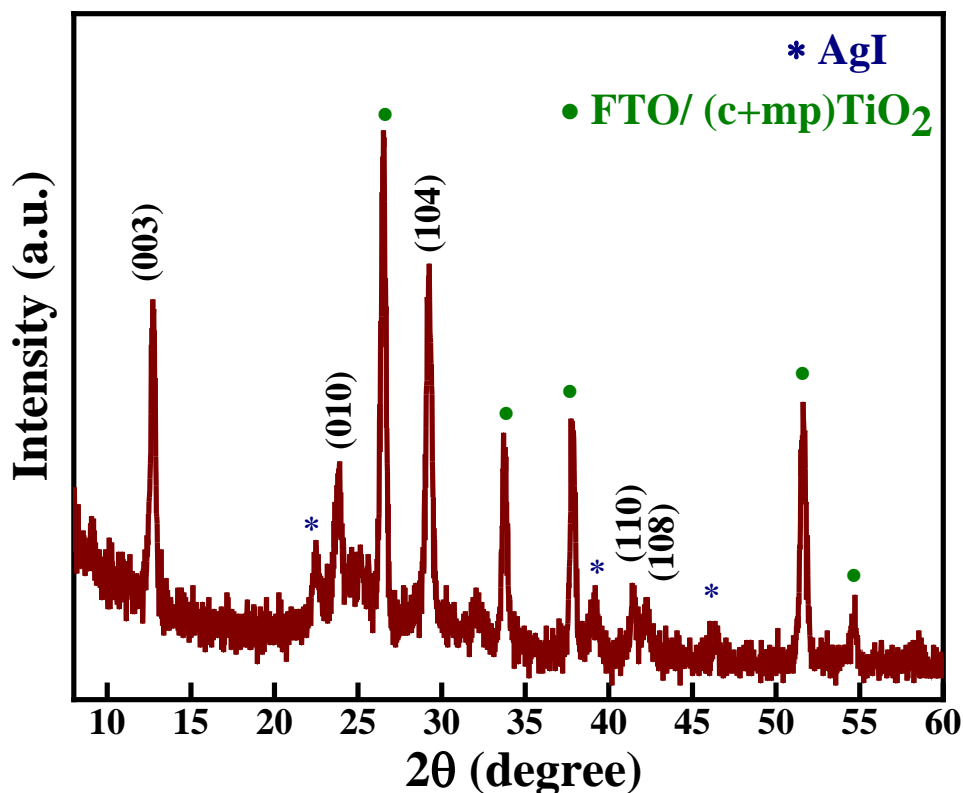


Figure 4.3 The XRD profile of 50 wt% Ag_3BiI_6 film, annealed at 100°C with CB antisolvent.

Based on the peak broadening, the average crystallite size might be calculated using the Debye-Scherrer equation, as detailed in **Chapter 3**.^{19,20} From the most intense peak, 17.11 nm is estimated to be the crystal size. A detailed XRD analysis of Ag_3BiI_6 provides an insight into the crystalline structure, confirming a trigonal phase and showing the presence of peaks for FTO, (c+mp) TiO_2 , and AgI . In order to optimize the material's properties for various applications, such as

photocatalysis, it is essential to understand these characteristics. To investigate the elemental composition of SBI films under optimal conditions, an Energy Dispersive X-ray (EDX) investigation at ambient temperature was conducted. According to **Table 4.2**, SBI consists of Ag, Bi, and I, and their respective proportions were determined from weight and atomic data. As an additional example, **Figure 4.5** shows the typical SEM image and corresponding EDS mapping images of Ag, Bi, and I for a sample annealed at 100°C. It is confirmed from the EDS profile that the constituent elements are distributed uniformly throughout the film. Moreover, the elemental composition of the film matches the nominal composition of SBI films according to the EDS spectrum.

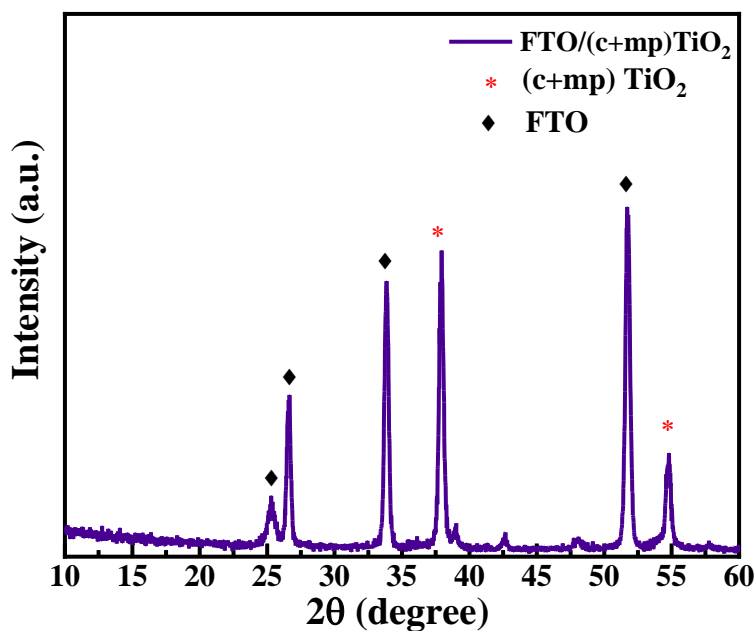


Figure 4.4 The XRD profile of FTO/(c+mp)TiO₂ thin film.

Table 4.2 The elemental analysis of Ag_3BiI_6 film measured using EDS under optimum conditions.

Element Name	Net count	ZAF	Weight Concentration%	Atom Concentration%
Ag L	841474	0.991	26.56	31.76
I L	1002922	1.060	57.43	58.37
Bi M	616707	1.112	16.00	9.87
Total			100.00	100.00

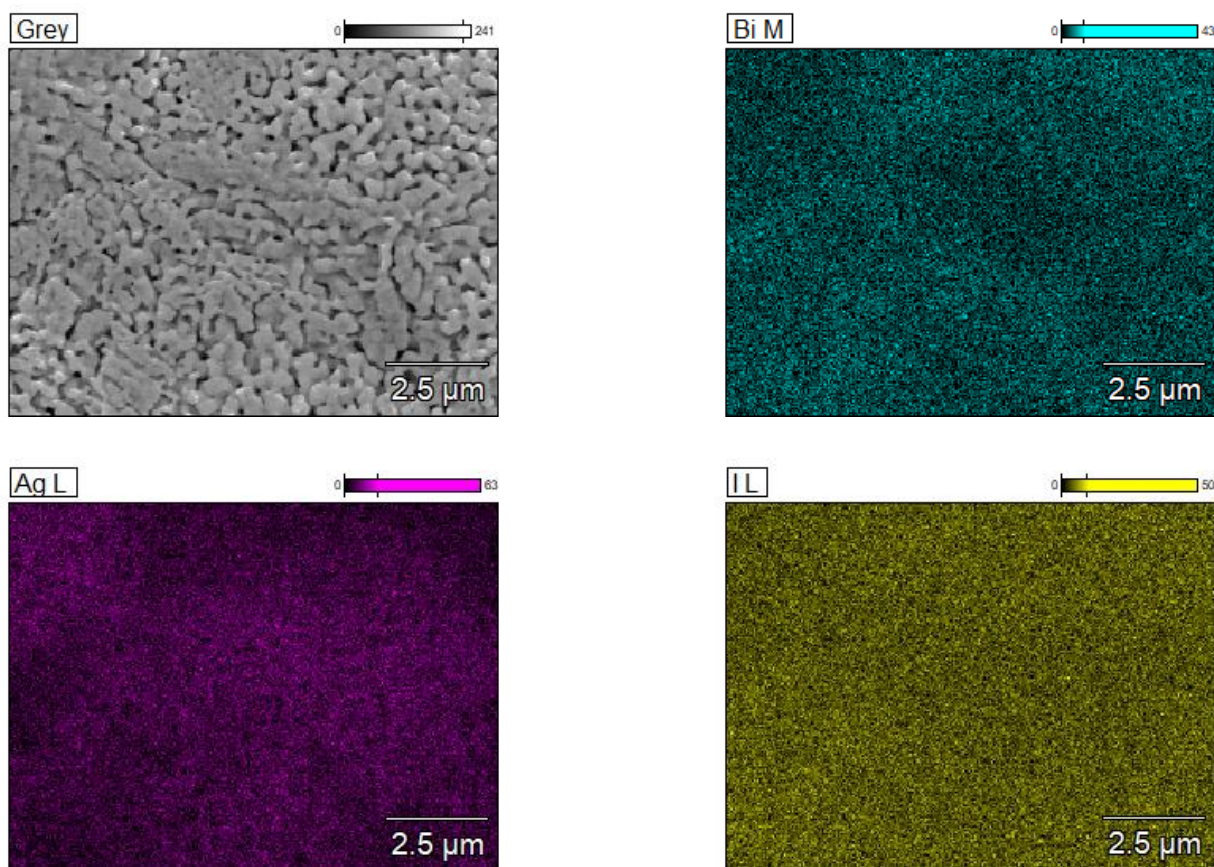


Figure 4.5 The EDS elemental distribution maps of Ag_3BiI_6 films under optimal conditions.

4.3.1.2 Morphology properties analysis

Figure 4.6 shows that the Ag_3BiI_6 coated surface displayed a good uniform distribution of grains, indicating that the coating process, under optimal conditions, resulted in a consistent distribution of grains across the surface. In solar cell applications, uniform coverage is crucial as it ensures efficient light absorption and electron transport. Although some pinholes were still observed on the surface, these minor defects can reduce the performance of solar cells as well as their reliability.²¹

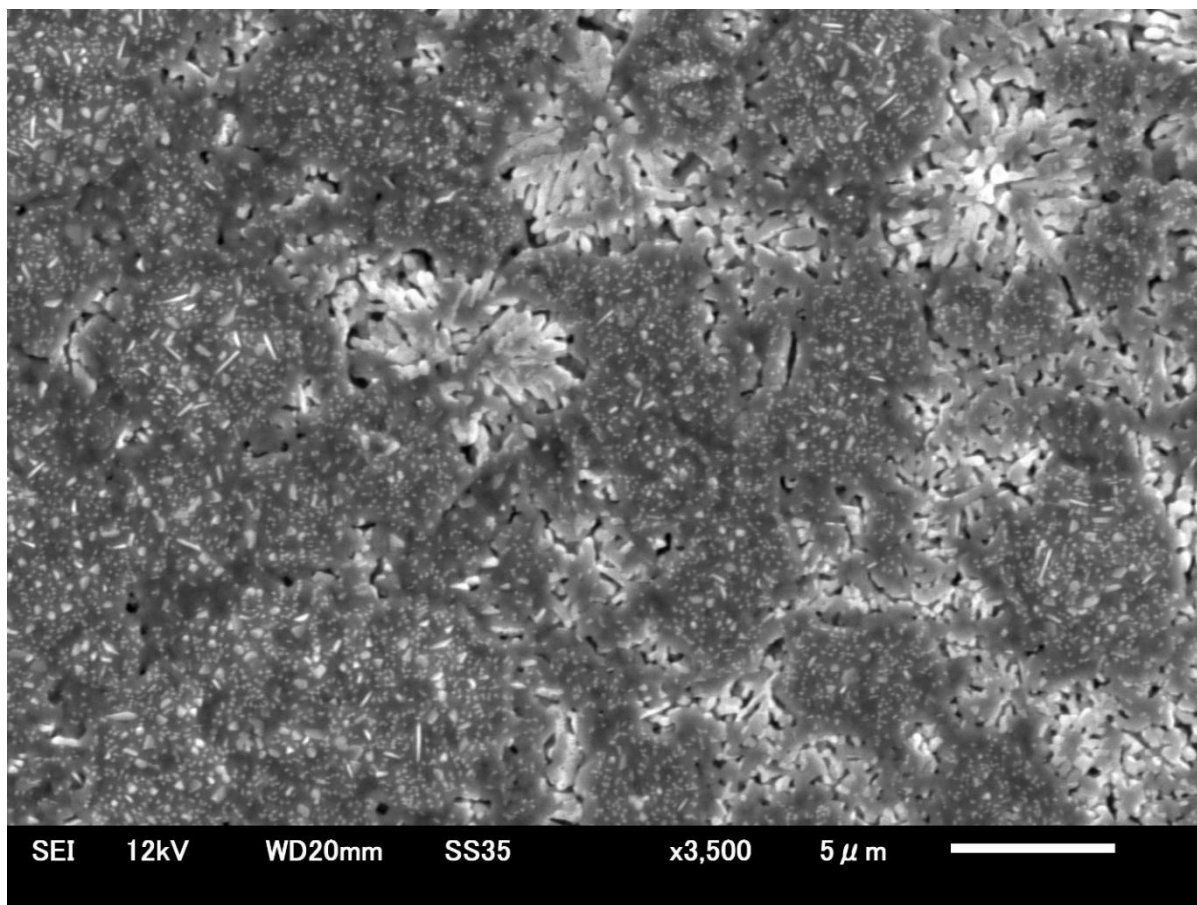


Figure 4.6 SEM image of Ag_3BiI_6 film on the FTO/ETL layer after annealing at 100°C in the presence of CB antisolvent.

4.3.1.3 Optical properties analysis

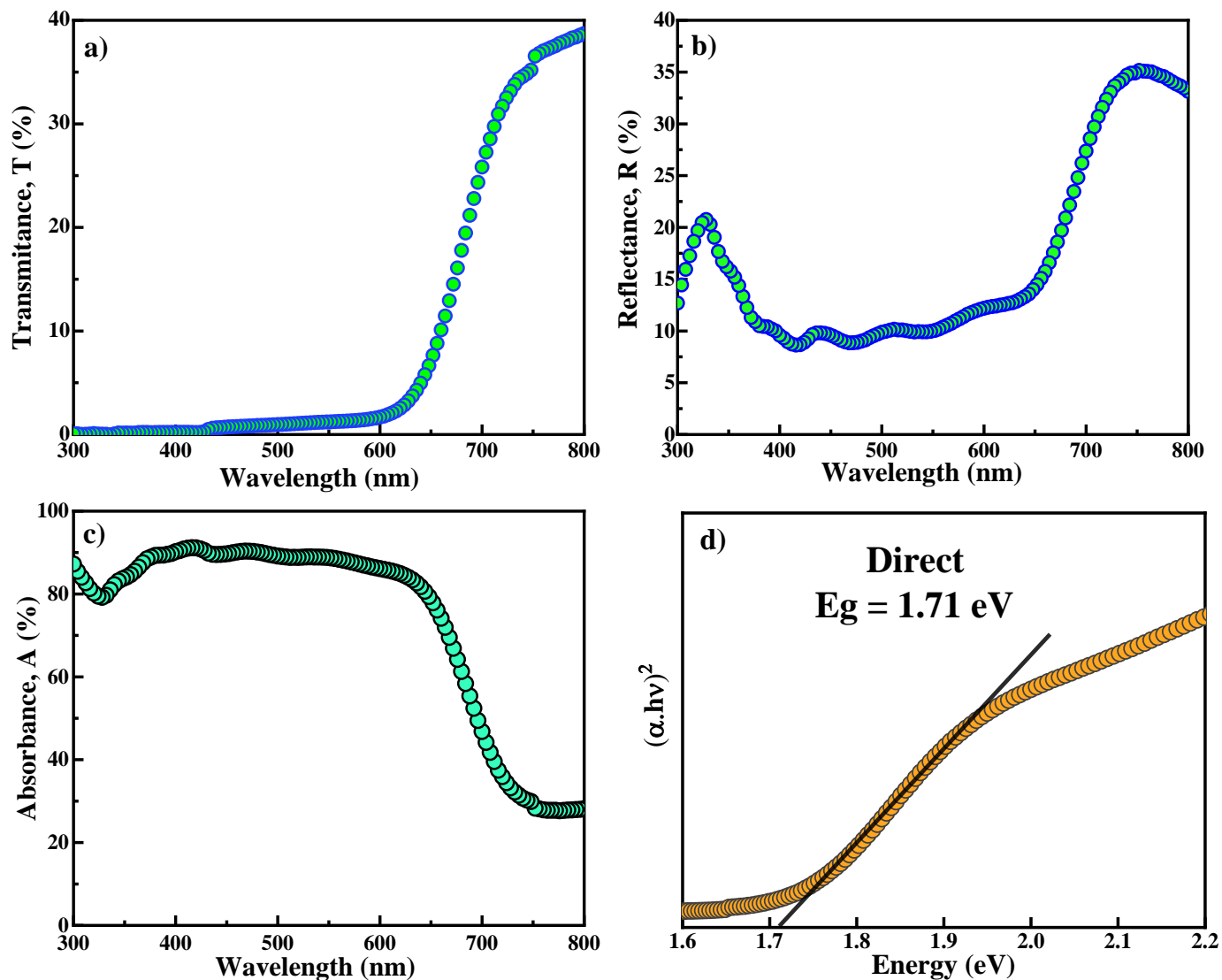


Figure 4.7 With 100°C annealing, Ag_3BiI_6 film shows a) transmittance spectrum, b) reflectance spectrum, c) absorbance spectrum, and d) Tauc plot for energy band gap calculation.

The quantity of light that can flow through solar cells is determined in large part by their transmittance spectrum. As for reflectance, this is a measurement of how much light is reflected from a surface as it crosses through it. According to **Figure 4.7**, it is evident that the Ag_3BiI_6 film exhibits low transmittances and reflectance in the human visible range, which leads to a significant

absorption within the range of visible light. As the Ag_3BiI_6 films have a thickness of 1100 nm, one of the key factors contributing to their high level of absorption is their thickness. We use the subsequent Tauc equation to get the Ag_3BiI_6 films' band gap:

$$\alpha h\nu = A(h\nu - E_g)^n \quad (1)$$

The Tauc variable is the situation in which A stays constant. The transition phase is then described by the number n .²¹ As shown in **Figure 4.7(d)**, the Ag_3BiI_6 film displays a band gap of 1.71 eV according to the Tauc equation. An in-depth look at other key optical properties, such as the extinction coefficient, refractive index, real and imaginary parts of the dielectric, loss function, and optical conductivity, is provided. It is possible to find Ag_3BiI_6 films in the fields of optics, photonics, materials science, and engineering by exploring the significance of these properties.

The Ag_3BiI_6 film's extinction coefficient (k) indicates how strongly it absorbs light at a particular wavelength. By using the equation (2), the extinction coefficient (k) was calculated,

$$k = \frac{\lambda \alpha}{4\pi} \quad (2)$$

Based on the following equation, where α represents the absorption coefficient and λ represents the wavelength.²² From **Figure 4.8(a)**, photons with shorter wavelengths have higher energies, so they absorb less light at 300 nm compared with longer wavelengths. This is suggested by the Ag_3BiI_6 films' lower extinction coefficient of 0.04. Its maximum extinction coefficient is 0.08 at 630 nm, as the photon energy decreases. The Ag_3BiI_6 film absorbs light more effectively at 630 nm than it does at shorter and longer wavelengths. The extinction coefficient decreases further as the wavelength increases to 800 nm, suggesting the Ag_3BiI_6 film absorbs less light again.

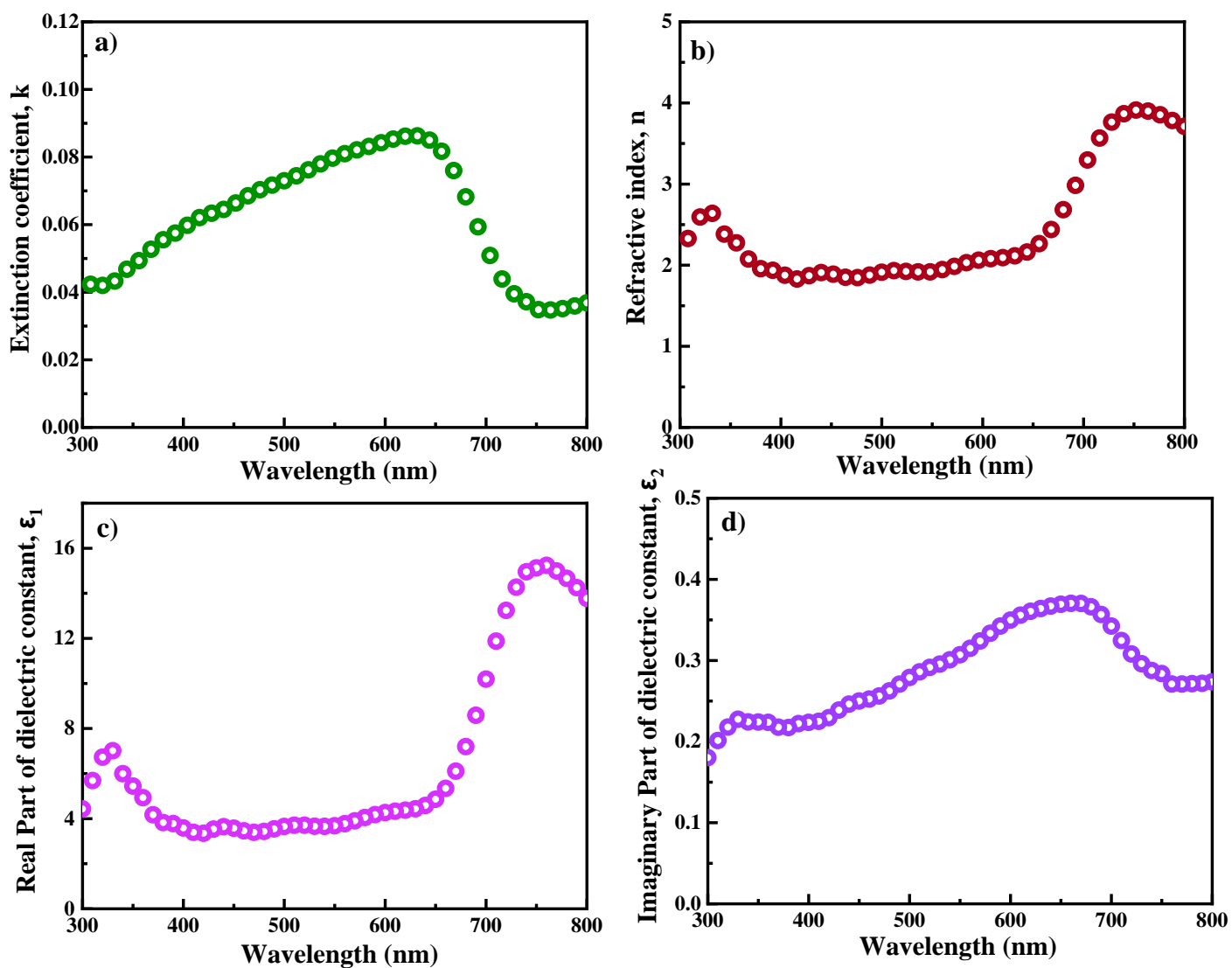


Figure 4.8 With 100°C annealing, Ag_3BiI_6 film shows a) extinction coefficient, b) refractive index, c) real part of dielectric constant, and d) imaginary part of dielectric constant with respect to wavelength.

When light passes from one medium to another, it bends according to the refractive index. By using equation (3), we can determine the refractive index of Ag_3BiI_6 film (n),²²

$$n = \frac{1+R}{1-R} + \sqrt{\frac{4R}{(1-R)^2} - k^2} \quad (3)$$

Here, R and k are the reflectance and extinction coefficients. According to **Figure 4.8(b)**, the refractive index increases very slowly after 400 nm since the energy of the photons slowly becomes sufficient to excite electrons across the bandgap. Within this range (400 -650 nm), the refractive index is therefore very slow to change. The refractive index increases, however, when photons are excited at longer wavelengths, such as 750 nm, across the bandgap.

The dielectric properties of Ag₃BiI₆ film describe how they react to an electric field. The film's ability to store electrical energy is represented by its real dielectric constant, while its imaginary dielectric constant represents its ability to dissipate electrical energy. From equations (4) and (5), we calculated the real (ϵ_r) and imaginary (ϵ_i) parts of dielectric constants,²²

$$\epsilon_r = n^2 - k^2 \quad (4)$$

$$\epsilon_i = 2nk \quad (5)$$

Based on **Figure 4.8(c)**, the real dielectric constant in the visible region is lower up to 700 nm, which correlates with a higher Ag₃BiI₆ absorption rate. **Figure 4.8(d)** illustrates the behavior of the imaginary part of the dielectric constant, which indicates the energy loss of the Ag₃BiI₆ film.

When a material is exposed to an alternating electric field, dielectric loss occurs, resulting in some of the electromagnetic energy dissipating into heat. The equation is used to determine the value of dielectric loss ($\tan\delta$) based on the ratio of ϵ_2 and ϵ_1 , and is derived from the following equation.²²

$$\tan\delta = \frac{\epsilon_2}{\epsilon_1} \quad (6)$$

Figure 4.9(a) shows the variation in dielectric loss as a function of wavelength. As shown in **Figure 4.9(a)**, its value gradually increases with wavelength, particularly in the visible region, due to a higher level of absorption, which means greater losses occur in that region.

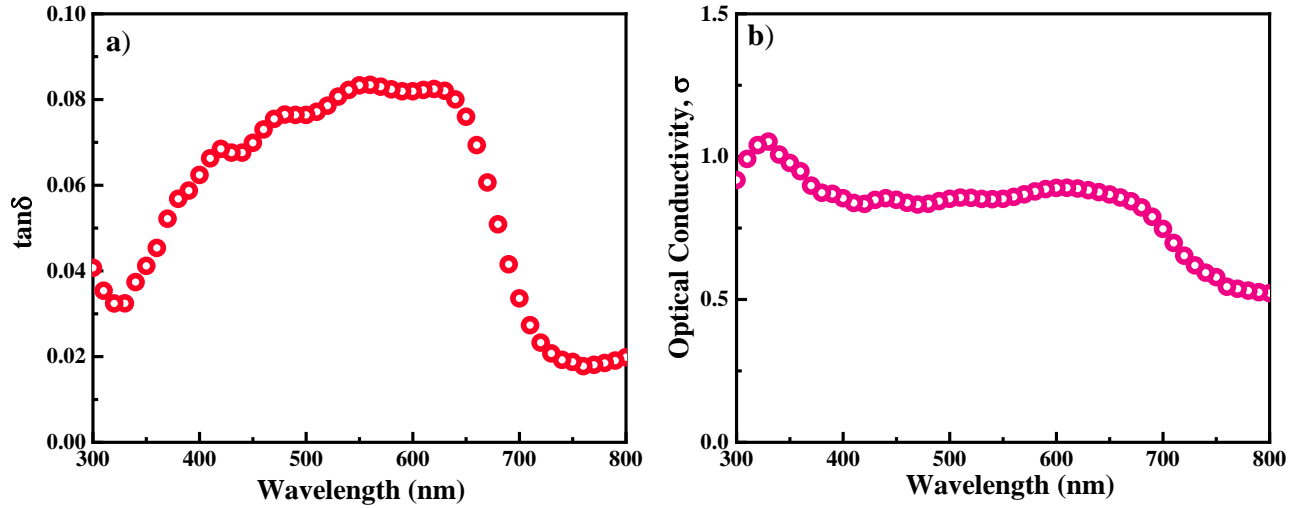


Figure 4.9 With 100°C annealing, Ag₃BiI₆ film shows a) dielectric loss and b) optical conductivity, with respect to wavelength.

An optical conductivity can be calculated using the following formula:

$$\sigma = \frac{\alpha n c}{4\pi} \quad (7)$$

In this equation, the absorption coefficient, refractive index, and light velocity are respectively represented by α , n , and c .²³ When the wavelength of the incident light increases, the energy of the incident light decreases, and fewer electrons are excited, decreasing the optical conductivity of Ag₃BiI₆.

4.3.2 Section of simulation analysis

4.3.2.1 Device band diagram with various organic HTLs

This band diagram of a photovoltaic cell may be used to see how holes and electrons are moving through the cell as well as how these energy levels are arranged. Solar cells typically consist of many layers of materials, each having a unique band arrangement and level of energy. How well these layers align determines how much voltage and current can be produced in the cell.²⁴⁻²⁶ In order to optimize solar cell efficiency, energy level alignments must be understood and managed. Several techniques may be used to achieve this, including interface optimization, band gap tailoring of the absorbent layer, and the use of appropriate HTL along with ETL materials.²⁷⁻³⁰

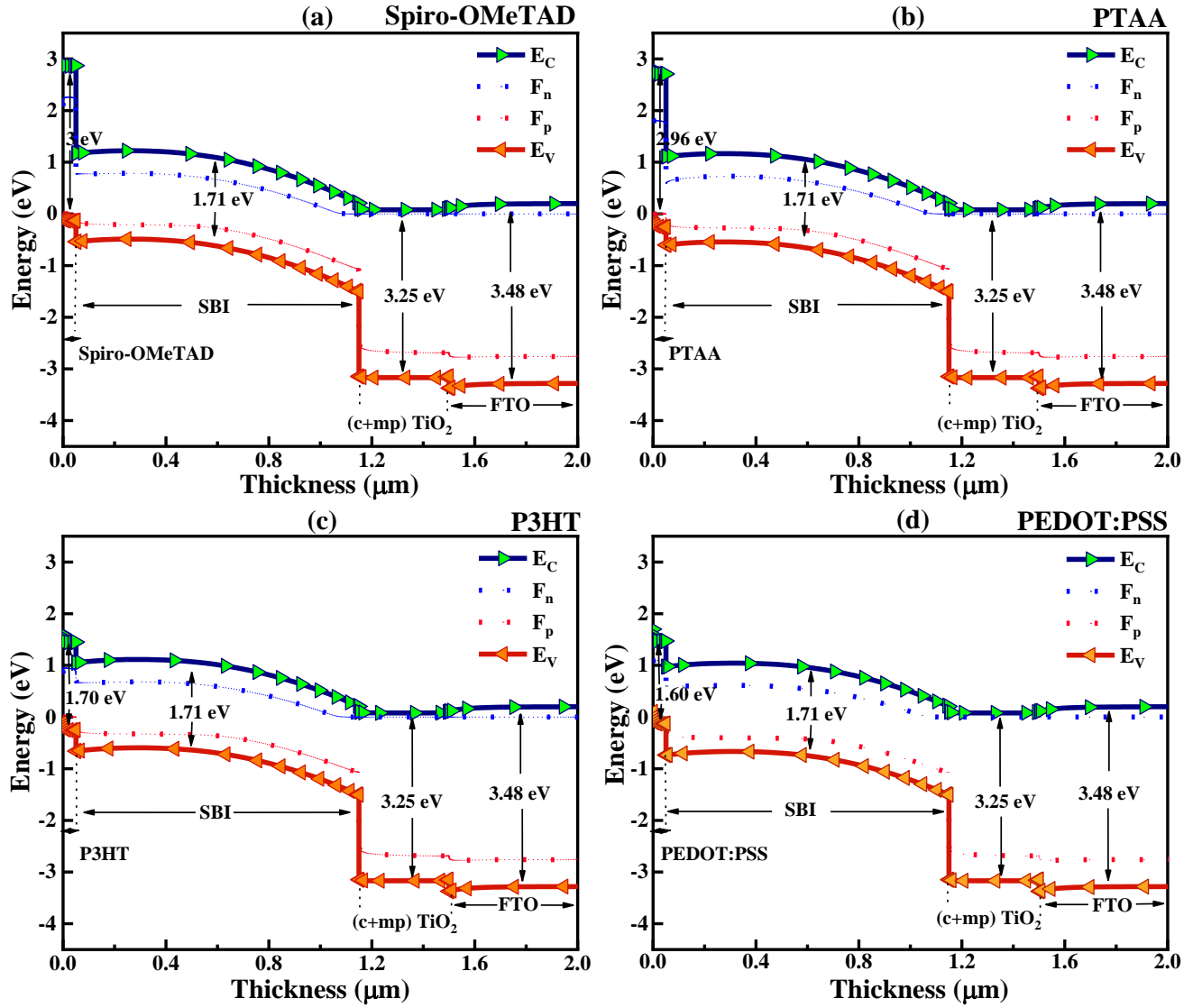


Figure 4.10 The Energy band diagram for four of SBI's solar cell devices (a) Spiro-OMeTAD, (b) PTAA, (c) P3HT, and (d) PEDOT:PSS.

In **Figure 4.10(a-d)** displays a set of band spectrum alignment diagrams for the SBI absorber alongside quasi-Fermi electron as well as hole levels. The diagrams are displayed as F_n and F_p , representing the conduction band minima as well as valence band maxima for the E_C and E_V , correspondingly. These four architectures all have the same three layers: FTO serves as a substrate, (c+mp) TiO_2 serves as the ETL layer, and SBI functions as an absorber. The favorable slope in the

band energy alignment has been achieved by using high band gap hole transport layers (HTLs), allowing for efficient carrier transport. As shown in **Figure 4.10**, spiro-OMeTAD and PTAA demonstrated the best energy alignment among the organic HTL options tested, outperforming P3HT and PEDOT:PSS. Accordingly, spiro-OMeTAD and PTAA provide better carrier pooling and transportation in the device than other HTLs. As shown in **Figure 4.10**, the concave upward shape of the band diagram is mainly due to acceptor density and defects inside the absorbing layer, which lead to strong electric field and localized states affecting energy distribution. By reducing defects at every layer and interface, this band bending can be flattened, leading to more efficient charge carriers and improved device performance. The I-V characteristics of the device are greatly impacted by the band gap as well as the band alignment of the HTLs, as seen by the built-in voltages displayed in **Figure 4.10**.

4.3.2.2 Variations of organic HTL in J-V and QE

Solar cells are evaluated, characterized, and optimized using J-V analysis, which allows researchers and manufacturers to improve the design, manufacturing process, and overall performance of solar cells. For photovoltaic cells, J-V evaluation is essential because it provides details on the electrical features of the cell, such as power conversion efficiency (PCE), fill factor (FF), voltage in the open circuit (V_{OC}), and short-circuit density of current (J_{SC}).³¹⁻³⁴ These are essential in figuring out how well the solar cell works. The efficiency of the Ag_3BiI_6 based PV was maximized by the employment of several organic HTLs with (c+mp)TiO₂ as the ETL and Au used as a back contact. **Table 4.1** shows the input parameters obtained from experimental characterization, in addition to data sourced from published journals. Some data points were held constant throughout the analysis, to ensure consistency.

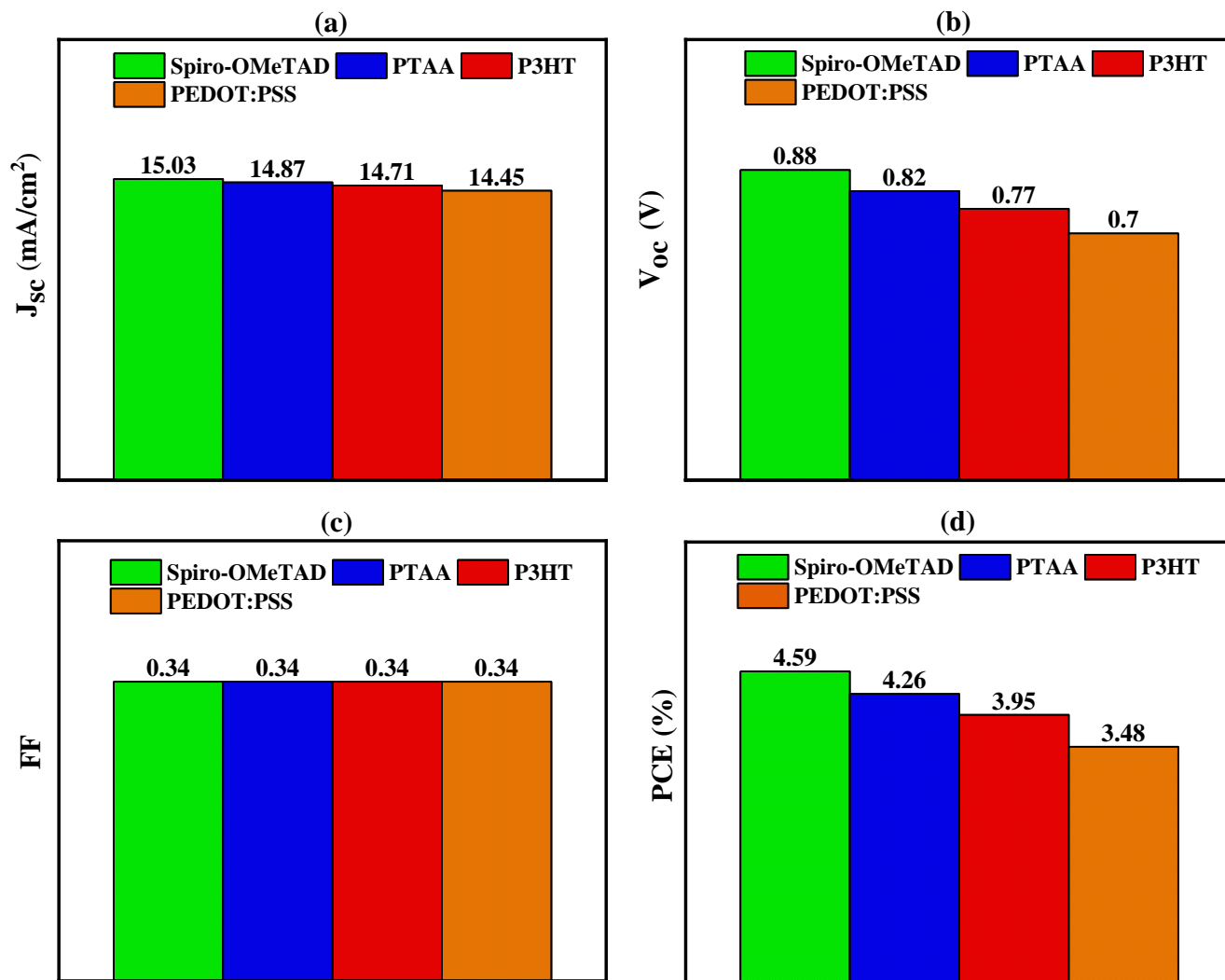


Figure 4.11 The PV devices optimized parameters e.g., the V_{oc} , J_{sc} , FF, and PCE, for FTO/(c+mp)TiO₂/Ag₃BiI₆/HTLs/Au structures with four HTLs such as (a) Spiro-OMeTAD, (b) PTAA, (c) P3HT, and (d) PEDOT:PSS.

As shown in **Figure 4.11**, Spiro-OMeTAD performed the best among all the HTLs when the parameters of each HTL were compared individually, at the initial optimization. As a result of its V_{oc} of 0.88 V, it was able to generate a higher voltage. Additionally, Spiro-OMeTAD demonstrated the highest J_{sc} of 15.03 mA/cm^2 , demonstrating its capability to generate a higher

current under short-circuit conditions. A further indicator of Spiro-OMeTAD's superior ability to convert incident light into electrical energy is its high PCE of 4.59%. Also, the PTAA showed good performance, with slightly lower values for V_{OC} , J_{SC} , and PCE. In contrast, P3HT and PEDOT:PSS showed relatively lower values for these parameters when compared to Spiro-OMeTAD and PTAA. According to the results, each HTL showed a similar fill factor (FF) of 0.34, which indicates that the efficiency with which photogenerated current was utilized was comparable. It has been found that Spiro-OMeTAD has a suitable band energy alignment with the ETL and Ag_3BiI_6 layer, enabling efficient charge extraction. The plotting of the efficacy J-V curve of various combinations, as illustrated in **Figure 4.12(a)**, made it evident that the first one of HTL is appropriate. **Figure 4.12(a)** shows a continuously decreasing current-density curve that can be attributed to changing fill factors as well as low parallel resistance and high series resistance in solar cell devices.

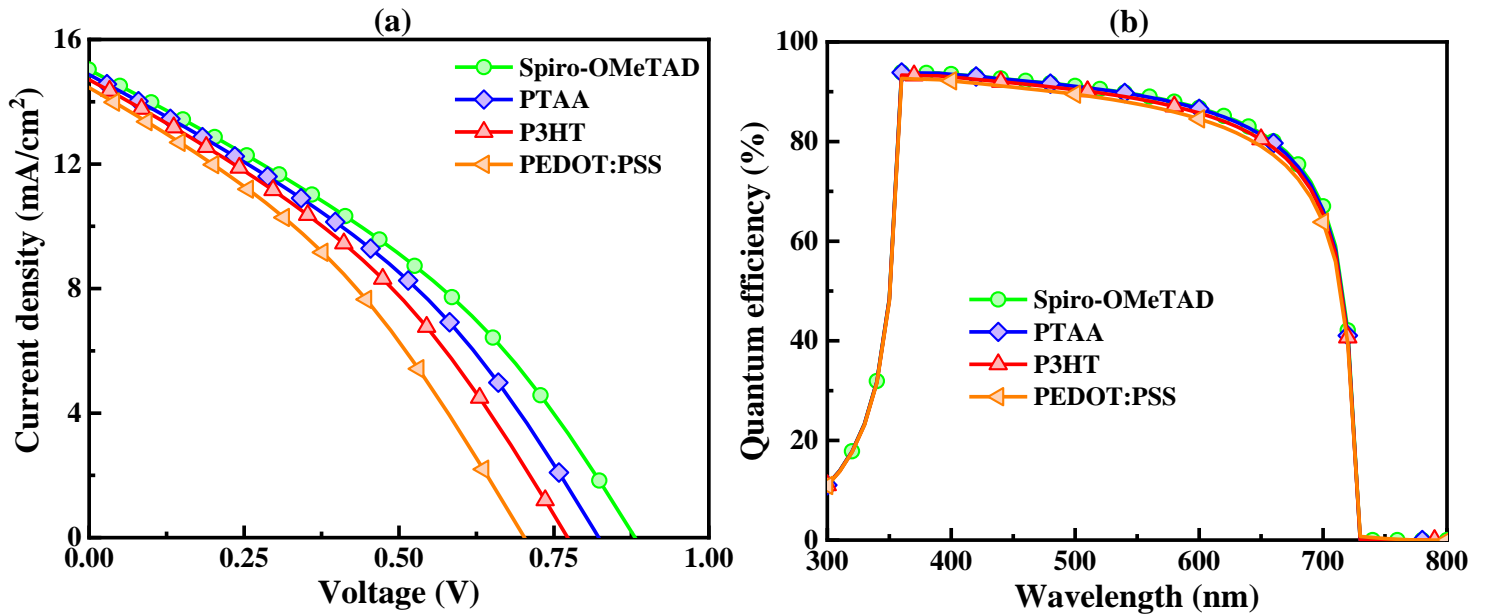


Figure 4.12 (a) J-V and (b) QE effects on Ag_3BiI_6 solar cells with different HTLs.

This quantum efficiency study has a significant impact on solar cells because it helps us to understand how light is absorbed, to identify mechanisms responsible for loss of energy, to evaluate material performance, to guide the design of devices, to monitor their degradation. It makes it possible to pinpoint regions in need of development and get a deeper comprehension of the processes behind cell energy loss. According to **Figure 4.12(b)**, the QE has been analyzed with respect to wavelengths between 300 and 800 nm. Starting at 300 nm, the quantum efficiency has been increasing rapidly, with an increase of over 90% in the 350 nm wavelength range afterward. As the value of each active material reduced, it eventually reached zero at around 725 nm when it reached the edge of the spectrum. According to **Figure 4.12(b)**, the QE decreases as the wavelength of light increases. As a result of this fact, photons of longer wavelengths carry lower energy, making it more likely for electron-hole pairs to recombine before they can be collected, resulting in a smaller quantum efficiency. As a result, a longer wavelength of light results in a smaller quantum efficiency.

4.3.2.3 Analysis of generation and recombination rates

Solar cells' efficiency and performance are greatly affected by their generation and recombination rates. If a solar cell is exposed to sunlight, it will create electron-hole pairs at a rate that can be referred to as the generation rate. In contrast to the electron-hole pair, the recombination rate describes the rate at which it is recombined in order to lose its ability to contribute to electrical currents. In order to optimize the efficiency and overall performance of solar cells, it is essential to understand and analyze their generation and recombination rates. The analysis of these rates will allow us to identify ways of minimizing recombination and enhancing generation, enabling us to produce more efficient solar cells that will be able to generate higher amounts of electricity from sunlight by reducing recombination and increasing generation.

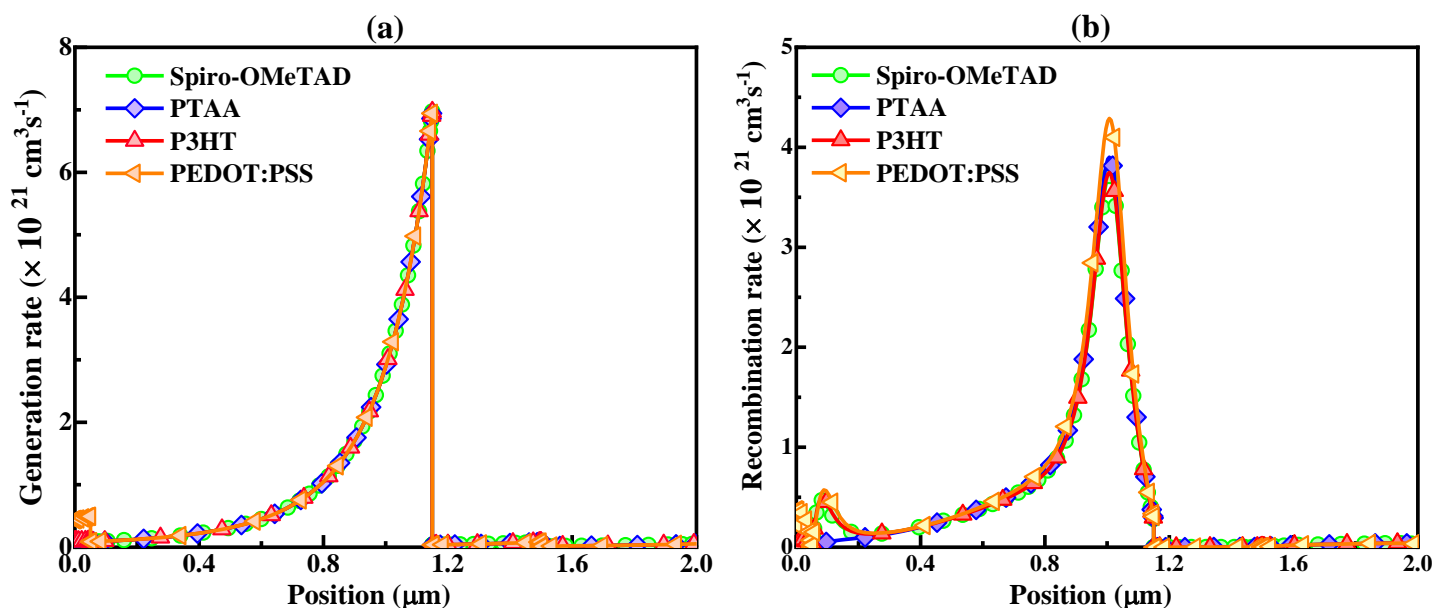


Figure 4.13 SBI solar cells with different organic HTLs for (a) generation and (b) recombination rates.

At a depth of 0.0–2.0 μm, the carrier production and recombination rates for four PSCs based on SBI are shown in **Figure 4.13(a, b)** with the other input parameters remaining the same. The findings indicate that the largest generation rate was recorded out of all the devices under study, with generation rates peaking between 0.9 and 1.1 μm. It was found that photons passing through (c+mp)TiO₂ into the SBI layer generated the highest rates of generation, specifically between 0.9 and 1.1 μm. All organic HTLs were nearly generating at the same rate at this point. Compared to other locations, this location absorbs more light, resulting in a greater production of electrons than other locations. The incoming photon flux $N_{\text{phot}}(\lambda, x)$ is used by SCAPS-1D to calculate the number of electron-hole pairs that contribute to $G(x)$. The value of $G(x)$ for each spectral area and location is then determined by the following equation:

$$G(\lambda, x) = \alpha(\lambda, x) \times N_{\text{phot}}(\lambda, x) \quad (14)$$

This recombination rate, on the contrary hand, eliminates the created electron-hole pairs thus preventing them from contributing to the photocurrent. It is the reverse of the creation rate. PSC recombination rate is dependent on charge carrier lifespan along with density. The amplification of the recombination of electrons and holes is caused by both interfaces and states of defect in the absorbers layer. PEDOT:PSS showed the largest recombination peak among all the HTLs under study, with optimal recombination rates falling between 0.9 and 1.1 μm . The majority of the energy levels that are produced in the valence-conduction band are responsible for the recombination losses. Grain boundaries and deficiencies that arise during the construction of junctions and structures may cause an uneven distribution of recombination rates in PSCs.

4.3.2.4 Effect of C-f and Nyquist plots

In solar cells, capacitance plays a crucial role in the movement and combination of charges within the device. It is crucial to understand the relationship between capacitance and frequency (C-f analysis) when it comes to analyzing the dynamic behavior, performance, and optimization of solar cells. The electrical characteristics of solar cells can be studied with C-f analysis, which provides information about both frequency and capacitance. By using this information, we can study diffusion, capturing, and carrier recombination as charge transport mechanisms. According to this study of SBI solar cells with different organic hole transport layers (HTLs), the capacitance (C) remains relatively constant at lower frequencies and exhibits higher values at lower frequencies. **Figure 4.14** illustrates this trend, where the capacitance decreases with an increase in frequency up to 1×10^7 Hz. Capacitance starts to shift from the positive side of the region to the negative side at this point. Minority carriers increase rapidly as the signal frequency rises over 10^6 Hz. Recombination rate at the junction exhibiting the highest capacitance-inducing value rises as a result of this process.

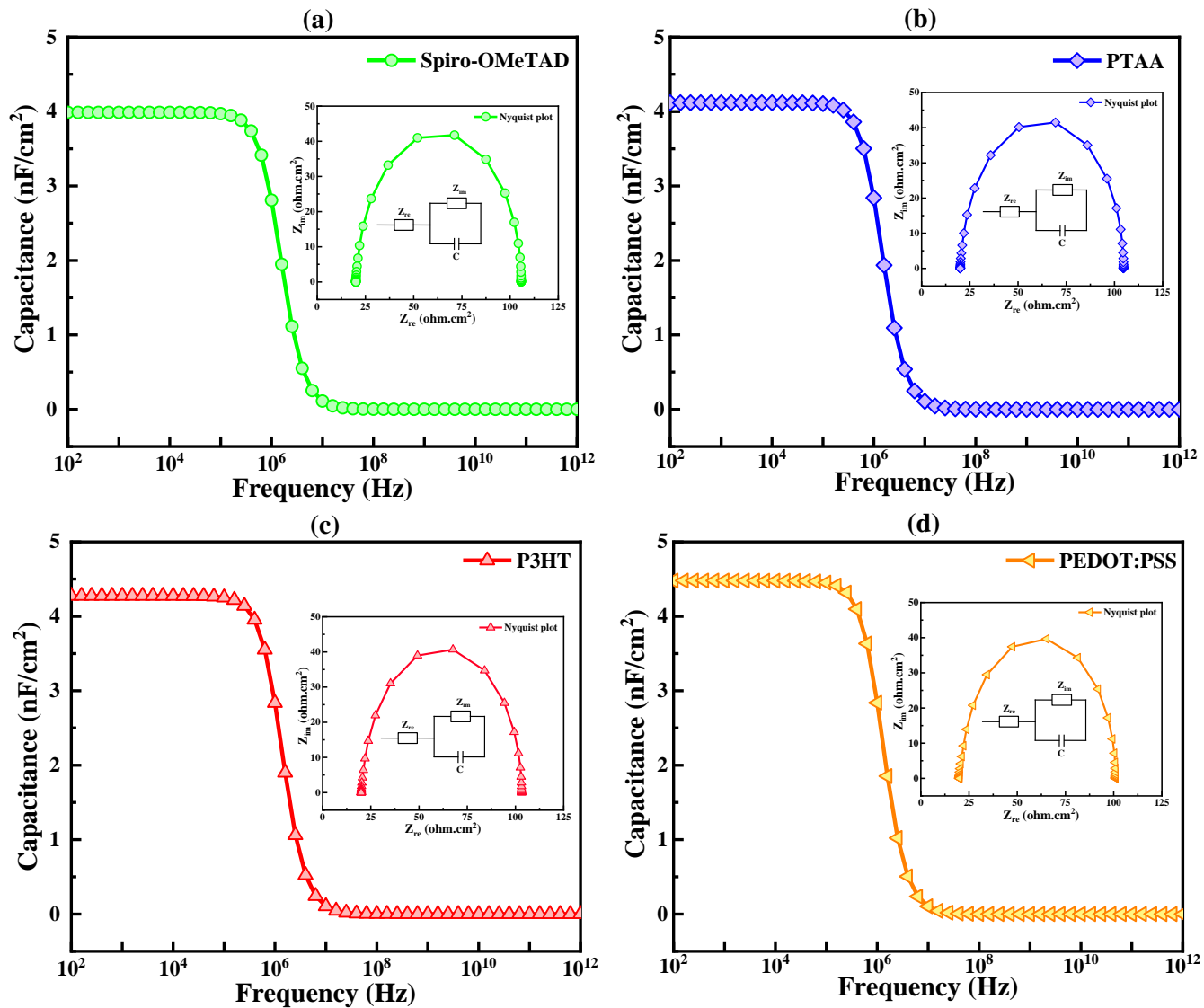


Figure 4.14 Curves of C - f with Nyquist plots of SBI absorb layers.

Figure 4.14 displays the impedance using a solar cell arrangement via the use of Nyquist plots. A semicircular arc is formed in the complex plane by plotting the real and imaginary components of the impedance on the vertical and horizontal axes, correspondingly. The transfer of charge along with recombination mechanisms that occur inside cells may be studied with the aid of the Nyquist diagrams. Together with the dominant frequency, the form shown in the Nyquist plot may provide details about the different capacitive and resistive characteristics of the solar cell. Utilizing this

data will help to enhance solar cell efficiency as well as design. **Figure 4.14**'s semicircle Nyquist diagram makes it clear that the semicircle's diameters for organic HTLs are almost similar with low values, indicating a minimum photovoltaic resistance. The low angle of the semicircle suggests that the solar cell has a relatively little capacity. It is plausible that low capacitance and low resistance are the result of poor doping concentration or fast recombination. Each of these elements may have a role in the decline in solar cell efficiency.

4.3.2.5 Effect of total defect density and thickness of SBI

Our analysis of the relationship between total defect density and the thickness of the absorbing layer can help us identify which thickness is optimal for minimizing defects and maximizing efficiency. Defects in the absorbing layer can affect charge carriers by hindering their movement and reducing the overall efficiency. On the other hand, the thickness of the absorbing layer affects both sunlight absorption and charge carrier generation. Proper tuning of the absorbers thickness and total defect density impacts the functionality and efficacy of the photovoltaic cells. The photons are absorbed by the outermost layer of the absorber to produce charge carriers, **Figures 4.15-4.18** indicate the computed contour maps for V_{OC} , J_{SC} , FF, and PCE of SBI-based photovoltaic cells using various total defect densities of SBI within 1×10^{12} to $1 \times 10^{18} \text{ cm}^{-3}$ considering the thickness of SBI layer in the 500 to 2000 nm range with different HTLs.

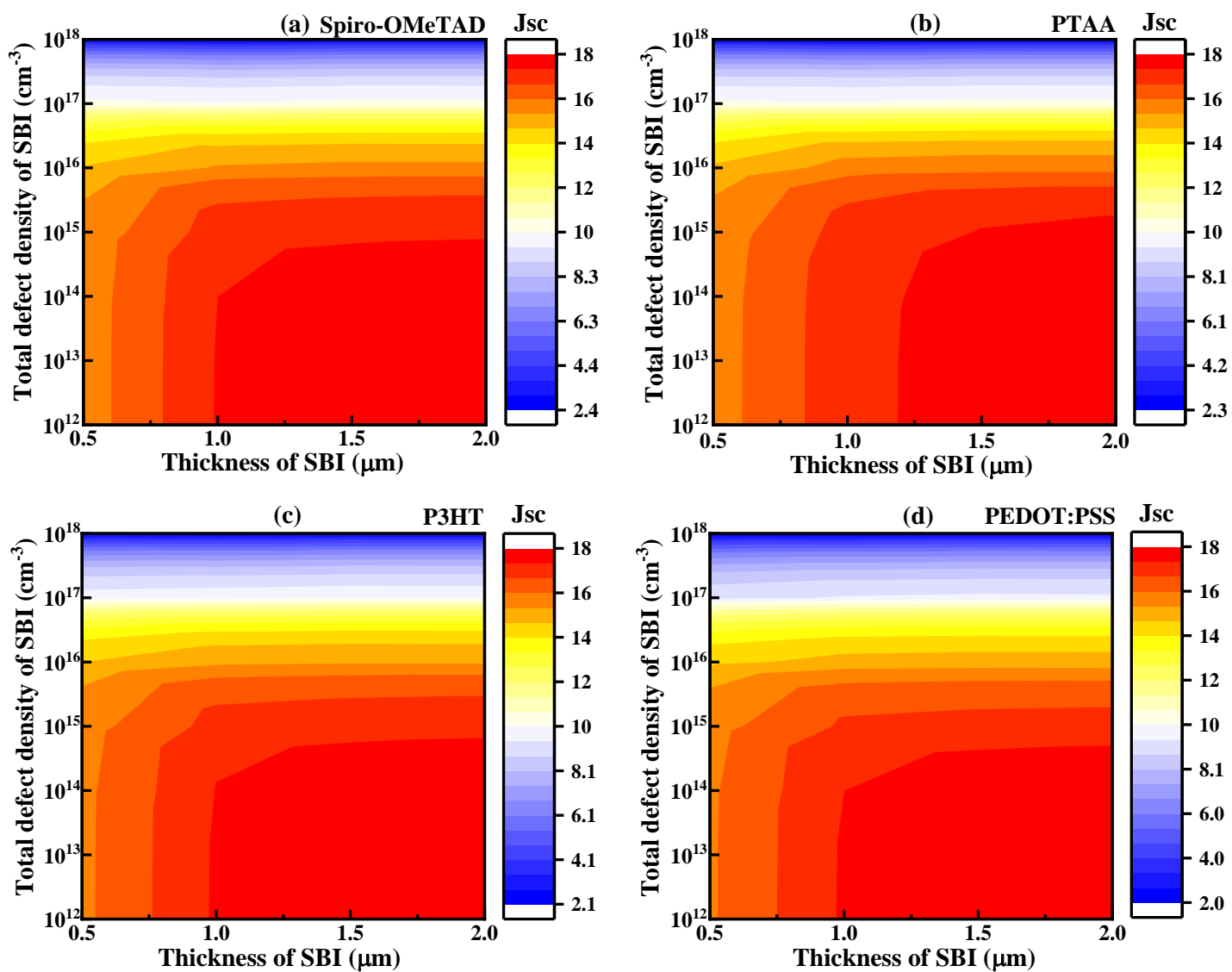


Figure 4.15 Contour mapping of J_{sc} relative to total defect density and thickness of the SBI, keeping the fixed ETL and HTLs.

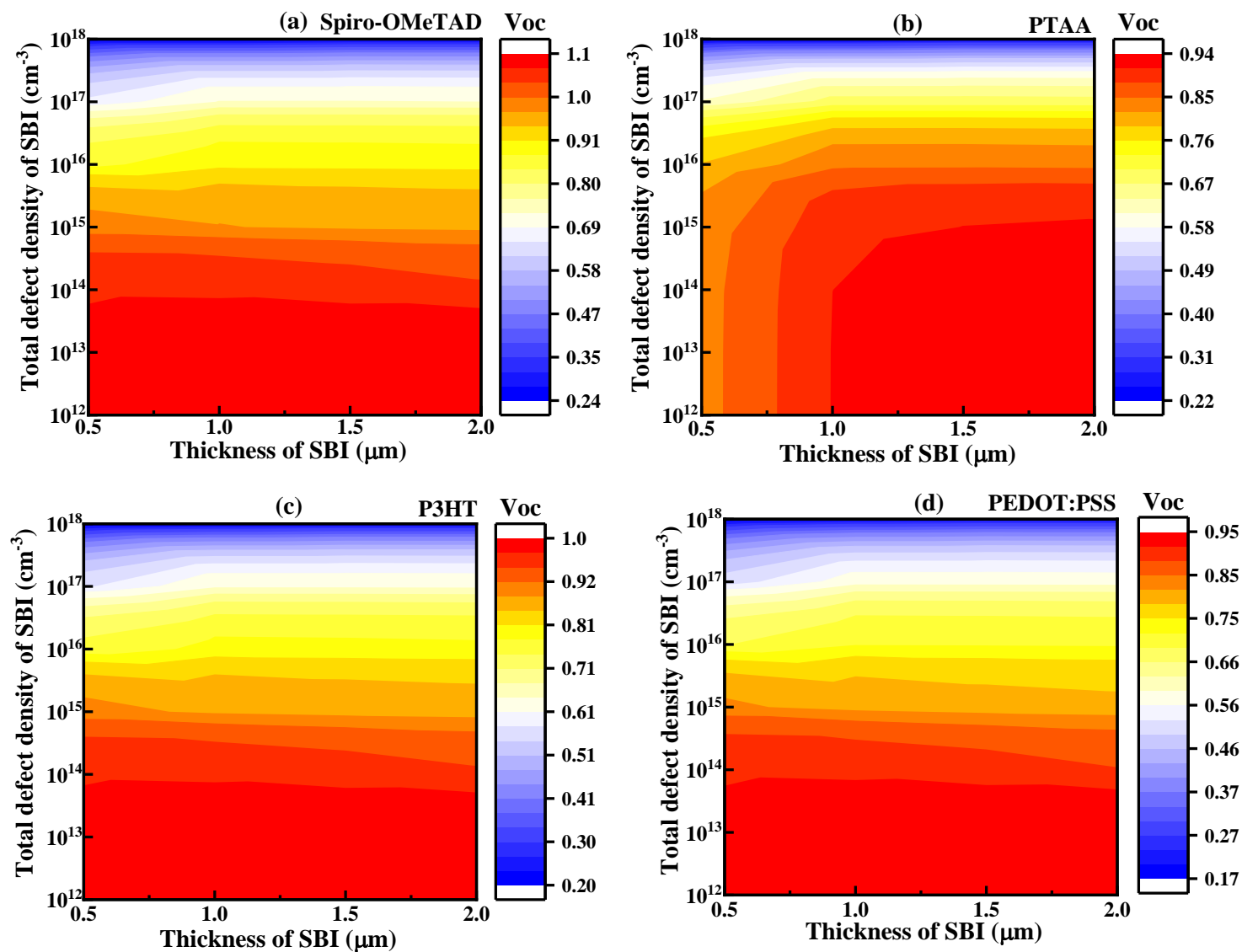


Figure 4.16 Contour mapping of V_{oc} relative to total defect density and thickness of the SBI, keeping the fixed ETL and HTLs.

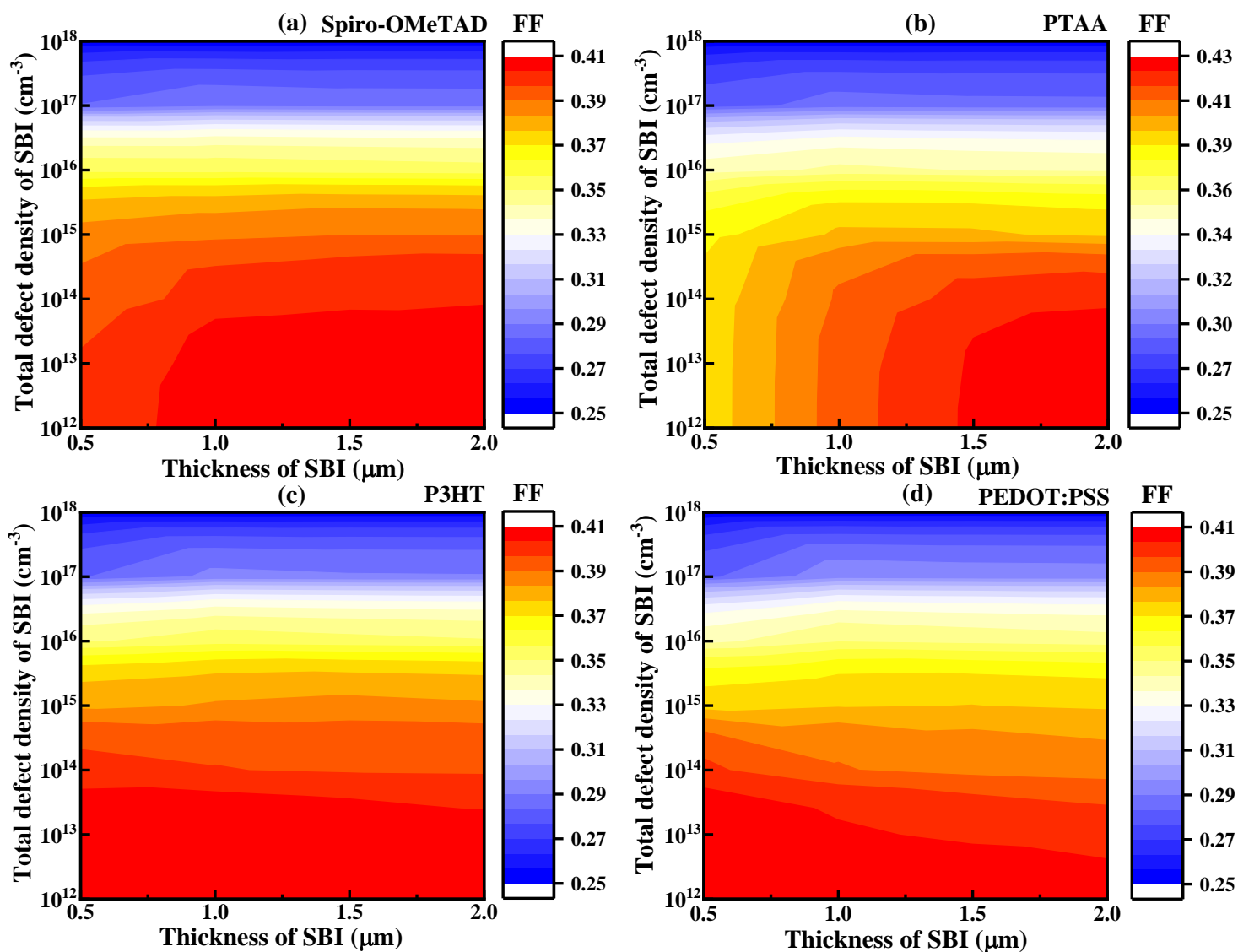


Figure 4.17 Contour mapping of FF relative to total defect density and thickness of the SBI, keeping the fixed ETL and HTLs.

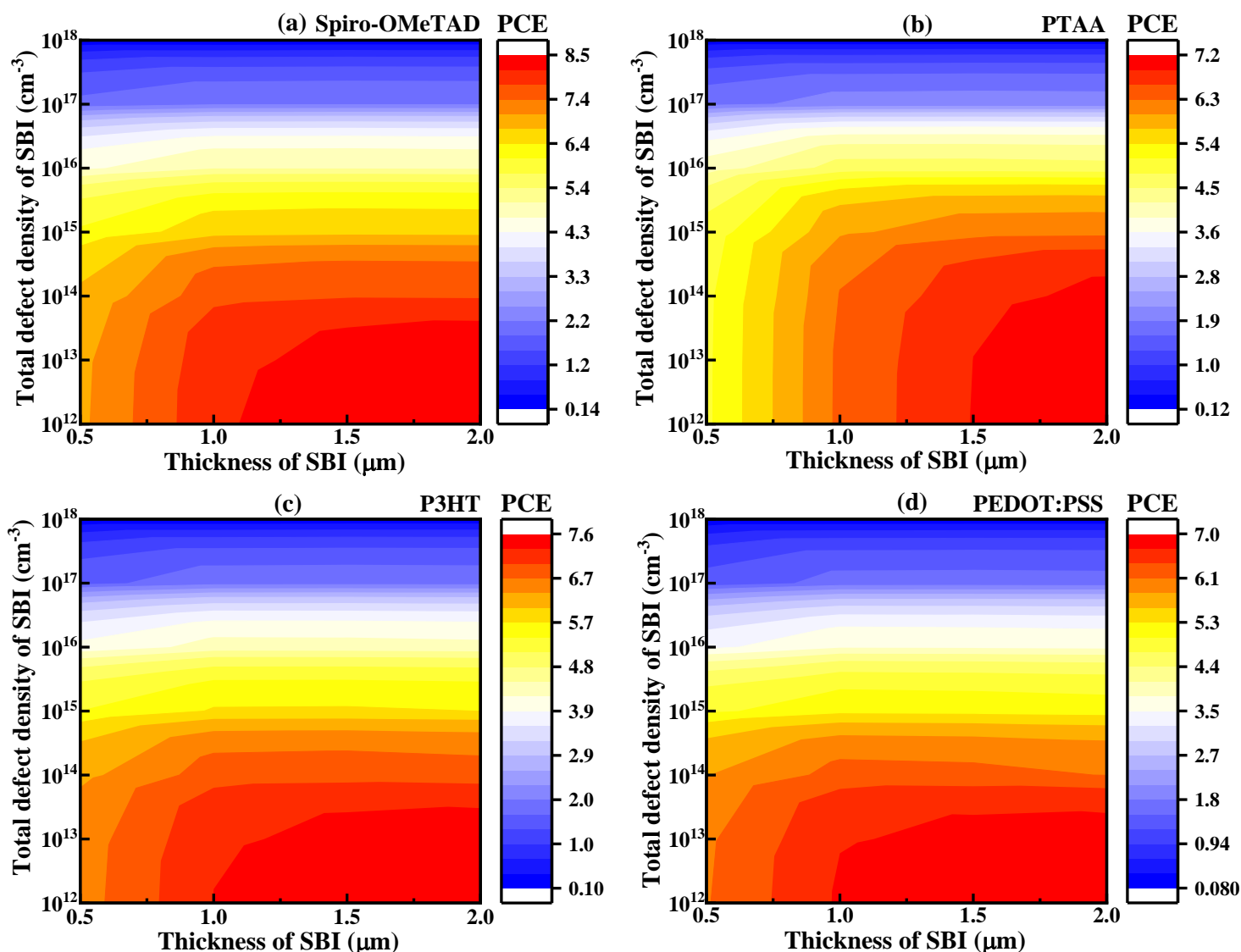


Figure 4.18 Contour mapping of PCE relative to total defect density and thickness of the SBI, keeping the fixed ETL and HTLs.

According to **Figure 4.15** and **Figure 4.18**, with the increased J_{sc} , the efficiency of the solar cell will be simultaneously increased. The J_{sc} of the device with Spiro-OMeTAD (**Figure 4.15(a)**) reached a maximum value of around 18 mA cm^{-2} when the total density of defect was less than or equal to $1 \times 10^{15} \text{ cm}^{-3}$ and the absorber thickness ranged from 1500 to 2000 nm. In this HTL, the J_{sc} value remains almost constant if the total defect density is less than $1 \times 10^{16} \text{ cm}^{-3}$ and the SBI

thickness is higher than 1000 nm. But the J_{sc} is reduced when the total density of defects goes beyond that limit. For PTAA at **Figure 4.15(b)**, when SBI thickness was higher than or equal 1000 nm and total defect density almost less than $1 \times 10^{16} \text{ cm}^{-3}$, J_{sc} value remains constant. As shown in **Figure 4.15(c, d)** for P3HT and PEDOT:PSS, similar behavior is observed for J_{sc} . The maximum value J_{sc} of PTAA, P3HT and PEDOT:PSS are found 18 mA cm^{-2} for each component when total defect density value is $1 \times 10^{12} \text{ cm}^{-3}$. When the absorbing layer thickness of the solar cell is greater than 1000 nm, the total defect density is lower, and J_{sc} is higher. As a result of low defect density, charge carriers can move freely, thus increasing performance. The easier it is for charge carriers to move in solar cells with a lower defect density and thicker absorbing layers, the higher the J_{sc} and PCE. **Figure 4.16** illustrates how altering the absorption layer's thickness as well as HTLs impacts the V_{oc} properties of SBI solar cells. When compared to V_{oc} , the J_{sc} is comparatively low. This may be the result of flaws, a wider band gap, or a faster rate of recombination. As shown in **Figure 4.16(a)**, when the absorber thickness was within 500 to 2000 nm and the total density of defects was less than or equal $1 \times 10^{14} \text{ cm}^{-3}$, the V_{oc} in the device with Spiro-OMeTAD remained constant. The V_{oc} deteriorated when the total density of defects surpassed $> 1 \times 10^{15} \text{ cm}^{-3}$. A maximum V_{oc} of 1.1 V was observed $1 \times 10^{12} \text{ cm}^{-3}$ of total defect density in case of Spiro-OMeTAD. On the other hand, the maximum voltage of 0.94 V was reached in the device for PTAA HTLs' when total defect density is around $1 \times 10^{12} \text{ cm}^{-3}$ and absorber thickness 1000 nm as shown in **Figure 4.16(b)**. The V_{oc} decreased when the total defect density surpassed $> 1 \times 10^{16} \text{ cm}^{-3}$ and the absorber thickness below 1000 nm. In case of P3HT (**Figure 4.16(c)**) when the total defect density was below $1 \times 10^{15} \text{ cm}^{-3}$ and over 1000 nm absorber thickness V_{oc} remained constant. The maximum value 1.00 V can be found at total defect density $1 \times 10^{12} \text{ cm}^{-3}$ and absorber thickness over 1000 nm. Finally, PEDOT:PSS HTLs', shown in **Figure 4.16(d)**, also show a similar trend as

P3HT, with a maximum value of 0.95 V being observed when defects total $1 \times 10^{12} \text{ cm}^{-3}$. In **Figure 4.17**, the highest fill factor (FF) value varies between 0.41 and 0.43 across different device structures. We observed an FF of 0.41 for Spiro-OMeTAD as shown in **Figure 4.17(a)**. It was found that FF was not significantly affected by the thickness of the absorber layer, which ranged from 500 to 2000 nm. In contrast, the fill factor decreased when the density of defects exceeded $1 \times 10^{14} \text{ cm}^{-3}$. Similarly, P3HT and PEDOT:PSS HTLs did not exhibit a significant effect on FF when the absorber layer thickness was changed. The FF sequences in these photovoltaic cells are almost the same as in all organic HTLs. With PTAA, only the FF was affected by the absorber layer thickness, with a decrease in fill factor below 1000 nm. There was no difference in the total defect behavior in PTAA from that in other HTLs. Due to their high resistance and recombination losses, these organic HTLs have a low FF. In **Figure 4.18**, it is evident that the maximum PCE achieved with Spiro-OMeTAD was 8.5%, among all the HTLs. The PCE has shown to improve with increasing thickness, especially between 1000 nm and 2000 nm, and as defect density decreased below $1 \times 10^{14} \text{ cm}^{-3}$, it has improved with a decrease in thickness. We found similar behavior with the PTAA, P3HT, and PEDOT:PSS HTLs, with PCEs of 7.2%, 7.6%, and 7.0%, respectively, for these three HTLs. According to the results, the maximum PCE was found to be within the thickness and total defect density range mentioned above. In this study, the significant improvement in PCE was largely due to the maximum J_{sc} that was observed within this range, which contributed to the overall improvement in PCE.

4.3.2.6 Impact of organic HTLs thickness on the solar device

The HTLs play a crucial role in facilitating the movement of positive charges in solar cell devices to the electrode. As the thickness of the HTLs in solar cells devices is critical in order to obtain efficient charge transport, to balance the charge injection, to reduce charge recombination, and to enhance the device stability, it is important that the thickness of the HTLs is optimized.

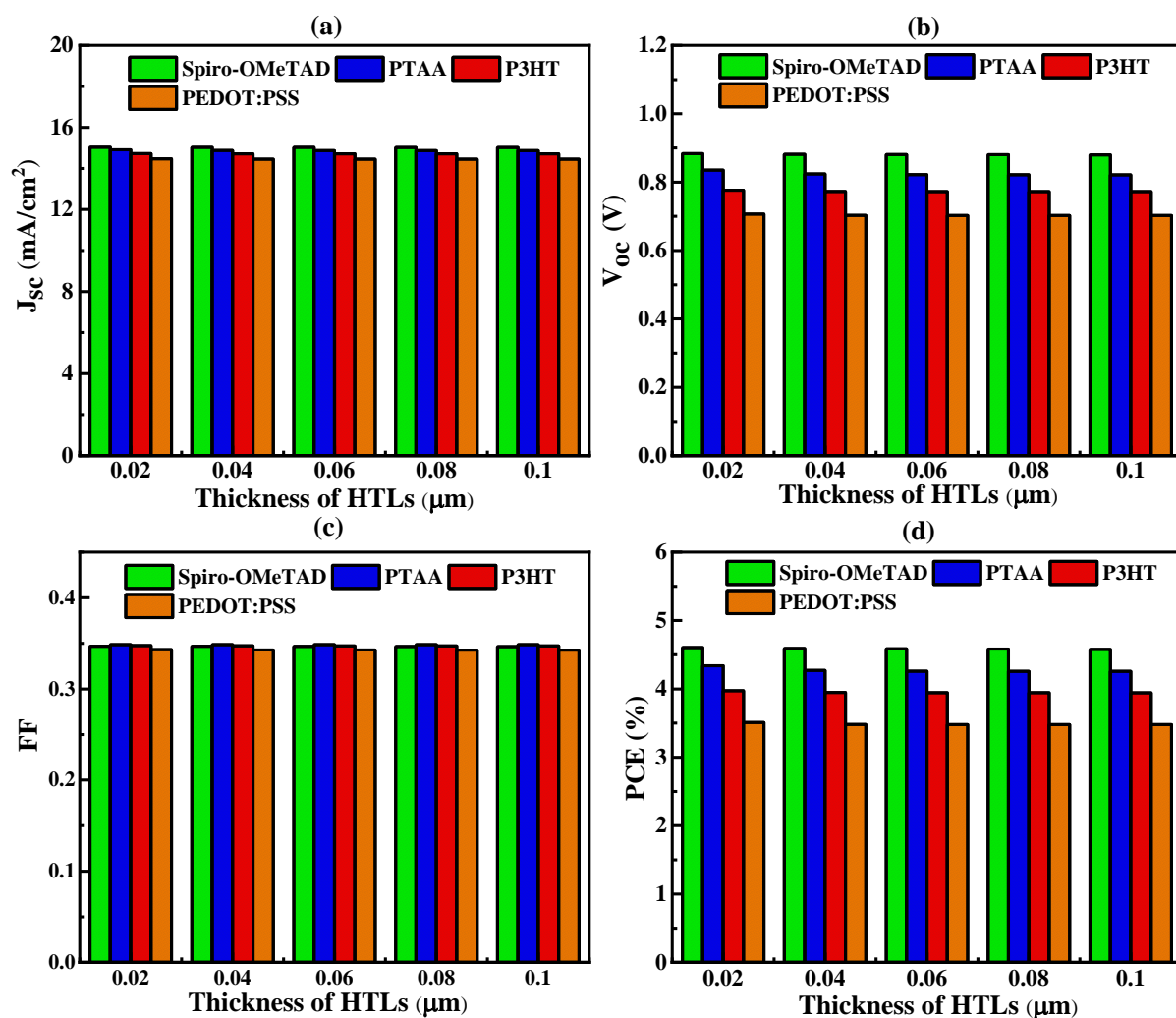


Figure 4.19 Variation of HTLs thickness such as (a) Spiro-OMeTAD, (b) PTAA, (c) P3HT, and (d) PEDOT:PSS with respect to performance, keeping the fixed SBI and ETL thickness.

HTLs also facilitate the efficient removal of photogenerated holes in the substance and their transfer to the cathode, which directly impacts the functionality and longevity of the device. A key component in the creation of powerful solar cells is the tuning of the HTL's thickness. **Figure 4.19** illustrates how altering the HTL's thickness affects the PV parameters in Ag_3BiI_6 -based PSCs. To optimize efficiency while minimizing the interaction between the cathode and its substrate, HTL thickness adjustment is essential. In addition, this layer acts as a capping layer.

As the thickness of the HTL increases, **Figure 4.19** shows that the values of V_{OC} , J_{SC} , FF, and PCE change in response to any variation in the thickness of the HTL. According to the analysis of J_{SC} with respect to the thicknesses of HTLs in the range of 20 to 100 nm, it is obvious, from all of the thickness variants of HTLs, spiro-OMeTAD stands out as the HTL most suitable for various applications. Then, the J_{SC} value of PTAA, P3HT, and PEDOT:PSS are in order. **Figure 4.19(a)** shows that J_{SC} values for various HTLs, including spiro-OMeTAD, PTAA, P3HT, and PEDOT:PSS, decreased with increasing HTL thickness. In contrast, the J_{SC} value of spiro-OMeTAD reached its maximum at 20 nm thickness, reaching 15.04 mA/cm^2 . Furthermore, PTAA, P3HT, and PEDOT:PSS also showed a decreasing trend in J_{SC} , with their respective maximum current density values at 20 nm of 14.91, 14.72, and 14.47 mA/cm^2 . As a result, these HTLs' J_{SC} values are negatively affected by increasing HTL thickness. A similar trend has been observed in the analysis of V_{OC} . In the case of HTL thickenings of 20, 40, 60, 80, and 100 nm thicknesses, V_{OC} follows the same trend for all thicknesses: spiro-OMeTAD > PTAA > P3HT > PEDOT:PSS. **Figure 4.19** illustrates that Spiro-OMeTAD achieves a maximum V_{OC} of 0.88 V by varying the thickness of the HTL within the range of 20 nm to 100 nm. In our simulations with different HTLs, we found that the FF did not change when the HTLs were changed. Moreover, even when we varied the thickness of the HTLs (from 20 nm to 100 nm) we found that the FF did not change, as

shown in **Figure 4.19**. In the case of HTL thickness values ranging from 20 to 100 nm, the FF was consistently measured to be 0.34 for values ranging from 20 to 100 nm. The FF for PTAA exhibited a slightly higher value of 0.348 than that of Spiro-OMeTAD, PTAA, P3HT, and PEDOT-PSS, among the organic HTLs tested. According to **Figure 4.19**, When the thickness is low, the PCE is maximum, but as the thickness increases, the PCE decreases slightly. In this study, PCE decreased as a result of a slight decrease in J_{SC} and V_{OC} . The device provides the maximum PCE values at a thickness of 20 nm for the following HTLs: Spiro (4.61%), PTAA (4.34%), P3HT (3.97%), and PEDOT-PSS (3.51%).

4.3.2.7 Comparing the SBI's PV parameter with earlier research

The comparison is presented in **Table 4.3** between the performance parameters of four enhanced device combinations using optimum data and the best configurations that have been published in the past. In contrast to the Ag_3BiI_6 device structure that was published earlier and included organic HTLs, the perovskite-based solar cell that was shown here demonstrates a greater PCE value compared to other organic HTLs. According to the findings of this study, there are four different device structures that have PCE values of 8.49%, 7.27%, 7.62%, and 6.97% respectively. The maximum previous reported PCE values of 5.44% and 15.98%, respectively, have been obtained for the device architecture FTO/ TiO_2 / $Ag_3BiI_{6-2x}S_x$ /Spiro-MeOTAD/Au (Experimental)⁴⁰ with organic HTL and FTO/ CeO_x / Ag_3BiI_6 / Cu_2O /Au (Simulation)³⁵ with inorganic HTL, respectively. The FF of our structure is not as good as the simulation results reported using inorganic HTL.³⁵ The low parallel resistance and high series resistance of solar cell devices account for this discrepancy. In turn, this resistance prevents the flow of current through the cell, which inhibits its efficiency.

Table 4.3 Ag₃BiI₆-based solar cell experimental and theoretical performance comparison.

Method	Year	Device Structure	V _{oc} (V)	FF	J _{sc} (mA/cm ²)	PCE (%)
Sim	2024 (This work)	FTO/TiO ₂ /Ag ₃ BiI ₆ /Spiro-MeOTAD/Au	1.13	0.41	18.09	8.49
Sim	2024 (This work)	FTO/TiO ₂ /Ag ₃ BiI ₆ /PTAA/Au	0.95	0.43	17.69	7.27
Sim	2024 (This work)	FTO/TiO ₂ /Ag ₃ BiI ₆ /P3HT/Au	1.02	0.41	18.09	7.62
Sim	2024 (This work)	FTO/TiO ₂ /Ag ₃ BiI ₆ /PEDOT:PS S/Au	0.95	0.41	18.13	6.97
Exp	2017 ³⁶	FTO/TiO ₂ /Ag ₃ BiI ₆ /PTAA/Au	0.63	0.64	10.70	4.30
Exp	2017 ³⁷	FTO/TiO ₂ /Ag ₃ BiI ₆ /PTAA/Au	0.65	0.70	2.36	1.08
Exp	2022 ¹⁵	FTO/TiO ₂ /Ag ₃ BiI ₆ /PTAA/Ag	0.71	0.65	5.35	2.60
Exp	2021 ⁴	FTO/TiO ₂ /Ag ₃ BiI ₆ /P3HT/Au	0.60	0.70	5.50	2.32
Exp	2019 ³⁸	FTO/TiO ₂ /Ag ₃ BiI _{6-2x} S _x /Spiro-MeOTAD/Au	0.57	0.65	14.60	5.44
Exp	2017 ³⁷	FTO/NiO _x /Ag ₃ BiI ₆ /PCBM/BC P/Ag	0.41	0.59	1.29	0.32
Exp	2020 ³⁹	ITO/NiO _x /Ag ₃ BiI ₆ /PCBM+C ₆₀ /Au	0.82	0.76	1.73	1.08
Sim	2024 ³⁵	FTO/CeO _x /Ag ₃ BiI ₆ /Cu ₂ O/Au	1.28	0.80	15.38	15.98

It is because of these factors that organic-based HTLs are less efficient than inorganic counterparts, which results in inferior performance. In addition, the V_{OC} values of the reported device configurations are in accord with those of the solar structures that are being shown. Beyond that, the J_{SC} values of the solar structure that is now being shown are higher than those of the Ag₃BiI₆-based device structure that was previously published. This research on photovoltaics utilizing this absorber has taken a different turn, which is noteworthy in comparison to the experimental studies

conducted on Ag_3BiI_6 absorber-based solar cells. When compared to analogous Ag_3BiI_6 -based solar cells with different organic HTLs designs that have been previously explored, we can state that our study on Ag_3BiI_6 solar cells demonstrates improved PCE based on the aforementioned characteristics.

4.4 Conclusions

According to the SEM characterization, the Ag_3BiI_6 coated surface showed an excellent, uniform distribution of grains, suggesting that, under ideal circumstances, the single-step spin-coating process produced an even distribution of grains throughout the entire surface. To explore Ag_3BiI_6 solar cells with different organic HTLs, experiments, and simulations are combined here for the first time. The materials used as HTLs in our investigation were Spiro-OMeTAD, PTAA, P3HT, and PEDOT:PSS in addition to the (c+mp) TiO_2 used as ETL. Due to its large band gap and excellent absorption coefficient, Spiro-OMeTAD also functions as the best HTL among the HTLs that have been studied which gives rise to open circuit voltage. The impact of varying the absorber layer as well as HTL thickness simultaneously on PV characteristics shows that it is not the primary factor in PCE output assessment. $\text{FTO}/(\text{c+mp})\text{TiO}_2/\text{Ag}_3\text{BiI}_6/\text{Spiro-OMeTAD}/\text{Au}$ exhibits the best performance, as shown by the examination of various structures, with a PCE of 8.50%, an FF of 0.41%, a J_{SC} of 18 mA/cm^2 , and a V_{OC} of 1.1 V. In order to gain an in-depth knowledge of the processes guiding PV efficiency, a thorough examination of the effects of capacitance, C-f analysis, generation and recombination rates, J-V, and QE characteristics of these frameworks is conducted. This thorough investigation may pave the way for creating lead-free, excellent-performance Ag_3BiI_6 based solar cells with outstanding effectiveness.

4.5 References

- (1) Yao, Y.; Cheng, C.; Zhang, C.; Hu, H.; Wang, K.; De Wolf, S. Organic Hole-transport Layers for Efficient, Stable, and Scalable Inverted Perovskite Solar Cells. *Adv. Mater.* **2022**, *34* (44), 2203794.
- (2) Li, X.; Yang, J.; Jiang, Q.; Lai, H.; Li, S.; Tan, Y.; Chen, Y.; Li, S. Perovskite Solar Cells Employing an Eco-Friendly and Low-Cost Inorganic Hole Transport Layer for Enhanced Photovoltaic Performance and Operational Stability. *J. Mater. Chem. A* **2019**, *7* (12), 7065–7073.
- (3) Shao, Y.; Zhang, C.; Wang, S.; Yan, Y.; Feng, Y.; Bian, J.; Shi, Y. Insight into the Interfacial Elastic Contact in Stacking Perovskite Solar Cells. *Adv. Mater. Interfaces* **2019**, *6* (7), 1900157.
- (4) Kulkarni, A.; Ünlü, F.; Pant, N.; Kaur, J.; Bohr, C.; Jena, A. K.; Öz, S.; Yanagida, M.; Shirai, Y.; Ikegami, M.; Miyano, K.; Tachibana, Y.; Chakraborty, S.; Mathur, S.; Miyasaka, T. Concerted Ion Migration and Diffusion-Induced Degradation in Lead-Free Ag_3BiI_6 Rudorffite Solar Cells under Ambient Conditions. *Solar RRL* **2021**, *5* (8), 2100077.
- (5) Chauhan, P.; Agarwal, S.; Srivastava, V.; Maurya, S.; Hossain, M. K.; Madan, J.; Yadav, R. K.; Lohia, P.; Dwivedi, D. K.; Alothman, A. A. Impact on Generation and Recombination Rate in $\text{Cu}_2\text{ZnSnS}_4$ (CZTS) Solar Cell for Ag_2S and In_2Se_3 Buffer Layers with CuSbS_2 Back Surface Field Layer. *Prog. Photovolt.* **2024**, *32* (3), 156–171.
- (6) Bhattarai, S.; Pandey, R.; Madan, J.; Ansari, M. Z.; Hossain, M. K.; Amami, M.; Ahammad, S. H.; Rashed, A. N. Z. Chlorine-Doped Perovskite Materials for Highly Efficient

- Perovskite Solar Cell Design Offering an Efficiency of Nearly 29%. *Prog. Photovolt.* **2024**, 32 (1), 25–34.
- (7) Burgelman, M.; Nollet, P.; Degrave, S. Modelling Polycrystalline Semiconductor Solar Cells. *Thin solid films* **2000**, 361, 527–532.
 - (8) Srivastava, A.; Dua, P.; Lenka, T. R.; Tripathy, S. K. Numerical Simulations on CZTS/CZTSe Based Solar Cell with ZnSe as an Alternative Buffer Layer Using SCAPS-1D. *Mater. Today Proc.* **2021**, 43, 3735–3739.
 - (9) Chen, Q.; Ni, Y.; Dou, X.; Yoshinori, Y. The Effect of Energy Level of Transport Layer on the Performance of Ambient Air Prepared Perovskite Solar Cell: A SCAPS-1D Simulation Study. *Crystals* **2022**, 12 (1), 68.
 - (10) Rahman, M. F.; Habib, M. J. A.; Ali, M. H.; Rubel, M. H. K.; Islam, M. R.; Abu, A. B.; Hossain, M. K. Design and Numerical Investigation of Cadmium Telluride (CdTe) and Iron Silicide (FeSi₂) Based Double Absorber Solar Cells to Enhance Power Conversion Efficiency. *AIP Adv.* **2022**, 12 (10).
 - (11) Bichave, S.; Mundupuzhakal, J.; Gajjar, P. N.; Gupta, S. K. Analysis of Varying ETL/HTL Material for an Effective Perovskite Solar Cell by Numerical Simulation. *Mater. Today Proc.* **2023**.
 - (12) Ali, M. H.; Al Mamun, M. A.; Haque, M. D.; Rahman, M. F.; Hossain, M. K.; Abu, A. Z. Performance Enhancement of an MoS₂-Based Heterojunction Solar Cell with an In₂Te₃ Back Surface Field: A Numerical Simulation Approach. *ACS Omega* **2023**, 8 (7), 7017–7029.

- (13) Giordano, F.; Abate, A.; Correa Baena, J. P.; Saliba, M.; Matsui, T.; Im, S. H.; Zakeeruddin, S. M.; Nazeeruddin, M. K.; Hagfeldt, A.; Graetzel, M. Enhanced Electronic Properties in Mesoporous TiO₂ via Lithium Doping for High-Efficiency Perovskite Solar Cells. *Nat. Commun.* **2016**, 7 (1), 1–6.
- (14) Islam, M. A. U.; Kato, S.; Soga, T. An Experimental and Simulation Study of Cu₆BiAgI₁₀ Photovoltaics with Various Organic and Inorganic Hole Transport Layers for the Improved Photovoltaic Performance of Solar Cells. *Energy and Fuels* **2023**, 37 (24), 19882–19897.
- (15) Wu, M.-C.; Wang, Q.-H.; Hsiao, K.-C.; Chen, S.-H.; Ho, C.-M.; Jao, M.-H.; Chang, Y.-H.; Su, W.-F. Composition Engineering to Enhance the Photovoltaic Performance and to Prolong the Lifetime for Silver Bismuth Iodide Solar Cell. *Chem. Eng. J. Adv.* **2022**, 10, 100275.
- (16) Hossain, M. K.; Rubel, M. H. K.; Toki, G. F. I.; Alam, I.; Rahman, M. F.; Bencherif, H. Effect of Various Electron and Hole Transport Layers on the Performance of CsPbI₃-Based Perovskite Solar Cells: A Numerical Investigation in DFT, SCAPS-1D, and WxAMPS Frameworks. *ACS Omega* **2022**, 7 (47), 43210–43230.
- (17) Karthick, S.; Bouclé, J.; Velumani, S. Effect of Bismuth Iodide (BiI₃) Interfacial Layer with Different HTL's in FAPI Based Perovskite Solar Cell – SCAPS – 1D Study. *Solar Energy* **2021**, 218, 157–168.
- (18) Crovetto, A.; Hajjifarassar, A.; Hansen, O.; Seger, B.; Chorkendorff, I.; Vesborg, P. C. K. Parallel Evaluation of the BiI₃, BiOI, and Ag₃BiI₆ Layered Photoabsorbers. *Chem. Mater.* **2020**, 32 (8), 3385–3395.

- (19) Islam, M. A.; Rahaman, M. Z.; Hasan, M. M.; Hossain, A. K. M. A. Analysis of Grain Growth, Structural and Magnetic Properties of Li-Ni-Zn Ferrite under the Influence of Sintering Temperature. *Heliyon* **2019**, 5 (2), e01199.
- (20) Islam, M. A.; Hasan, M.; Hossain, A. K. M. A. Enhancement of Initial Permeability and Reduction of Loss Factor in Zn Substituted Nanocrystalline $\text{Li}_{0.35-0.5x}\text{Ni}_{0.3}\text{Zn}_x\text{Fe}_{2.35-0.5x}\text{O}_4$. *J. Magn. Magn. Mater.* **2017**, 424, 108–114.
- (21) Islam, M. A.; Kato, S.; Kishi, N.; Soga, T. Enhanced Surface Morphology and Photovoltaic Properties of a New Class of Material Copper Silver Bismuth Iodide Solar Cell. *J. Mater. Res. Technol.* **2023**, 25, 4171–4186.
- (22) Paul, T. C.; Podder, J.; Babu, M. H. Optical Constants and Dispersion Energy Parameters of Zn-Doped TiO_2 Thin Films Prepared by Spray Pyrolysis Technique. *Surf. Interfaces.* **2020**, 21, 100725.
- (23) Paul, T. C.; Podder, J. Synthesis and Characterization of Zn-Incorporated TiO_2 Thin Films: Impact of Crystallite Size on X-Ray Line Broadening and Bandgap Tuning. *Appl. Phys. A* **2019**, 125 (12), 1–14.
- (24) Kumar, M.; Kumar, S. Investigation of All Inorganic Lead-Free Perovskite CsSnI_3 /Silicon Heterojunction Solar Cell Using SCAPS-1D. *Adv. Theory Simul.* **2023**, 6 (11), 2300401.
- (25) Barman, B.; Ingole, S. Analysis of Si Back-Contact for Chalcogenide Perovskite Solar Cells Based on BaZrS_3 Using SCAPS-1D. *Adv. Theory Simul.* **2023**, 6 (7), 2200820.
- (26) Porwal, S.; Paul, M.; Dixit, H.; Mishra, S.; Singh, T. Investigation of Defects in Cs_2SnI_6 -

- Based Double Perovskite Solar Cells Via SCAPS-1D. *Adv. Theory Simul.* **2022**, 5 (9), 2200207.
- (27) Zhang, A.; Duan, R. Design and Numerical Investigation of CsPbI₃/CsSn_{0.5}Ge_{0.5}I₃ Double-Absorption-Layer Heterojunction Perovskite Solar Cells Based on SCAPS-1D. *Phys. Status Solidi a* **2023**, 220 (21), 2300525.
- (28) You, L.; Zhang, X.; Ma, Q.; Zhu, W.; Wu, J. Optimization of Electron Transport Layer-Free Cs₂TiBr₆/MASnBr₃ Laminated Structure Perovskite Solar Cells by SCAPS-1D Simulation. *Phys. Status Solidi a* **2023**, 220 (14), 2300071.
- (29) Sultana, M. R.; Islam, B.; Ahmed, S. R. Al. Modeling and Performance Analysis of Highly Efficient Copper Indium Gallium Selenide Solar Cell with Cu₂O Hole Transport Layer Using Solar Cell Capacitance Simulator in One Dimension. *Phys. Status Solidi a* **2022**, 219 (5), 2100512.
- (30) Kumar, M.; Kumar, A.; Raj, A.; Kr. Singh, P.; Anshul, A. Effect of Band-Gap Tuning and Series Resistance on PCE of Optimized MAPbI₃-Based PSC by SCAPS-1D Simulation. *Macromol. Symp.* **2023**, 407 (1), 2100464.
- (31) Zhang, H.; Chan, K. Y.; Ng, Z. N. Modeling of Copper Zinc Tin Sulfide Solar Cells with Various Buffers Using SCAPS-1D. *Phys. Status Solidi b* **2023**, 260 (11), 2300270.
- (32) Rehman, U. ur; Almousa, N.; Sahar, K. ul; Ashfaq, A.; Mahmood, K.; Shokralla, E. A.; Al-Buriahi, M. S.; Alrowaili, Z. A.; Capangpangan, R. Y.; Alguno, A. C. Optimizing the Efficiency of Lead-Free Cs₂TiI₆-Based Double Halide Perovskite Solar Cells Using SCAPS-1D. *Energy Technol.* **2023**, 11 (9), 2300459.

- (33) Houmomou, A. M.; Mohammadou, S.; Dzifack Kenfack, G. M.; Tchangnwa Nya, F.; Laref, A.; Mohamadou, A. Toward High-Efficiency CIGS-Based Thin-Film Solar Cells Incorporating Surface Defects Layer, through a Comparative Study of Electrical Characteristics—SCAPS 1D Modeling. *Energy Technol.* **2023**, *11* (9), 2201476.
- (34) Liu, X.; Li, T.; Hao, L.; Wu, J.; Ling, Y.; Fu, Z.; Zhou, F.; Zhang, X.; Liu, Y.; Zhang, C. Lead Free CsSn_{0.5}Ge_{0.5}I₃ Perovskite Solar Cell with Different Layer Properties via SCAPS-1D Simulation. *Can. J. Chem. Eng.* **2023**, *101* (12), 6792–6806.
- (35) Sekar, K.; Marasamy, L.; Mayarambakam, S.; Selvarajan, P.; Bouclé, J. Highly Efficient Lead-Free Silver Bismuth Iodide (Ag₃BiI₆) Rudorffite Solar Cells with Novel Device Architecture: A Numerical Study. *Mater. Today Commun.* **2024**, *38*, 108347.
- (36) Turkevych, I.; Kazaoui, S.; Ito, E.; Urano, T.; Yamada, K.; Tomiyasu, H.; Yamagishi, H.; Kondo, M.; Aramaki, S. Photovoltaic Rudorffites: Lead-Free Silver Bismuth Halides Alternative to Hybrid Lead Halide Perovskites. *Chem. Sus. Chem* **2017**, *10* (19), 3754–3759.
- (37) Baranwal, A. K.; Masutani, H.; Sugita, H.; Kanda, H.; Kanaya, S.; Shibayama, N.; Sanehira, Y.; Ikegami, M.; Numata, Y.; Yamada, K.; Miyasaka, T.; Umeyama, T.; Imahori, H.; Ito, S. Lead-Free Perovskite Solar Cells Using Sb and Bi-Based A₃B₂X₉ and A₃BX₆ Crystals with Normal and Inverse Cell Structures. *Nano Conver.* **2017**, *4* (1), 1–14.
- (38) Pai, N.; Lu, J.; Gengenbach, T. R.; Seeber, A.; Chesman, A. S. R.; Jiang, L.; Senevirathna, D. C.; Andrews, P. C.; Bach, U.; Cheng, Y. B.; Simonov, A. N. Silver Bismuth Sulfoiodide Solar Cells: Tuning Optoelectronic Properties by Sulfide Modification for Enhanced

- Photovoltaic Performance. *Adv. Energy Mater.* **2019**, 9 (5), 1803396.
- (39) Seo, Y.; Ha, S. R.; Yoon, S.; Jeong, S. M.; Choi, H.; Kang, D. W. Dynamic Casting in Combination with Ramped Annealing Process for Implementation of Inverted Planar Ag_3BiI_6 Rudorffite Solar Cells. *J. Power Sources* **2020**, 453, 227903.
- (40) Tang, S.; Huang, S.; Wilson, G. J.; Ho-Baillie, A. Progress and Opportunities for Cs Incorporated Perovskite Photovoltaics. *Trends Chem.* 2020, 2 (7), 638– 653.

Chapter 5

Tandem solar cell approach to unlocking the potential of Rudorffite/silicon combinations

5.1 Introduction

This study used the structure ITO/PEDOT:PSS/Rudorffites/PCBM/Ag to investigate the performance of three rudorffite structures (Ag_3BiI_6 , Ag_2BiI_5 , and AgBiI_4), evaluate their initial efficiencies, and use optimization strategies to enhance their overall performance. The experimental results were in near agreement with the initial efficiency measurement of 5.77% for the Ag_3BiI_6 structure. The efficacy increased substantially to 15.26% after the optimization strategies were implemented, which is in close proximity to the simulation results that were reported. The optimization techniques were effective in maximizing the efficiencies of the Ag_2BiI_5 and AgBiI_4 structures, respectively, from an initial efficiency of 4.10% and 10.59%, and from an initial efficiency of 4.06% and 10.44%, respectively. We have attained the highest efficiency possible for a single junction in a p-i-n configuration in our work. In order to improve efficiency further, we have explored the Rudorffite/Si 2T tandem structure as an innovative configuration. Rudorffite is classified as a rudorffite structure, which belongs to the broader classes of perovskites family. Rudorffite has a crystal structure that closely resembles that of perovskite, making it a distinct form of perovskite material. The perovskite/Si tandem has become the leading choice in the solar industry because of the perovskites' competitive advantages and the high demand for Si solar cells. Si-based prototype industrial lines are ideal complement for perovskite/Si tandem solar cells, which seek to overcome the obstacles encountered by the PV community, as they provide

considerable possibility for cooperation with perovskite solar cells. The PCE of perovskite/Si tandem solar cells has seen a tremendous increase, rising from 13.7% in 2015 to an astonishing 33.9% by 2023.¹⁻⁵ This surpasses the theoretical limit of any single-junction solar cell. The 45% efficiency limit imposed by the detailed balancing principle on double-junction PVs is the maximum performance achievable.⁶ This serves as a benchmark for the potential improvement in next-generation perovskite-based multi-junction PVs. In simulation research done in 2024, Kumer et. al. examined the effectiveness of the Bi-based inorganic $\text{Cs}_3\text{Bi}_2\text{I}_9$ perovskite/Si tandem structure. Their greatest efficiency reached 31.59%.⁷ In 2021, Amri et. al. conducted a study on the effectiveness of the Bi-based double perovskite $\text{Cs}_2\text{AgBi}_{0.75}\text{Sb}_{0.25}\text{Br}_6$ perovskite/Si tandem structure. They were able to obtain a maximum efficiency of 24.4%.⁸ This work focused on assessing the effectiveness of Rudorffite/Si tandem solar cells with Ag_3BiI_6 , Ag_2BiI_5 , and AgBiI_4 structures. The maximum efficiencies observed for these structures were 22.31%, 18.63%, and 18.89%, respectively. These efficiencies are the highest yet reported for rudorffite structures in solar cells. Although rudorffite structures are not significantly more efficient than other tandem solar cells, they are still progressing stage than other structures. The reason for this is because the short-circuit current (J_{sc}) of the top cell in the rudorffite structures is comparatively lower than that of other tandem solar cells based on Pb-based perovskite/Si.

5.2 Simulation methodology

Understanding the Solar Cell Capacitance Simulator within One Dimension (SCAPS-1D) modeling technique is necessary for comprehending the fundamental characteristics and device parameters of high-efficiency solar cells.⁹⁻¹¹ It was developed by Burgelman et. al.¹² in order to study and optimize solar cell efficiency under different situations. Since Poisson's and continuation equations are crucial to understanding semiconductor device physics, they are used in SCAPS 1D.

Poisson's equation establishes the link between the semiconductor device's electric voltage and charge density. On the other hand, the continuity equations describe how charged carriers-holes and electrons-move through the device.

5.2.1 Device structure and simulation parameters

The top and bottom cells comprise a typical tandem solar device. The absorber material's relative spectral efficiency determines which specific cell is chosen. Under normal conditions, the bottom cell only gets partial of AM1.5G solar spectrum, but the top cell receives the whole spectrum.¹³ Interestingly, absorbers with a larger bandgap convert a lower percentage of incoming radiation to photonic energy. The bandgap of the top cell absorber is typically 1.6–2 eV.¹⁴ Therefore, the top cells cannot take in photons with energy below that threshold. Meanwhile, the bottom cell's reduced bandgap (<1.3 eV) allows it to maximize absorption potential by absorbing low-energy photons.¹⁵ Optical losses may occur between the top and bottom cell interfaces in tandem devices. Furthermore, the cells in a 4T arrangement are mechanically stacked, and the optical loss may be more significant than in a monolithic 2T configuration. Also, it has been reported that 2T tandem cell's efficiency is better than 4T tandem cell.¹⁵ The absorption coefficient of the top device (ETL, absorber, and HTL) and the thickness of these matching layers determine the percentage of filtered sunlight that reaches the bottom cell. Consequently, it is critical to remember that SCAPS-1D does not support multi-junction solar cell simulation.^{16,17} Particular care was given while calculating the tandem device using SCAPS-1D. The multi-junction solar cell must have a filtered spectrum computed to be quantitatively analyzed. The bottom cell gets a filtered spectrum due to the top cell being exposed to the AM 1.5G 1 sun spectrum.^{18,19} The present study matched the currents for the 2T tandem cell by adjusting the top cell's absorber thickness, resulting in the bottom and top cells having the same J_{SC} . Rudorffite materials (Ag_3BiI_6 , Ag_2BiI_5 , $AgBiI_4$), whose respective bandgap

values are close to those of the perovskite substance (1.71 eV, 1.90, and 1.87 eV), have been employed as the top cell absorber and c-Si as the bottom cell material in tandem devices that are the subject of ongoing study. Numerical studies of mechanically stacked monolithic 2T designs have been conducted to compare them. In **Tables 5.1** and **5.2**, input parameters are given for top and bottom cells. The single junction and double junction tandem device designs used in our research are shown in **Figures 5.1(a, b)**. And **Figure 5.1(b)** shows the 2T monolithic tandem device with an ITO recombination layer positioned in between. The non-toxic rudorffite structure was the top cell absorber used in the investigation for both arrangements. Every manner of research was compared to a control device using the industry's usual. The PEDOT: PSS acted as the HTL and PCBM as the ETL for each device.

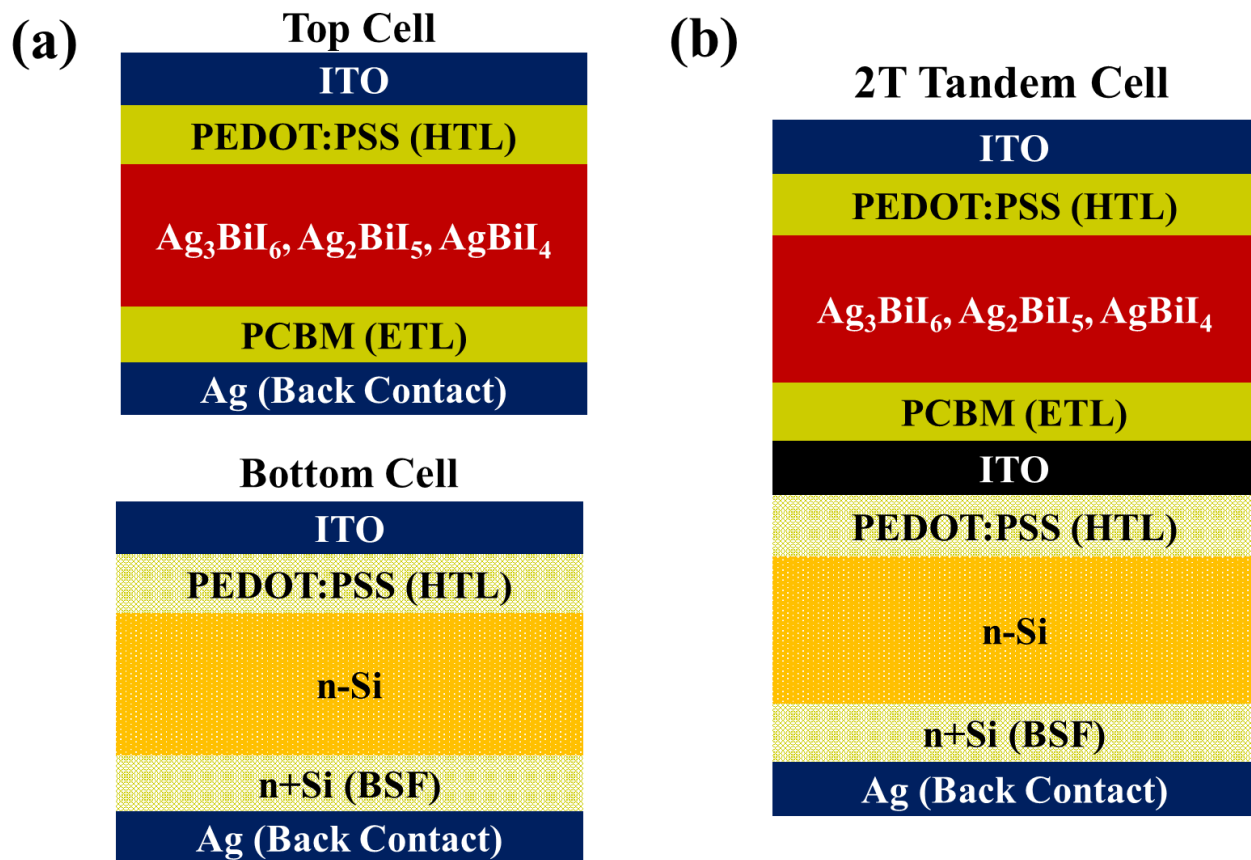


Figure 5.1 illustrates the device layout of a typical (a) single junction of Top and Bottom Cell and (b) 2T double junction Tandem cell.

Table 5.1 Presents the top cell input parameters that were collected from both the experiment and simulation studies.

Parameters	ITO	PEDOT: PSS	Ag ₃ BiI ₆	Ag ₂ BiI ₅	AgBiI ₄	PCBM
Thickness (nm)	230	33	1200	1200	1200	20
Band Gap (eV)	3.50	2.2	1.71	1.90	1.87	2
Electron affinity (eV)	4	2.9	3.94	3.99	4.04	4.13
Permittivity	9	3	6.5	6.5	6.5	4
DOS at CB (cm ⁻³)	2.2×10 ¹⁸	2.2×10 ¹⁵	1×10 ¹⁹	1×10 ¹⁹	1×10 ¹⁹	1×10 ¹⁹
DOS at VB (cm ⁻³)	1.8×10 ¹⁹	1.8×10 ¹⁸	1×10 ¹⁹	1×10 ¹⁹	1×10 ¹⁹	1×10 ¹⁹
Electron thermal velocity (cm.s ⁻¹)	1×10 ^{7C}	1×10 ^{7C}	1×10 ^{7C}	1×10 ^{7C}	1×10 ^{7C}	1×10 ^{7C}
Hole thermal velocity (cm.s ⁻¹)	1×10 ^{7C}	1×10 ^{7C}	1×10 ^{7C}	1×10 ^{7C}	1×10 ^{7C}	1×10 ^{7C}
Mobility of electron (cm ² .V ⁻¹ .s ⁻¹)	20	10	1	1	1	1×10 ⁻²
Mobility of hole (cm ² .V ⁻¹ .s ⁻¹)	10	10	1	1	1	1×10 ⁻²
Shallow uniform donor density, N_D (cm ⁻³)	1×10 ²¹	0	0	0	0	5×10 ¹⁷
Shallow uniform acceptor density, N_A (cm ⁻³)	0	3.17×10 ¹⁴	1×10 ¹⁵	1×10 ¹⁵	1×10 ¹⁵	0
Defect density (cm ⁻³)	1×10 ¹⁵	1×10 ¹⁵	1×10 ¹⁵	1×10 ¹⁵	1×10 ¹⁵	1×10 ¹⁵
References	20	21	21,22	21,22	21,22	23

Table 5.2 Presents the bottom cell input parameters that were collected from both the experiment and simulation studies.

Parameters	PEDOT: PSS	n-Si	n+Si
Thickness (nm)	100	50000	500
Band Gap (eV)	1.60	1.12	1.12
Electron affinity (eV)	3.55	4.05	4.05
Permittivity	2.58	11.9	11.9
DOS at CB (cm ⁻³)	2.1×10 ²¹	2.80×10 ¹⁹	2.819×10 ¹⁹
DOS at VB (cm ⁻³)	2.0×10 ²¹	1.04×10 ¹⁹	1.04×10 ¹⁹
Electron thermal velocity (cm.s ⁻¹)	1×10 ⁷	2.30×10 ⁷	2.30×10 ⁷
Hole thermal velocity (cm.s ⁻¹)	1×10 ⁷	1.65×10 ⁷	1.65×10 ⁷
Mobility of electron (cm ² .V ⁻¹ .s ⁻¹)	1	1400	1400
Mobility of hole (cm ² .V ⁻¹ .s ⁻¹)	20	450	450
Shallow uniform donor density, N _D (cm ⁻³)	0	1×10 ¹⁷	1×10 ²⁰
Shallow uniform acceptor density, N _A (cm ⁻³)	3×10 ²⁰	0	0
Defect density (cm ⁻³)	1×10 ¹⁴	1×10 ¹³	1×10 ¹³
References	24	24	25

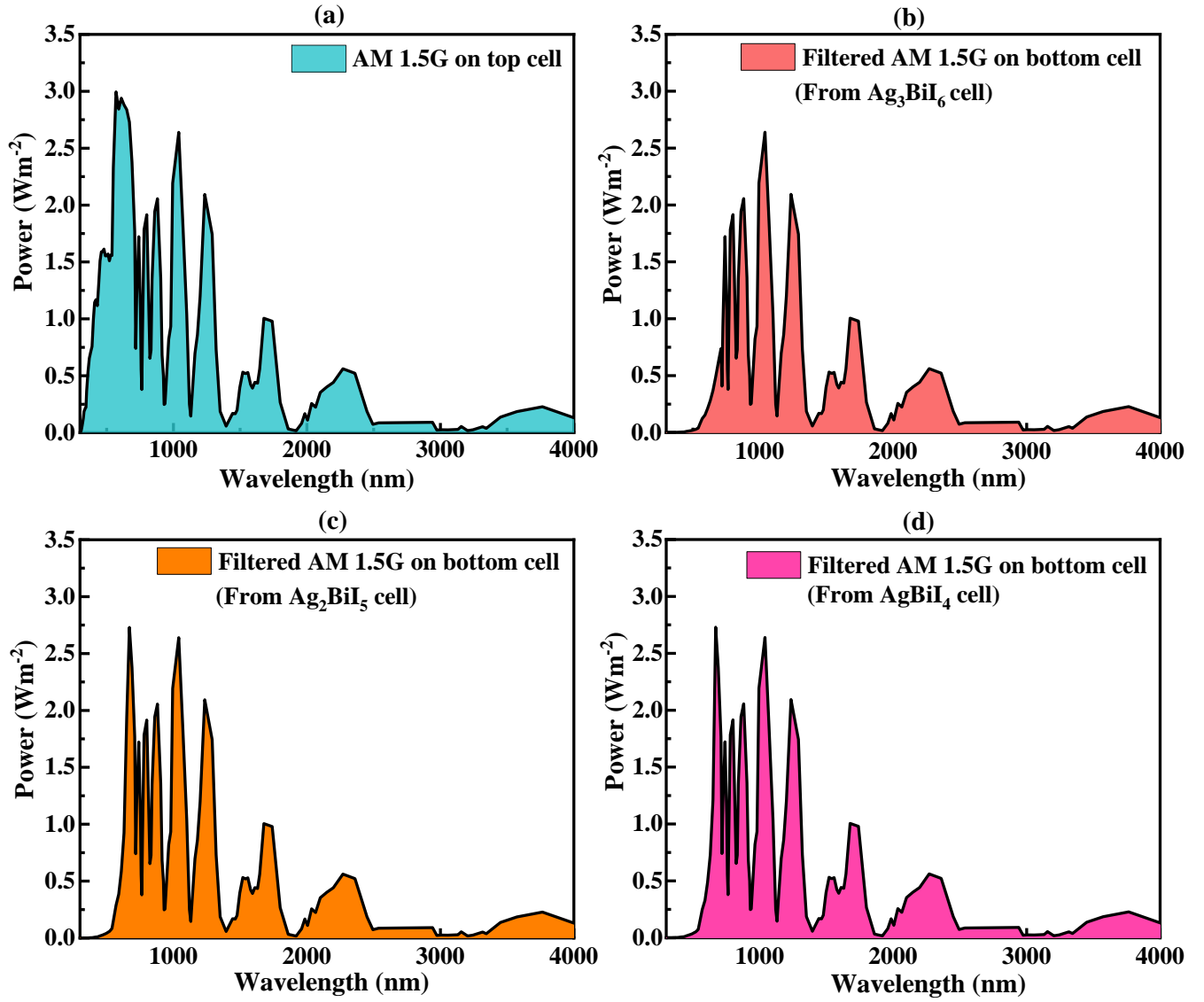


Figure 5.2 shows the device spectrums for (a) the top sub-cell's AM1.5 spectrum illumination, (b) the bottom sub-cell's filtered AM1.5 spectrum illumination (from Ag_3BiI_6 cell), (c) the bottom sub-cell's filtered AM1.5 spectrum illumination (from Ag_2BiI_5 cell), and (d) the bottom sub-cell's schematic illumination by AM1.5 spectrum illumination (from AgBiI_4 cell).

Three layers are included in the silicon-based structure's bottom cell: PEDOT:PSS is the HTL, the light-absorbing layer is n-Si, and the back surface field (BSF) is n+Si. The ITO substrate serves as the foundation for this design, while silver (Ag) is used as the electrode to maximize the efficiency and overall performance of the cell as shown in **Figure 5.1(a)**. According to **Figure 5.1(b)**, multiple semiconductor layers are connected in series via two junctions. For monolithic integration to be achieved, the interconnection layer ensures that every layer generates just about the same current. In opto-electronic devices, the ITO layer serves as a crucial interconnection between top and bottom cells. ITO's excellent electrical conductivity and optical transparency enhance charge transport while minimizing resistive losses.

This commonly used modeling technique for tandem solar cell exposes the bottom cell to the electromagnetic spectrum filtered through the top cell, while the top cell illuminates the typical AM1.5G solar spectrum.^{26,27} It is possible to compute the light spectrum, $S_T(\lambda)$, that is transmitted via the top cell as²⁸

$$S_T(\lambda) = S_0(\lambda) \times \exp\left(\sum_{i=1}^n -(\alpha_i(\lambda) \times d_i)\right) \quad (1)$$

Where AM1.5G happens to be the solar radiation incident on the top cell, $\alpha(\lambda)$ denotes the absorption constant, and d denotes the thickness of the separate layers in the top cell.²⁹ Here, $\alpha(\lambda)$ is acquired as it develops.

$$\alpha(\lambda) = A \sqrt{(h\nu - E_g)} \quad (2)$$

Where E_g represents the material's bandgap, ν is the inward photon frequency, as well as h is Planck's constant. The model element is A. In **Figure 5.2**, the spectrum associated with each sub-cell is shown.

5.3 Result and discussion

5.3.1 Analysis of Rudorffite base top cell

5.3.1.1 Effect of absorber layer thickness

In the top cell absorb layers, Ag_3BiI_6 , Ag_2BiI_5 , and AgBiI_4 , electron-hole pairs are created based on the absorption of light. The efficiency of solar cells is greatly impacted by the thickness of these layers because charge carriers recombine before they reach the electrodes if the absorber is longer than their diffusion length. Increasing the thickness of absorbers leads to a higher capture of photons, which in turn increases the creation of electron-hole pairs and enhances the J_{sc} . In contrast, thinner layers have a lower capacity to absorb photons, resulting in reduced efficiency. Exposed to the AM1.5G solar spectrum, **Figure 5.3(a–f)** shows the photovoltaic properties of the top cell with layer thickness varying between 100 and 1200 nm. As Ag_3BiI_6 , Ag_2BiI_5 and AgBiI_4 thickness increases, the J_{sc} experiences significant growth, reaching a saturation point of around 600 nm as shown in **Figure 5.3**. After the thickness exceeds 700 nm, the J_{sc} starts to decrease as a result of the recombination of electron-hole pairs. In this case, the V_{oc} decreases slightly from 1.03 V to 0.99 V when Ag_3BiI_6 thicknesses from 100 to 1200 nm. Similar trends have been seen in Ag_2BiI_5 and AgBiI_4 . Also, fill factor (FF) tends to decrease with increasing rudorffite thickness. The PCE is unique depending on Ag_3BiI_6 , Ag_2BiI_5 , and AgBiI_4 variation. At first, with the variation of absorber thickness, the PCE of Ag_3BiI_6 slightly increases from 6.20% to 8.32% until

the value when J_{SC} also becomes saturated. When the thickness goes over 600 nm, the PCE drops by as much as 5.77%. For the solar cell, both PCE and J_{SC} are highest approximately 600 nm.

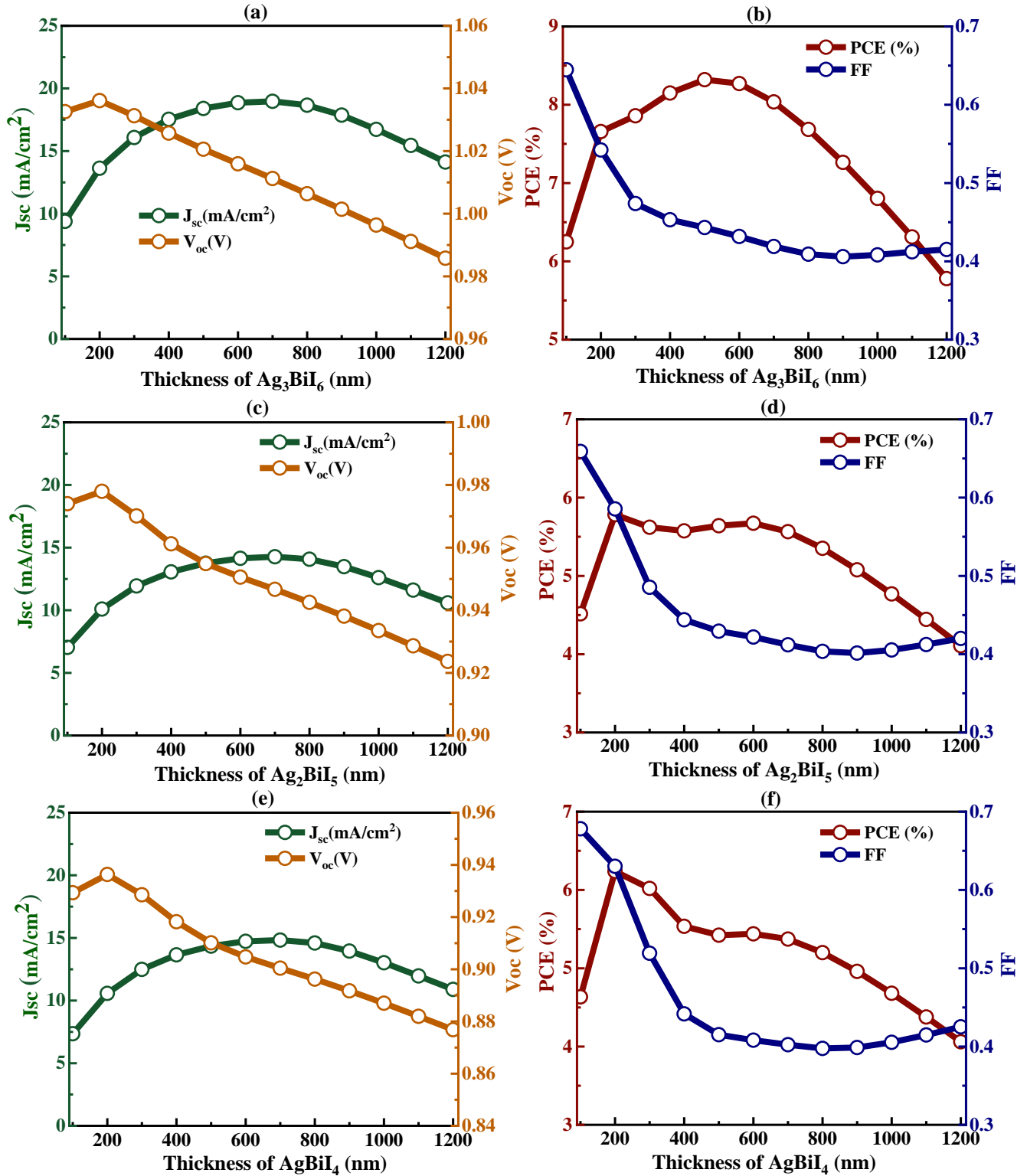


Figure 5.3 Solar cell's parameters as a function of thickness of absorbing layer (a, b) Ag_3BiI_6 (c, d) Ag_2BiI_5 (e, f) AgBiI_4 .

Conversely, in the case of the two additional rudorffite structures, the PCE value for Ag_2BiI_5 and AgBiI_4 is measured at different thicknesses: 100 nm, 600 nm, and 1200 nm. The recorded PCE values for Ag_2BiI_5 are 4.52%, 5.67%, and 4.11%, while for AgBiI_4 they are 4.63%, 5.44%, and 4.06% as shown in **Figure 5.3**. This solar cell achieves its maximum performance when the J_{SC} and PCE are maximized, showing that all layers efficiently capture sunlight and produce a high electric current.

5.3.1.2 Effect of HTL layer thickness

Solar cells with HTL may have a higher photoelectric conversion efficiency since they move holes more quickly from the active layer. Furthermore, it stops electrons from traveling toward the back electrode, which lowers carrier recombination and lengthens the PV solar cell's stability. The PEDOT:PSS polymer, which is the HTL in solar cells and is one of the most popular ones, is the subject of this investigation. **Table 5.1** provides further details on the HTL's parameters. The PEDOT:PSS is preferred because of its strong optical transparency in the visible range and low processing temperature. It is applicable to both inflexible and flexible Perovskite solar cell (PSC) structures. Variation of PV parameters with regard to HTL thickness is shown in **Figure 5.4(a-d)**. Remarkably, when the thickness of HTL is as low as 50 nm, all photovoltaic metrics, including J_{SC} , V_{OC} , FF, and PCE, achieve their highest values. Due to the fact that HTL does not absorb light, thinner layers yield better performance. However, PV parameters decrease with increasing thickness due to greater recombination losses. It has been observed that this behavior is consistent across all three rudorffite materials, and it has also been observed that similar trends have been observed in other bismuth-based perovskites as well.²¹

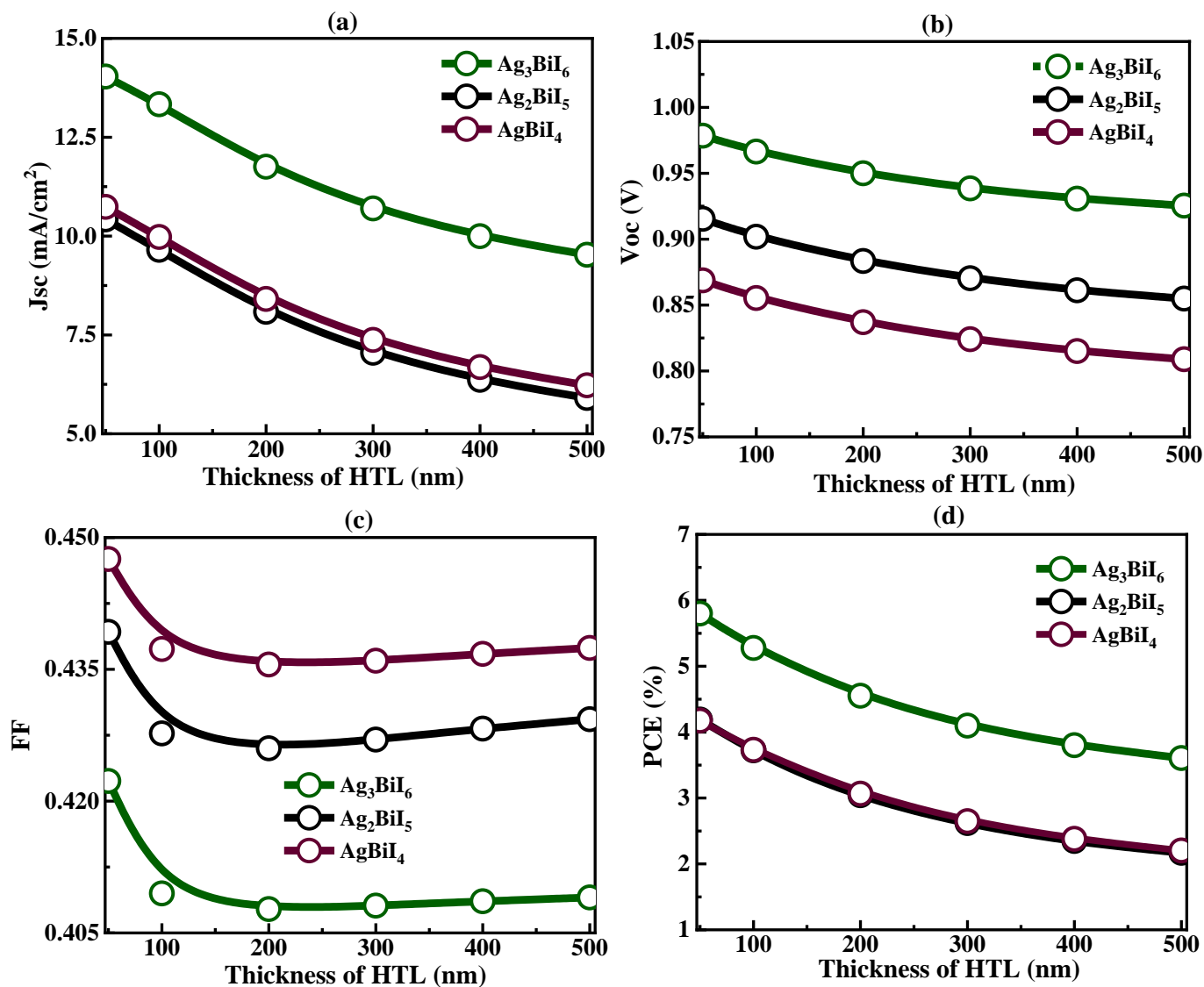


Figure 5.4 illustrates the variation of (a) J_{sc} , (b) V_{oc} , (c) FF, and (d) PCE in relation to the thickness variation of PEDOT:PSS as HTL.

5.3.1.3 Effect of ETL thickness on J-V characteristics

In p-i-n structured perovskite solar cells, PCBM is the most commonly used organic ETL material with extraordinary advantages. It is easily synthesized and purified, has adjustable frontier molecular orbitals, acceptable electron mobility, is inexpensive, soluble in various organic solvents, and has adequate chemical and thermal durability. The effect of variation of thickness

ETL is illustrated in **Figure 5.5(a-c)** for three different rudorffite structures in the current density vs voltage characteristics.

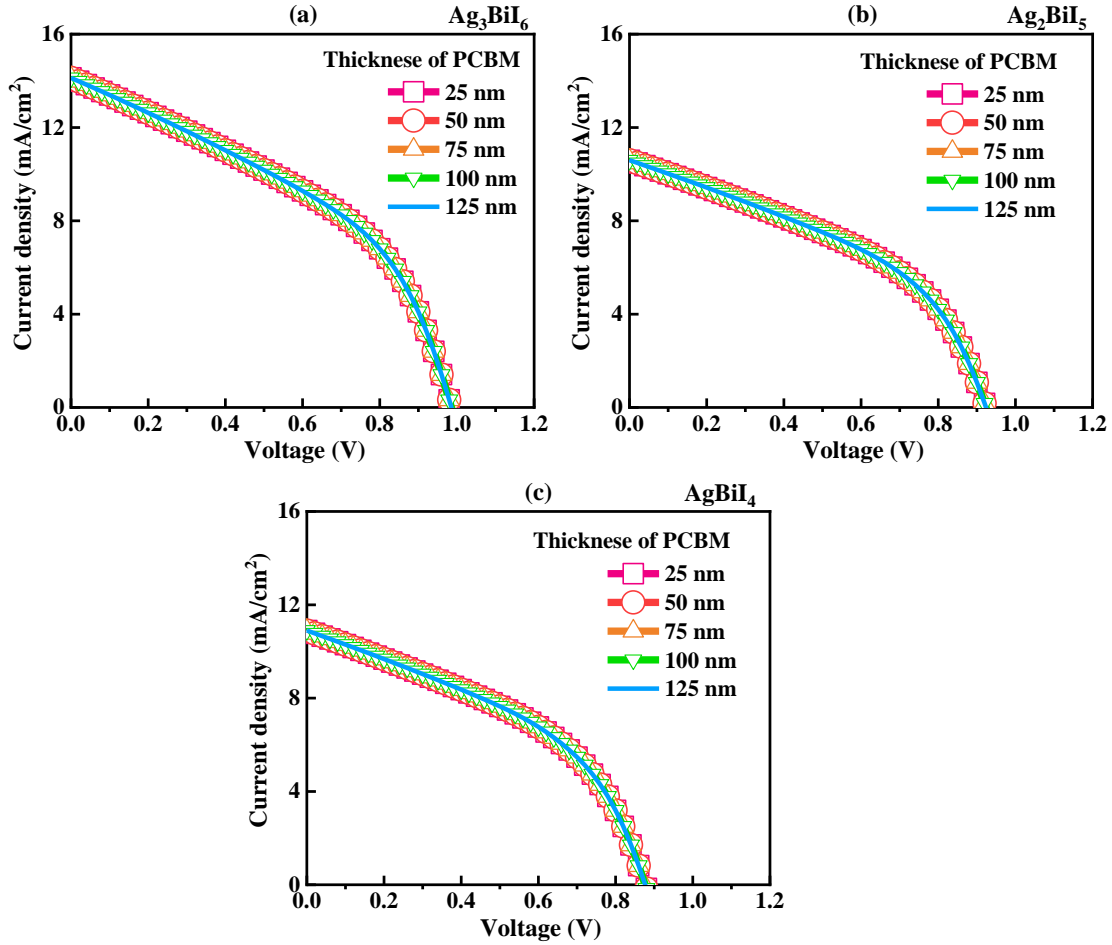


Figure 5.5 The impact of J-V on solar cell devices as the PCBM thickness varies for (a) Ag₃BiI₆, (b) Ag₂BiI₅, and (c) AgBiI₄ devices.

The J-V characteristics data of Ag₃BiI₆, Ag₂BiI₅, and AgBiI₄ are almost identical for 25 to 125 nm, proving the ETL thickness effect is not that dominant. Previous studies have also reflected this validation.²¹

5.3.1.4 Effect of total defect density on PV parameters

For future advancements in PCE, it is essential to investigate high-quality rudorffite-based solar cells with low defect densities and less non-radiative recombination processes. A thorough understanding of interlayer and absorption layer defect creation is essential for successfully constructing stable, highly effective PSCs. In this investigation, we showed that an increase in defects density in the rudorffite layer reduces solar cell performance metrics such as J_{SC} , V_{OC} , PCE, and FF. **Figure 5.6(a-c)** demonstrates that as the total defect density increased from 1.0×10^{10} to $1.0 \times 10^{16} \text{ cm}^{-3}$, the PCEs of different materials experienced a significant decrease. Among the three materials, Ag_3BiI_6 , which initially had the highest PCE of 16.94%, dropped to 0.92%. Ag_2BiI_5 also experienced a decline from 12.15% to less than 0.75%. Similarly, AgBiI_4 , initially with an 11.85% PCE, decreased to less than 0.72%, making it the material with the lowest performance. In the case of Ag_3BiI_6 , the J_{SC} value decreases from 20.50 to 3.56 mA/cm^2 , the FF value decreases from 0.76 to 0.30, and also V_{OC} , following a similar trend, decreases from 1.09 to 0.86 V compared to when defect density is 1.0×10^{10} to $1.0 \times 10^{16} \text{ cm}^{-3}$. On the other hand, for Ag_2BiI_5 , J_{SC} , V_{OC} , and FF values decrease from 15.54 to 2.78 mA/cm^2 , 1.02 to 0.81 V, and 0.76 to 0.33, respectively, at the same reference point of total defect density. Last but not least, the same trend is followed by AgBiI_4 . J_{SC} , V_{OC} , and FF values decrease from 16.05 to 2.77 mA/cm^2 , 0.98 to 0.76 V, and 0.76 to 0.34, respectively, comparing total defect density points 1.0×10^{10} and $1.0 \times 10^{16} \text{ cm}^{-3}$.

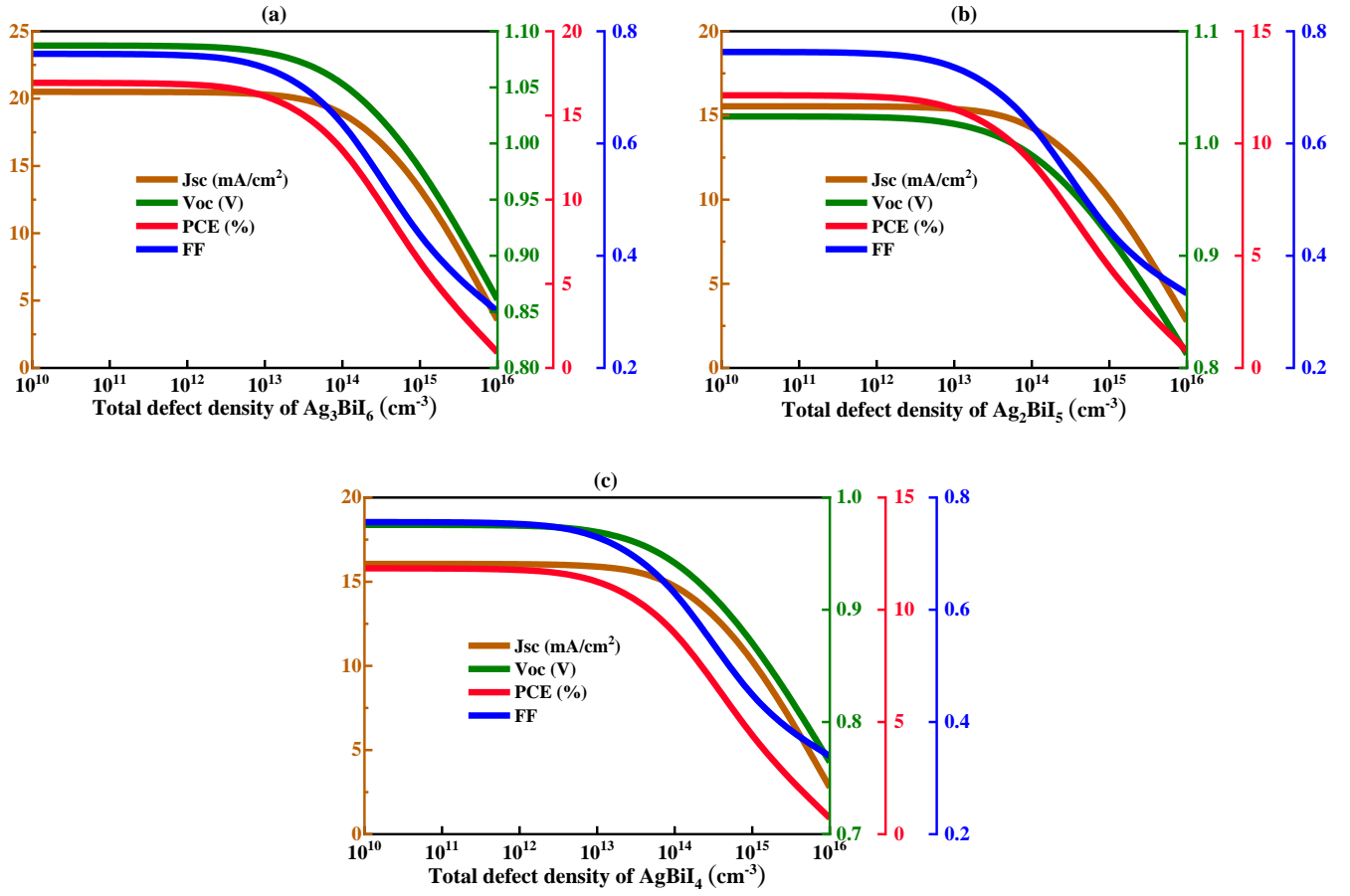


Figure 5.6 Impact of J_{SC} , V_{OC} , FF, and PCE on the total defect density of (a) Ag_3BiI_6 , (b) Ag_2BiI_5 , and (c) AgBiI_4 solar devices.

Increasing defect density can lower J_{SC} and V_{OC} , reduce charge carrier lifetimes, and increase the amount of recombination in a solar cell. In addition, it may lead to higher levels of leakage currents, which in turn reduces efficiency. These combined causes ultimately lead to a decline in the overall performance of the solar cell.

5.3.1.5 Impact of HTL/Rudorffites and ETL/Rudorffites interface defect

The efficiency and overall performance of a solar cell device are directly affected by interfacial recombination, which is essential to its operation. Furthermore, the efficacy of the device may be determined by analyzing and comprehending the solar cell's performance in terms of interfacial defect density. In **Figures 5.7(a, c, e)** illustrate the HTL/Rudorffite interfacial defect density. On the contrary, **Figures 5.7(b, d, f)** illustrate the Rudorffite/ETL interfacial defect density. The interfacial defect density was adjusted in our study from $1.0 \times 10^{10} \text{ cm}^{-2}$ to $1.0 \times 10^{14} \text{ cm}^{-2}$. It is evident that when defect concentrations are above $1.0 \times 10^{12} \text{ cm}^{-2}$ at either contact for the HTL/Rudorffite interface, the PCE drops off quickly. In the PEDOT:PSS/Ag₃BiI₆ interface, an increase in interfacial defect density from $1.0 \times 10^{10} \text{ cm}^{-2}$ to $1.0 \times 10^{14} \text{ cm}^{-2}$ results in a 52.2% drop in PCE. And 50.4% reduction in PCE is attained by increasing the interfacial defect density from $1.0 \times 10^{10} \text{ cm}^{-2}$ to $1.0 \times 10^{14} \text{ cm}^{-2}$ in the PEDOT:PSS/Ag₂BiI₅ interface case. At the PEDOT:PSS/AgBiI₄ interface, PCE decreases by 51.6% when interfacial defect density rises from $1.0 \times 10^{10} \text{ cm}^{-2}$ to $1.0 \times 10^{14} \text{ cm}^{-2}$. In the case of Ag₃BiI₆/PCBM, Ag₂BiI₅/PCBM, and AgBiI₄/PCBM, power conversion efficiency remains unchanged even after increasing Rudorffite/ETL interface defect density as shown in **Figure 5.7(b, d, f)**. The J_{SC} falls fast when the defect concentrations exceed $1.0 \times 10^{13} \text{ cm}^{-2}$ at the three interface contacts for the HTL/Rudorffite. For the interface between PEDOT:PSS and Ag₃BiI₆, a little increase in the density of defects at the interface, from $1.0 \times 10^{10} \text{ cm}^{-2}$ to $1.0 \times 10^{14} \text{ cm}^{-2}$, leads to a fall in J_{SC} from 14.12 mA/cm² to 10.32 mA/cm², representing a considerable decline of 26.9%.

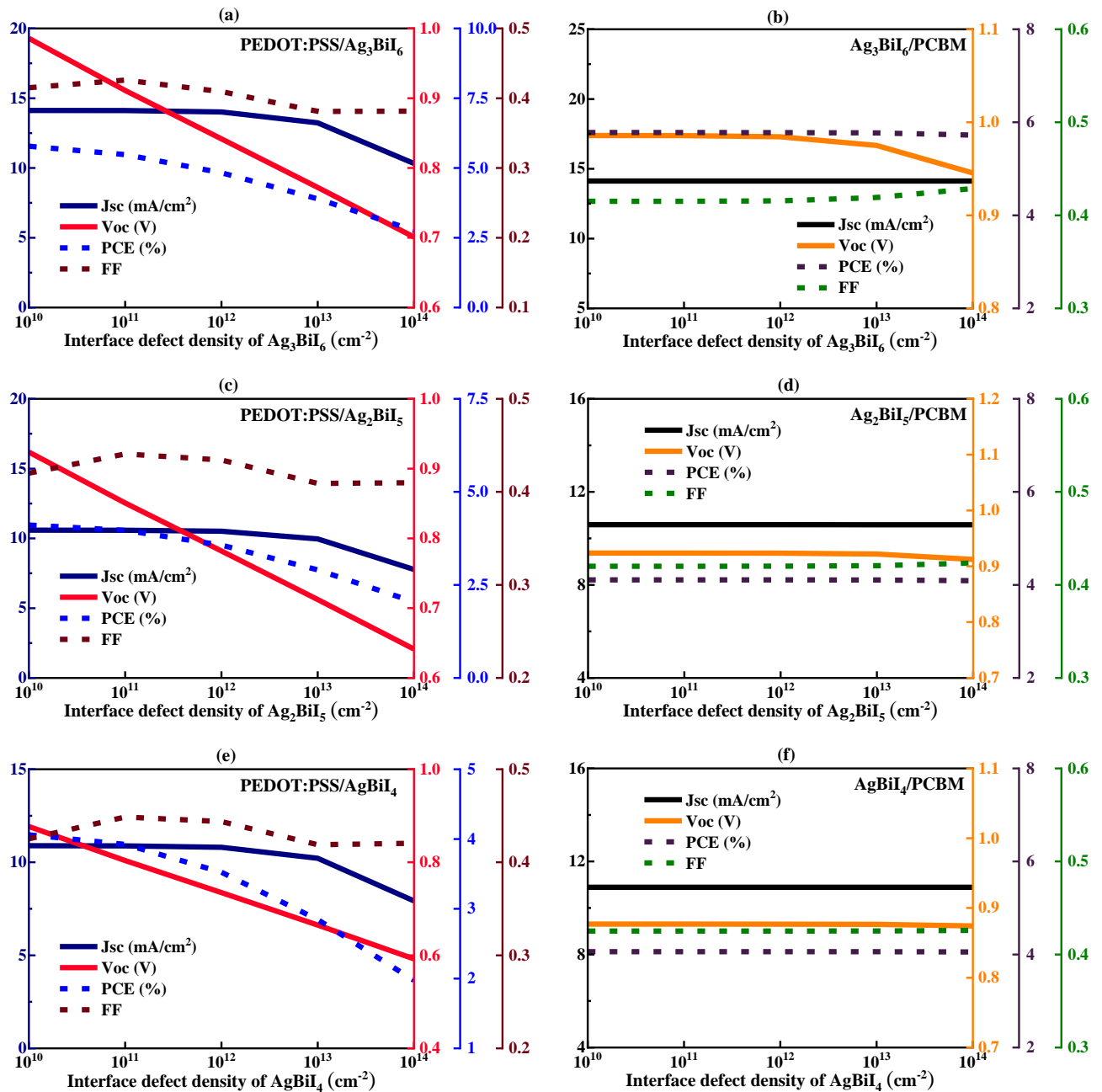


Figure 5.7 The PV parameters vary in relation to the interface defect density for the following scenarios: (a) PEDOT:PSS/Ag₃BiI₆ interface, (b) Ag₃BiI₆/PCBM interface, (c) PEDOT:PSS/Ag₂BiI₅ interface, (d) Ag₂BiI₅/PCBM interface, (e) PEDOT:PSS/AgBiI₄ interface, and (f) AgBiI₄/PCBM interface.

Additionally, PEDOT:PSS/Ag₂BiI₅ interfaces have a 26.5% reduction in J_{SC} , whereas PEDOT:PSS/AgBiI₄ interfaces have a 27.2% reduction. In contrast, the interface defect density does not affect the Ag₃BiI₆/PCBM interface, Ag₂BiI₅/PCBM interface, or AgBiI₄/PCBM interface. Moreover, earlier observations have shown that changes in ETL thickness have no effect on the photovoltaic characteristics. The stability of J_{SC} is due to the efficient electron transport from the rudorffite to the ETL layer. According to **Figures 5.7(a, c, e)**, the linear decrease in V_{OC} for HTL/Rudorffites interfaces indicates that a higher interface defect density results in a greater recombination of charge carriers at interfaces. Voltage is lost due to charge carrier recombination because fewer carriers are available to produce voltage. Charge carriers may get trapped in interface defects, impeding their motion. This trap-assisted recombination shortened the lifespan of charge carriers, which lowers the V_{OC} . Interface defects can cause charge redistribution inside the material by causing band bending at the interface. V_{OC} may drop due to changing the energy levels available for charge separation and collection. For PEDOT:PSS/Ag₃BiI₆, PEDOT:PSS/Ag₂BiI₅, and PEDOT:PSS/AgBiI₄, the reduction in percentage is obtained at 29.3%, 30.4%, and 32.9%, respectively. As shown in **Figures 5.7(b, d, f)**, the V_{OC} for PCBM/Ag₃BiI₆, PCBM/Ag₂BiI₅, and PCBM/AgBiI₄ interfaces was constant across defect densities.

The FF is calculated by multiplying the open-circuit voltage (V_{OC}) and the short circuit current (I_{SC}) of the solar cell by the maximum power output. The decrease in V_{OC} and I_{SC} may be partly balanced as interface defect density rises, resulting in a negligible net change in FF. It can be validated from **Figures 5.7(a, c, e)** for all HTL/Rudorffite interfaces. On the other hand, also, for all Rudorffite/ETL interfaces, it is flat, with no impact at all, which can be vindicated in **Figures 5.7(b, d, f)**. This can occur if compensating changes are made to the variables impacting V_{OC} and J_{SC} . The solar cell's series resistance (R_s) and shunt resistance (R_{sh}) may be impacted by increases

in interface defect density. However, the total effect on FF can be minimal if changes in R_s and R_{sh} cancel each other out. Interface defects may only sometimes hinder carrier collection efficiency, but they may cause more recombination and shorter carrier lifetimes. The FF may hold steady if carriers can efficiently reach the contacts without significant loss. Only a small area of the device may be impacted by interface defect, with other areas mainly remaining unaffected as shown in **Figures 5.7(a, c, e)**. In **Figures 5.7(b, d, f)**, it is also evident that FF remains unchanged even though the interface defect density was increased for all three Rudorffites/ETL interfaces.

5.3.1.6 Complex impedance analysis

In order to examine the combined effects of ion migration and the recombination-transport dynamics of charge carriers in the tandem solar cell device, the complex impedance (Z) was generated in order to investigate further the effect of the bias voltage on V_{OC} , J_{SC} , FF, and PCE obtained from J-V characteristics. The Nyquist plot of complex impedance, which plots the development of the imaginary component (Z_{im}) against the real part (Z_{re}) for various bias voltages, is shown in **Figure 5.8(a, b, c)**. The impedance spectra shown only one semi-circle for every bias voltage value. These Nyquist plots' semi-circular shape confirms that the space charge area in these solar cells pre-dominates. Furthermore, the semi-circle's circumference shrinks when the bias voltage value rises.

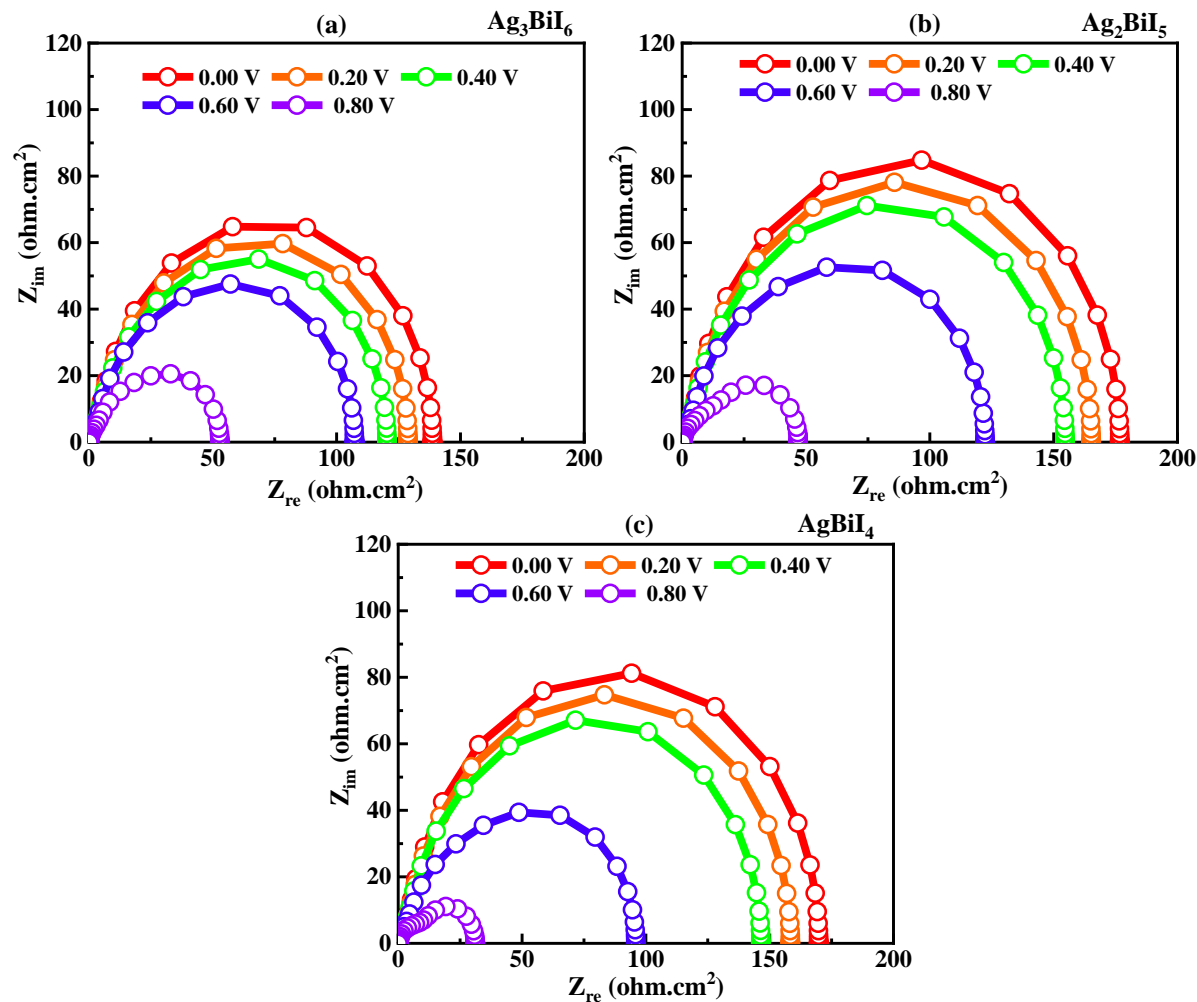


Figure 5.8 The Nyquist plot of impedance for (a) Ag_3BiI_6 , (b) Ag_2BiI_5 , and (c) AgBiI_4 solar cells varies with bias voltage.

Higher bias voltages produce an enhanced interface driving force, enhancing charge transfer kinetics. This leads to decreased charge transfer resistance and a corresponding shrinking of the semi-circle in the Nyquist plot, which explains the observed phenomena. This phenomenon is consistent for all three rudorffites such as Ag_3BiI_6 , Ag_2BiI_5 , and AgBiI_4 .

5.3.2 Performance analysis of tandem cell

5.3.2.1 Study on top and bottom cell

The J-V properties and quantum efficiency (QE) are improved, as shown in **Figure 5.9 (a, b)**, by optimizing the thickness and minimizing defects of the rudorffite base top cell. We ultimately reached the optimal PV parameters, which led to our optimum PCE, after optimizing the thickness of the absorber, ETL, HTL, and reducing defects in the absorber and interfaces. The top sub-cell recorded an initial J_{SC} value of 14.50 mA/cm^2 for Ag_3BiI_6 . This number increased to 18.91 mA/cm^2 after optimization, which is a considerable improvement of 30.41%. Similarly, the optimized J_{SC} value in Ag_2BiI_5 increased by 33.33% from the first measurement of 10.58 mA/cm^2 , reaching 14.11 mA/cm^2 . Lastly, AgBiI_4 showed a 35.18% increase from its starting value of 10.88 mA/cm^2 to an optimum value of 14.71 mA/cm^2 . And 1.01 V for Ag_2BiI_5 , 0.96 V for AgBiI_4 , and 1.07 V for Ag_3BiI_6 are the V_{OC} values for the optimized top sub-cells. The values were initially 0.98 V, 0.92 V, and 0.87 V, in that order. For Ag_3BiI_6 , Ag_2BiI_5 , and AgBiI_4 , the optimized values of 0.75, 0.74, and 0.73 are almost double the original values, indicating a considerable improvement in the FF as well. At the start, Ag_3BiI_6 , Ag_2BiI_5 , and AgBiI_4 had FFs of 0.41, 0.42, and 0.42, correspondingly. The initial PCE of Ag_3BiI_6 was determined to be 5.77%. After optimizing the photovoltaic parameters, this figure skyrocketed to 15.26%, indicating a remarkable gain of almost three times. The initial PCE values for Ag_2BiI_5 and AgBiI_4 were 4.10% and 4.06% correspondingly. After optimization, the PCE values for both materials increased to 10.59% and 10.44%, respectively, representing a more than twofold improvement. These improvements show how well the process of optimizing the top sub-cells in the tandem arrangement performs. The findings of this investigation, which yielded the best PCE, are shown in **Figure 5.9(a)**.

The ability of a particular device designed to convert photons into a pair of electrons and holes (excitons) is known as quantum efficiency. We computed the QE of the single cell arrangement using Ag_3BiI_6 , Ag_2BiI_5 , and AgBiI_4 as the absorber layer for the top cell.

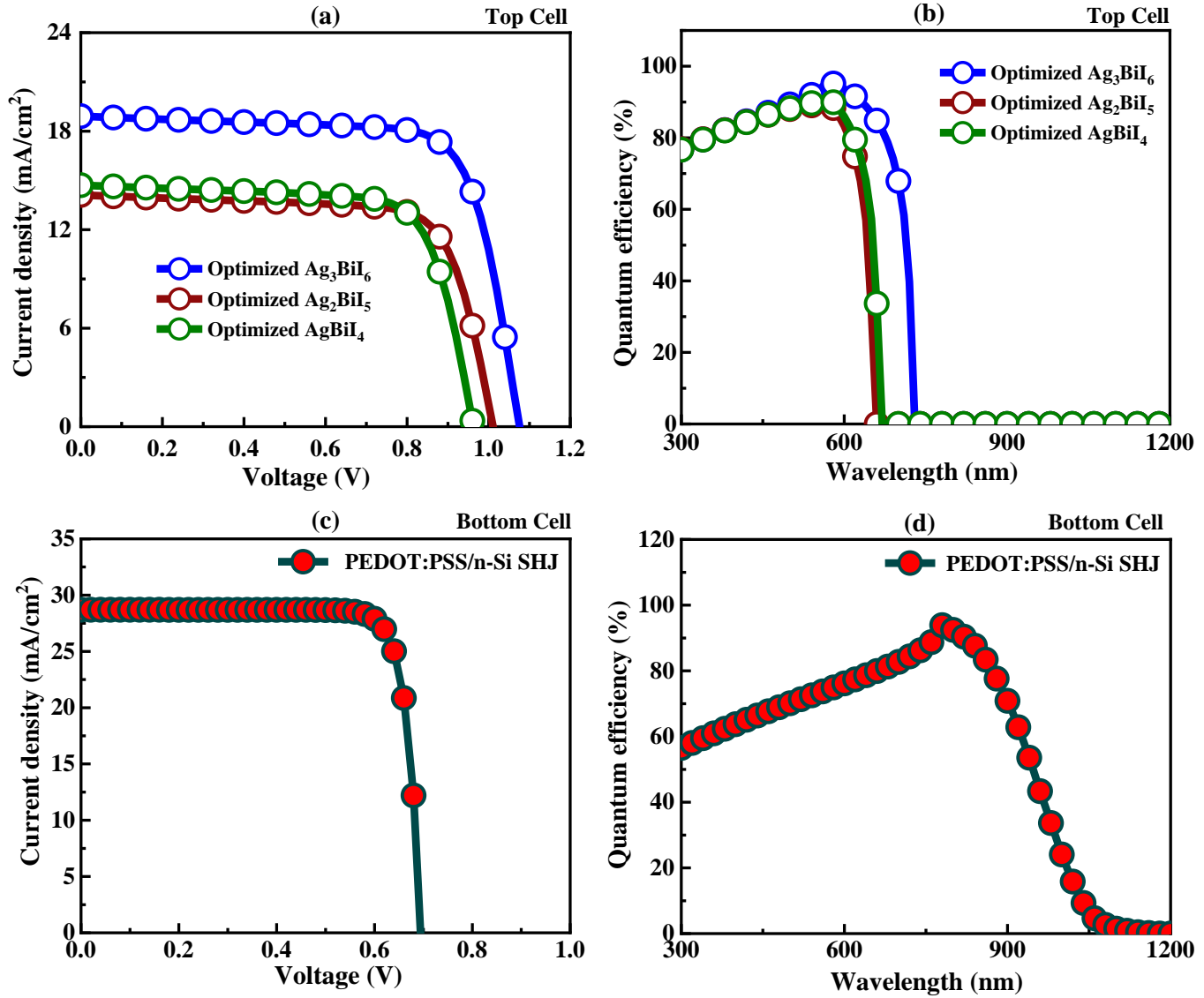


Figure 5.9 (a) The J-V characteristics of rudorffite cells under optimized condition, (b) the QE with respect to wavelength of the rudorffite cells under optimized condition, (c) J-V characteristics of the Si base cell (unfiltered Spectrum), (d) QE with respect to wavelength of the Si base cell.

Across varying wavelengths, the QE of the materials exhibits distinctive behavior in the visible spectrum, as shown in **Figure 5.9(b)**. Rudorffites have a QE of 78% at wavelength 300 nm in the beginning. It reaches its peak at about 600 nm, when Ag_3BiI_6 achieves 97% QE and Ag_2BiI_5 and AgBiI_4 achieve 90% QE. In contrast to Ag_2BiI_5 and AgBiI_4 , the peak of Ag_3BiI_6 shifts to the right, indicating an enhanced QE. The QE gradually declines after this maximum, eventually resulting in zero for Ag_3BiI_6 around 730 nm; Ag_2BiI_5 and AgBiI_4 also exhibit similar declines, approaching zero at 670 nm.

For our investigation of the PEDOT:PSS/Si-based heterojunction (SHJ) solar cell, we used an n+Si as the back surface field (BSF) structure. This structure consisted of the following configuration: ITO/PEDOT:PSS/n-Si/n+Si/Ag. **Figures 5.9(c, d)** exhibit the J-V characteristics and QE results of SHJ. Our investigation yielded the following photovoltaic parameters: a PCE of 16.77%, an FF of 0.84, a J_{sc} of 28.70 mA/cm², and a V_{oc} of 0.70 V. The findings show that the materials and structure work well to improve the performance of tandem solar cells and advance photovoltaics, which is in line with earlier research.^{30,31} Our investigation revealed the following QE values at various wavelengths, as shown in **Figure 5.9(d)**: a modest conversion efficiency in the ultraviolet range is indicated by a QE of 57% at 300 nm. The QE rises to 75% at 600 nm, indicating increased absorption in the visible range. The QE achieves its maximum value of 95% at a wavelength of 777 nm, indicating excellent performance in the near-infrared region. The QE, however, decreases to 73% at 900 nm, indicating a lower capacity for photon conversion at longer wavelengths. The QE eventually drops to zero at 1090 nm, suggesting that the solar cell is unable to convert photons into electrical energy at this wavelength.

5.3.2.2 Energy band diagram of the proposed tandem cell

For the comprehension of tandem solar cells, energy band diagrams are essential, as they depict the energy levels of electrons in various semiconductor materials. The bandgap energies of each layer are optimized by this visualization, which enables the upper cell to absorb high-energy photons while the bottom cell captures lower-energy photons.

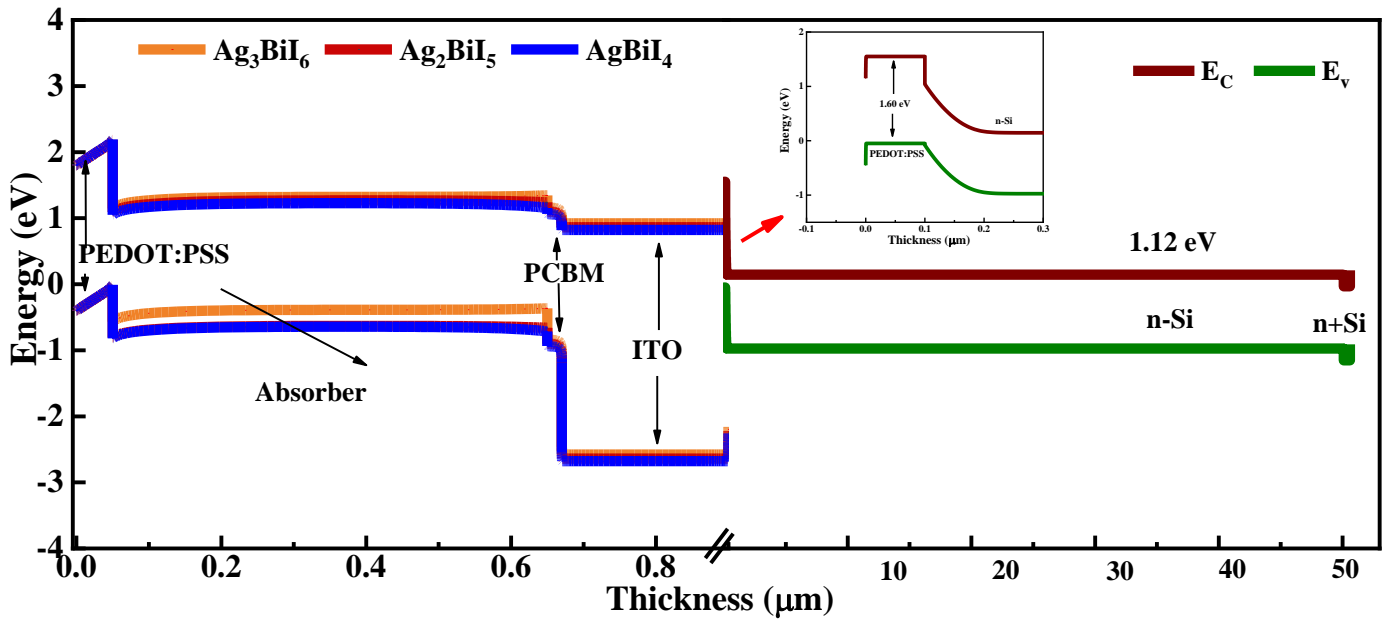


Figure 5. 10 The 2T Tandem Cell's Energy Band Diagram.

Figure 5.10 shows the energy band diagram for the proposed tandem cell, showing the conduction and valence band boundaries. The band gap and doping levels shown in **Tables 5.1** and **5.2** show that there is a p-i-n junction at the top and bottom of the sub-cell. The top rudorffite layer, either Ag_3BiI_6 , Ag_2BiI_5 , or AgBiI_4 , produces electron-hole pairs when exposed to sunshine. While the holes go to the HTL, the electrons are collected and sent to the ETL. The conduction band minimum (E_C) of the ETL is lower, and that of the HTL is greater than the E_C of the layer, resulting in a potential gradient that facilitates the passage of electrons. Similarly, as the valence band

maximum (E_v) of the HTL is more significant and the ETL is lower than the E_v of the perovskite, the extraction of holes into the HTL is preferred. From **Figure 5.10**, it is evident that Ag_3BiI_6 's performance is better than Ag_2BiI_5 or AgBiI_4 . The interface layer and bottom cell's energy band diagrams are in good alignment with the top cell's rudorffite-based schematic.

5.3.2.3 Current matching keeping constant top cell thickness

Tandem solar cells need current matching in order for both layers to operate well and generate their optimum amount of electricity. High-energy photons are captured by the top layer of these cells, while lower-energy photons are captured by the bottom layer. Energy losses happen when the currents from these levels are not aligned, which reduces overall efficiency. In a 2T tandem design, the top and bottom sub-cells are linked in series such that their open-circuit voltages sum up. The top rudorffite cell limits the total J_{SC} and PCE of the tandem design since its J_{SC} is lower than the bottom cell c-Si. Numerous experiments have shown that by modifying the thickness of the absorber layers in the top and bottom sub-cells, 2T tandem cell may achieve greater PCE compared to each of the sub-cells and reach the current-matching circumstance, whereby the J_{SC} readings for the top and bottom cells are made equivalent. Current matching is accomplished in this study by varying the thickness of the c-Si layer in the bottom cell while maintaining the thickness of Ag_3BiI_6 , Ag_2BiI_5 , and AgBiI_4 in the top sub-cell at 600 nm.

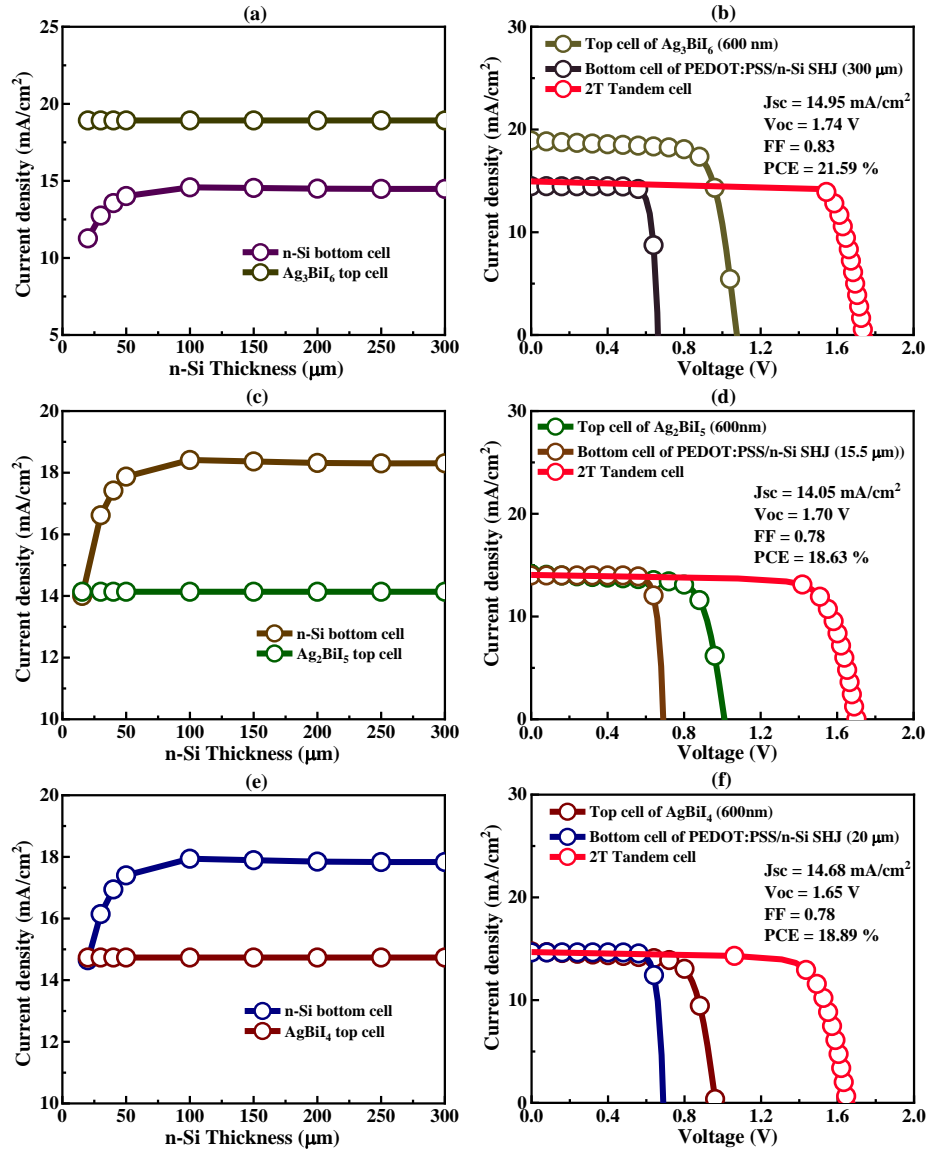


Figure 5.11 The current matching between the top cells, namely (a) Ag₃BiI₆, (c) Ag₂BiI₅, and (e) AgBiI₄, and the bottom sub-cells are dependent on the thickness of c-Si in the bottom cell. The J-V characteristics for the 2T tandem cell and the top and bottom sub-cells under the present without matching and matching situation are shown in (b), (d), and (f).

Table 5.3 PV parameters of top, bottom and 2T tandem cell.

Solar cell	V _{oc} (V)	J _{sc} (mA/cm ²)	FF	PCE (%)
Ag ₃ BiI ₆ top cell	1.08	18.92	0.75	15.32%
PEDOT:PSS/n-Si SHJ bottom cell	0.66	14.48	0.83	7.93%
2T tandem cell (without current matching)	1.74	14.95	0.83	21.59%
Ag ₂ BiI ₅ top cell	1.01	14.14	0.74	10.57%
PEDOT:PSS/n-Si SHJ bottom cell	0.69	14.00	0.84	8.11%
2T tandem cell (with current matching)	1.70	14.05	0.78	18.63%
AgBiI ₄ top cell	0.96	14.74	0.74	10.46%
PEDOT:PSS/n-Si SHJ bottom cell	0.69	14.65	0.84	8.49%
2T tandem cell (with current matching)	1.65	14.68	0.78	18.89%

Figures 5.11 (a, c, e) show the current density vs c-Si thickness graph for three different absorbing layers of rudorffite. As seen in **Figures 5.2(b, d)**, the top cell was lighted by the AM1.5G solar spectrum, while the lower cells were illuminated by the filtered AM1.5G solar spectrum. **Figures**

5.11 (c, e) illustrate that the current matches when the c-Si thickness is 15.5 and 20 μm for Ag_2BiI_5 and AgBiI_4 . **Figure 5.11(a)** shows that in the case of Ag_3BiI_6 , the current densities of the top and bottom cells do not match because the top cell current is larger than the bottom cell current, even when the bottom sub-cell's optimum thickness is up to 300 μm . For Ag_2BiI_5 and AgBiI_4 , **Figures 5.11(d, f)** show the J-V characteristics of tandem solar cells when the currents of the top and bottom cells are matched. Furthermore, **Figure 5.11(b)** displays the J-V characteristics of the Ag_3BiI_6 tandem solar cell without current matching. **Table 5.3** shows the output PV parameters for the top, bottom, and tandem cell. The 2T tandem cell consisting of Ag_2BiI_5 has a PCE of 18.63% under the current matching situation, with the PCEs of the top and bottom cells being 10.57% and 8.11%, respectively. In AgBiI_4 , where current matching also occurs, the PCE for the 2T tandem cell is 18.89%, whereas the PCEs for the top and bottom cells are 10.46% and 8.49%, respectively. During the without current-matching scenario, the PCE associated with the 2T tandem cell containing the Ag_3BiI_6 absorber layer is 21.59%. In contrast, the PCEs of the top and bottom cells are 15.32% and 7.93%, respectively.

5.3.2.4 Current matching keeping constant bottom cell thickness

As we have seen, Ag_3BiI_6 performs best regarding PCE among the three. So, we have implemented the current matching situation by keeping the bottom sub-cell constant with the thickness variation of Ag_3BiI_6 as shown in **Figure 5.12(a)**. When the top sub-cell's thickness is decreased, the current density is also decreased, matching with the current of the bottom sub-cell. After current matching at $J_{\text{SC}} \sim 16.53 \text{ mA/cm}^2$, the V_{OC} is 1.73 V. Currently, the maximum efficiency is reported, which is 22.31% as shown in **Figure 5.12(b)**. Among all rudorffite configurations, the top cell, consisting of 350 nm thickness Ag_3BiI_6 and the bottom cell, 300 μm thickness c-Si, reach a record-high efficiency.

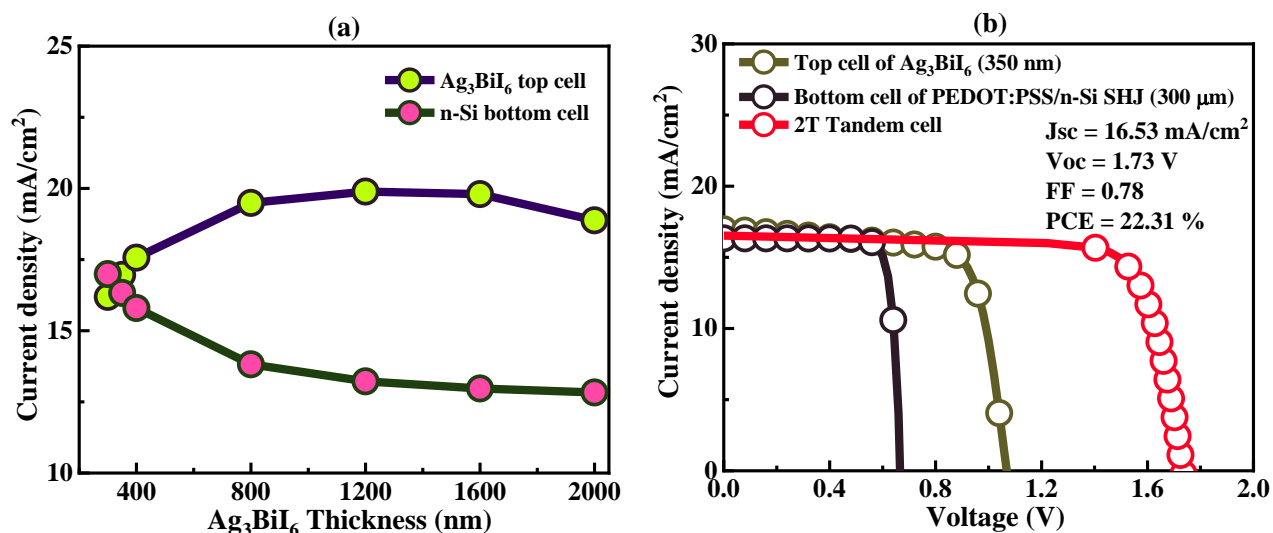


Figure 5. 12 (a) The current matching between the top cells and the bottom sub-cells with varying thickness of Ag₃BiI₆ base top cell, and (b) The J-V characteristics for the 2T tandem cell and the top and bottom sub-cells under the present matching situation.

5.4 Conclusion

For the first time, we have successfully investigated the efficiency of 2T monolithic rudorffites/c-Si tandem solar cells in this work. Through the optimization of the top cells' properties such as absorber's thickness, ETL, and HTL, we achieved notable enhancements in PCE. To be more specific, the PCE of Ag₃BiI₆ rose from 5.77% to 15.26% when it was used as a single cell, which led to a tandem solar cell efficiency of 22.31%. Similarly, Ag₂BiI₅ and AgBiI₄ showed enhancements from 4.10% to 10.59% and 4.06% to 10.44% as a single cell, respectively, achieving tandem efficiencies of 18.63% and 18.89%. These results demonstrate how rudorffite-based materials may advance solar cell technology and open the door to more cost-effective and environmentally friendly energy sources.

5.5 References

- (1) Hasan, S. A. U.; Zahid, M. A.; Park, S.; Yi, J. Stability Challenges for a Highly Efficient Perovskite/Silicon Tandem Solar Cell: A Review. *Solar RRL* **2024**, 8 (6), 2300967.
- (2) Li, X.; Ying, Z.; Wang, X.; Zeng, Y.; Yang, X.; Ye, J. How to Enable Highly Efficient and Large-Area Fabrication on Specific Textures for Monolithic Perovskite/Silicon Tandem Solar Cells? *Inf. Funct. Mater.* **2024**, 1–21.
- (3) Richter, A.; Hermle, M.; Glunz, S. W. Reassessment of the Limiting Efficiency for Crystalline Silicon Solar Cells. *IEEE J. Photovolt.* **2013**, 3 (4), 1184–1191.
- (4) Mailoa, J. P.; Bailie, C. D.; Johlin, E. C.; Hoke, E. T.; Akey, A. J.; Nguyen, W. H.; McGehee, M. D.; Buonassisi, T. A 2-Terminal Perovskite/Silicon Multijunction Solar Cell Enabled by a Silicon Tunnel Junction. *Appl. Phys. Lett.* **2015**, 106 (12), 121105.
- (5) Interactive Best Research-Cell Efficiency Chart | Photovoltaic Research | NREL <https://www.nrel.gov/pv/interactive-cell-efficiency.html> (accessed Jul 29, 2024).
- (6) Zheng, J.; Wang, G.; Duan, W.; Mahmud, M. A.; Yi, H.; Xu, C.; Lambertz, A.; Bremner, S.; Ding, K.; Huang, S.; Ho-Baillie, A. W. Y. Monolithic Perovskite-Perovskite-Silicon Triple-Junction Tandem Solar Cell with an Efficiency of over 20%. *ACS Energy Lett.* **2022**, 7 (9), 3003–3005.
- (7) Hanmandlu, C.; Singh, A.; Karunakara, M.; Boopathi, A.; Huang, Y.-T.; Kavanagh, S. R.; Scanlon, D. O.; Goutham Kumar, S.; Surya, T.; Reddy, T.; Suraj, N.; Honnavar, G. V. Performance Analysis of $A_3B_2X_9$ ($CS_3Bi_2I_9$) Based Perovskite Photovoltaic Tandem

- Structure with Crystalline Silicon (c-Si). *IOP Conf. Ser. Mater. Sci. Eng.* **2024**, 1300 (1), 012005.
- (8) Amri, K.; Belghouthi, R.; Aillerie, M.; Gharbi, R. Device Optimization of a Lead-Free Perovskite/Silicon Tandem Solar Cell with 24.4% Power Conversion Efficiency. *Energies* **2021**, 14 (12), 3383.
 - (9) Owolabi, J. A.; Onimisi, M. Y.; Ukwenya, J. A.; Bature, A. B.; Ushiekpan, U. R. Investigating the Effect of ZnSe (ETM) and Cu₂O (HTM) on Absorber Layer on the Performance of Pervoskite Solar Cell Using SCAPS-1D. *Am. J. Phys. Appl.* **2020**, 8 (1), 8–18.
 - (10) Barman, B.; Ingole, S. Analysis of Si Back-Contact for Chalcogenide Perovskite Solar Cells Based on BaZrS₃ Using SCAPS-1D. *Adv. Theor. Simul.* **2023**, 6 (7), 2200820.
 - (11) Hossain, M. K.; Rubel, M. H. K.; Toki, G. F. I.; Alam, I.; Rahman, M. F.; Bencherif, H. Effect of Various Electron and Hole Transport Layers on the Performance of CsPbI₃-Based Perovskite Solar Cells: A Numerical Investigation in DFT, SCAPS-1D, and WxAMPS Frameworks. *ACS Omega* **2022**, 7 (47), 43210–43230.
 - (12) Verschraegen, J.; Burgelman, M. Numerical Modeling of Intra-Band Tunneling for Heterojunction Solar Cells in SCAPS. *Thin Solid Films* **2007**, 515 (15), 6276–6279.
 - (13) Li, H.; Chen, C.; Jin, J.; Bi, W.; Zhang, B.; Chen, X.; Xu, L.; Liu, D.; Dai, Q.; Song, H. Near-Infrared and Ultraviolet to Visible Photon Conversion for Full Spectrum Response Perovskite Solar Cells. *Nano Energy* **2018**, 50, 699–709.

- (14) Mahawela, P.; Sivaraman, G.; Jeedigunta, S.; Gaduputi, J.; Ramalingam, M.; Subramanian, S.; Vakkalanka, S.; Ferekides, C. S.; Morel, D. L. II–VI Compounds as the Top Absorbers in Tandem Solar Cell Structures. *Mater. Sci. Eng. B* **2005**, *116* (3), 283–291.
- (15) Chen, C.; Zheng, S.; Song, H. Photon Management to Reduce Energy Loss in Perovskite Solar Cells. *Chem. Soc. Rev.* **2021**, *50* (12), 7250–7329.
- (16) Singh, N.; Agarwal, A.; Agarwal, M. Numerical Simulation of Highly Efficient Lead-Free Perovskite Layers for the Application of All-Perovskite Multi-Junction Solar Cell. *Superlattice Microst.* **2021**, *149*, 106750.
- (17) Kowsar, A.; Billah, M.; Dey, S.; Debnath, S. C.; Yeakin, S.; Farhad, S. F. U. Comparative Study on Solar Cell Simulators. *IEEE 2nd International Conference on Innovation in Engineering and Technology (ICIET)* **2019**; 1–6.
- (18) Mondol, N.; Islam, K. S.; Islam, M. R.; Das, S. K. Enhancing Solar Cell Efficiency: Investigation of High-Performance Lead-Based Perovskite-on-Silicon (PVK–Si) Tandem Solar Cells through Design and Numerical Analysis. *AIP Adv.* **2024**, *14* (1).
- (19) Islam, M. A.; Jawad, A.; Jahan, N. A.; Hossain, M. M. Outstanding Conversion Efficiency of 38.39% from a Perovskite/CIGS Tandem PV Cell: A Synergic Optimization through Computational Modeling. *Heliyon* **2023**, *9* (10).
- (20) Hossain, M. K.; Rubel, M. H. K.; Toki, G. F. I.; Alam, I.; Rahman, M. F.; Bencherif, H. Effect of Various Electron and Hole Transport Layers on the Performance of CsPbI₃-Based Perovskite Solar Cells: A Numerical Investigation in DFT, SCAPS-1D, and WxAMPS Frameworks. *ACS Omega* **2022**, *7* (47), 43210–43230.

- (21) Islam, M. A. U.; Kato, S.; Soga, T. An Experimental and Simulation Study of $\text{Cu}_6\text{BiAgI}_{10}$ Photovoltaics with Various Organic and Inorganic Hole Transport Layers for the Improved Photovoltaic Performance of Solar Cells. *Energy and Fuels* **2023**, *37* (24), 19882–19897.
- (22) Wu, M. C.; Wang, Q. H.; Hsiao, K. C.; Chen, S. H.; Ho, C. M.; Jao, M. H.; Chang, Y. H.; Su, W. F. Composition Engineering to Enhance the Photovoltaic Performance and to Prolong the Lifetime for Silver Bismuth Iodide Solar Cell. *Chem. Eng. J. Adv.* **2022**, *10*, 100275.
- (23) Gholami-Milani, A.; Ahmadi-Kandjani, S.; Olyaeefar, B.; Kermani, M. H. Performance Analyses of Highly Efficient Inverted All-Perovskite Bilayer Solar Cell. *Sci. Rep.* **2023**, *13* (1), 1–15.
- (24) Kumari, P.; Punia, U.; Sharma, D.; Srivastava, A.; Srivastava, S. K. Enhanced Photovoltaic Performance of PEDOT:PSS/Si Heterojunction Solar Cell with ZnO BSF Layer: A Simulation Study Using SCAPS-1D. *Silicon* **2023**, *15* (5), 2099–2112.
- (25) Sarker, S.; Islam, M. T.; Rauf, A.; Al Jame, H.; Jani, M. R.; Ahsan, S.; Islam, M. S.; Nishat, S. S.; Shorowordi, K. M.; Ahmed, S. A SCAPS Simulation Investigation of Non-Toxic MAGeI_3 -on-Si Tandem Solar Device Utilizing Monolithically Integrated (2T) and Mechanically Stacked (4T) Configurations. *Solar Energy* **2021**, *225*, 471–485.
- (26) Schygulla, P.; Müller, R.; Lackner, D.; Höhn, O.; Hauser, H.; Bläsi, B.; Predan, F.; Benick, J.; Hermle, M.; Glunz, S. W. Two-terminal III–V//Si Triple-junction Solar Cell with Power Conversion Efficiency of 35.9% at AM1.5G. *Prog. Photovolt.* **2022**, *30* (8), 869–879.
- (27) Chowdhury, M. M.; Debnath, B. Approximation of Carrier Generation Rate in Common

- Solar Cells and Studies for Optimization of N+ p Silicon Solar Cell for AM1. 5G and AM1. 5D. *IEEE 7th International Conference on Electrical and Computer Engineering*, **2012**; 327–330.
- (28) Yang, P.; Liu, P.; Ullah, S.; Wang, J.; Liu, L.; Yang, S.-E.; Guo, H.; Wang, L.; Chen, Y. The Investigation of CsPb (I_{1-x}Br_x)₃/Crystalline Silicon Two-and Four-Terminal Tandem Solar Cells. *Solar Energy* **2021**, *216*, 145–150.
- (29) Hossain, M. J.; Hossain, M. Over 32% Efficient All-Inorganic Two-Terminal CsPbI₂Br/Si Tandem Solar Cells: A Numerical Investigation. *Energy Technol.* **2023**, *11* (3), 2201297.
- (30) Jiang, W.; Wang, Y.; Jiao, C.; Wang, Y.; Zhao, Y.; Lv, M.; Fan, Z.; Fu, Y.; Li, J.; Liu, Q.; He, D. Solution-Processed PEDOT:PSS/p-Si/ZnO Heterojunction Solar Cells. *Phys. Status Solidi* **2023**, *17* (9), 2300168.
- (31) Yang, C.; Luo, Z.; Ma, W.; Li, S.; Lv, G.; Fu, K.; Liu, K.; Li, H.; Sun, H.; Chen, X. Study on the Fabrication of PEDOT:PSS/Si Hybrid Solar Cells Incorporated with F4TCNQ and VTMO. *J. Phys. Chem. C*. **2023**, *127* (17), 7974–7986.

Chapter 6

Integrated study of perovskite/perovskite/c-Si triple junction solar cells with methylammonium bismuth iodide as a key component

6.1 Introduction

The potential cost effectiveness of triple-junction perovskite/perovskite/silicon solar cells is driving their popularity. Perovskite materials are renowned for their affordable manufacturing methods, which include straightforward solutions such as inkjet printing and spin coating. As compared with III-V solar cells, this might result in lower manufacturing costs as well as greater scalability and suitability for large-scale production.¹⁻⁴ Liu et al. achieved a significant breakthrough in their investigation by effectively integrating cyanate-substituted perovskite into a triple-junction solar cell (TJSC) composed of perovskites/perovskites/silicon.⁵ This innovative structure accomplished 27.10% of certified efficiency.⁵ However, Yang et al. predicted, the perovskite/perovskite/Si triple-junction configuration can achieve power conversion efficiencies of up to 35%.⁶ The study shows how perovskite-based solar cells have enormous potential to transform the renewable energy industry. The structure of tandem solar cells affects their performance significantly, especially in contrast with n-i-p and p-i-n structures. Our study is investigating p-i-n based tandem cells that combine perovskite/perovskite and c-Si junctions. Due to the fact that the p-i-n perovskite solar cell has so far demonstrated the best efficiency in tandem solar cell.⁷⁻⁹ On the other hand, the n-i-p shape has been used to get most of the best performance from single-junction perovskite solar cells.^{10,11} The intriguing aspect is that by integrating p-i-n

perovskite solar cells with silicon, we can achieve a higher power conversion efficiency and short-circuit current density, while also minimizing parasitic absorption.^{9,12}

It is crucial to choose the ideal bandgaps for each of the various sub-cells in a triple-junction solar cell in order to maximize the power conversion efficiency (PCE).¹ The band gap of the bottom cell has a significant impact on the theoretical PCE of triple junction. The bandgap of 1.12 eV is used by the bottom cell in our study, which uses crystalline silicon (c-Si). It is reported that Bi-based perovskite materials have band gap of 1.8 – 2.1 eV,¹³ which is suitable for the top cell material of triple junction solar cell. In order to improve the efficiency of the middle cell in this triple junction, we suggest changing the CsPbI₃ bandgap of 1.73 eV to a FAPbI₃ bandgap of 1.51 eV with the introduction of FA doping. This correction is corroborated by the results of Heydarian et al., which demonstrate that the middle cell's efficiency is within this specified range.¹ The overall PCE of the triple-junction solar cell configuration can be substantially enhanced by optimizing the bandgap of the middle cell in this manner. In this research, we aimed to investigate new configurations that would enhance tandem solar cells' efficiency and cost-effectiveness. As part of this study, we examined the characteristics of methylammonium bismuth iodide (MA₃Bi₂I₉) samples both experimentally and in simulation to uncover its potential as a top layer in double and triple junction solar cells. As far as we know, this is the first study to investigate the effectiveness of MA₃Bi₂I₉ as a top layer in tandem structures. In tandem structures of Perovskite/Perovskite and Perovskite/Perovskite/c-Si double and triple junctions, we obtained PCEs of 22.66% and 29.89%, respectively. We find that these results represent a significant improvement over the previous single junction efficiency results obtained by Jain et al. and Ahmad et al.^{14,15} In addition to our research on double and triple junction structures, our study presents a significant step forward in developing cost-effective tandem solar cells.

6.2 Experimental and simulation procedures

6.2.1 Chemicals and reagents

In this experiment, materials purchased from different sources were used. Furuuchi Chemical provided an Indium tin oxide (ITO) coating on a glass substrate, Kanto Chemical provided high-purity solvents such as acetone (99.8%), ethanol (99.5%), and 1-Butanol (99%), Peccell provided TiO₂ paste, and Sigma-Aldrich provided Bismuth (III) iodide (BiI₃, 99%), methylammonium iodide (MAI, ≥99%), and Titanium Diisopropoxidebis (acetylacetonate). This experiment also used an extremely purified N₂ gas and purified distilled water and is also using solvents such as Dimethyl formamide (DMF, 99.5%) and toluene (99.5%).

6.2.2 Fabrication of MBI top cell material

First, we clean and cut (2 × 2) cm pieces of ITO glass substrate to prepare the sample. A total of three ultrasonic washes are conducted on these ITO pieces, twice in acetone and once in ethanol, each for five minutes, at 45 kHz. Any remaining organic solvents are blown off with a nitrogen blower after the substrate has been washed, and then the substrate is treated with ozone for 10 minutes to ensure thorough cleaning. In the next step, we deposited the Compact-TiO₂ (c-TiO₂) layer using 60μL of Titanium Diisopropoxidebis (acetylacetonate) and 1000μL of 1-Butanol. The mixture is homogenized by ultrasonic waves just before the spin coating process, after being mixed for two hours with a rotor. Deposition of the c-TiO₂ layer is achieved by spinning the substrate at 1000rpm for 35 seconds, followed by annealing at 450°C for 30 minutes. We deposit the Mesoporous TiO₂ (mp-TiO₂) layer on top of the c-TiO₂, using 0.15g of TiO₂ paste and 1000μL of ethanol, and these components are mixed for one day with a rotor. Before spin coating, ultrasonic homogenization is performed to ensure a uniform layer. In the case of mp-TiO₂ layer deposition,

the annealing condition remains unchanged, except for the spin-coating process, in which the rpm value has been changed to 1500. Finally, we work in a nitrogen-filled glove box to deposit the absorbing layer of $\text{MA}_3\text{Bi}_2\text{I}_9$ (MBI). Our solution contains 0.4718g of BiI_3 powder and 0.2384g of MAI powder mixed with 1000 μL of DMF as a solvent. In order to effectively disperse the mixture, it is placed on a hot stirrer set at 700rpm and 60°C and stirred for at least 1 hour. The mixture is then dispersed in an ultrasonic homogenizer for 45 minutes immediately before deposition. The MBI spin coating process is conducted at a rotational speed of 4000 rpm for 40 seconds, and 50 μL of MBI solution are dripped onto the (c+mp) TiO_2 substrate. 15 seconds before the spin coating process is ended, 500 μL of toluene is introduced as an anti-solvent. In the final step, the MBI substrate is heated and dried on a hot plate set at 150°C for 10 minutes during the annealing process. We can prepare the samples for further analysis and experimentation by following the steps outlined in **Figure 6.1**.

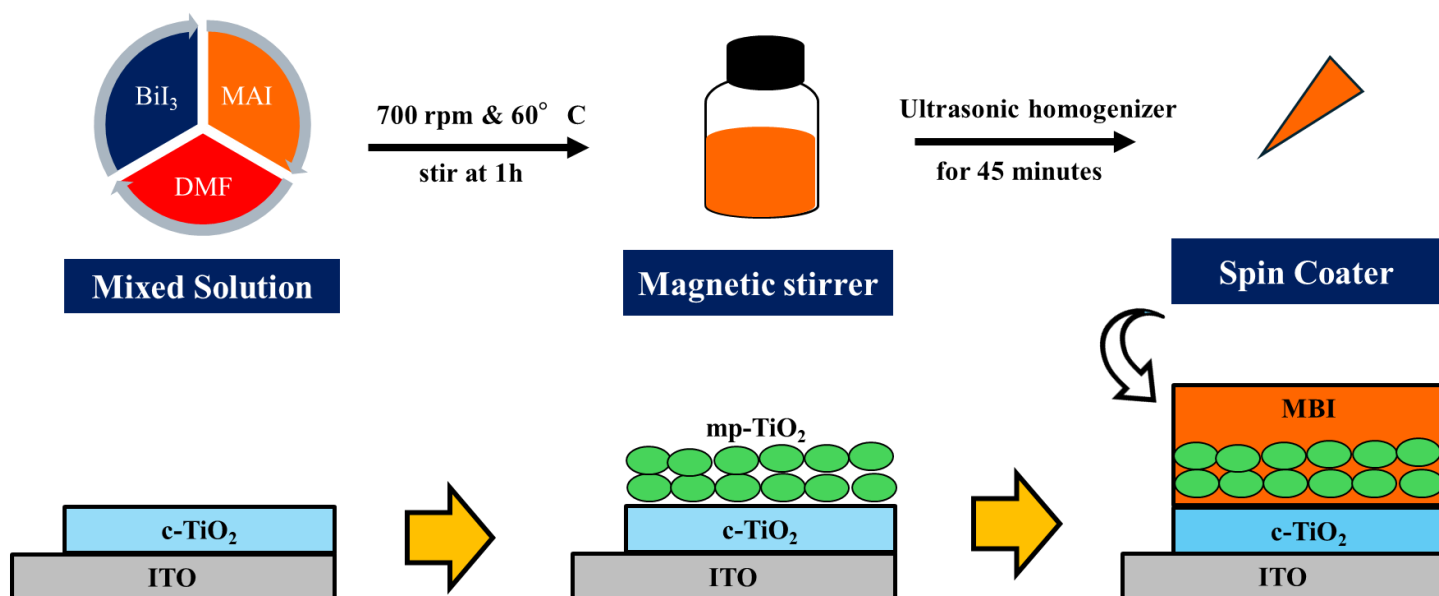


Figure 6.1 Diagram showing the deposition steps for ITO/(c+mp)TiO₂/MA₃Bi₂I₉ film preparation.

6.2.3 Measurements and characterizations

As part of the Rigaku SmartLab facility, X-ray diffraction (XRD) was utilized to analyze the crystallographic characteristics of $\text{MA}_3\text{Bi}_2\text{I}_9$ film, with the following parameters: a scanning step of 0.02 and a scanning speed of 5 degrees per minute, using the Cu-K α target source. We examined the surface morphology of the $\text{MA}_3\text{Bi}_2\text{I}_9$ film using a JSM 6510 model scanning electron microscope, which operated at 8 kV, enabling detailed surface structure analysis. The UV-vis profiles were obtained using a JASCO V-570 spectrophotometer, using both reflection and transmission modes to measure freshly prepared $\text{MA}_3\text{Bi}_2\text{I}_9$ films deposited on (c+mp) TiO_2 /FTO layers. The SCAPS-1D solar simulation software was used to evaluate the performance of photovoltaics, while the Veeco Dektak machine measured film thicknesses.

6.2.4 Device structure and simulation methodology

To determine carrier concentrations, spectral response, energy bands, and J-V characteristics, SCAPS-1D model and simulates the devices using drift-diffusion, Poisson, and continuity equations. In **Figure 6.2**, the top, middle, and bottom sub-cells of a simulated 2T triple junction solar cell are shown. The standard AM1.5G solar spectrum (**Figure 6.3(a)**) at 1 sun intensity is exposed to the p-i-n structure in the top sub-cell. The MBI/(c+mp) TiO_2 /ITO layer was deposited and characterized experimentally, extracting data for simulation analysis. Our next step was to determine the optimal structure for the top cell of the triple junction by exploring different HTL layers. In order to optimize the top cell's HTL and MBI layers, we conducted various characterizations. **Figure 6.1** illustrates the ITO/(c+mp) TiO_2 / $\text{MA}_3\text{Bi}_2\text{I}_9$ film that we fabricated in order to increase our understanding of this film and derive appropriate variables based upon our experiments. In **Figures 6.4, 6.5, and 6.6**, we show different aspects of the film's surface morphology, structural properties, and optical characteristics. Having detailed information on the

MA₃Bi₂I₉ film's characteristics is crucial to assessing its performance. **Figure 6.3(b)** illustrates the first filtered AM1.5G solar spectrum being exposed to the middle sub-cell structure while the top sub-cell absorbs some of the incident light. As shown in **Figure 6.2**, the composition of the middle sub-cell in this triple junction. The ETL consists of SnO₂, the absorber consists of FA_xCS_{1-x}PbI₃, and the HTL consists of Spiro-OMeTAD. The bottom sub-cell structure is also illuminated by the second solar spectrum filtered according to AM1.5G because before reaching the bottom sub-cell, the incident light is partially absorbed by both top and middle sub-cells. The silicon heterojunction (SHJ) structure completes the bottom sub-cell of this triple junction. Triple junctions have the following band gaps: 2.11 eV for the top sub-cell, 1.73 to 1.51 eV for the middle sub-cell, and 1.12 eV for the bottom sub-cell. The recombination layer in the 2T triple junction configuration establishes a series connection between the three sub-cells. By interconnecting the sub-cells, this recombination layer ensures an efficient flow of current. In this triple junction structure, the recombination layer acts as a perfect tunnel junction with no losses in either electrical or optical signals at the interfaces. Consequently, the recombination layer is not taken into consideration throughout the process of the simulation. It is crucial to highlight that this approach is often used for simulating tandem solar cells.¹⁶⁻¹⁸

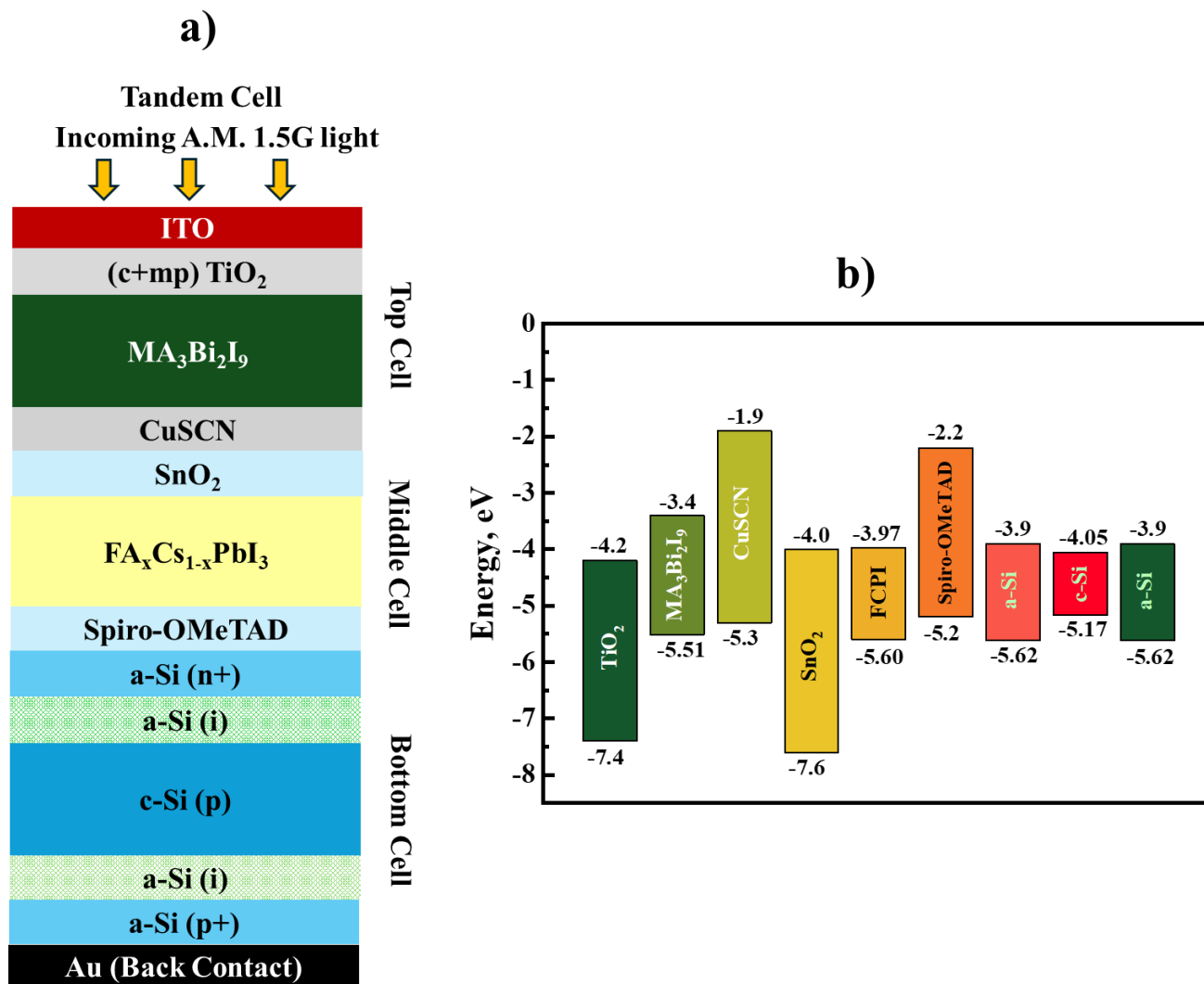


Figure 6.2 (a) The configuration of 2T Perovskite/Perovskite/c-Si Triple junction solar cell, and (b) the alignment of each energy band. FA_{0.45}CS_{0.55}PbI₃ was assumed as FCPI.

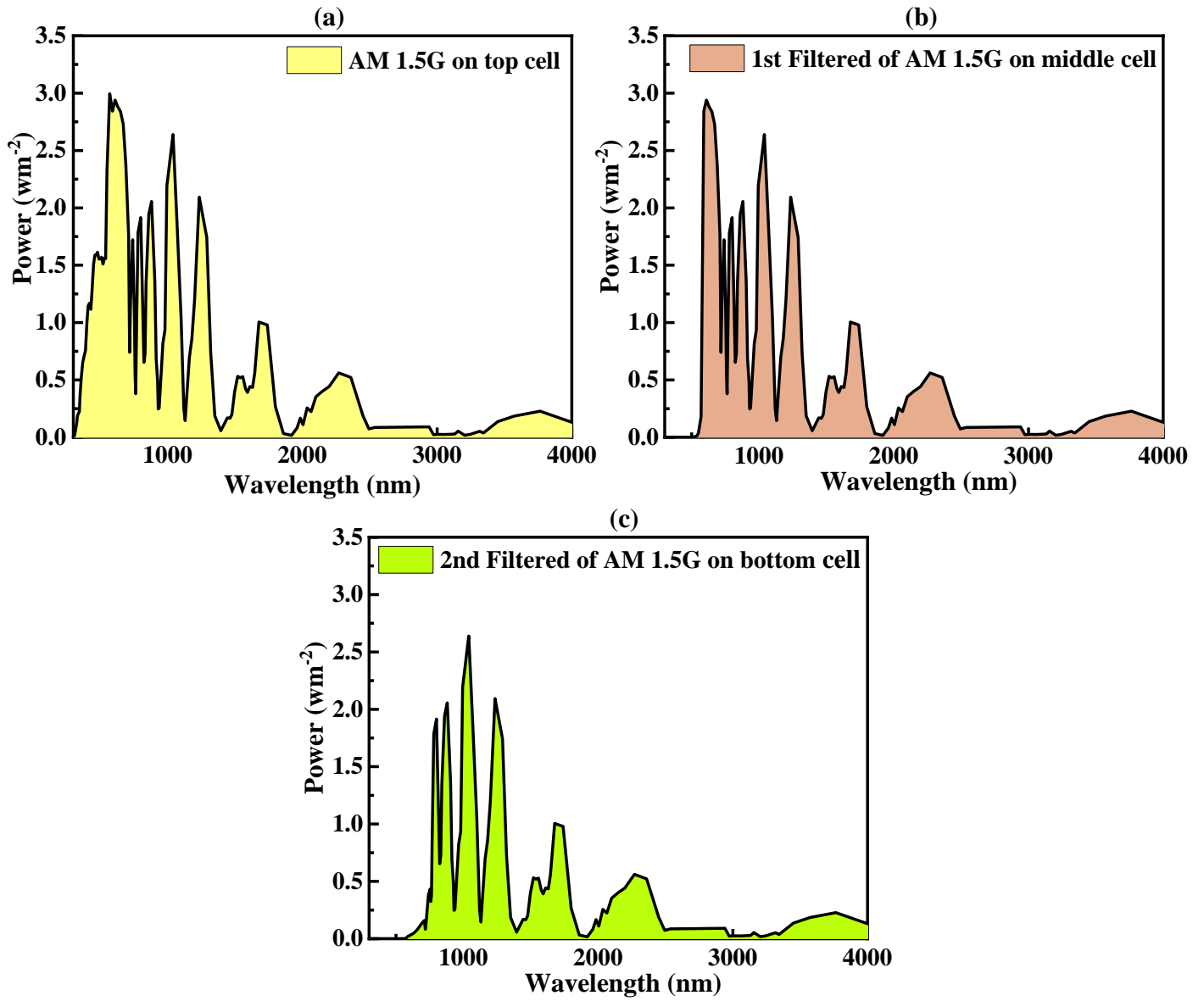


Figure 6.3 (a) the standard AM1.5G spectrum illuminates on the top cell, (b) middle cell uses 1st filtered spectrum from top sub-cell, and (c) bottom cell uses 2nd filtered spectrum from both top and middle cells.

Based on **Equation 1**, we can calculate the light spectrum transmitted through the top and middle cell as follows:

$$S(\lambda) = S_0(\lambda) \times \exp\left(\sum_{i=1}^n -(\alpha_i(\lambda) \times d_i)\right) \quad (1)$$

The primary solar spectrum, denoted as $S_0(\lambda)$, represents the AM 1.5 spectrum. The variable d refers to the thickness of the active layer, while α represents the absorption coefficient of the substance. As a result of experiments and theoretical reports, **Tables 6.1** and **6.2** summarize the material parameters used to validate the present simulation. Additionally, **Table 6.3** provides details on the interface defects parameters for each interface.

Table 6.1 Employed input parameters for SCAPS-1D's top and middle sub cells.

Parameters	(c+mp) TiO ₂	MA ₃ Bi ₂ I ₉	CuSCN	Spiro- OMeTAD	NiOx	PEDOT:PS S	SnO ₂	CsPbI ₃	FAPbI ₃
Thickness (nm)	150	586 [±]	50	200	100	33	100	2000	320
Band Gap (eV)	3.20	2.11 [±]	3.4	3	3.8	2.2	3.60	1.73	1.51
Electron affinity (eV)	4.2	3.4	1.9	2.20	1.46	2.9	4	3.95	4
Permittivity	10	9.68	10	3	10.7	3	9	6.6	6.6
DOS at CB (cm ⁻³)	2.2×10 ¹⁸	4.98×10 ¹⁹	2.2×10 ¹⁹	2.2×10 ¹⁸	2.8×10 ¹⁹	2.2×10 ¹⁵	2.2×10 ¹⁸	1.2×10 ¹⁹	1.2×10 ¹⁹
DOS at VB (cm ⁻³)	1.8×10 ¹⁹	2.11×10 ¹⁹	1.8×10 ¹⁸	1.8×10 ¹⁹	1×10 ¹⁹	1.8×10 ¹⁸	1.8×10 ¹⁹	2.9×10 ¹⁸	2.9×10 ¹⁸
Electron thermal velocity (cm.s ⁻¹)	1×10 ⁷	1×10 ⁷	1×10 ⁷	1×10 ⁷	1×10 ⁷	1×10 ⁷	1×10 ⁷	1×10 ⁷	1×10 ⁷
Hole thermal velocity (cm.s ⁻¹)	1×10 ⁷	1×10 ⁷	1×10 ⁷	1×10 ⁷	1×10 ⁷	1×10 ⁷	1×10 ⁷	1×10 ⁷	1×10 ⁷
Mobility of electron (cm ² .V ⁻¹ .s ⁻¹)	100	1	100	2.1×10 ⁻³	12	10	100	16	2.7
Mobility of hole (cm ² .V ⁻¹ .s ⁻¹)	25	29.7	25	2.16×10 ⁻³	2.8	10	25	16	1.8
Shallow uniform donor density, N _D (cm ⁻³)	1×10 ¹⁹	1×10 ⁹	0	0	0	0	1×10 ¹⁷	1.3×10 ¹⁶	1.3×10 ¹⁶
Shallow uniform acceptor density, N _A (cm ⁻³)	0	1×10 ⁹	1×10 ¹⁸	1×10 ¹⁸	1×10 ¹⁸	3.17×10 ¹⁴	0	1.3×10 ¹⁶	1.3×10 ¹⁶
Density of defect (cm ⁻³)	1×10 ¹⁵	1×10 ¹⁵	1×10 ¹⁵	1×10 ¹⁵	1×10 ¹⁵	1×10 ¹⁴	1×10 ¹⁵	1.5×10 ¹⁴	1.5×10 ¹⁴
References	14	14	19	19	20	19	20	37	21

In the Superscript ±: experimentally calculated.

Table 6.2 Employed input parameters for SCAPS-1D's bottom sub cell.

Parameters	a-Si:H (n ⁺)	a-Si:H (i)	c-Si (p)	a-Si:H (i)	a-Si:H (p ⁺)
Thickness (nm)	10	5	250000	5	10
Band Gap (eV)	1.72	1.72	1.12	1.72	1.72
Electron affinity (eV)	3.90	3.90	4.05	3.90	3.90
Permittivity	11.9	11.9	11.9	11.9	11.9
DOS at CB (cm ⁻³)	4.5×10 ²¹	4.5×10 ²¹	2.8×10 ¹⁹	4.5×10 ²¹	4.5×10 ²¹
DOS at VB (cm ⁻³)	6.4×10 ²¹	6.4×10 ²¹	1.04×10 ¹⁹	6.4×10 ²¹	6.4×10 ²¹
Electron thermal velocity (cm.s ⁻¹)	1×10 ⁷	1×10 ⁷	1×10 ⁷	1×10 ⁷	1×10 ⁷
Hole thermal velocity (cm.s ⁻¹)	1×10 ⁷	1×10 ⁷	1×10 ⁷	1×10 ⁷	1×10 ⁷
Mobility of electron (cm ² .V ⁻¹ .s ⁻¹)	20	20	1500	20	20
Mobility of hole (cm ² .V ⁻¹ .s ⁻¹)	5	5	450	5	5
Shallow uniform donor density, N _D (cm ⁻³)	1×10 ²⁰	0	0	0	0
Shallow uniform acceptor density, N _A (cm ⁻³)	0	0	1×10 ¹⁷	0	1×10 ²⁰
Density of defect (cm ⁻³)	1×10 ¹⁸	1×10 ¹⁸	2×10 ¹²	1×10 ¹⁸	1×10 ¹⁸
References	16	16	16	16	16

Table 6.3 The input parameter for the interface layer with defects.

Parameters	TiO ₂ /MBI	MBI/CuSCN	SnO ₂ /FCPI	FCPI/Spiro-OMeTAD	a-Si:H/c-Si	c-Si/a-Si:H
Defect type	neutral	neutral	neutral	neutral	neutral	neutral
Capture cross-section of electron (cm ²)	1×10^{-19}	1×10^{-19}	1×10^{-19}	1×10^{-19}	1×10^{-19}	1×10^{-19}
Capture cross-section of holes (cm ²)	1×10^{-19}	1×10^{-19}	1×10^{-19}	1×10^{-19}	1×10^{-19}	1×10^{-19}
Energetic distribution	single	single	single	single	single	single
Reference for defect energy level	0.600	0.600	0.600	0.600	0.600	0.600
Total defect density (cm ⁻³)	1×10^{10}	1×10^{10}	1×10^{10}	1×10^{10}	1×10^{10}	1×10^{10}

6.3 Experimental properties of top cell material

6.3.1 Morphology and structural properties analysis

The morphology of a photovoltaic cell's surface is crucial to its efficiency and ability to convert sunlight into electricity. During the fabrication process, elements such as grain size, pinholes, surface quality, and annealing temperature have a significant influence on solar cell performance. By refining the physical properties of the films, we may improve their absorption of light.²²⁻²⁴ The morphology of the MBI solar cells fabricated using DMF and the influence of the preparation method showed a distinctive flake-like morphology with equally distributed crystal grains, as shown in **Figure 6.4**. The growth of flakes parallels the surface of the film.

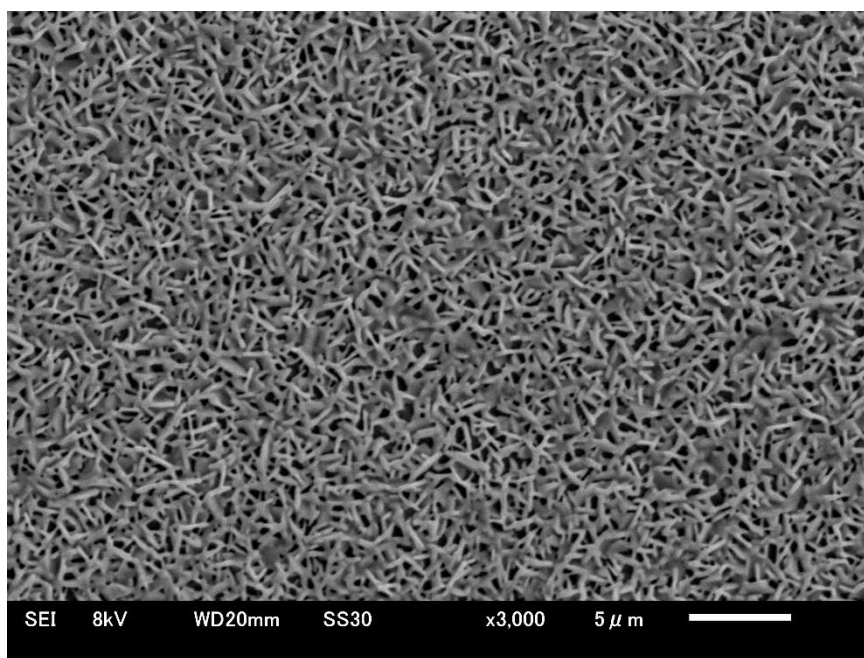


Figure 6.4 The Flake-shaped MBI surface morphology at 150°C.

The few pinholes are visible between the two flake-type grains, where filled (c+mp)TiO₂ scaffolds can be seen on the substrate. However, the MBI perovskite layer is not completely covered on the surface. Researchers in the past have also observed this incomplete coverage.²⁵⁻²⁸ Due to the rate of grain growth exceeding the rate of nucleation the film experiences few pores.²⁹

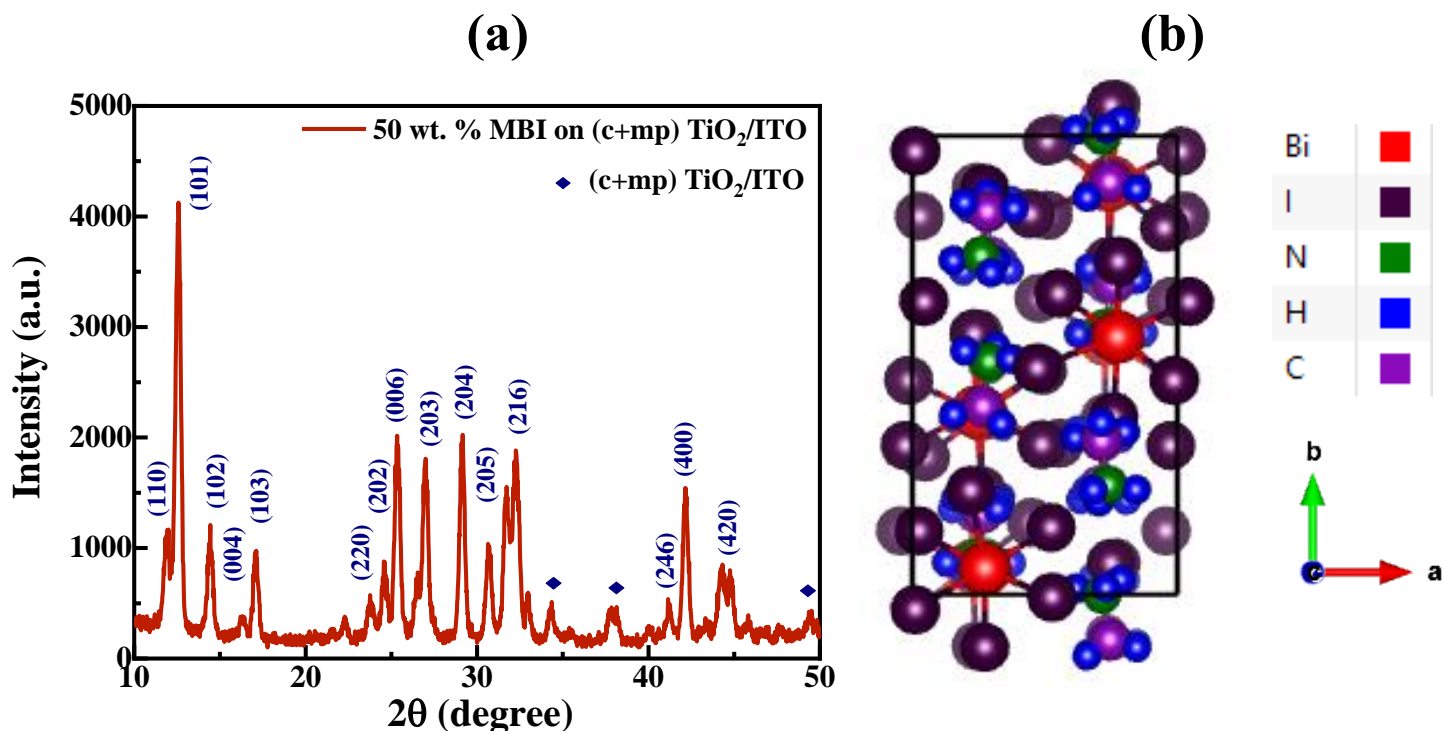


Figure 6.5 (a) XRD analysis of MBI film annealed at 150°C and (b) crystal structure.

Solar cell research is greatly aided by XRD analysis as it provides insights into the crystal structure and phase purity of materials, which directly influence the efficiency and performance of the cells. Through the use of XRD spectroscopy, the structural properties of the MBI film on a (c+mp)TiO₂/ITO substrate have been thoroughly analyzed, as illustrated in **Figure 6.5(a)**. The analysis of the XRD pattern in the MBI film indicated that it crystallizes with a hexagonal crystal structure and displays discrete peaks at different angles of 2θ. In **Figure 6.5(b)**, we can see the three-dimensional view of MBI's hexagonal crystal structure. The peaks in the spectrum were

observed at 11.92°, 12.50°, 14.51°, 16.31°, 17.04°, 23.80°, 24.65°, 25.50°, 26.98°, 29.19°, 30.78°, 32.27°, 41.13°, 42.09° and 44.32°, corresponding to the planes of (110), (101), (102), (004), (103), (220), (202), (006), (203), (204), (205), (216), (246), (400), and (420). The (101) plane showed the highest intensity peak at 12.53°, indicating a high degree of crystallinity and a preference for this orientation. Moreover, there are three additional peaks at 34.39°, 37.98°, and 49.38° corresponding to the composite (c+mp)TiO₂/ITO substrate, which confirms that the composite film was successfully deposited. In order to optimize the performance of photovoltaic materials, valuable structural insights can be gained from the XRD analysis.

6.3.2 Optical Properties Analysis

To maximize solar cell efficiency, material choice, and device quality, it is crucial to understand optical properties. In addition to evaluating how solar cells absorb, transmit, and reflect light, metrics such as absorption coefficients provide insight into how well materials capture photons and convert sunlight into energy. There is a wide range of efficacy demonstrated by different materials, largely determined by the optical properties of those materials.²⁸¹ The unique optical property of MBI film is that they are highly interconnected with their properties of transmittance, reflectance, and absorption as shown in **Figure 6.6**. A film's transmittance measures the amount of light it allows to pass through it, while its reflectance measures how much light it reflects back. It is apparent from **Figure 6.6** that the MBI film exhibits low transmittance and reflectance up to nearly 600 nm in the visible wavelength range, also representing a high absorption of light within those wavelength ranges. For solar cells to absorb light efficiently, this is essential.

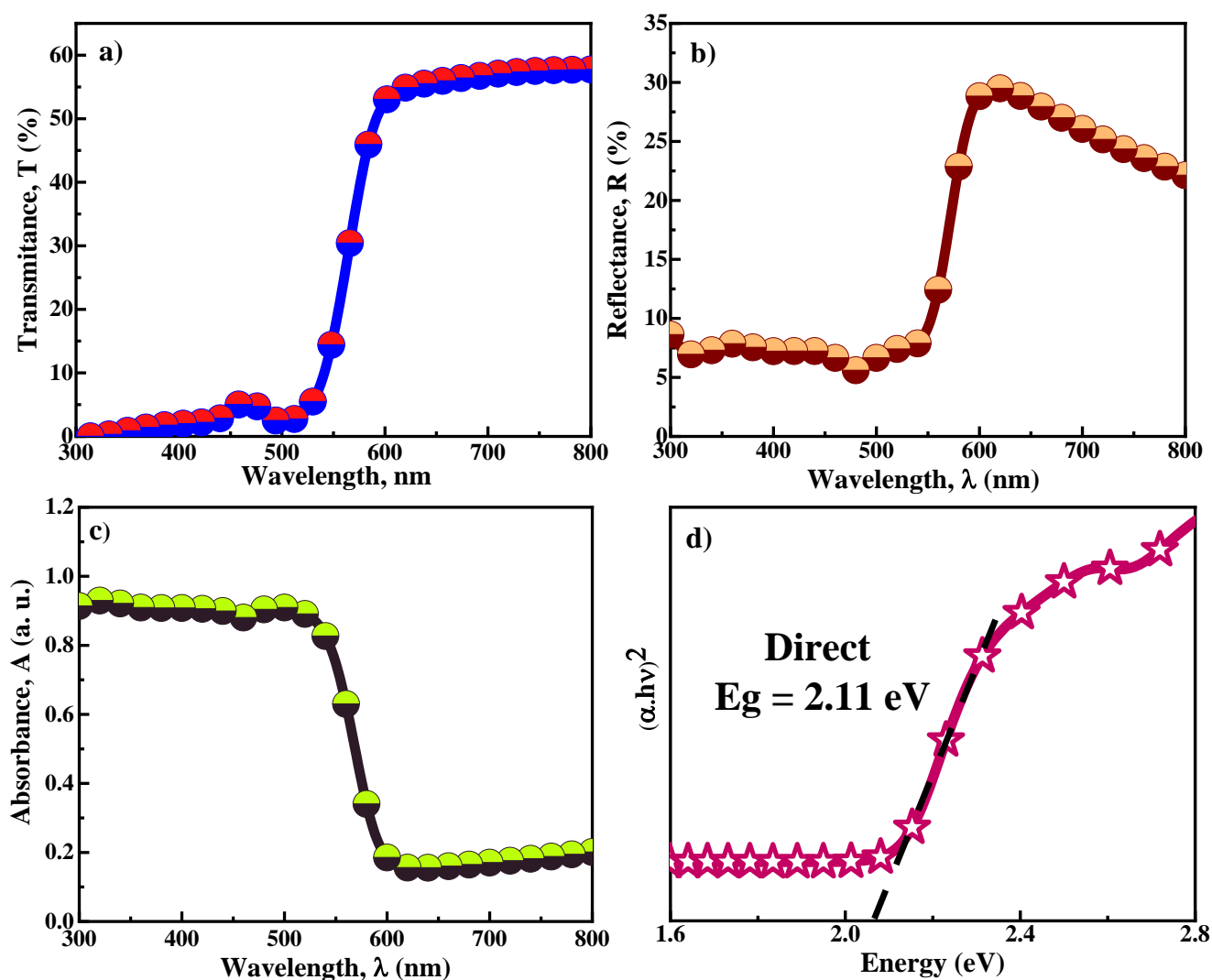


Figure 6.6 At the post-annealing temperature, MBI film presents the following: (a) transmittance spectrum; (b) reflectance spectrum; (c) absorbance spectrum; and (d) optical band gap.

The exceptional absorption characteristics of this material are attributed to its distinct structure and composition, along with a narrow optical band gap of 2.11 eV. The MBI film has a thickness of 586 nm, which helps improve its significant amount of absorption. The film exhibits somewhat higher transmittance and reflectance at wavelengths between 600 and 800 nm, which suggests slightly reduced absorption in that region. **Figure 6.6(d)** shows that the band gap of the MBI film,

as calculated by the Tauc equation, is 2.11 eV. To get the band gap of a film, we may express the Tauc equation as follows:

$$\alpha h\nu = A(h\nu - E_g)^n \quad (1)$$

The scenario in which A remains constant is known as the tauc variable. Next, the number n describes the transition phase.^{31,32} In this experiment n=2 was used due to direct transition.

6.4 Simulation analysis of top cell

6.4.1 Energy alignment, generation and recombination rate analysis

For understanding of the energy levels within a photovoltaic cell is greatly enhanced by seeing the band diagram of a photovoltaic cell, which serves to visualize both the intricate movements of holes and electrons within the cell. Due to the multiple layers and diverse types of materials in solar cells, they exhibit distinct energy levels and bands. Depending on how well these layers harmonize, a cell will be able to generate voltage and current. In order to achieve this, various techniques can be used, including optimizing interfaces, adjusting the band gaps of absorbent layers, and carefully selecting suitable materials for HTLs and ETLs. In **Figure 6.7(a-d)** illustrates a series of band spectrum alignment diagrams between MBI absorber and other layers for different HTLs, as well as the quasi-Fermi electron and hole levels. According to these diagrams, the minima and maxima of the conduction and valance band in the E_C and E_V are visually represented by F_n and F_p , respectively. There are same three layers in each of these architectures: the substrate is FTO, the ETL is (c+mp)TiO₂, and the absorber layer is MBI.

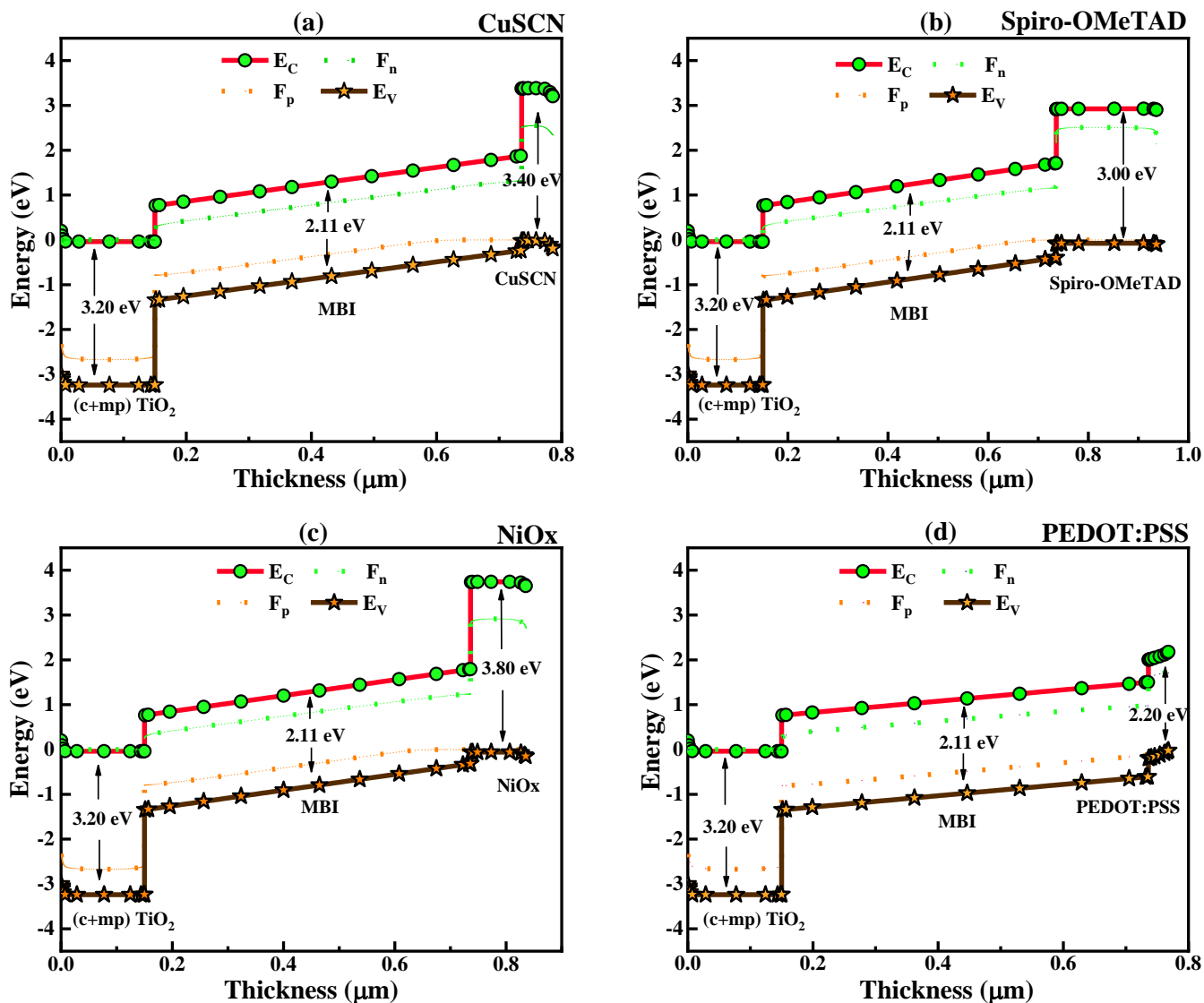


Figure 6.7 The alignment of the energy bands of MBI base solar cells with different HTLs: (a) CuSCN, (b) Spiro-OMeTAD, (c) NiOx, and (d) PEDOT:PSS.

The alignment of various HTLs with respect to the MBI perovskite layer is shown in **Figure 6.7**. As CuSCN, Spiro-OMeTAD, and NiOx have conduction bands that align well with the MBI conduction band, high PCEs are made possible to transport carriers efficiently. As shown in **Figure 6.7(d)**, PEDOT:PSS also exhibits good band alignment, however due to its low optical bandgap, it has a low conversion efficiency. In comparison with Spiro-OMeTAD, NiOx, and PEDOT:PSS,

CuSCN stands out for its higher conductivity, enhancing charge extraction and reducing recombination.

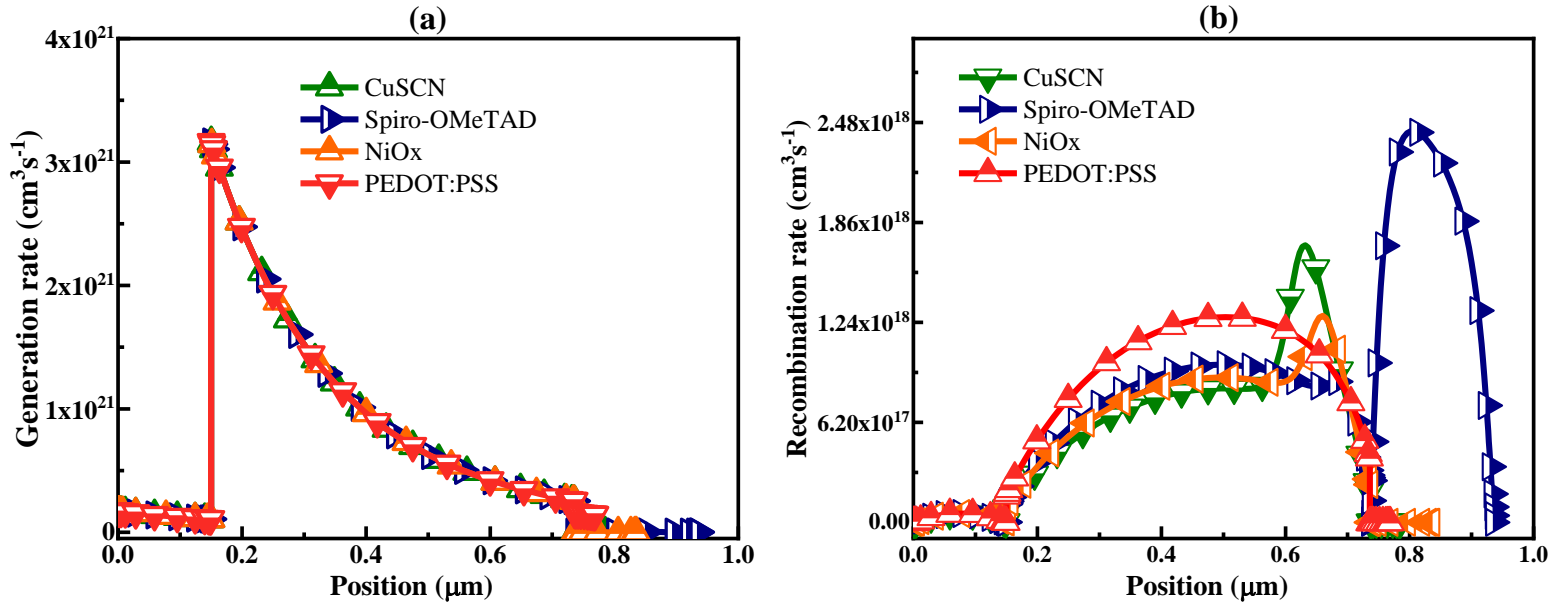


Figure 6.8 MBI base solar cells with various HTLs: (a) generation and (b) recombination rates.

Solar cells produce charge carriers directly based on the generation rate, which affects their device output. By figuring out the recombination rate, you can determine how many of these charge carriers are lost before contributing to the device. In the presence of high generation rates and high recombination rates, many of these carriers are lost before providing current. It is therefore important to increase generation rates while minimizing recombination rates in order to maximize solar cell efficiency. It is shown in **Figure 6.8(a)** how the generation rate of electron-hole pairs in a solar cell is related to the position of MBI base solar devices. Most of the photon generation occurs when photons penetrate ETL to the MBI absorb layer, especially in the 0.10 to 0.20 μm range. In these junctions, it is seen that the highest generation rate for all HTLs is $3.4 \times 10^{21} \text{ cm}^3 \text{s}^{-1}$. Generation rates are uniform because absorption layers are identical in all HTLs, and therefore are

the major determinants. The rate at which these pairs are generated is directly influenced by the efficiency of the MBI layer in photon absorption.

Solar cells lose electrical energy through recombination, the process by which electrons and holes come together, resulting in a loss of electrical energy. There are a number of factors that influence recombination rates of solar cells, including their physical characteristics, their doping levels, and their defects. In **Figure 6.8(b)**, we illustrate the recombination rates in solar cells at different HTLs. In comparison with CuSCN, Spiro-OMeTAD, and NiOx, PEDOT:PSS with MBI exhibits the highest recombination rate in the absorber region. In between the MBI and PEDOT:PSS have a lower barrier potential than others, which is probably due to their higher recombination. Energy mismatches result in increased recombination and, therefore, a decline in device functionality. However, Spiro-OMeTAD displays lower hole mobility and a thicker layer within the HTL region, which leads to higher recombination rates. During recombination, both mobility and lifetime of charge carriers play a significant role, with resulting energy levels playing a crucial role.

6.4.2 Current density vs voltage (J-V) and quantum efficiency (QE) analysis

Conducting a J-V analysis is essential for assessing the efficiency of solar cells and acquiring data on open-circuit voltage, short-circuit current, fill factor, and PCE. These parameters provide valuable information on potential performance improvements. In order to optimize the performance of MBI-based perovskite solar cells, multiple HTLs were used, such as CuSCN, Spiro-OMeTAD, NiOx and PEDOT:PSS with (c+mp)TiO₂ as the ETL and Au as the back contact. In **Table 6.1**, input parameters are displayed for the ETL, various HTLs, and the top cell's absorbing layer. However, the input parameters particularly associated with interface defects are shown in **Table 6.3**. **Figure 6.9(a)** shows the performance characteristics of the MBI solar cell device with organic and inorganic HTLs.

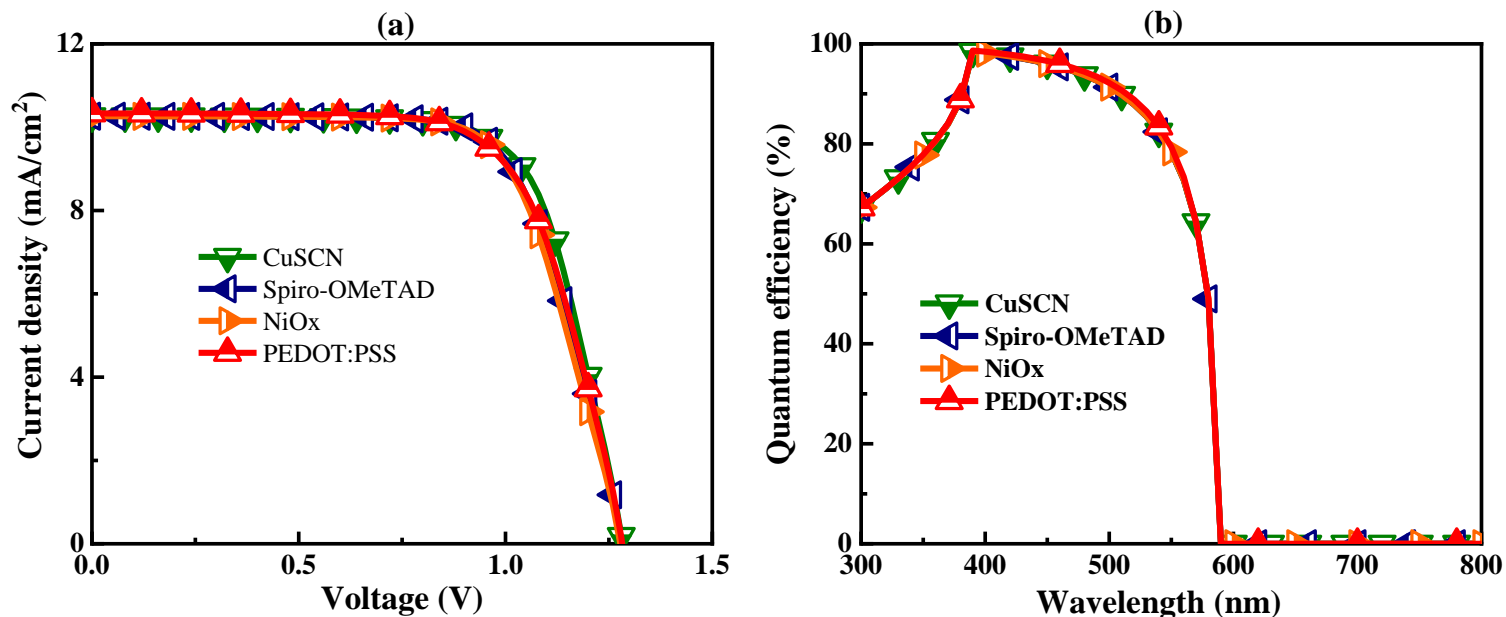


Figure 6.9 Examination of the (a) J-V and (b) QE characteristics of MBI solar cells with varying HTLs.

In comparing the J-V characteristics of all HTLs for MBI perovskite solar cells, CuSCN was found to be the most effective. As compared to other HTLs, CuSCN had higher mobility, low recombination, and better energy alignment. It is due to these factors that PCE and FF are higher. Consequently, CuSCN with MBI perovskite solar cells received 9.4768% efficiency, FF of 0.7201, Voc of 1.2827 V, and Jsc of 10.26 mA/cm². We also compared Spiro-OMeTAD, NiOx, and PEDOT:PSS HTLs. However, their efficiencies ranged from 9.2772% to 9.1427%, giving them slightly lower performances than CuSCN. This series of HTLs had fill factors ranging from 0.7056 to 0.6901 while their open-circuit voltages ranged from 1.2812 to 1.2823 V. PEDOT:PSS had a short-circuit current density of 10.33 mA/cm², while Spiro-OMeTAD and NiOx had values of 10.26 mA/cm². It may be because there is no barrier between the electrode and the thin HTL layer that PEDOT:PSS shows a slightly higher Jsc. According to our analysis, CuSCN has the best potential of all HTLs.

Photovoltaic devices are evaluated based on their QE, which is based on their ability to convert incident photons into electricity. We observed that the QE properties of perovskite solar cells with different HTLs in the structure ITO/(c+mp)TiO₂/MBI/Au remain fairly consistent in comparison to the various HTLs examined. There appear to be no major differences among the HTLs regarding PCE, FF, Voc, and Jsc, anyway, QE properties are relatively unaffected as shown in **Figure 6.9(b)**. These findings indicate that the selection of HTL has little influence on the essential mechanisms of light absorption and charge production in the active layer (MBI) of the perovskite solar cell. **Figure 6.9(b)** illustrates how the QE properties can vary based on the wavelength of the incident photon. As indicated by **Figure 6.9(b)** given, the QE starts at 66% at a wavelength of 300 nm, increases gradually to 100% at 388 nm, and then gradually decreases. As the wavelength increases above 560 nm, the QE drops sharply and becomes zero at 590 nm. It is apparent from this wavelength-dependent behavior that the MBI perovskite solar cell is sensitive to different solar spectral regions.

6.4.3 Impact of MBI thickness and total defect density

To maximize photovoltaic cell efficiency, our analysis searches for MBI absorbing layer thicknesses that minimize energy loss and enhance overall performance. Charge carriers can be impeded by defects within the absorbing layer, reducing their ability to generate electricity. Similarly, the absorbing layer's thickness has dual implications.

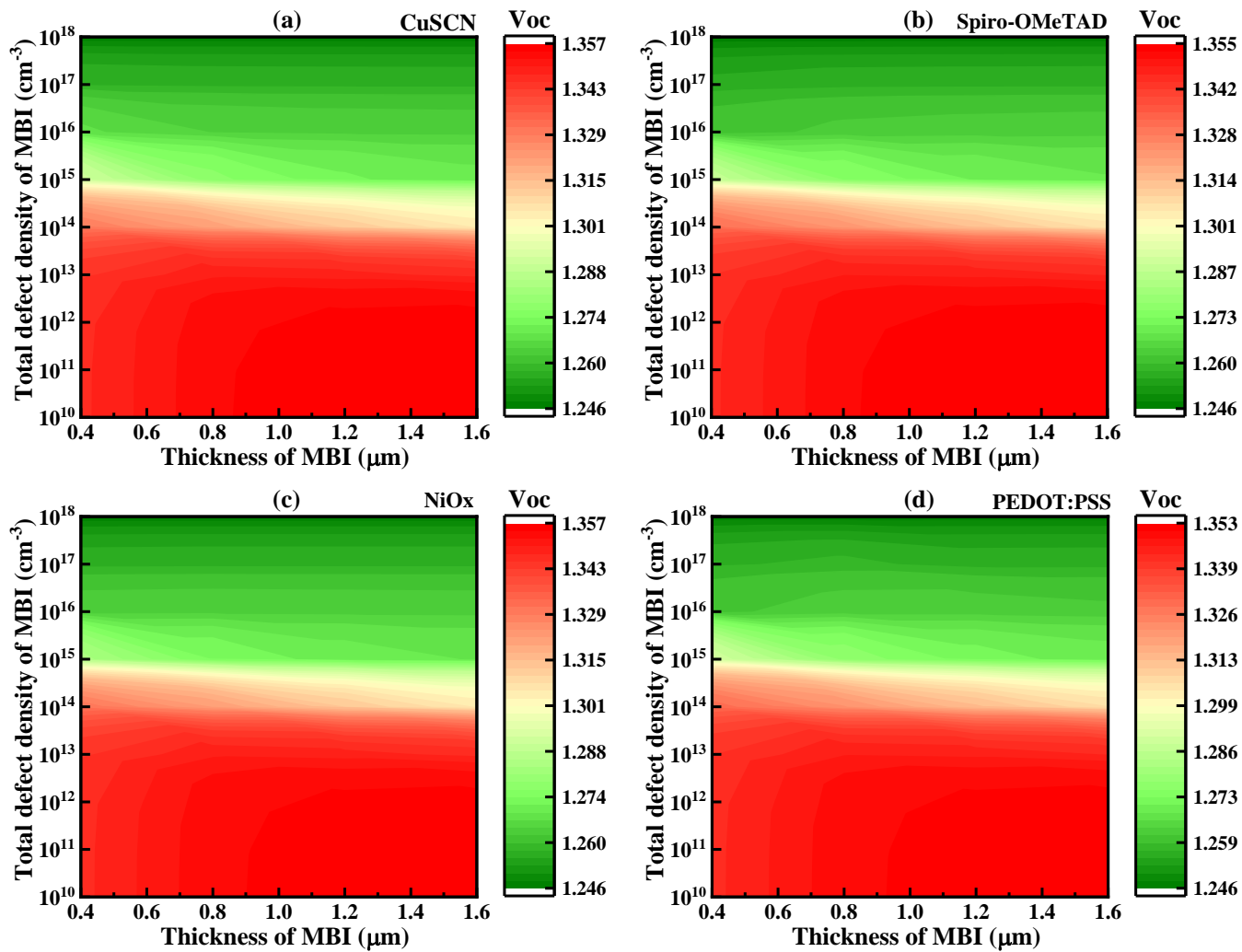


Figure 6.10 Contour mapping: the variation of V_{oc} with respect to the combined total defect density and thickness of the MBI, for (a) CuSCN, (b) Spiro-OMeTAD, (c) NiOx and (d) PEDOT:PSS.

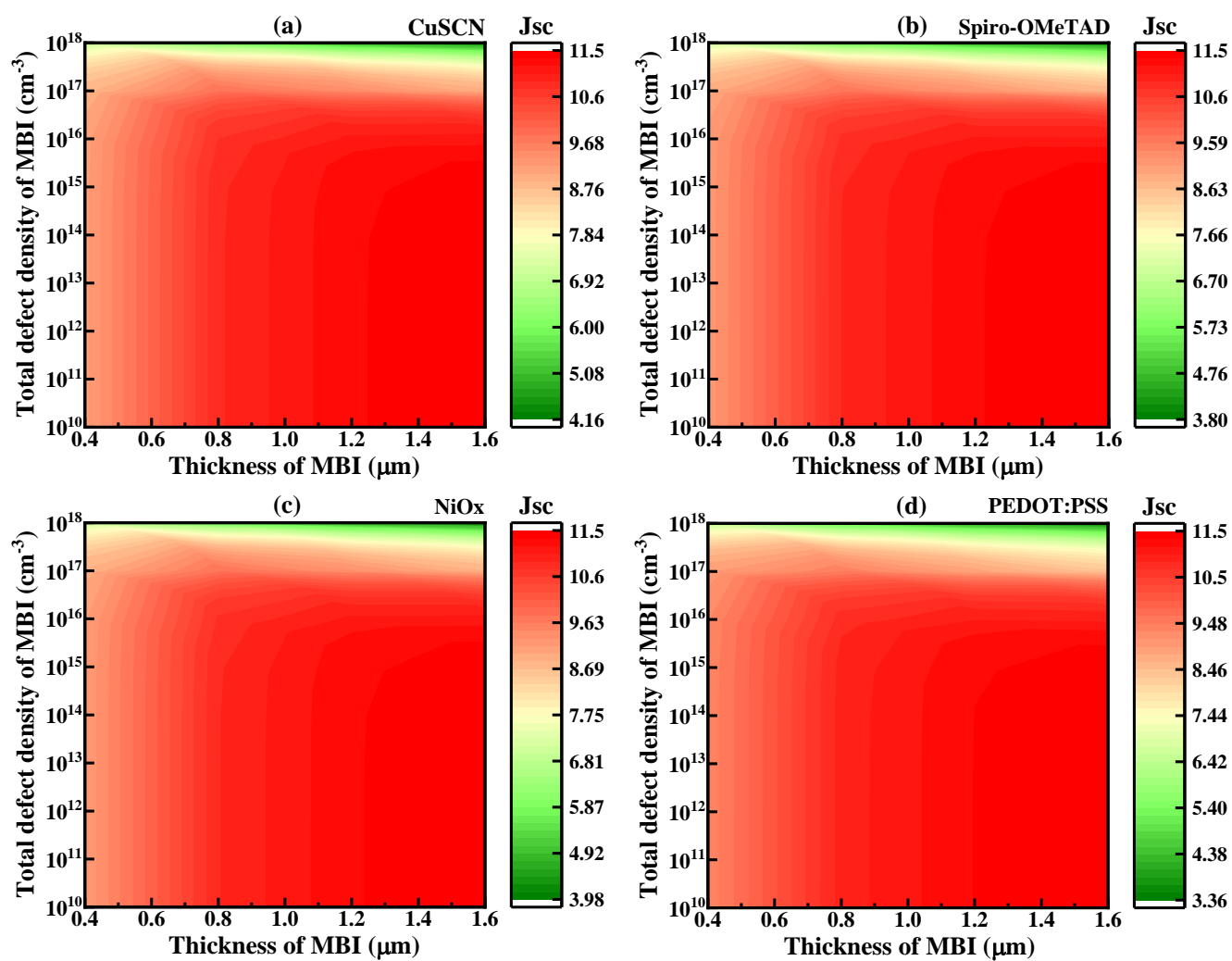


Figure 6.11 Contour mapping: the variation of J_{sc} with respect to the combined total defect density and thickness of the MBI, for (a) CuSCN, (b) Spiro-OMeTAD, (c) NiO_x and (d) PEDOT:PSS.

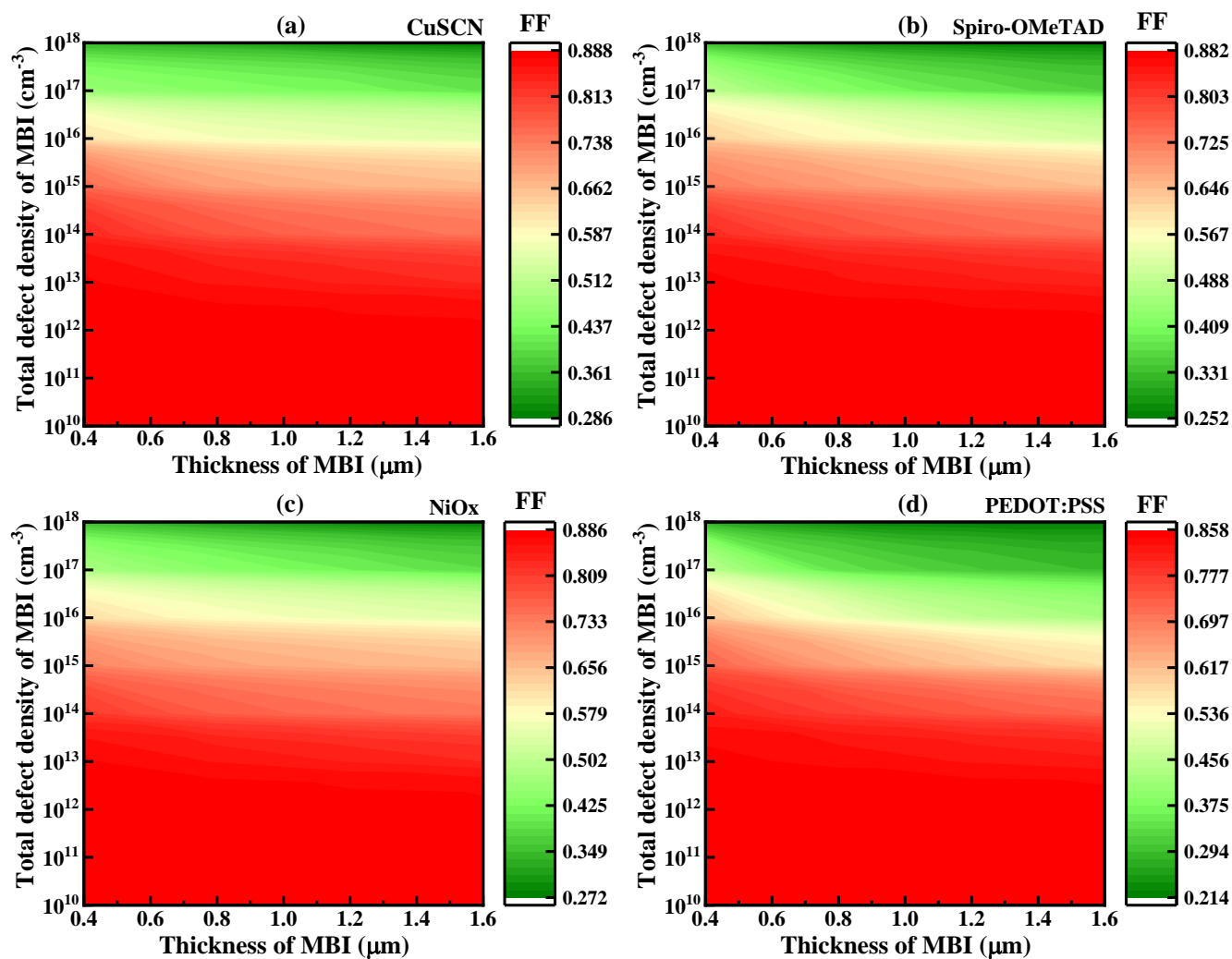


Figure 6.12 Contour mapping: the variation of FF with respect to the combined total defect density and thickness of the MBI, for (a) CuSCN, (b) Spiro-OMeTAD, (c) NiO_x and (d) PEDOT:PSS.

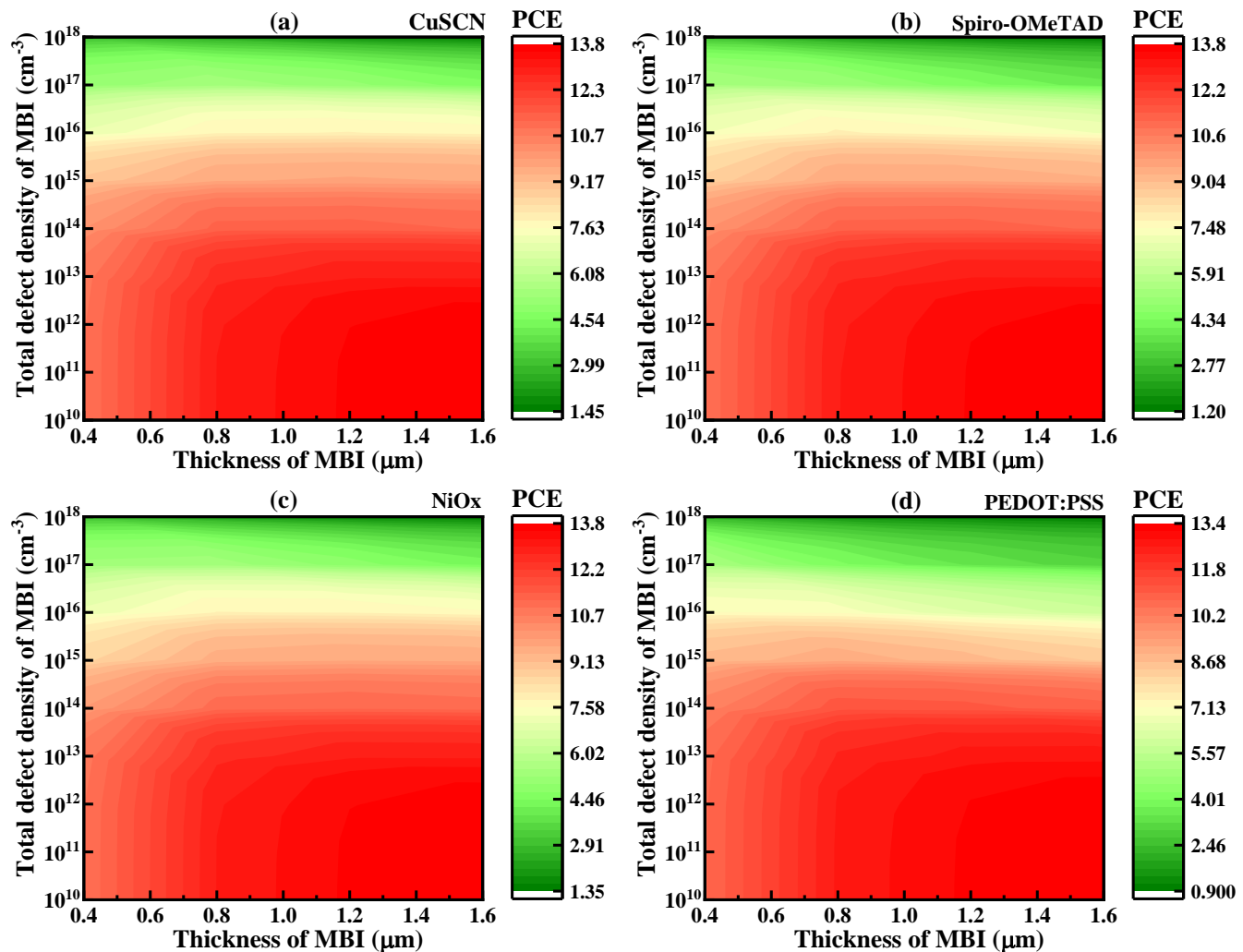


Figure 6.13 Contour mapping: the variation of PCE with respect to the combined total defect density and thickness of the MBI, for (a) CuSCN, (b) Spiro-OMeTAD, (c) NiO_x and (d) PEDOT:PSS.

First, it influences solar absorption, which determines how much energy the cell can capture. It also affects the production of charge carriers, which are necessary for converting light into electrical energy. Through this approach, we will be able to better understand how active layer MBI thickness and total defect density interact, leading to the development of more stable and

effective solar cell designs. In **Figures 6.10-6.13**, we present contour maps for key parameters, such as J_{SC} , V_{OC} , FF, and PCE, for MBI-based photovoltaic cells. These maps examine the effects of changing the thickness of the MBI layer within the 400-1600 nm range, in combination using various HTLs, and take into account a range of overall defect densities of MBI, from 1×10^{10} - $1 \times 10^{18} \text{ cm}^{-3}$.

Figures 6.10(a-d) exhibit similar behavior of V_{OC} across all the different HTL structures using MBI base solar cells. The V_{OC} does not change considerably when the HTLs in the solar cell structures are changed, suggesting that the particular HTL has little effect on V_{OC} . In addition, when the total defect density of the MBI is between 1×10^{10} and $1 \times 10^{14} \text{ cm}^{-3}$, the V_{OC} stays almost constant regardless of the thickness of the MBI, which may range from 400 to 1600 nm. Nevertheless, it is crucial to recognize that the V_{OC} attains its utmost value inside this range. The voltage ranges for various structures are as follows: CuSCN (1.357-1.329 V), Spiro-OMeTAD (1.355-1.328 V), NiOx (1.357-1.329 V), and PEDOT:PSS (1.353-1.326 V), with the total defect density being within the range of 1×10^{10} to $1 \times 10^{14} \text{ cm}^{-3}$. In contrast, the V_{OC} drops to its minimum value and begins to rise again when the total defect density approaches a range of 1×10^{14} to $1 \times 10^{18} \text{ cm}^{-3}$. Here are the V_{OC} ranges for several structures: CuSCN (1.315-1.246 V), Spiro-OMeTAD (1.314-1.246 V), NiOx (1.315-1.246 V), and PEDOT:PSS (1.313-1.246 V). When the total defect density falls within the given range, these findings show that the V_{OC} is unaffected by the MBI thickness. The V_{OC} , on the other hand, drops with increasing total defect density.

The J_{SC} behavior seen in **Figures 6.11(a-d)** remains the same with various HTLs utilizing MBI base solar cells and does not vary significantly. This study investigates the connection between the change in MBI thickness, overall defect density, and how it affects the J_{SC} . In the range of 400 to 800 nm for the MBI thickness, the J_{SC} stays low and reasonably steady; in the region of 900 to

1600 nm, it follows a consistent pattern with larger values, irrespective of the total defect density. The J_{sc} remains very stable within the range of 1×10^{10} to $1 \times 10^{17} \text{ cm}^{-3}$ for the total defect density of the MBI layer, however it does exhibit some variation based on the thickness of the MBI layer. This indicates that the J_{sc} does not drop until the defect density surpasses 1×10^{18} , implying that the J_{sc} stays constant while the thickness stays constant, but the defect density fluctuates within this range. However, the J_{sc} maximizes at different MBI thicknesses between 900 and 1600 nm. The highest J_{sc} values are seen for CuSCN, Spiro-OMeTAD, NiOx, and PEDOT:PSS structures, which are all 11.5 mA/cm^2 . CuSCN (4.16 mA/cm^2), Spiro-OMeTAD (3.80 mA/cm^2), NiOx (3.98 mA/cm^2), and PEDOT:PSS (3.36 mA/cm^2) are the lowest J_{sc} values for each structure. There are a number of factors that influence J_{sc} with thickness, including changes in charge transport mechanisms, light absorption, and charge recombination mechanisms within MBI base solar cells. If we look at **Figure 6.12(a-d)**, we can see that the total defect density rises within the range of 1×10^{10} to $1 \times 10^{18} \text{ cm}^{-3}$, which ultimately leads to a drop in the FF. The FF achieves its maximum and stays reasonably stable between the range of 1×10^{10} to $1 \times 10^{14} \text{ cm}^{-3}$. This indicates negligible change. However, beyond this range, there is a considerable reduction in the FF. MBI thickness does not affect FF when defect density is the same. It can be seen that the FF ranges for several of the structures are as follows: CuSCN (0.8888-0.286), Spiro-OMeTAD (0.882-0.252), NiOx (0.886-0.272), and PEDOT:PSS (0.858-0.214).

Figure 13(a-d) illustrates that the PCE of the MBI solar cell achieves its highest value between 900 and 1600 nm MBI thickness, while maintaining a total defect density ranging from 1×10^{10} to $1 \times 10^{14} \text{ cm}^{-3}$, involving different HTLs. The PCE of MBI solar cells clearly decreases as the thickness falls between 400 and 800 nm. Total defect density, which ranges from 1×10^{14} to $1 \times 10^{18} \text{ cm}^{-3}$, is greater in conjunction with this decline in PCE. With thin MBI thickness, light is limited

to be absorbed, and charges are generated, also with high defect density, there are recombination centers which reduce PCE.

6.5 Simulation performance of 2T tandem cell

6.5.1 MA₃Bi₂I₉/FA_xCs_{1-x}PbI₃ double junction cell

In order to achieve high efficiency when using solar cells, it is important to study and use multi-junctions' solar cells. Multijunction solar cells provide several benefits, such as increased efficiency, a broader absorption spectrum, possible cost reduction, high efficiency, and longevity. For these reasons, they are an exciting new development in solar energy technology. In order to identify the most suitable material for the bottom cell, we incorporated formamidinium (FA) into cesium lead iodide (CsPbI₃), which led to the formation of the alloy FA_xCs_{1-x}PbI₃. Our primary emphasis for the absorber in the bottom cell was FA_{0.45}Cs_{0.55}PbI₃. We operated under the assumption that there is a linear connection between the composition of the alloy (X) and its bandgap (E_g), as well as its electron affinity (χ). The mathematical representation of this connection is as follows²⁸²:

$$E_g(\text{FA}_x\text{Cs}_{1-x}\text{PbI}_3) = X E_g(\text{FAPbI}_3) + (1-X) E_g(\text{CsPbI}_3) \quad (2)$$

$$\chi(\text{FA}_x\text{Cs}_{1-x}\text{PbI}_3) = X \cdot \chi(\text{FAPbI}_3) + (1-X) \chi(\text{CsPbI}_3) \quad (3)$$

Whereas FAPbI₃ has a bandgap of 1.51 eV and an electron affinity of 4.00 eV, while CsPbI₃ has values of 1.73 eV and 3.95 eV.³⁷ We determined the bandgap and electron affinities for the alloys FA_{0.15}Cs_{0.85}PbI₃, FA_{0.45}Cs_{0.55}PbI₃, and FA_{0.75}Cs_{0.25}PbI₃ by analyzing compositions of X = 0.15, 0.45, and 0.75. The bandgap values obtained were 1.70 eV, 1.63 eV, and 1.56 eV, while the electron affinity values were 3.96 eV, 3.97 eV, and 3.99 eV, respectively. **Figure 6.14.**

demonstrates that CsPbI_3 and $\text{FA}_{0.15}\text{Cs}_{0.85}\text{PbI}_3$ do not show any current alignment with the $\text{MA}_3\text{Bi}_2\text{I}_9$ up to a thickness of 2000 nm. Despite both reaching their maximum current, it still remained lower than that of the $\text{MA}_3\text{Bi}_2\text{I}_9$, with PCE of 19.29% and 21.12%, respectively. In contrast, $\text{FA}_{0.75}\text{Cs}_{0.25}\text{PbI}_3$ and FAPbI_3 exhibited successful current matching with $\text{MA}_3\text{Bi}_2\text{I}_9$ when their thicknesses were 450 nm and 320 nm, respectively, as seen in **Figure 6.14**. Significantly, $\text{FA}_{0.45}\text{Cs}_{0.55}\text{PbI}_3$ demonstrated superior performance compared to the other materials that were examined. Using advanced photon management strategies allows the 2T double junction to perform significantly better. Higher-energy photons are efficiently captured by the $\text{MA}_3\text{Bi}_2\text{I}_9$ layer, while lower-energy photons are effectively absorbed by the $\text{FA}_{0.45}\text{Cs}_{0.55}\text{PbI}_3$ substrate. The 2T double junction enhances its overall performance and efficiency by means of this strategic arrangement. In standalone sub-cell simulations, the top cell was illuminated by the AM1.5G solar spectrum, while the bottom cells were illuminated by the first-filtered AM1.5G solar spectrum as shown in **Figure 6.3(a, b)**. In **Table 6.4** lists the optimized simulation parameters for the top cell, and **Table 6.1** lists the parameters for the bottom sub-cell. However, it is crucial to acknowledge that in the tandem design with optimized parameter, the current levels of the top (1600 nm) and bottom (600 nm) sub-cells are not matched. The top sub-cell, which has a smaller J_{sc} than the bottom sub-cell, and the tandem cell have almost the same J_{sc} . Mismatches between currents can cause energy losses and heat generation, which negatively impacts the device's performance. For a tandem system to function properly, heat dissipation must be carefully managed to prevent thermal stress, material degradation, and potential damage.

Table 6.4 Optimized numerical input parameters of the top cell and middle cell.

Parameters	(c+mp) TiO ₂	MA ₃ Bi ₂ I ₉	CuSCN	FA _{0.15} CS _{0.85} PbI ₃	FA _{0.45} CS _{0.55} PbI ₃	FA _{0.75} CS _{0.25} PbI ₃
Thickness (nm)	150	1600	50	2000	800	450
Band Gap (eV)	3.20	2.11	3.4	1.70	1.63	1.56
Electron affinity (eV)	4.2	3.4	1.9	3.96	3.97	3.99
Permittivity	10	9.68	10	6.6	6.6	6.6
DOS at CB (cm ⁻³)	2.2×10 ¹⁸	4.98×10 ¹⁹	2.2×10 ¹⁹	1.2×10 ¹⁹	1.2×10 ¹⁹	1.2×10 ¹⁹
DOS at VB (cm ⁻³)	1.8×10 ¹⁹	2.11×10 ¹⁹	1.8×10 ¹⁸	2.9×10 ¹⁸	2.9×10 ¹⁸	2.9×10 ¹⁸
Electron thermal velocity (cm.s ⁻¹)	1×10 ⁷	1×10 ⁷	1×10 ⁷	1×10 ⁷	1×10 ⁷	1×10 ⁷
Hole thermal velocity (cm.s ⁻¹)	1×10 ⁷	1×10 ⁷	1×10 ⁷	1×10 ⁷	1×10 ⁷	1×10 ⁷
Mobility of electron (cm ² .V ⁻¹ .s ⁻¹)	100	1	100	16	16	2.7
Mobility of hole (cm ² .V ⁻¹ .s ⁻¹)	25	29.7	25	16	16	1.8
Shallow uniform donor density, N _D (cm ⁻³)	1×10 ¹⁹	1×10 ⁹	0	1.3×10 ¹⁶	1.3×10 ¹⁶	1.3×10 ¹⁶
Shallow uniform acceptor density, N _A (cm ⁻³)	0	1×10 ⁹	1×10 ¹⁸	1.3×10 ¹⁶	1.3×10 ¹⁶	1.3×10 ¹⁶
Defect density (cm ⁻³)	1×10 ¹⁵	1×10 ¹⁰	1×10 ¹⁵	1.5×10 ¹⁴	1.5×10 ¹⁴	1.5×10 ¹⁴

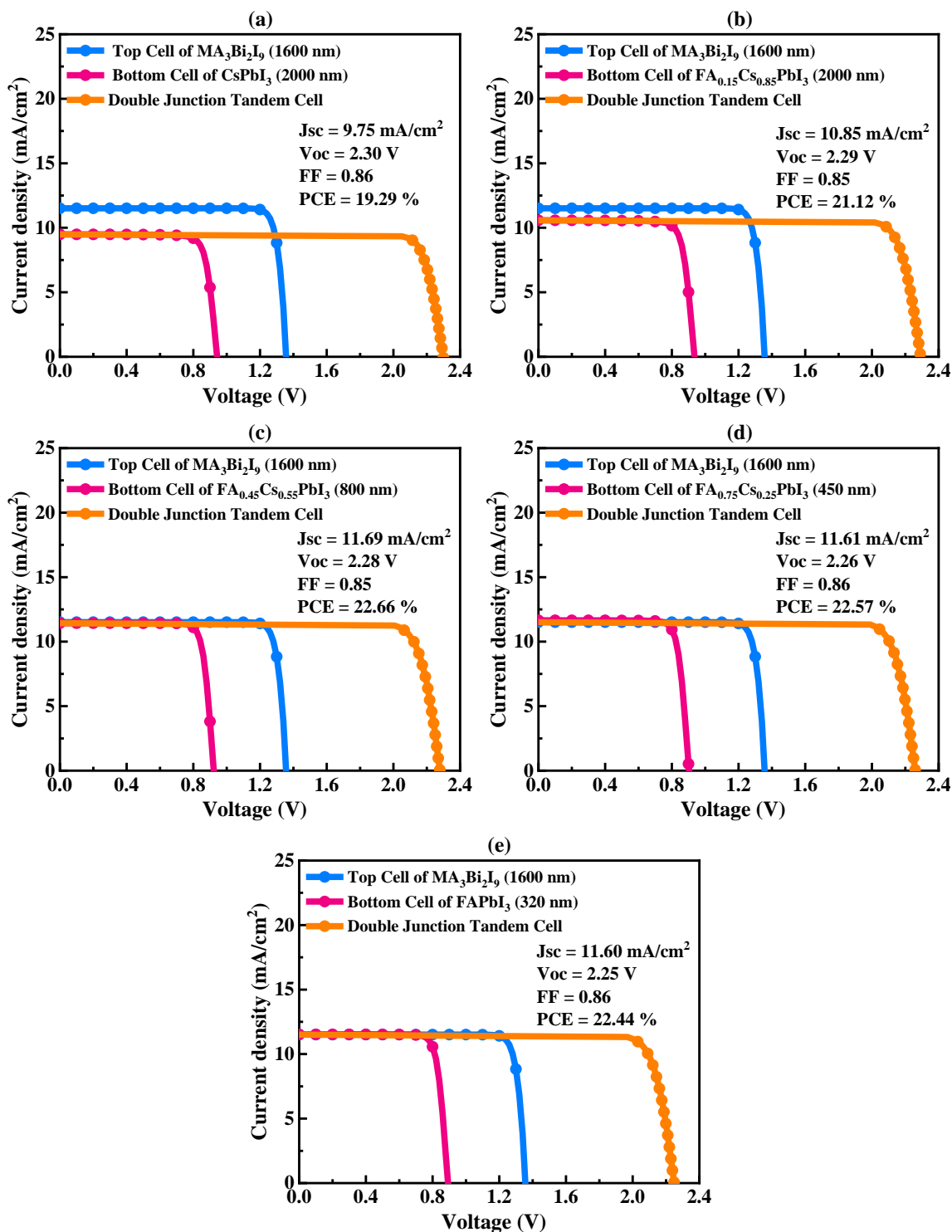


Figure 6.14 J-V characteristics 2T double junction solar cells with current matching conditions for the various middle cells: (a) CsPbI₃, (b) FA_{0.15}Cs_{0.85}PbI₃, (c) FA_{0.45}Cs_{0.55}PbI₃, (d) FA_{0.75}Cs_{0.25}PbI₃, and (e) FAPbI₃.

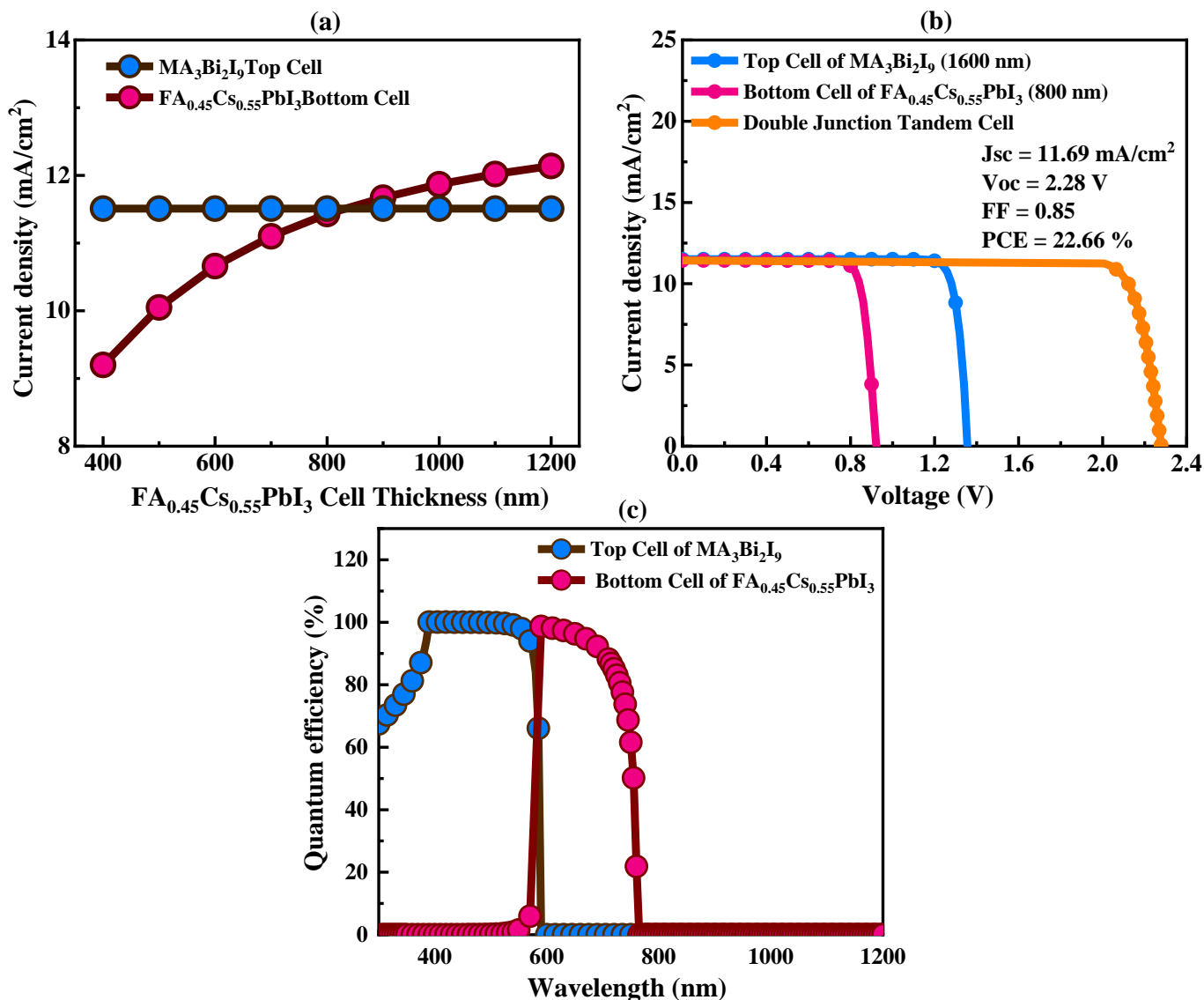


Figure 6.15 (a) Jsc for the top and bottom junction solar cell depending on the two absorbing thicknesses, (b) J-V characteristics top, bottom and 2T double junction solar cells with current matching, and (c) their top and bottom junction QE.

The tandem architecture's total Jsc and PCE are limited by the lower Jsc of the top perovskite cell compared to the middle perovskite cell. According to several studies, 2T double junctions can achieve higher PCE than individual junctions if the current-matching condition is achieved, where the Jsc values of the top and bottom cells are equalized by adjusting the thickness of absorbent

layers.^{34,35} This study achieves current matching by adjusting the thickness of the $\text{FA}_{0.45}\text{Cs}_{0.55}\text{PbI}_3$ layer of the bottom cells while maintaining the thickness of the MBI (1600 nm) in the top cell. In addition, the PCE becomes saturated above 1600 nm, so the MBI thickness is fixed at 1600 nm. Simulation was performed using the 1st filtered AM1.5G solar spectrum, which was filtered through the top junction, for the middle junction of the tandem configuration. According to the findings, which are shown in **Figure 6.15(a)**, when the bottom cell's $\text{FA}_{0.45}\text{Cs}_{0.55}\text{PbI}_3$ layer has a thickness of 800 nm, the current densities of the top and bottom cells match. Accordingly, **Figure 6.15(b)** illustrates the top and bottom junctions' current density versus voltage characteristics, as well as the 2T double junction, illustrating this current-matching condition. **Table 6.5** provides a summary of the output parameters from these simulations for analysis and reference. The 2T double junction has a PCE of 22.66% when the current matches. With PCE values of 13.79% and 8.83%, respectively, the top and middle cells help to achieve this efficiency. Current matching helps to reduce energy loss. As seen in **Table 6.5**, the 2T double junction tandem cell is able to reduce energy losses that would arise in a mismatched situation by making sure that the current densities of the top and middle sub-cells are matched.

Figure 6.15(c) illustrates the relationship between QE and wavelength (λ) for the two sub-cells of the 2T double junction tandem cell with current-matched. The cutoff wavelengths of the two cells are 763 nm for the bottom cell, which is formed of lower-bandgap $\text{FA}_{0.45}\text{Cs}_{0.55}\text{PbI}_3$, and 592 nm for the top cell, which is made up of higher-bandgap perovskite $\text{MA}_3\text{Bi}_2\text{I}_9$. The J_{sc} of $\text{MA}_3\text{Bi}_2\text{I}_9$ and $\text{FA}_{0.45}\text{Cs}_{0.55}\text{PbI}_3$ is comparable because of their nearly comparable spectrum widths. Due to the fact that $\text{MA}_3\text{Bi}_2\text{I}_9$ is thicker than $\text{FA}_{0.45}\text{Cs}_{0.55}\text{PbI}_3$, it has a larger scale QE than the latter. Because of its greater thickness, $\text{MA}_3\text{Bi}_2\text{I}_9$ can absorb more light, which enhances QE. Equivalent heights of the top and bottom cells' QE improve light absorption and electrical performance. The

2T double junction's Voc is calculated by adding the Voc readings that accumulate from each sub-cell.

6.5.2 MA₃Bi₂I₉/FA_{0.45}Cs_{0.55}PbI₃/Si triple junction cell

In the triple junction design, the assessment procedure for the middle cell is identical to that of the bottom cell in the double junction. **Figure 6.16.** shows that FA_{0.45}Cs_{0.55}PbI₃ exhibits the highest performance compared to the other compositions evaluated. This indicates that it is very successful in enhancing the overall efficiency of the triple junction solar cell design. Higher power conversion efficiency and better performance are achieved in triple junction solar cells by using a wider spectrum of sunlight and matching the current across sub-cells to minimize energy losses. According to the simulation conditions, the current in 2T triple junction solar cells current does not match with the bottom cell. The simulation conditions are given in **Table 6.2**, and the bottom cell which is based on silicon heterojunction solar cells was illuminated using the second filter of the AM1.5G solar spectrum, as shown in **Figure 6.3(c)**. This configuration results in energy losses because the bottom cell's (250 μm) current does not match the top (1600 nm) and middle cells' (800 nm) currents. It is necessary to match the currents among the sub-cells in order to resolve this issue. **Figure 6.17(a)** shows how current matching is achieved by fixing the thickness of the top cell while varying that of the bottom cell. When the bottom cell thickness is 41 μm , the current becomes very close to the top and the bottom cell's. As shown in **Figure 6.17(b)**, the current-matched 2T triple junction solar cells have the following J-V characteristics. The output characteristics of the 2T triple junction arrangement are as follows: PCE of 29.89%, FF of 0.84, Jsc of 11.82 mA/cm², and Voc of 3.01 V.

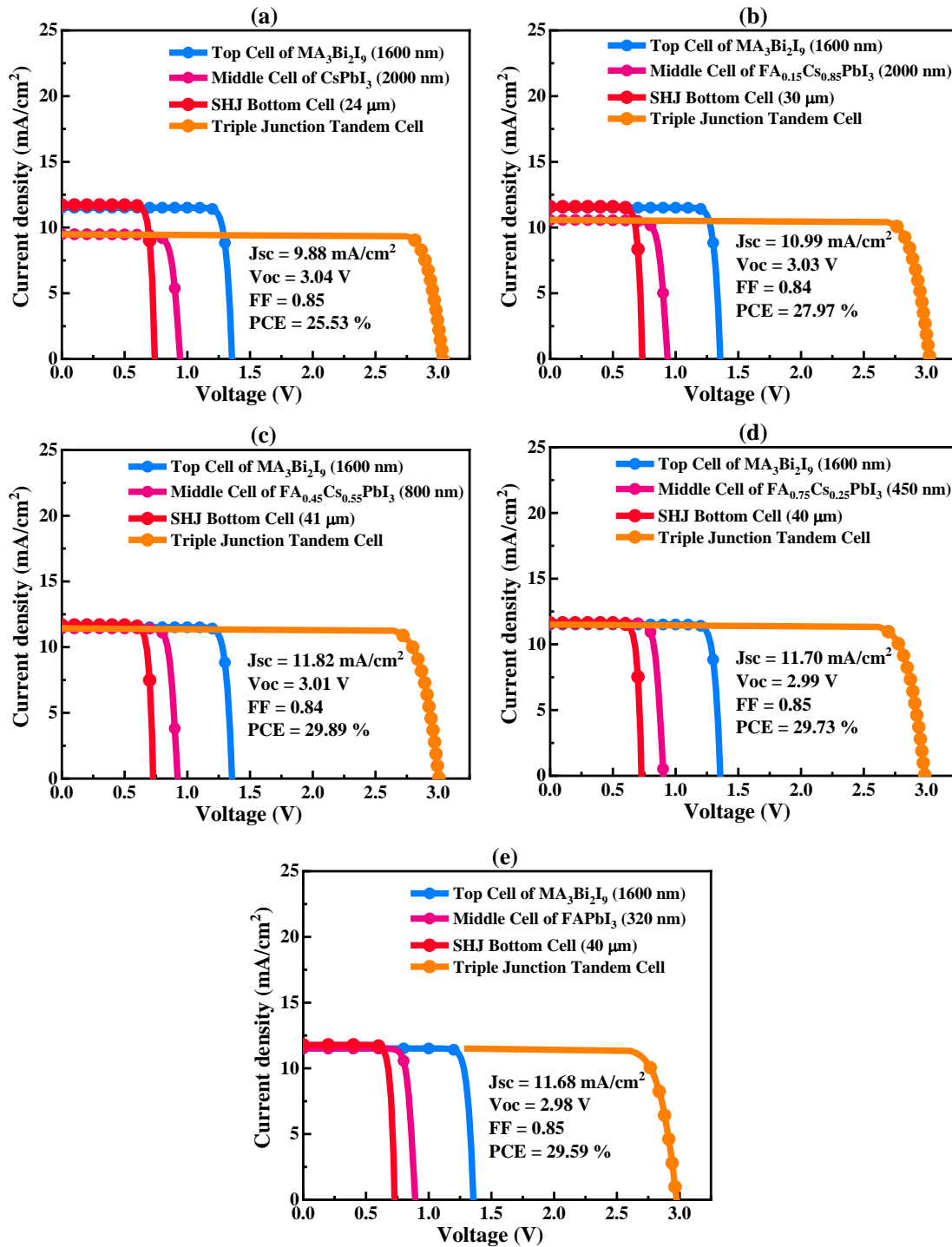


Figure 6.16 J-V characteristics 2T triple junction solar cells with current matching conditions for the various middle cells: (a) CsPbI₃, (b) FA_{0.15}Cs_{0.85}PbI₃, (c) FA_{0.45}Cs_{0.55}PbI₃, (d) FA_{0.75}Cs_{0.25}PbI₃, and (e) FAPbI₃.

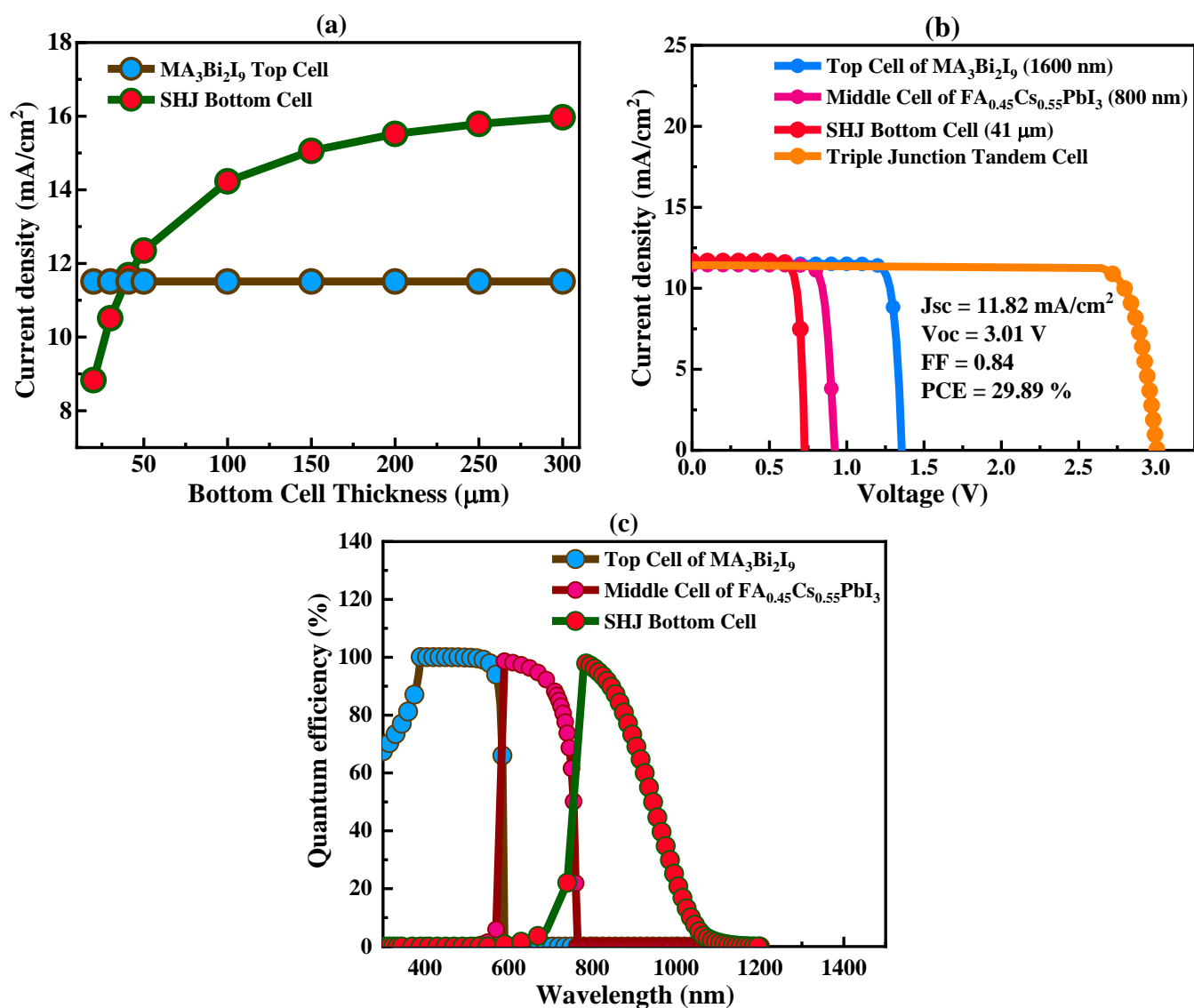


Figure 6.17 (a) J_{sc} for the top and bottom junction solar cell depending on the two absorbing thicknesses, (b) J-V characteristics top, middle, bottom and 2T triple junction solar cells with current matching, and (c) their top, middle and bottom junction QE.

Table 6.5 Compared with and without current matching, output parameters of top, middle, and bottom, 2T double junction and 2T triple junction solar cells.

Solar cell type	Voc (V)	Jsc (mA/cm²)	FF	PCE (%)
Top cell of MA₃Bi₂I₉ (1600 nm)	1.36	11.51	0.88	13.79
Middle cell of FA_{0.45}Cs_{0.55}PbI₃ (800 nm)	0.92	11.43	0.84	8.83
SHJ Bottom cell (41 μm)	0.73	11.68	0.85	7.23
2T Double junction Tandem cell (with current match)	2.28	11.69	0.85	22.66
2T Triple junction Tandem cell (with current match)	3.01	11.82	0.84	29.89

The three junction voltages top, middle, and bottom cells considered all together are the 2T triple junction Voc. The total efficiency, however, rises to 29.89% for the three junction's perovskite/perovskite/c-Si type tandem from 22.66% for the double junction perovskite/perovskite tandem configuration. In recent work, Xu et al. created an outstanding 4-terminal triple-junction tandem solar cell featuring perovskites, perovskites, and silicon, achieving a PCE of 31.5%, an outcome that is extremely similar to that which we acquired.³⁶ The PCE of our double and triple junction cells is, however, slightly lower when compared to reported maximum PCEs. The reason for this disparity is our MA₃Bi₂I₉'s slightly wider band gap, which has an impact on the total performance. Additionally, FA_{0.45}Cs_{0.55}PbI₃ cells exhibited high defects that further affected our results. The achievement of a high PCE despite these limitations is a sign of tandem solar cells' potential to improve solar energy conversion efficiency.

In **Figure 6.17(c)**, we observe QE for the triple sub-cells of the 2T triple junction tandem cell under current-matched conditions. As shown in **Figure 6.15(c)**, the cutoff wavelengths and widths for the middle and top cells are similar. It appears that the bottom cell, which has a lower band gap and a thicker absorbing layer, initially exhibits a lower QE because it penetrates into the middle cell. Increasing wavelength leads to a gradual increase in QE, reaching 100% at 783 nm and then declining to zero at 1080 nm. By increasing the thickness of the bottom cell, more light is absorbed, improving the QE of the device.

6.6 Conclusion

This study contributes several novel thoughts to the investigation of multijunction perovskite base tandem solar cells. Compared to conventional single-junction solar cells, multijunction solar cells provide several benefits. By providing important insights into the characteristics of the $\text{MA}_3\text{Bi}_2\text{I}_9$ sample, the experimental investigation lays the groundwork for future tandem research in solar cell applications. Through experimental analysis, the structural, morphological, and optical characteristics of the $\text{MA}_3\text{Bi}_2\text{I}_9$ sample were revealed. The $\text{MA}_3\text{Bi}_2\text{I}_9$ material proved highly effective for optimizing solar cell performance in simulations. In this study, the MBI base single-junction PCE of 13.80% was achieved by reducing the defect density and increasing the film thickness. As well as this, a remarkable PCE of 22.66% was achieved in a double junction cell configuration with $\text{FA}_{0.45}\text{Cs}_{0.55}\text{PbI}_3$ as the bottom cell. The breakthrough, however, came with the triple junction cell, which achieved a PCE of 29.89% by optimizing its thickness and using $\text{FA}_{0.45}\text{Cs}_{0.55}\text{PbI}_3$ as the middle cell and c-Si as the bottom cell. This study offers a viable path forward for the advancement of solar energy technology in terrestrial applications by creating new opportunities to produce efficient and reasonably priced tandem solar cells.

6.7 References

- (1) Wang, J.; Zardetto, V.; Datta, K.; Zhang, D.; Wienk, M. M.; Janssen, R. A. J. 16.8% Monolithic All-Perovskite Triple-Junction Solar Cells via a Universal Two-Step Solution Process. *Nat. Commun.* **2020**, *11* (1), 1–10.
- (2) Zheng, J.; Wang, G.; Duan, W.; Mahmud, M. A.; Yi, H.; Xu, C.; Lambertz, A.; Bremner, S.; Ding, K.; Huang, S.; Ho-Baillie, A. W. Y. Monolithic Perovskite-Perovskite-Silicon Triple-Junction Tandem Solar Cell with an Efficiency of over 20%. *ACS Energy Lett.* **2022**, *7* (9), 3003–3005.
- (3) Hu, H.; An, S. X.; Li, Y.; Orooji, S.; Singh, R.; Schackmar, F.; Laufer, F.; Jin, Q.; Feeney, T.; Diercks, A.; Gota, F.; Moghadamzadeh, S.; Pan, T.; Rienäcker, M.; Peibst, R.; Nejand, B. A.; Paetzold, U. W. Triple-Junction Perovskite–Perovskite–Silicon Solar Cells with Power Conversion Efficiency of 24.4%. *Energy Environ. Sci.* **2024**, *17* (8), 2800–2814.
- (4) Heydarian, M.; Heydarian, M.; Bett, A. J.; Bivour, M.; Schindler, F.; Hermle, M.; Schubert, M. C.; Schulze, P. S. C.; Borchert, J.; Glunz, S. W. Monolithic Two-Terminal Perovskite/Perovskite/Silicon Triple-Junction Solar Cells with Open Circuit Voltage >2.8 V. *ACS Energy Lett.* **2023**, *8* (10), 4186–4192.
- (5) Liu, S.; Lu, Y.; Yu, C.; Li, J.; Luo, R.; Guo, R.; Liang, H.; Jia, X.; Guo, X.; Wang, Y. D.; Zhou, Q.; Wang, X.; Yang, S.; Sui, M.; Müller-Buschbaum, P.; Hou, Y. Triple-Junction Solar Cells with Cyanate in Ultrawide-Bandgap Perovskites. *Nature* **2024**, *628* (8007), 306–312.
- (6) Yang, T. C. J.; Fiala, P.; Jeangros, Q.; Ballif, C. High-Bandgap Perovskite Materials for

- Multijunction Solar Cells. *Joule* **2018**, 2 (8), 1421–1436.
- (7) Jung, E. H.; Jeon, N. J.; Park, E. Y.; Moon, C. S.; Shin, T. J.; Yang, T. Y.; Noh, J. H.; Seo, J. Efficient, Stable and Scalable Perovskite Solar Cells Using Poly(3-Hexylthiophene). *Nature* **2019**, 567 (7749), 511–515.
 - (8) Rech, B.; Jäger, K.; Korte, L.; Albrecht, S. Numerical Optical Optimization of Monolithic Planar Perovskite-Silicon Tandem Solar Cells with Regular and Inverted Device Architectures. *Opt. Express* **2017**, 25 (12), A473–A482.
 - (9) Shi, Y.; Berry, J. J.; Zhang, F. Perovskite/Silicon Tandem Solar Cells: Insights and Outlooks. *ACS Energy Lett.* **2024**, 9 (3), 1305–1330.
 - (10) Sahli, F.; Werner, J.; Kamino, B. A.; Bräuninger, M.; Monnard, R.; Paviet-Salomon, B.; Barraud, L.; Ding, L.; Diaz Leon, J. J.; Sacchetto, D.; Cattaneo, G.; Despeisse, M.; Boccard, M.; Nicolay, S.; Jeangros, Q.; Niesen, B.; Ballif, C. Fully Textured Monolithic Perovskite/Silicon Tandem Solar Cells with 25.2% Power Conversion Efficiency. *Nat. Mater.* **2018**, 17 (9), 820–826.
 - (11) Chen, B.; Yu, Z.; Liu, K.; Zheng, X.; Liu, Y.; Shi, J.; Spronk, D.; Rudd, P. N.; Holman, Z.; Huang, J. Grain Engineering for Perovskite/Silicon Monolithic Tandem Solar Cells with Efficiency of 25.4%. *Joule* **2019**, 3 (1), 177–190.
 - (12) Shen, H.; Walter, D.; Wu, Y.; Fong, K. C.; Jacobs, D. A.; Duong, T.; Peng, J.; Weber, K.; White, T. P.; Catchpole, K. R. Monolithic Perovskite/Si Tandem Solar Cells: Pathways to Over 30% Efficiency. *Adv. Energy Mater.* **2020**, 10 (13), 1902840.

- (13) Correa Guerrero, N. B.; Guo, Z.; Shibayama, N.; Jena, A. K.; Miyasaka, T. A Semitransparent Silver-Bismuth Iodide Solar Cell with Voc above 0.8 V for Indoor Photovoltaics. *ACS Appl. Energy Mater.* **2023**, *6* (20), 10274–10284.
- (14) Ahmad, K.; Quasim Khan, M.; Alsulmi, A.; Kim, H. Numerical Simulation and Experimental Study of Methyl Ammonium Bismuth Iodide Absorber Layer Based Lead Free Perovskite Solar Cells. *Chem. Eur. J.* **2023**, *29* (35), e202300513.
- (15) Jain, S. M.; Phuyal, D.; Davies, M. L.; Li, M.; Philippe, B.; De Castro, C.; Qiu, Z.; Kim, J.; Watson, T.; Tsoi, W. C.; Karis, O.; Rensmo, H.; Boschloo, G.; Edvinsson, T.; Durrant, J. R. An Effective Approach of Vapour Assisted Morphological Tailoring for Reducing Metal Defect Sites in Lead-Free, $(\text{CH}_3\text{NH}_3)_3\text{Bi}_2\text{I}_9$ Bismuth-Based Perovskite Solar Cells for Improved Performance and Long-Term Stability. *Nano Energy* **2018**, *49*, 614–624.
- (16) Hossain, M. J.; Hossain, M. Over 32% Efficient All-Inorganic Two-Terminal $\text{CsPbI}_2\text{Br/Si}$ Tandem Solar Cells: A Numerical Investigation. *Energy Technol.* **2023**, *11* (3), 2201297.
- (17) Kim, K.; Gwak, J.; Ahn, S. K.; Eo, Y. J.; Park, J. H.; Cho, J. S.; Kang, M. G.; Song, H. E.; Yun, J. H. Simulations of Chalcopyrite/c-Si Tandem Cells Using SCAPS-1D. *Solar Energy* **2017**, *145*, 52–58.
- (18) Madan, J.; Shivani; Pandey, R.; Sharma, R. Device Simulation of 17.3% Efficient Lead-Free All-Perovskite Tandem Solar Cell. *Solar Energy* **2020**, *197*, 212–221.
- (19) Islam, M. A. U.; Kato, S.; Soga, T. An Experimental and Simulation Study of $\text{Cu}_6\text{BiAgI}_{10}$ Photovoltaics with Various Organic and Inorganic Hole Transport Layers for the Improved Photovoltaic Performance of Solar Cells. *Energy and Fuels* **2023**, *37* (24), 19882–19897.

- (20) Hossain, M. K.; Rubel, M. H. K.; Toki, G. F. I.; Alam, I.; Rahman, M. F.; Bencherif, H. Effect of Various Electron and Hole Transport Layers on the Performance of CsPbI₃-Based Perovskite Solar Cells: A Numerical Investigation in DFT, SCAPS-1D, and WxAMPS Frameworks. *ACS Omega* **2022**, 7 (47), 43210–43230.
- (21) Hasanzadeh Azar, M.; Ayneband, S.; Abdollahi, H.; Alimohammadi, H.; Rajabi, N.; Angizi, S.; Kamraninejad, V.; Teimouri, R.; Mohammadpour, R.; Simchi, A. SCAPS Empowered Machine Learning Modelling of Perovskite Solar Cells: Predictive Design of Active Layer and Hole Transport Materials. *Photonics* **2023**, 10 (3), 271.
- (22) Islam, M. A.; Rahaman, M. Z.; Hasan, M. M.; Hossain, A. K. M. A. Analysis of Grain Growth, Structural and Magnetic Properties of Li-Ni-Zn Ferrite under the Influence of Sintering Temperature. *Heliyon* **2019**, 5 (2), e01199.
- (23) Zeng, W.; Liu, X.; Guo, X.; Niu, Q.; Yi, J.; Xia, R.; Min, Y. Morphology Analysis and Optimization: Crucial Factor Determining the Performance of Perovskite Solar Cells. *Molecules* **2017**, 22 (4), 520.
- (24) Ameri, T.; Khoram, P.; Heumüller, T.; Baran, D.; MacHui, F.; Troeger, A.; Sgobba, V.; Guldi, D. M.; Halik, M.; Rathgeber, S.; Scherf, U.; Brabec, C. J. Morphology Analysis of near IR Sensitized Polymer/Fullerene Organic Solar Cells by Implementing Low Bandgap Heteroanalogue C-/Si-PCPDTBT. *J. Mater. Chem. A* **2014**, 2 (45), 19461–19472.
- (25) Wang, H.; Tian, J.; Jiang, K.; Zhang, Y.; Fan, H.; Huang, J.; Yang, L. M.; Guan, B.; Song, Y. Fabrication of Methylammonium Bismuth Iodide through Interdiffusion of Solution-Processed BiI₃/CH₃NH₃I Stacking Layers. *RSC Adv.* **2017**, 7 (69), 43826–43830.

- (26) Wenderott, J. K.; Raghav, A.; Shtein, M.; Green, P. F.; Satapathi, S. Local Optoelectronic Characterization of Solvent-Annealed, Lead-Free, Bismuth-Based Perovskite Films. *Langmuir* **2018**, *34* (26), 7647–7654.
- (27) Park, B.-W.; Philippe, B.; Zhang, X.; Rensmo, H.; Boschloo, G.; Johansson, E. M. J. Bismuth Based Hybrid Perovskites $A_3Bi_2I_9$ (A: Methylammonium or Cesium) for Solar Cell Application. *Adv. Mater.* **2015**, *27* (43), 6806–6813.
- (28) Achoi, M. F.; Aiba, S.; Kato, S.; Kishi, N.; Soga, T. Influence of Post-Annealing on the Properties of Methylammonium Bismuth Iodide Perovskite Solar Cells Through the Hot Immersion Method. *J. Electron. Mater.* **2023**, *52* (1), 351–367.
- (29) Masawa, S. M.; Li, J.; Zhao, C.; Liu, X.; Yao, J. 0D/2D Mixed Dimensional Lead-Free Caesium Bismuth Iodide Perovskite for Solar Cell Application. *Materials* **2022**, *15* (6), 2180.
- (30) Al Ghaithi, A. O.; Aravindh, S. A.; Hedhili, M. N.; Ng, T. K.; Ooi, B. S.; Najar, A. Optical Properties and First-Principles Study of $CH_3NH_3PbBr_3$ Perovskite Structures. *ACS Omega* **2020**, *5* (21), 12313–12319.
- (31) Sen, S. K.; Jalil, M. A.; Hossain, M.; Manir, M. S.; Hoque, K.; Islam, M. A.; Hossain, M. N. Silver Incorporated α - MoO_3 Nanoplates to Nanorods: Exploring the Effects of Doping on Structural, Morphological and Optical Properties. *Mater. Today Commun.* **2021**, *27*, 102404.
- (32) Islam, M. A.; Kato, S.; Kishi, N.; Soga, T. Enhanced Surface Morphology and Photovoltaic Properties of a New Class of Material Copper Silver Bismuth Iodide Solar Cell. *J. Mater.*

Res. Technol. **2023**, *25*, 4171–4186.

- (33) Azadinia, M.; Ameri, M.; Ghahrizjani, R. T.; Fathollahi, M. Maximizing the Performance of Single and Multijunction MA and Lead-Free Perovskite Solar Cell. *Mater. Today Energy* **2021**, *20*, 100647.
- (34) Kumar, A.; Singh, S.; Mohammed, M. K. A.; Shalan, A. E. Computational Modelling of Two Terminal CIGS/Perovskite Tandem Solar Cells with Power Conversion Efficiency of 23.1 %. *Eur. J. Inorg. Chem.* **2021**, (47), 4959–4969.
- (35) Cheng, Y.; Ding, L. Perovskite/Si Tandem Solar Cells: Fundamentals, Advances, Challenges, and Novel Applications. *SusMat* **2021**, *1* (3), 324–344.
- (36) Xu, F.; Liu, J.; Xu, L.; Razzaq, A.; Zhang, X.; Aydin, E.; Wolf, S. De. Four-Terminal Perovskite/Perovskite/Silicon Triple-Junction Tandem Solar Cells with over 30% Power Conversion Efficiency. *ACS Energy Lett.* **2024**, *10*, 3501–3504.
- (37) Hasanzadeh Azar, M.; Ayneband, S.; Abdollahi, H.; Alimohammadi, H.; Rajabi, N.; Angizi, S.; Kamraninejad, V.; Teimouri, R.; Mohammadpour, R.; Simchi, A. SCAPS Empowered Machine Learning Modelling of Perovskite Solar Cells: Predictive Design of Active Layer and Hole Transport Materials. *Photonics* **2023**, *10* (3), 271.

Chapter 7

Conclusions

7.1 Conclusions

We investigated the characteristics of lead-free materials in this study, with a particular emphasis on films of copper silver bismuth iodide ($\text{Cu}_6\text{AgBiI}_{10}$), silver bismuth iodide (Ag_3BiI_6), and methylammonium bismuth iodide ($(\text{CH}_3\text{NH}_3)_3\text{Bi}_2\text{I}_9$). These compounds are meticulously analyzed for their potential as novel active materials in solar cell technology. The examination of these materials underscores their distinct structural and electrical properties while also affirming their potential as sustainable alternatives in the pursuit of effective energy conversion solutions. In **Chapter 2**, we see how the incorporation of inorganic $\text{Cu}_6\text{AgBiI}_{10}$ (CABI) films into photovoltaic applications greatly improves the stability and efficiency of solar cells. For the fabrication of CABI films, a one-step spin coating process was used with hot casting aid. The films were then optimized by annealing temperature. In addition to energy-dispersive spectroscopy (EDS) and scanning electron microscopy (SEM) for morphological evaluations, X-ray diffraction (XRD) examination verified that the films have a homogeneous, pure trigonal crystal structure devoid of impurity peaks. The CABI films' direct bandgap, strong absorbance, and minimal reflection improve their photovoltaic characteristics. The optimized device structure achieved PCE 0.041%. In **Chapter 3**, the research showed that photovoltaic performance is highly dependent on the thickness of the absorbing layer and the electron transport layer (ETL), whereas the thickness of the hole transport layer (HTL) had little effect. In particular, the investigation found that inorganic materials like CuSCN , CuI , and NiOx were better HTLs than organic materials like Spiro-OMeTAD, P3HT, and PEDOT:PSS, demonstrating greater open circuit voltage (V_{oc}) values and efficiency. This

thorough study not only delineates the advantageous properties of CABI films but also functions as a significant resource for researchers aiming to enhance the efficacy of solar energy technology. In **Chapter 4**, we discuss the efficiency of Ag_3BiI_6 solar cells, particularly the uniform grain distribution observed by SEM characterization, indicating that the single-step spin-coating method is effective. This work demonstrates that Spiro-OMeTAD, with its beneficial features, greatly improves the open circuit voltage by combining it with other organic hole transport layers (HTLs) including PTAA, P3HT, and PEDOT:PSS, and using (c+mp)TiO₂ as the electron transport layer (ETL). In particular, FTO/(c+mp)TiO₂/Ag₃BiI₆/Spiro-OMeTAD/Au with an optimized configuration achieved an efficiency of 8.5%, setting the stage for further analysis of various photovoltaic characteristics in order to develop efficient, lead-free Ag₃BiI₆-based solar cells. In **Chapter 5** further examines the development of 2T monolithic rudorffites/c-Si tandem solar cells, representing a notable progression in solar technology. The Ag₃BiI₆'s PCE was improved from 5.77% to 15.26% by optimizing absorb thickness and ETL and HTL properties, contributing to a 22.31% tandem cell efficiency. Additionally, Ag₂BiI₅ and AgBiI₄ were shown to be capable of tandem efficiencies of 18.63% and 18.89%, respectively. The results of this study highlight the viability of rudorffite-based materials as a source of cost-effective, environmentally friendly solar energy. In **Chapter 6** of this research provides innovative perspectives on multijunction perovskite tandem solar cells, emphasizing their superiority compared to single-junction cells. The structural, morphological, and optical features of the MA₃Bi₂I₉ film were disclosed by experimental investigation, laying the groundwork for future study. It is important to note that a single-junction PCE of 13.80% was obtained by optimizing defect density and film thickness, while a double-junction configuration with FA_{0.45}CS_{0.55}PbI₃ achieved a PCE of 22.66%. The triple junction cell achieved the highest level of success with a PCE of 29.89% after extensive optimization. The

results of this study open the door to more practical and economical tandem solar cell technologies for use on earth.

7.2 Future prospective

The potential of bismuth-based perovskite materials for solar cell technology is evident, rendering them viable alternatives to lead-based materials for sustainable energy solutions. To create efficient and economically feasible solar cell technologies, additional study is needed to optimize their performance. For faster advancement and field innovation, future research should deliberately concentrate on many crucial topics. First, future research must concentrate on two crucial experimental analyses: cost-effective production techniques and tandem cell preparation. Researchers may improve production efficiency and scalability by researching alternate synthesis methods. Novel chemical routes and enhanced manufacturing methods will increase solar cell performance by controlling material attributes. This dual approach optimizes solar cell functioning and tackles economic issues necessary for their wider adoption in the renewable energy industry. Second, novel device architecture must be studied. Researchers can improve solar cell efficiency by testing various structures and materials. This involves testing multi-junction designs to improve light absorption and conversion and combining complimentary materials to maximize energy production with lead-free perovskites. In addition, Bi-base perovskite materials must overcome stability concerns to survive in real-world applications. Due to environmental changes that degrade and diminish performance, these materials are difficult to commercialize. To prevent deterioration, future research must study degradation processes and propose techniques like optimizing material composition or encapsulating cells in protective layers to protect them from environmental stresses.

In conclusion, Bi-base perovskite materials have great potential for solar cells. Researchers can help create more sustainable and efficient solar cells by addressing synthesis, device design, and stability issues. Investing in these areas will improve Bi-base perovskite solar cells and help reduce our dependence on fossil fuels and promote renewable energy.

LIST OF PUBLICATIONS

Journals (Included in thesis)

1. **M. A. Islam**, S. Kato, N. Kishi, and T. Soga, “Enhanced surface morphology and photovoltaic properties of a new class of material copper silver bismuth iodide solar cell,” *Journal of Materials Research and Technology*, 25 (2023), 4171-4186 (Publisher: Elsevier) IF: 6.40
DOI: 10.1016/j.jmrt.2023.06.182
2. **Md Arif Ul Islam**, S. Kato, T. Soga, “An Experimental and Simulation Study of $\text{Cu}_6\text{BiAgI}_{10}$ Photovoltaics with Various Organic and Inorganic Hole Transport Layers for the Improved Photovoltaic Performance of Solar Cells.” *Energy & Fuels*, 37 (2023), 19882–19897 (Publisher: American Chemical Society) IF: 5.20
DOI: 10.1021/acs.energyfuels.3c03730
3. **Md Arif Ul Islam**, O. Das, S. Kato, T. Soga, Role of Organic HTLs in Pushing Ag_3BiI_6 Solar Cells to New Heights by Combining Experiment and Simulation: Achieving Maximum Efficiency. *Energy & Fuels*, 38 (2024), 15662–15680 (Publisher: American Chemical Society) IF: 5.20
DOI: 10.1021/acs.energyfuels.4c01791
4. **Md Arif Ul Islam**, T. Kato, S. Kato, T. Soga, The effectiveness of 2-terminal perovskite/perovskite/c-Si triple junction solar cells: An integrated study with an emphasis on methylammonium bismuth iodide. *ACS Applied Materials & Interfaces*, 16 (2024), 53904–53917 (Publisher: American Chemical Society) IF: 8.40
DOI: 10.1021/acsami.4c11816

Accepted

5. **Md Arif Ul Islam**, O. Das, D. B. Khadka, S. Kato, T. Soga, Tandem Solar Cell Approach: Unveiling the Potential of Rudorffite/Silicon Combinations for Providing the Best Solar Cell Performance. *Physica Status Solidi (a)*, (2025) (Publisher: Wiley) IF: 1.9

Journals (Not included in thesis)

6. **M. A. Islam**, M. R. Islam, M. Z. Rahaman, and T. Soga, “First-principles study of physical, and superconducting properties of newly discovered full-Heusler compound MgPd_2Sb ,” *Physica Scripta*, 97 (2022), 125705 (Publisher: IOP Science) IF: 2.90.

DOI: 10.1088/1402-4896/ac9f86

7. **M. A. Islam**, M. R. Islam, O. das, S. Kato, N. Kishi, and T. Soga, “First-Principles Calculations to Investigate the Stability and Thermodynamic Properties of a Newly Exposed Lithium–Gallium–Iridium-Based Full-Heusler Compound,” *ACS Omega*, 8, 24 (2023), 21885–21897 (Publisher: American Chemical Society) IF: 4.10.

DOI: 10.1021/acsomega.3c01534

8. **Md Arif Ul Islam**, O. das, D. B. Khadka, M. R. Islam, M. F. Rahman, S. Kato and T. Soga, “Effect of Low to High Pressure on the Structural, Mechanical, Electrical, and Optical Properties of Inorganic Material Ca_3AsBr_3 : An Ab Initio Investigation,” *ACS Omega*, (2024), (Publisher: American Chemical Society) IF: 4.10.

DOI: 10.1021/acsomega.3c08131

9. D. B. Khadka, **Md Arif Ul Islam**, S. Kato, T. Soga, Fabrication and Properties of Bi_2S_3 Nanowire Thin Film Solar Cells by Spin Coating with Varying Sulfur Concentrations in the Precursor. *Journal of Electronic Materials*, (2024) (Publisher: Springer Nature) IF: 2.20.

List of Conferences

1. Annealing temperature dependent structural, optical, and photovoltaic properties of $\text{Cu}_6\text{AgBiI}_{10}$ solar cells, **Md. Arif Ul Islam**, Keigo Aida, Shinya Kato, Tetsuo Soga, The 84th JSAP Autumn Meeting 2023, Kumamoto, Japan.
2. Effect of Overlayer Coating in Perovskite Thin Film: $\text{CsBi}_3\text{I}_{10}$, Keigo Aida, Taito Kato, **M. A. Islam**, Shinya Kato, Tetsuo Soga, The 84th JSAP Autumn Meeting 2023, Kumamoto, Japan.
3. Photovoltaic performance analysis of organic and inorganic hole transport layer for Cu-Ag-Bi-I based perovskite Solar Cell, **Md. Arif Ul Islam**, Shinya Kato, Tetsuo Soga, 2023 MRS Fall Meeting in Boston, USA
4. A study on Rudorffite Ag_3BiI_6 photo-absorber to improve optoelectronic performance, **Md. Arif Ul Islam**, Shinya Kato, Tetsuo Soga, APSPT-13/ISPlasma 2024/IC Plants 2024, Japan.